

Antiaromaticity, s-Indacene, and Molecular Electronics

by

Isabella S. Demachkie

A dissertation accepted and approved in partial fulfillment of the

requirements for the degree of

Doctor of Philosophy

in Chemistry

Dissertation Committee:

David Johnson, Chair

Christopher Hendon, Advisor

Victoria DeRose, Core Member

Benjamín Alemán Institutional Representative

University of Oregon

Winter 2025

© 2025 Isabella S. Demachkie
This work is openly licensed via CC BY 4.0.



DISSERTATION ABSTRACT

Isabella S. Demachkie

Doctor of Philosophy in Chemistry

Title: Antiaromaticity, *s*-Indacene, and Molecular Electronics

Almost 100 years ago, the publication of Hückel's $[4n + 2]$ π -electrons rule for identifying aromatic compounds piqued the interest of theorists and experimentalists alike. F. London published his quantum theory of interatomic currents in aromatic compounds, commonly referred to as London diamagnetism only one year later. The idea in a nutshell, is that the delocalized ring current of π -electrons found in aromatic molecules behaves like a conductive metal wire. In the 1950's R. Breslow, proposed the idea of antiaromatic $[4n]$ π -electron molecules, (formally referred to as pseudo aromatic) as potentially much more conductive molecular wires. Significant developments in synthetic organic chemistry methodology and techniques over the last 75 years have facilitated the study and isolation of a multitude of antiaromatic and aromatic-antiaromatic hybrid molecules. The valuable molecular properties associated with this class of molecules (such as a small HOMO-LUMO gap, amphoteric redox properties, and low energy absorbance) has motivated further investigation due to their potential materials applications in organic electronics. Antiaromatic molecules have maintained a fundamentally interesting status within the chemistry community because they are extremely reactive, difficult to isolate, and possess interesting electronic properties.

In this dissertation I will discuss conductive materials composed of organic molecules, conductivity as it applies to molecular circuits, molecular wires, the structure-property relationships of antiaromatic heterocycle-fused-*s*-indacene derivatives, and the synthesis and study of donor-acceptor heterocycles fused across *s*-indacene in a set of structural isomers. Chapter I is a historical review of conductive organic materials, electrical conduction in molecular wires, and explanation of the relationship between paratropic ring current strength and diradical character in antiaromatic molecules. Chapter II describes the synthetic methodology of *s*-indacene derivatives developed by the Haley lab, the effect of

heterocycle fusion on the magnetic properties of *s*-indacene, and rationalization of such based on physical organic principals and the rule of topological charge stabilization. Chapter III details the synthesis and effects of asymmetric donor-acceptor heterocycle fusion on the *s*-indacene core and explains the potential impact of this work with reference to superconductivity. Chapter IV is a conclusion. This dissertation includes previously published and unpublished co-authored material.

CURRICULUM VITAE

NAME OF AUTHOR: Isabella S. Demachkie

GRADUATE AND UNDERGRADUATE SCHOOLS ATTENDED:

University of Oregon, Eugene
University of California at Santa Cruz, Santa Cruz

DEGREES AWARDED:

Doctor of Philosophy, Chemistry, 2025 University of Oregon
Bachelor of Science, Chemistry, 2017, University of California at Santa Cruz

AREAS OF SPECIAL INTEREST:

Physical Organic Chemistry
Intermolecular forces and Supramolecular Assembly
Materials Science
Conductive Organic Materials

PROFESSIONAL EXPERIENCE:

Graduate Employee, University of Oregon, 2019-2025
Nanopore Research Associate, Two Pore Guys Inc., 2018-2019

GRANTS, AWARDS, AND HONORS:

Research Scholarship, Synthesis and Study of Novel Helicene Compounds, Deutscher Akademischer Austauschdienst (DAAD), 2024

Research Training Fellowship, Indenoflourene Cyclophanes, National Science Foundation (NSF), 2021

Dean's Academic Honors, University of California at Santa Cruz, 2017

PUBLICATIONS:

I. S. Demachkie, M. P. Miller, G. I. Warren, J. E. Barker, E. T. Strand, L. N. Zakharov, M. M. Haley, *Angew. Chem. Int. Ed.* **2024**, *64*, e202420989.

G.I. Warren, K. Młodzikowska-Pieńko, S. Jalife, I. S. Demachkie, J. I. Wu, M. M. Haley, R. Gershoni- Poranne, *Chem. Sci.*, **2025**, *16*, 575-583.

T. A. Shear, L. J. Zocchi, I. S. Demachkie, H. J. Trubenstein, L. N. Zakharov, D. W. Johnson.
Expanding *Eur. J. Org. Chem.* **2022**, 26, e202200056.

ACKNOWLEDGMENTS

I would first and foremost like to thank my parents, family, and friends in California, Washington, Germany, and New Zealand for being with me from far away, I never would have made it this far without your relentless support. I love you guys.

I would like to thank Prof. Chris Hendon for graduating me and reading weird verbose drafts of the same 10 paragraphs, patiently listening to lose ideas, and tolerating me and my relationship with the moon. The happiest I've been in grad school has been the last year I got to spend with Robin, Eoghan, Casey, Brian, Parker, Doran, Byoung-Yong, Tekalign and all the undergrads at the coffee bar and in your student office. Thank you for advising me through the end of my degree. Thank you to Dr. Josh Barker, who mentored me through the beginning of my PhD journey, taught me how to make my favorite molecules in the world, and that presentations, papers, posters, and dissertations are most efficiently done with a lot of candy and an impending deadline. Thank you from the bottom of my heart to Josh and Prof. Jeremy Bard, I will be forever grateful for everything you guys did for me my first and second years, it's been a bumpy road, and I never would have made it without you. Thank you to Augie Witkowski and Allison Van Cleve, I wouldn't have even made it through first year without you two. Thank you to Efrain, Nolan, Gabby, Michael, Megan, Nathan, and all the undergrads and REU students for 4 years of comradery in the Haley lab. Thank you to Prof. Mike Haley and Prof. Darren Johnson for an interesting 4 years, funding, and conferences, I will always appreciate it. Thank you to Prof. Victoria DeRose for sticking with me to the end, and my whole committee; Prof. David Johnson, Prof. Christopher Hendon, Prof. Victoria DeRose, Prof. Benjamin Aleman for being very understanding with deadlines and letting me graduate. Thank you to Prof. Mike Pluth, for positive feedback when I really needed it, and Prof. Ramesh Jasti and the Jasti Lab for the good times along the way. Thank you to Helen, Leah, Zoe, Kathy, Jannet, Carissa, Christi, Casey, Nanette, Natalie, and Seth, this department would collapse without you. I must thank the University of Oregon for the facilities, the US taxpayer for the NSF funding, and the Germans (and Prof. Oliver Dumele) for the DAAD scholarship and 3 months in Berlin!

Thank you to Diana Gentry, for my first research opportunity at NASA, my first conference, and being a truly inspirational woman in STEM. I would like to thank Prof. Bakthan Singaram, Prof. Gabriella Amberchan, and Prof. Chad Higa for showing me the magic of organic synthesis and taking a chance on a curious undergrad. Thank you, Prof. William Dunbar and Dr. Andrew Smith, for my first industry research opportunity at Two Pore Guys. Thank you, David Klech and Primrose Pisares, (and my high school and college XC teams) for coaching and mentoring me, and making me strong. I would like to thank my undergraduate institution, UC Santa Cruz and all my professors for a strong foundation and well-rounded chemistry education. This work was supported by the National Science Foundation, by grants NRT DGE-2022168, CHE-1954389, and CHE-2246964

DEDICATION

This dissertation is dedicated to all the women in STEM who came before me and blazed a trail, those who hiked it with me, those we lost along the way, and those who will follow in our footsteps. Watch out for snakes.

TABLE OF CONTENTS

Chapter	Page
I. INTRODUCTION	15
1.0 Preamble	15
1.1 A Brief and Selective History of Organic Conductive Materials.....	16
1.2 Molecular Wires	19
1.3 [4n] π -electron Molecules along the AADCC.....	25
1.4 Rational Design and Synthesis of s-Indacene Hybrids	32
II. STRUCTURE PROPERTY RELATIONSHIPS OF S-INDACENE HYBRIDS	35
2.1 Introduction.....	35
2.2 The Heterocycle Effect.....	37
2.3 The Donor Acceptor Topological Charge Argument	41
III. DONOR ACCEPTOR-FUSED-S-INDACENE-DERIVATIVES	48
3.1 Introduction.....	48
3.2 Results and Discussion.....	51
3.2.1 Molecular Design and Solid-State Structures	51
3.2.2 Optical and Electrochemical Properties	55
3.2.3 Magnetic Properties	61
IV. CONCLUSION	69
4.1 Molecular Electronics	69
4.2 Conclusion	71
APPENDIX.....	72
REFERENCES CITED.....	165

LIST OF FIGURES

Figure	Page
1. Figure 1.1 Conductive HMTSF-TCNQ molecules.....	17
2. Figure 1.2 Electrical conduction in π -stacked benzene rings	19
3. Figure 1.3 Structural explanations of benzene	20
4. Figure 1.4 Aromatic vs. Antiaromatic charge density	22
5. Figure 1.5 The AADCC from CBD to <i>s</i> -Indacene	28
6. Figure 1.6 The AADCC from <i>s</i> -Indacene to DCPA	30
7. Figure 1.7 General retrosynthesis of <i>s</i> -Indacene derivatives.....	33
8. Figure 2.1 Reported benzoheterocycle-fused- <i>s</i> -indacene derivatives.....	38
9. Figure 2.2 Isoelectronic, unreported, and imaginary analogs	39
10. Figure 2.3 GIMIC plots and resonance structures	40
11. Figure 2.4 Topological charge and donor acceptor resonance structures	42
12. Figure 2.5 Further arrow pushed resonance structures	43
13. Figure 2.6 Asymmetric donor acceptor resonance structures	45
14. Figure 2.7 Induced charge transfer in UV-vis studies.....	46
15. Figure 3.1 Fusion orientations.....	49
16. Figure 3.2 8 new asymmetric <i>s</i> -indacene derivatives	50
17. Figure 3.3 X-ray crystal structures and bond length alternation	54
18. Figure 3.4 Absorbance spectra	57
19. Figure 3.5 Solvatochromic UV-vis studies	58
20. Figure 3.6 Cyclic Voltammograms.....	61

21. Figure 3.7 NICS scans.....	63
22. Figure 3.8 ^1H NMR spectra	67
23. Figure 3.9 ^1H NMR spectra in cyclohexane.....	68

LIST OF TABLES

Table	Page
1. Table 1. Electrochemical, optical, and HOMO-LUMO gaps.....	59
2. Table 2. NICS and ^1H NMR shifts	64

LIST OF SCHEMES

Scheme	Page
1. Scheme 1. General 5 step synthesis for s-indacene derivatives.....	36
3. Scheme 2. Synthesis of IBFBTs and IBFBTS.....	53

CHAPTER I INTRODUCTION

This chapter was written by me with helpful input from Doran Pennington and Prof. Chris Hendon.

1.0 Preamble

The ability for a material to transfer electrical charge (electrons) is conductivity, which is an inherent property of the element or alloy the material is composed of and therefor has limited ability to be *tuned* (increased or decreased ability to transfer charge). In this context, *conductive materials* typically refer to metal and metal alloy-based materials with a 0 eV band gap. A superconducting material is a conductive material that beyond some critical temperature, has zero electrical resistance. Semiconducting materials are defined by their small (<4 eV) band gap, and insulating materials have large band gaps (>4 eV). Most materials composed of organic molecules (plastics) are insulating or semiconducting (based on their fundamental material properties) with low conductivities (<10⁻⁸ mho/cm) that decrease with decreasing temperature, unlike traditional metal based semiconducting materials. The benefits of organic materials over traditional metal based semiconducting materials include flexibility, transparency, and weight to name a few. Semiconducting materials made from organic molecules (organic conductors) come in an ever-growing variety, because of their promise of designer properties and accessed through synthetic modification. Despite their potential, the implementation of organic conductors into commercially available devices is just getting started. Continued progress in this area necessitates an improved understanding of the relationship between the fundamental molecular properties these organic molecules, and the desired properties of resulting materials such as temperature dependent conductivity.

The following is a tangentially related PhD dissertation on antiaromaticity, *s*-indacene derivatives, and molecular electronics.

1.1 A brief and selective overview of the history of organic electronics

In the fall of 1948, a sassy retort from Fritz. London titled, *On the Problem of the Molecular Theory of Superconductivity*, pointed out the assumptions and paradoxes that lead to Heisenberg's electronic superlattice theory.¹ London proposed that instead, superconductivity should be characterized as a condensed state in momentum space and is based on second order perturbation rather than first.² This idea of molecular superconductivity in combination with his theory of the diamagnetic susceptibility of conjugated hydrocarbons,³ lead to a flurry of publications throughout the late 50's and 1960's centered around the idea that the electron delocalization found in the conjugated π -bonds of organic molecules could be considered as a form of conductivity and could (in theory) be thought of as *molecular wires*. Polyacetylene (polyethylene, repeating units of C_2H_2) is the simplest version of a molecular wire and is the basis of 2/5 of the most common plastics used today. Plastics are typically insulators which do not conduct electricity. Nevertheless, at the end of the 1970's a collaborative cross-disciplinary effort between Hideki Shirakawa (polymer chemistry), Alan MacDiarmid (inorganic chemistry), and Alan Heeger (physics), demonstrated that by using halogen mediated doping, free electrons and holes could be introduced rendering the formally insulating polyethylene polymer conductive.⁴ This seminal publication earned its authors the Nobel prize in Chemistry in 2000, and paved the way for the field of conductive polymer (CP) chemistry, which is sustained today. The effective limit of the doping approach is the formation of polarons (sometimes called bipolarons, meaning the recombination of charges). Past a certain amount of doping too many free charges are too close together, so they start recombining, which decreases conductivity because conductivity requires the separation of charges. More information about the development of novel CPs, and the broad range of applications in organic electronics and biomedical applications, can be found in several reviews and texts that the reader is encouraged to check out if interested.^{5,6,7}

In 1964 Little proposed a theoretical infinite, linear, π -conjugated chain appended with polarizable side chains as a CP with room temperature superconductivity. In a nutshell,

the idea was that molecular conductivity requires the exchange of electron density in one direction to facilitate conductivity along a perpendicular axis.⁸ This design would likely be quite difficult to produce because wave functions of the pendant groups are supposed to match the oscillation of the chain. The theoretical chain Little proposes is of infinite length, but the oscillation of a real chain would be dependent on chain length. Assuming chain growth could be controlled, the design of pendant groups with matching wave functions would have to be chain length specific and would require substantial (if not unending) optimization when considering the other requirements of reality such as solubility and synthetic feasibility.

Organic conductors composed of individual organic molecules (as opposed to CPs composed of repeating monomers), promise increased tunability due to the lack of required polymerizable functional groups, and (increased hope for) crystallinity. Polymerizable monomers are challenging to modify synthetically because of the physical space the functional groups require, as well as the limited reaction conditions they can tolerate. The obstacles present in designing organic conductors composed of individual molecules with *interesting electronic properties* are that they are often extremely air sensitive (pentacene and pentacene derivatives), as well as the π -stacking (in order to facilitate proper orbital alignment) requirements in the solid state.⁹ Air sensitivity can often be reduced with synthetic modification, but engineering the crystal packing of organic molecules remains a dark art.

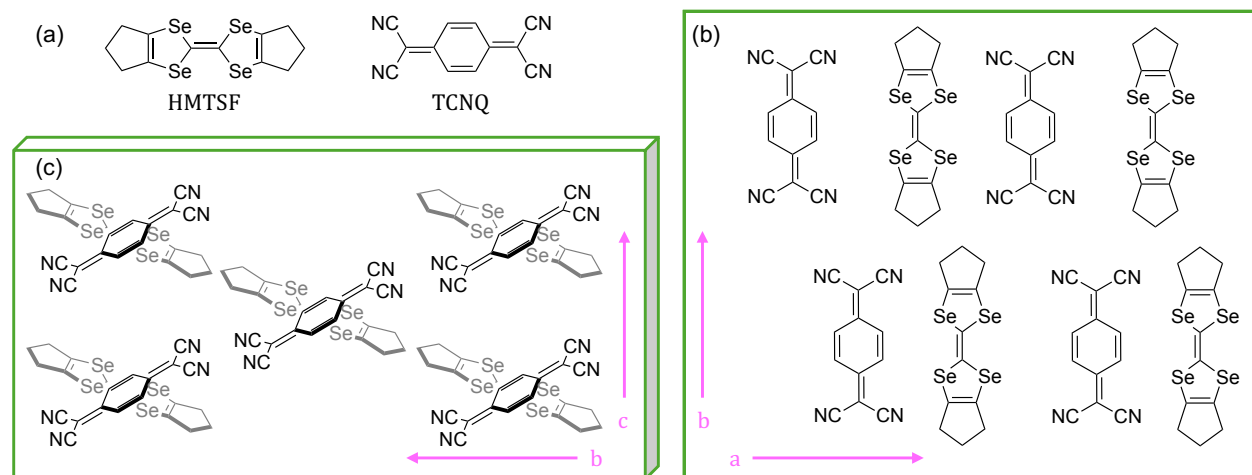


Figure 1.1: (a) Conductive organic donor (HMTSF) and acceptor (TCNQ) molecules. (b) Donor-acceptor interactions between molecules and interchain coupling in the ab plane. (c) Orientation of HMTSF-TCNQ donor-acceptor pairs projected along the a axis. Single crystal conductivity measurements are strongest along the c axis.

Chemists at duPont first reported electrical conductivities (as high as 100 mho/cm) in salts of 7,7,8,8-tetracyanoquinodimethane (TCNQ) in the early '60s.¹⁰ A short while later, materials chemists at Bell Labs and Johns Hopkins had developed several derivatives of tetrathiofulvalenium-7,7,8,8-tetracyanoquinodimethane (TTF-TCNQ) donor acceptor pairs, and by 1972 the first room temperature organic conductor was reported, with conductivity increasing as temperature decreases, to a maximum (10^4 mho/cm) at 59 K.¹¹ Finally, in 1975 Poehler and coworkers reported hexamethylene-tetraselenafulvalenium-7,7,8,8-tetracyanoquinodimethane (HMTSF-TCNQ), the first organic conductor to exhibit metallic conductivity at all temperatures (Figure 1.1).¹² Perhaps the most valuable insight from these studies was the realization that conductivity was strongest in the direction perpendicular to the donor-acceptor interactions, through space via end-to-end orbital overlap (π -stacking) between the aromatic rings. The authors also note temperature dependent phase transitions (metallic to insulating states) in several TTF-TCNQ derivatives because of a Peierls distortion caused by the strong interactions in only one crystallographic direction. HMTSF-TCNQ, the only derivative that exhibited metallic like conductivity at all temperatures, is the largest of the donor molecules and has the strongest interchain coupling (interactions in two crystallographic directions). Weak interactions between chains of alternating molecules establishes the Fermi level of the system. The highest occupied wave functions of the individual molecules are the π -orbitals of aromatic rings perpendicular to the plane of the molecule. π -stacking between layers (c direction) allows for end to end π orbital overlap of the highest energy orbitals facilitating electrical conduction vertically through the stacks of molecules. These results corroborated Little's theory, albeit not with a linear chain, but between the p_z orbitals of *aromatic ring* systems, perpendicular to the direction of the donor acceptor and interchain coupling interactions. These results imply the mechanism of conductivity in the π -stacking direction between aromatic ring systems is analogous to the right-hand rule for determining electromagnetic force (EMF), Figure 2. A helpful review of the theory behind magnetoelectricity, and progress in the area of multiferroics in condensed matter physics can be found in the perspectives referenced.^{13,14}

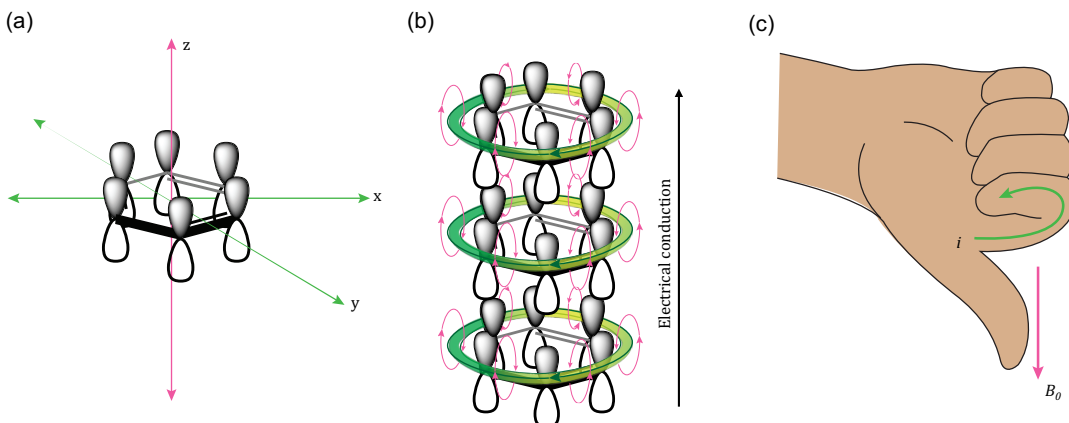


Figure 1.2. (a) Benzene and p_z orbitals with x, y, and z axes defined. (b) π -stacked benzene rings with clockwise ring current in green and induced magnetic field in pink. Electrical conduction flows vertically along the magnetic field lines. (c) The right-hand-rule dictates that a clockwise current in the x-y plane will induce a perpendicular magnetic moment, which is in the negative z-direction.

1.2 Molecular Wires

224 years ago, one of the most influential scientists of all time was born in a village called Newington Butts (now London England). Michael Faraday was a self-made chemist and physicist with very little formal education, who single handedly discovered electromagnetic rotation, induction, and diamagnetism, and was an early pioneer in the field of electrochemistry (among other scientific achievements). Faraday visualized magnetic fields as “magnetic curves... which would be depicted by iron filings” which induction occurred along. After 10 years of work, in 1831 he was able to prove through demonstration that an electric current can be induced by moving a magnet, by turning an electromagnet on and off, or by moving a wire in earth’s magnetic field. These demonstrations converted mechanical energy into electrical energy, which paved the way for the first electric generator and transformer.^{15,16} Between discovering electromagnetic rotation in 1821 and proving induction in 1831, Faraday worked for Humphrey Davey as a chemist and was the first person to isolate benzene (from the condensed gases of pyrolyzed whale oil) in 1825.¹⁷

Several other people synthesized and accessed benzene in different ways throughout Europe and about 40 years after Faraday’s initial report, Kekulé proposed two resonance structures oscillating at equilibria to explain the reactivity of benzene, which informed Thiele’s visual depiction (later popularized by Pauling) of the delocalized structure of

benzene we all know today (Figure 1.3).¹⁸ 100 years of synthesis, study, and daydreaming about benzene and various benzene derivatives finally culminated in Hückel's $[4n+2]$ π -electrons rule for the identification of aromatic molecules in 1931.¹⁹

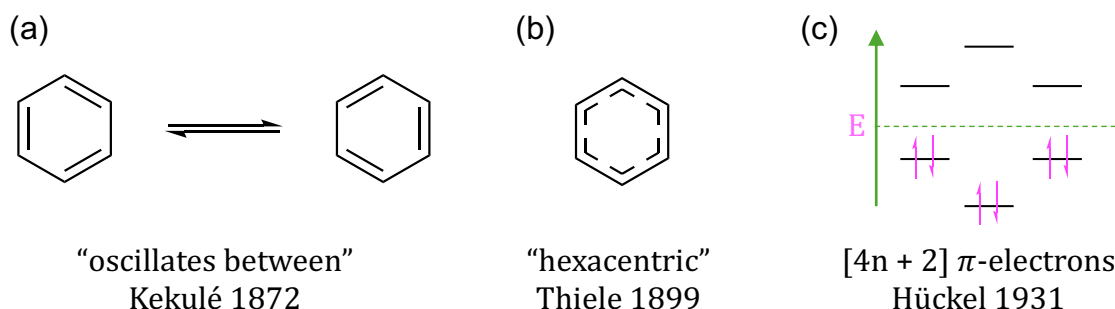


Figure 1.3: a) Kekulé's explanation for the 6-membered cyclic structure of benzene. b) Thiele's suggestion of a hexacentric delocalized electronic structure to explain aromatic stability. c) Hückel's rules for monocyclic aromatic molecules based on the MO diagram for benzene.

Aromatic molecules are defined by their unusual stability. In other words, the difference between the observed heats of formation of benzene and cyclohexatriene (the hypothetical unconjugated resonance structure of benzene), is the resonance energy of benzene.²⁰ This resonance energy manifests as the delocalization of $[4n+2]$ π -electrons in planar, conjugated, cyclic molecules. With Hückel's aromaticity criteria in hand, one year later London published a quantum theory of interatomic currents in aromatic compounds based on Bloch's approximation method and molecular orbital bonding theory, commonly referred to as “London diamagnetism”.³ In the 1950's Pople's ring current model elaborated on London's theory to include the relationship between the strength, size, and shape of the ring current and corresponding induced magnetic field generated.²¹ The works of the aforementioned (and many more unmentioned) chemists and physicists in the 19th and early 20th centuries provided the foundation for some really exciting ideas in the mid 20th century.²²

In the early 1960's several theories emerged with the same core idea, that the electron delocalization found in the conjugated π -bonds of aromatic molecules could be thought of as a form of conductivity and could be described as looped *molecular wires*.²³ In 1965, Ronald Breslow, an organic chemist at Columbia University, first proposed the concept of *antiaromaticity*, based on cyclobutadiene's molecular orbital configuration.²⁴ Breslow's

work in this area largely focused on differentiating antiaromaticity from pseudoaromaticity, and developing experimental methods to quantify antiaromatic character.^{25,26,27} This led to the widely accepted theory that reduced aromaticity or molecules with pronounced antiaromatic character should be more conductive as *molecular wires*. What I think is convoluted is the relationship between the direction of the ring current and the direction of electrical conduction measurable with single molecule conductance studies. The development of the field of molecular electronics necessitates a functional understanding of the relationship between the electronic structure of a given molecule and conductivity.

Chemistry, Physics, and (I'm sure) all fields of study to some extent, have their own language, so words like conductivity mean different things in different contexts. Physics defines conductance (σ) as the reciprocal of resistivity (ρ), and is measured in siemens per meter (S/m). Conductivity is generally defined as the ability of some material to conduct electricity, so $S = \text{amperes/volts (A/V)}$. A material with a conductivity of 1 S would exhibit a conductance increase of 1 amp per every 1 volt increase across some length of that material (m). Electrochemistry measures conductivity of molecules or electrolytes in solution as voltage over impedance, which can also be used to study kinetics of charge transfer in that solution. Charge transfer between molecules in solution is driven by potential energy which comes from the separation of charges (further apart, greater potential energy).^{28,29} Molecular conductivity can be measured and defined in a variety of ways, one of which is single molecule conductance studies where a molecule is held between two electrode tips with an applied current. Breslow's work focused on diamino functionalized aromatic polycyclic ring systems, which are typically thought of as 2-dimensional in the direction the conductivity is measured. So, the conductivity of the molecule is determined as reciprocal of the change in current (resistance) between the electrodes. This method measures the conductivity parallel to the plane of the molecule, which could also be described as intramolecular charge transfer.

When a looped metal wire (and in theory a molecular wire), is subjected to an applied magnetic field, an electrical current is induced in the wire, which in turn produces an induced magnetic field. The direction of induced current in metal wire is dependent only on the relative orientation of the applied magnetic field and the direction the metal wire is being

moved, while the direction of induced current in a molecular wire also depends on the type of molecular wire (Figure 1.4).³⁰ Importantly, in all cases, the direction of electrical current follows the path of the wire, and conductance between wires flows along the magnetic field lines of the induced magnetic field, the strength of which is proportional to the flux of the induced magnetic field? Charge transfer (or conductivity) within molecules relies on orbital overlap, so if the highest occupied wave functions of the individual molecules are the π -orbitals of aromatic rings perpendicular to the plane of the molecule, charge transfer should be strongest in the direction of maximum orbital overlap (end-to-end), which would be perpendicular to the plane of the molecule, not parallel to it.

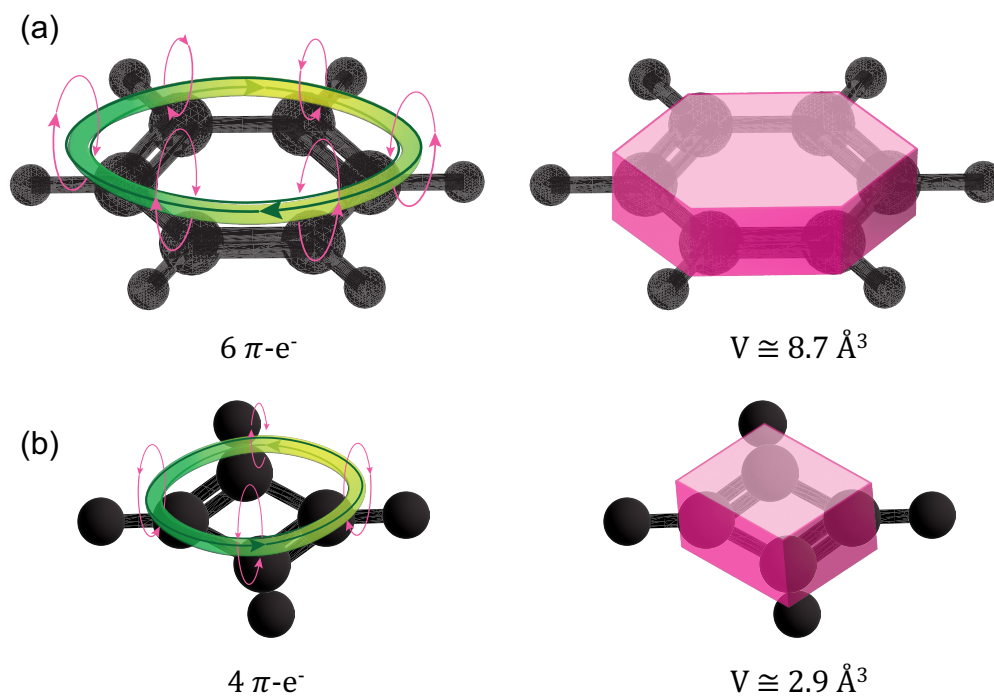


Figure 1.4 (a) Left, 6 π -electron diatropic ring current of benzene illustrated in green. Right, the volume of benzene (approximated as $V = \frac{3\sqrt{3}}{2}(a^2 \cdot h)$, when a = the bond lengths of delocalized benzene, and h = the diameter of a carbon atom) illustrated in pink. (b) Left, 4 π -electron paratropic ring current of cyclobutadiene illustrated in green. Right, the volume of cyclobutadiene (approximated as $V = a^2 \cdot h$), illustrated in pink.

This is why the way molecular conductivity is defined is important. Antiaromatic molecules have stronger ring currents (destabilizing resonance energies)³¹ because of the greater charge density in cyclic structures with $[4n]$ π -electrons (Figure 1.4).^{21,32} When single molecule conductance studies include aromatic analogs, the single molecule

conductance is higher in the antiaromatic molecules.³³ When π -stacked aromatic rings are measured as the junction in scanning tunneling microscope-based break-junctions (STM-BJ) studies, conductance decreases with increasing rings, ohmic behavior.³⁴ In the HOMO energy level of aromatic and antiaromatic ring systems are typically the π -bonding orbitals of the conjugated ring.

The direction of conductivity that would be significantly greater in materials composed of antiaromatic molecular subunits (relative to analogous aromatic subunits) would be in the direction of π -stacking between the p_z orbitals of vertically aligned molecular subunits.³⁵ As a conducting layer between other materials, the valence band (HOMO) will be higher in energy in antiaromatic molecules, which should be closer to the Fermi level of inorganic conductive materials.³⁶ The Breslow group's initial STM-BJ publication in the early 2000's, included a correlation between the relative aromatic character of a set of molecular wires and oxidation potentials as measured by solution state CV.^{37,38} However, this correlation is frequently mis-cited, and later proved to be limited to aromatic molecules. In the group's 2010 publication, several derivatives of biphenylene were investigated and no correlation between oxidation potential and molecular conductivity as measured by single molecule conductance studies was found.³⁹ Although the authors stated that the antiaromatic character of biphenylene was not prominent (because biphenylene is not antiaromatic), so the study was inconclusive. The body of work generated by the Haley lab over the last 12 years proves that increasing antiaromatic character (in a family of structural isomeric *s*-indacene hybrids) has no correlation with increased or decreased oxidation potential, and instead correlates with decreasing reduction potential as measured by solution state CV.⁴⁰ The difference in electrochemical property trends in aromatic and antiaromatic molecules reminds me of p-type and n-type doped semiconductors. The concept of antiaromaticity is difficult to articulate, which makes identification of structure property relationships in this class of molecules a unique challenge.

Computational studies with decreasingly aromatic 3-coordinate subunits (organic linkers) in metal-organic-frameworks (MOFs) indicate conductivity (based on computed band gaps) increases between layers (π -stacking direction) with decreasing aromaticity

(increasing NICS values) of the linkers.^{41,42,43} Single crystal conductivity measurements of conductive MOFs corroborate this with consistent highest conductivity measured in the direction of π -stacking between the organic linkers.^{44,45} The strength of conduction is determined by the identity (and corresponding HOMO energy level) of the linker.^{42,46,47} Single molecule conductance studies are not a direct way of measuring relative strengths of aromatic or antiaromatic ring current conductivity in fused ring systems.⁴⁸

Conductance increases with decreasing aromatic character in single molecule conductance studies because as the ring current gets weaker (from benzene to naphthalene to anthracene), the molecule's resistance to charge transfer in and out the current decreases. Likewise, single molecule conductance studies with *antiaromatic* molecules have been described as possessing anti-ohmic resistance. The term anti-ohmic refers to Ohm's law which dictates that the resistance of a conductive wire should increase with increasing wire length, so anti-ohmic means the relationship is inverse. It's a term that is relevant for linear (cumulene-like) molecular wires, but in this context it is a convoluted way of saying; molecules composed of fused ring systems do not behave like linear stretches of metal wires, instead they behave like looped metal wires (rings) when they are composed of one or a few rings. As the number of rings increases, the ring current in the single molecule junction gets weaker (regardless of direction), the voltage across the length of the molecule remains constant, and conductivity along the length of the molecule experiences less resistance as it passes through the molecules ring current (becomes more wire like).^{49,50,51} It is interesting that both aromatic and antiaromatic molecules become more conductive with increasing conjugation, because would be anti-ohmic behavior. They also both poses increased diradical character with increased conjugation. As acenes get progressively longer, they become increasingly air sensitive because of cycloaddition reactions with O₂. Antiaromatic molecules are significantly less air sensitive, because their reactivity is fundamentally different.⁵² Unfortunately, the limiting factor for synthesizing novel extended acene like structures (aromatic, antiaromatic, or hybrid) is solution processability (solubility).

1.3 [4n] π -Electron Molecules along the Antiaromatic-Diradical Character Continuum

Antiaromaticity is defined by in the Gold Book of the international Union of Pure and Applied Chemistry (IUPAC),⁵³ based on Minkin's definition as "*antiaromaticity (antithetical to aromaticity) In contrast to aromatic compounds, antiaromatic ones are prone to reactions causing changes in their structural type, and display tendency to alternation of bond lengths and fluxional behavior (see fluxional molecules) both in solution and in the solid. Antiaromatic molecules possess negative (or very low positive) values of resonance energy and a small energy gap between their highest occupied and lowest unoccupied molecular orbitals. In antiaromatic molecules, an external magnetic field induces a paramagnetic electron current. Whereas benzene represents the prototypical aromatic compound, cyclobutadiene exemplifies the compound with most clearly defined antiaromatic properties.*"⁵⁴

Assuming the electronic nature of antiaromatic-aromatic-hybrid molecules can be accurately described as being along a continuum, the following is how I would explain it. I prefer to define the classes of cyclic, conjugated organic molecules as: *formally aromatic*, *formally antiaromatic*, and *nonaromatic* molecules based on structural criterial alone. A molecule is *aromatic* or *antiaromatic* if it belongs to the corresponding formal class (based on planarity and number of π -electrons) AND has a detectable diatropic or paratropic ring current. Therefore, aromaticity and antiaromaticity are not properties themselves, unless those terms are synonymous with diatropic and paratropic ring current respectively. Planar, conjugated, cyclic molecules with [4n] π -electrons exist on a size dependent continuum of antiaromatic to diradical character continuum (AADCC).

For the remainder of this discussion, the following terms will be defined as such:

1. *Formally aromatic*: A class of organic molecules which are conjugated, cyclic, and planar with [4n+2] π -electrons, and behave like increasingly conductive molecular wires with increasing aromatic character.
2. *Aromatic*: A subset of formally aromatic molecule which displays empirical evidence of a diatropic ring current, behave like moderately conductive molecular wires.

3. *Formally antiaromatic*: A class of organic molecules which are conjugated, cyclic, and planar with $[4n]$ π -electrons, and behave like increasingly conductive molecular wires with increasing antiaromatic character.
4. *Antiaromatic*: A subset of formally antiaromatic molecules which displays empirical evidence of a paratropic ring current, behave like highly conductive molecular wires.
5. *Nonaromatic*: A molecule missing one or more criteria that define the classes of formally aromatic and formally antiaromatic molecules, should not behave like a molecular wire.

The first highly coveted antiaromatic synthetic target (which maintains its status today the defining example of antiaromaticity) was cyclobutadiene (CBD). CBD (C_4H_4) delocalizes 4 π -electrons in a conjugated, planar, square shaped ring, resulting in a strongly destabilizing paratropic ring current. Unsubstituted CBD was finally tamed by Cram and coworkers in 1988, and evidence of a paratropic ring current can be found in the 1H NMR spectra which exhibits a sharp peak at 2.3 ppm (below the expected range for isolated alkenes).⁵⁵ However, when tetra-substituted with *t*-butyl groups, Masamune et al. found 4 bands by IR spectroscopy, disproving a D_{4h} symmetry (i.e. no delocalization, no ring current), making (along with several other examples) substituted CBD *formally antiaromatic*.⁵⁶ Interest permitting, the reader is directed to a comprehensive review of the early work on cyclobutadiene, and its various substituted derivatives which informed the community about the reactivity and electronic structure of this strange little molecule, and motivates the study of antiaromatic molecules in perpetuity.⁵⁷ Cyclooctatetraene (COT) is *nonaromatic*, not *formally antiaromatic* because it is not planar. It is cyclic, conjugated, and contains $4n$ π -electrons, but the ring current does not exist because the molecule forms a tub shape. It is (relatively) stable and can be isolated in its unsubstituted form as liquid at room temperature.⁵⁸ COT can be planarized through aromatic ring fusion, at which point it does exhibit evidence of a weak local antiaromatic ring current, but the native (unsubstituted) molecule is *nonaromatic*.⁵⁹ On the other hand, pentalene (the bicyclic analog of COT) is *antiaromatic*. Pentalene contains the same number of π -electrons and carbons as COT but has two less hydrogens and is planar. Pentalene has been isolated in a variety of substituted forms and shows empirical evidence of a paratropic ring current.^{60,61} These definitions

primarily rely on structural and magnetic properties because the structural criteria can be described numerically (by π -electron count) and with symmetry labels.^{62,63} Magnetic properties are definitive because they are experimentally quantified and are directly related to the direction and strength of the ring current.^{16,21,30,64} The magnetic properties define the relative antiaromatic character of molecules along this spectrum. The trends in magnetic properties as measured by proton NMR for a set core length, align with expected energetic property trends as measured by UV-vis and solution state cyclic voltammetry (CV). The HOMO-LUMO gap (can be approximated by the optical gap, which) decreases with increasing antiaromatic character (ring current strength). If antiaromatic molecules can be thought of as molecular wires, and ring current strength is proportional to conductivity, then the susceptibility of the wire to electromagnetic forces should be related on the conductivity of the wire. More specifically, an electronic current is more easily induced in wires with strong ring currents (more antiaromatic character) by magnetic fields, and more sensitive to electromagnetic radiation (absorbs more broadly and lower energy light). The detailed description of the continuum is important because energetic molecular properties (decreasing HOMO-LUMO gap) trend with increasing *n* and corresponding decreasing antiaromatic character. Energetic measurements should only ever be used to compare the effects of synthetic modification of a single structure, for example the optical gap decreases from *anti*-IDBF to *syn*-IDBF because the *syn*-fusion of benzofuran increases the paratropic ring current strength more than the *anti*-fusion of the same heterocycle to the same core (*s*-indacene).^{65,66} The HOMO-LUMO gap decreases from *syn*-IDBF to *syn*-IIDBF with decreasing paratropic ring current strength because conjugation increases from IDBF to IIDBF.^{62,67,68,69}

A small HOMO-LUMO gap is a characteristic of antiaromatic molecules but cannot be a definitive criterion for antiaromaticity, because lots of aromatic molecules have small HOMO-LUMO gaps, and small is relative. Additionally, based on molecular orbital calculations at the TPSSh/def2tzvp level of theory, the HOMO-LUMO gap varies considerably along the AADC. The HOMO-LUMO gap decreases from CBD to pentalene, increases to *s*-indacene, and then decreases to DCPN and DCPA (Figure 1.5 and 1.6). The pseudo-Jahn-Teller (pJT) distortion associated with weakly antiaromatic molecules is a result of the small

HOMO-LUMO gap and refers to the pseudo degenerate HOMO and HOMO-1 energy levels in s-indacene and beyond on the AADC. Jahn-Teller distortion is the molecular equivalent of a peierls distortion, the effects of which increase with increasing density of states near the fermi level in materials, and analogously density of molecular orbital energy levels near the fermi level in materials, and analogously density of molecular orbital energy levels near the HOMO-LUMO gap in molecules. The distortion in molecules with $[4n]$ π -electrons is *pseudo* because the (D_{4h} or D_{2h} for CBD, and D_{2h} or C_{2h} for pentalene and beyond depending on the method of calculation) symmetry does not have any degenerate orbitals, in contrast to benzene (Figure 1.5 b, c). The pJT distortion occurs in molecules with increasing n along the AADCC to stabilize the HOMO-1 bond-alternant ground state (valence tautomer), to avoid forbidden transitions to higher energy and increasingly antiaromatic states.

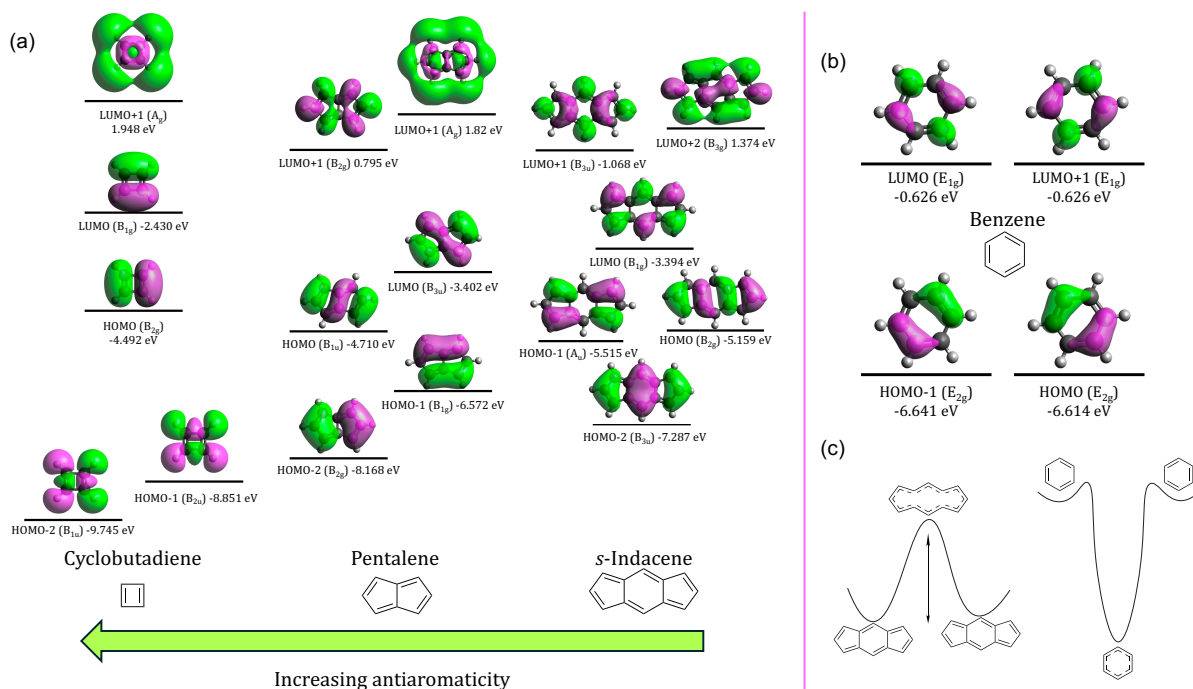


Figure 1.5. (a) AADCC from CBD to s-indacene depicted with molecular orbitals. (b) Benzene's D_{6h} symmetry results in degenerate orbitals (for contrast). (c) pseudo-Jahn-Teller distortion of s-indacene depicted as an energy barrier between two bond-alternant ground states with a delocalized transition state, next to benzene which has a delocalized ground state in an energetic well between two bond alternant resonance structures. Molecular orbital calculations preformed at the TPSSh/def2tzvp level of theory with isosurface values at 0.015 a.u.

It is well established that as the number of π -electrons increase within the class of formally antiaromatic molecules, the strength of the paratropic ring current decreases

(increasing the stability of the delocalized state).⁷⁰ The LUMO+1 state (which is above the vacuum in these calculations, and are meant to be qualitative) for CBD and pentalene looks like delocalized ring currents that becomes increasingly wobbly with increasing n and is no longer continuous in *s*-indacene (LUMO+2). With increasing n , the ring current gets larger and weaker, the stability of the delocalized state increases, dropping from the LUMO+2 of *s*-indacene (above the vacuum) to the LUMO+2 of DCPN (below the vacuum) and then back up to the LUMO+3 of DCPA. This is a visual representation of the antiaromaticity cutoff at *s*-indacene. Also at this point on the continuum, the HOMO and HOMO-1 reverse, and the transition from the HOMO to the LUMO+1 (diradical state) is facilitated by the decreasing HOMO-LUMO gap which trends with increasing conjugation and diradical character from *s*-indacene to dicyclopenta[b,g]anthracene (Figure 1.6).^{71,72} The antiaromaticity cut-off at *s*-indacene aligns with Berger and Viel's interpretation of symmetry criteria for antiaromaticity. Pentalene ($n=2$) and *s*-indacene ($n=3$) are still S_2 symmetric (in terms of K_{ae} cyclic-based point groups) and are antiaromatic, but dicyclopenta[b,g]naphthalene DCPN ($n=4$) and dicyclopenta[b,g]anthracene DCPA ($n=5$) are diradicaloids, and are S_{2n+2} symmetric.⁶³

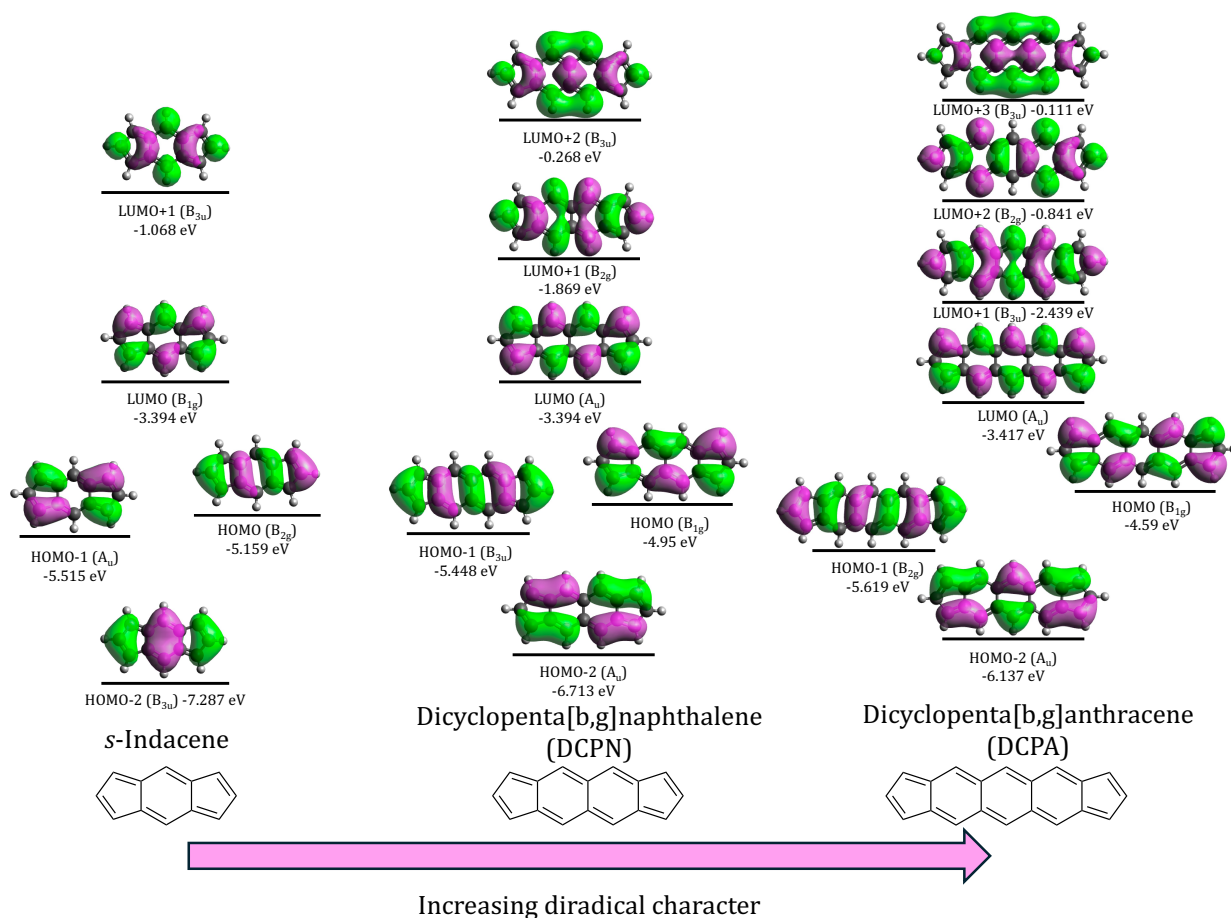


Figure 1.6 AADCC from *s*-indacene to DCPA. Molecular orbital calculations preformed at the TPSSh/def2tzvp level of theory with isosurface values at 0.015 a.u.

The continuum begins at cyclobutadiene (4π -electrons, $n=1$), which has significant *antiaromatic* character in its unsubstituted form, but any thermodynamic (aryl ring fusion) or kinetic (sterically bulky groups i.e. *t*-butyl) render it *formally antiaromatic*. This is because stabilization of the ground state (valence tautomers of D_{2h} symmetry) result in a larger activation barrier and making the delocalized structure less frequently occupied. This differentiation between *antiaromatic* and *formally antiaromatic* is particularly important for CBD derivatives because of the bond length alternation (BLA) discussions in the literature. BLA (in combination with the remaining structural criteria) is evidence of a formally antiaromatic ground state, (or a frozen transition state)⁷³ but not antiaromaticity. For example, multiple reports of aromatic ring fused CBDs (in the absence of protons on the 4-membered ring), cite highly alternating bond lengths and crystal structure bond angles as

evidence of strong antiaromatic character.⁷⁴ There is no reason to believe some novelly substituted phenanthrene fused CBD derivative would be antiaromatic, when every other example reported is only formally antiaromatic because any substitution of CBD stabilizes the bond alternant ground state making the delocalized transition state inaccessible.^{75,76} If it doesn't delocalize it's not *antiaromatic*. Maybe I'm biased, I just think zirconacene chemistry is too perplexing for CBD derivatives.⁷⁷

A recent report from the Yasuda group describes taming the pseudo-Jahn-Teller distortion effect in a pair of dibenzothieno[*a,f*]pentalene isomers via fusion orientation of the thiophene moieties. The authors attribute the decreased energy barrier (E_{a^\ddagger} of less than 1 kcal/mol) to the decreased aromatic character of the fused thiophene rings (relative to benzene), stabilizing the transient C_{2v} -symmetric structure. This could also be thought of as destabilizing the bond alternant ground state, resulting in more pronounced antiaromatic character in the hybrid molecules because of the increased time spent in the transition/excited state.⁷⁸ A similar phenomena (opposite approach, increasing the E_{a^\ddagger}) has also been observed in *s*-indacene and dicyclopenta[*b,g*]naphthalene derivatives, (*syn*-IDBTS and IIDBTS). Thermodynamic stabilization of the ground state was *increased* upon oxidation of the fused (*aromatic*) benzothiophene moieties to (*nonaromatic*) benzothiophene-S,S-dioxides, causing in an increased HOMO-LUMO gap (based on experimental optical and electrochemical gaps). This was described by the authors as "decreasing the antiaromaticity via late-stage modification". Anyway, the result was evidence of valence tautomerization (post oxidation) in the crystal structures, where the bond alternation pattern in the *s*-indacene core reversed. ¹H and ¹³C NMR peaks are sharp at room temperature and indicate a significant E_{a^\ddagger} , and upfield shifted ¹H core proton peaks post oxidation corroborates the claim of decreased antiaromatic character. The observation that this is due to spending less time in the transition state is not mentioned but fits with the reported data.⁷⁹

Thermally accessible diradical character is present in several derivatives of DCPN and DCPA reported by the Haley lab.^{80,81,82} The trends in the optical and electrochemical properties of DCPN and DCPA derivatives indicate increased conjugation is responsible for decreased HOMO-LUMO gaps, because ¹H NMR data (corroborated by NICS scans) implies the deshielding effects of the paratropic ring current decrease from *s*-indacene to DCPN to

DCPA in heterocycle fused and hydrocarbon derivatives.^{62,81,69,83,84,85} Further information on the structure property relationships of formally antiaromatic molecules past the antiaromaticity cutoff ($n > 3$) on the antiaromatic-diradical character can be found in the impending review article from the Haley group at the University of Oregon.

1.4 Rational Design and Synthesis of *s*-Indacene Hybrids

s-Indacene occupies a unique intersection of the antiaromaticity-diradicaloid continuum, at the point of maximum ring current size and the end of the accessibly antiaromaticity. The size of the ring current is inversely related to the strength of the ring current, so compared to cyclobutadiene and pentalene, *s*-indacene is relatively stable. Relatively being the key word, *s*-indacene cannot be isolated in its native form because it will readily react with oxygen to form Janus dione in addition to other degradation pathways under ambient conditions.⁸⁶ However, through the power of organic synthesis, *s*-Indacene can be effectively stabilized through aromatic ring fusion to the outer five-membered rings, and the reactive apical carbons can be kinetically blocked with bulky substituents.

The indeofluorene project began with reports of hydrocarbon structural isomers of indenofluorene, which identified the optimal 12 π -electron scaffold to study the structure property relationships of antiaromatic-hybrid molecules as *s*-indacene.^{87,88} *s*-Indacene can be thermodynamically stabilized by fusion of aryl rings to the outside of the 5-membered rings of the core, the most basic form of which would be symmetric fusion of benzene rings to make indeno[1,2b]fluorene (IF).⁸⁹ Initial investigations into the structure property relationships of IF involved tuning through addition, by altering the identity of the protecting group at the apical carbons.⁹⁰ This tuning direction was not very effective in altering the electronic or magnetic properties of the molecule but does control solid state packing.⁹¹ Relatively quickly, the Haley lab moved from tuning by addition to tuning by fusion through several different methods including π -extension of the *s*-indacene core, π -extension of peripheral aromatics, and the inclusion of heterocycles in the core and peripheral aromatics

in an extremely thorough effort to probe the structure property relationships of this strange class of molecules (Figure 1.7).^{40,92,93}

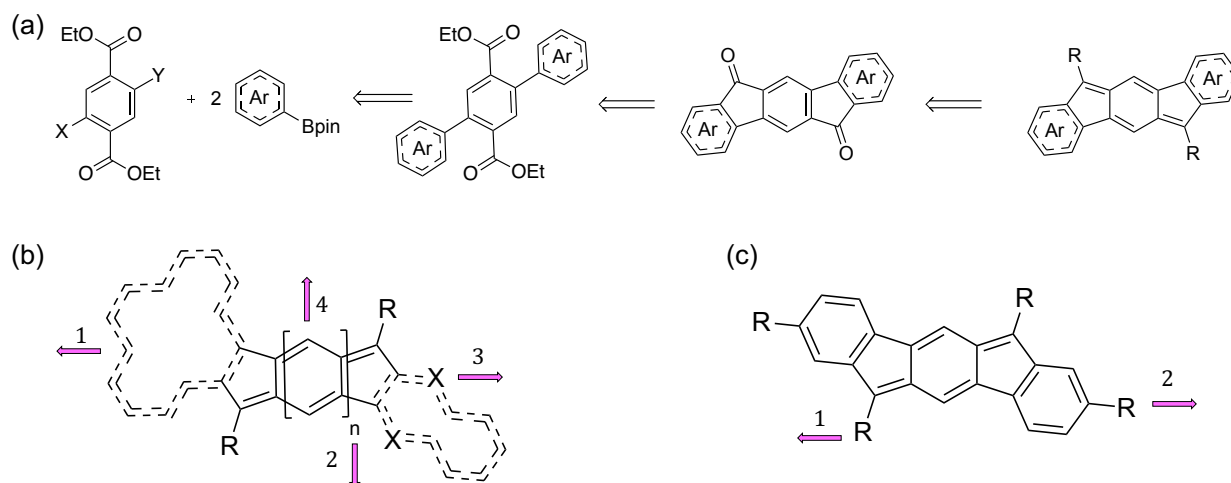


Figure 1.7. (a) general retrosynthesis of IF derivatives. (b) Tuning through fusion occurs within the first set of synthetic steps. Arrows 1 and 3 illustrate tuning through π -extension and heterocycle incorporation of the peripheral aromatics, respectively. Arrows 2 and 4 illustrate π -extension of the core and desymmetrization of the core, respectively. (c) Tuning by addition for arrow 1 occurs as a variable lithiation addition to the diketone intermediate. Tuning by addition for arrow 2 refers to pendant functional groups attached to the peripheral aromatics, which occurs before the first step of the synthesis.

π -Extension of the core by $n=2$, which lead to the synthesis and isolation of fluoreneofluorenes (FF)^{83,94} and eventually by $n=4$ to diarenoanthracene (Dian).^{95,96} The most notable impact of π -extension of the core on the molecular properties is the increasing diradical character with increased core conjugation (relative to *s*-indacene core IFs), which provided valuable insight about the antiaromatic-diradical continuum. The study (and further synthetic modification)^{97,98,99,100,68,101} of extended diradicaloid scaffolds based on the original *s*-indacene IF core is essentially a separate project at this point and is for that reason outside the scope of this discussion.^{102,103} π -Extension of the peripheral aromatics from benzene to naphthalene, had some minor impact on the molecular properties, which was attributed to the change in bond order along the fusion bonds of *s*-indacene. Heterocycle incorporation into the peripheral aromatic stabilizing groups has by far in a way been the most impactful method of synthetic modification for tuning the molecular properties of this family of molecules.^{98,62} I am skipping past several impressive projects that combined multiple modifications (such as π -extended heterocycle peripheral aromatics).^{104,105} The

impact of heterocycle incorporation is dramatic and clearly illustrated by the breadth of NICS values (representative of paratropic ring strength), but the structure property relationships across all heterocycle-fused-s-indacene has yet to be explained (in a way that includes π -accepting heteroatoms).^{106,62,81}

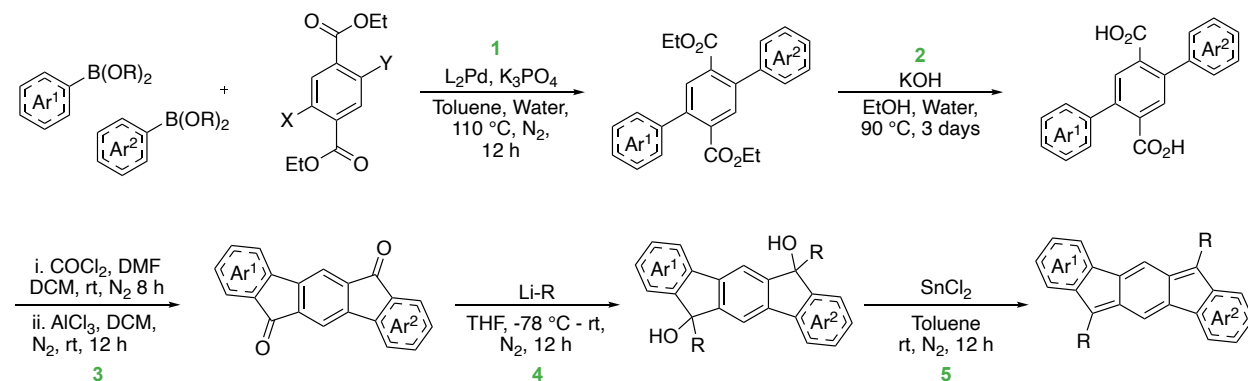
CHAPTER II HETEROCYCLE FUSED S-INDACENE HYBRIDS

The experimental work in this chapter was performed by Isabella S. Demachkie and is unpublished. The computational work in this chapter was performed by Dr. Said Jalifo Jacobo with the help of Prof. Judy I. Wu and is unpublished. This chapter was written by me with computational assistance from Dr. Said Jalifo Jacobo, and helpful input from Brian Diamond, Parker Brodale, and Prof. Chris Hendon.

2.1 Introduction

Aromaticity is a fundamental concept in organic chemistry which explains the stability of benzene and other molecules with $4n+2$ π -electrons in a planar, conjugated ring. Initially proposed by Ronald Breslow in 1965, the term *antiaromaticity* refers to a class of organic molecules with $4n$ π -electrons in a planar, conjugated ring.^[1-4] Antiaromaticity is the “opposite” of aromaticity in that the delocalized ring current (in an applied magnetic field) is diatropic (clockwise) for aromatic molecules, and paratropic (counterclockwise) for antiaromatic molecules. Antiaromatic molecules are fundamentally interesting because they are extremely reactive in a unique way, are nearly impossible to isolate in their unsubstituted form. However, significant work undertaken by various groups has resulted in a library of aromatic-antiaromatic hybrids based on cyclobutadiene,^{107,108} pentalene,¹⁰⁹⁻¹¹¹ and indacene,^{40,112} among others. This work has been in part, motivated by the molecular properties associated with antiaromatic molecules such as a small HOMO-LUMO gap, concomitant red-shifted absorption, amphoteric redox properties, and induced magnetism.¹¹³ These properties are desirable for applications in organic electronics such as organic field effect transistors (OFETs), organic photovoltaics (OPVs), and organic solar cells (OSCs), among other potential future possibilities. They are fundamentally interesting because when fused between diatropic aromatic rings, a paratropic antiaromatic ring current is induced by polarization. The paratropic ring current is detectable by ¹H NMR spectroscopy, and the relative strengths of the ring current (in isomers of the same aromatic-antiaromatic-aromatic system) are accurately illustrated by NICS $\pi_{ZZ1.7}$ plots.^{21,30,93}

The strength of the induced paratropic ring current can be tuned through organic synthesis. The Haley lab has spent the last 15 years systematically synthetically tuning the *s*-indacene scaffold (and extended quinoidal analogs along the antiaromaticity-diradical character continuum (ADCC)). Tetra-iododo-dibenzo[*a,g*]*s*-indacene, first reported by Swager and coworkers in 1994, was not incredibly stable, but provided the inspiration and basis for tetrayne-indeno[1,2*b*]fluorene, which is reasonably stable and was reported by Chase et al a short 16 years later.^{86,114} There were other successful synthetic routes developed in-between the two, which deserve recognition, but are omitted for brevity. Over the last 15 years, the Haley lab has developed a synthetic route that is robust and adaptable enough to facilitate a systematic study of the structure property relationships of *s*-indacene through an isomeric study of aryl-fused-*s*-indacene hybrid molecules. For an in-depth review of the various synthetic methods developed by the Haley lab, please refer to Gabrielle Warren's dissertation.¹¹⁵ The general synthesis is as follows: Beginning with diethyl 2,5-dihaloterephthalate, two equivalents of arylboronic acids or arylboronate esters can be Suzuki cross-coupled either simultaneously or sequentially (to introduce asymmetry), to yield the diester intermediate. The diester is then saponified and then undergoes a subsequent Friedel-Crafts alkylation or (acylation depending on coupling partners) to form the dione. Following the ensuing lithiation addition, a tin-mediated reductive dearomatization yields the antiaromatic *s*-indacene-aromatic-hybrid product (Scheme 1).



Scheme 1. General 5 step synthesis for *s*-indacene derivatives from commercially available starting materials

While the synthesis is robust, the purification of the final products is not for the faint of heart. Organotin compounds (the inevitable biproducts and degradation products of the final

reaction) are notoriously toxic. Making cool molecules usually requires skill and strong reagents, so you (usually) get to pick your poison and how many times you poison yourself. I never ran mine with heat, and I obsessively cleaned my starting material, but increased exposure frequency is inherent to late-stage synthetic optimization projects. Despite the potential health risks, I appreciate the structural diversity of the library of molecules the synthetic methodology has facilitated.

Through a large library of antiaromatic-hybrid molecules, physical organic intuition, topological charge theory, and experimental and computational data I have developed an understanding of the structure property relationships of molecules on the ADCC.^{81,62,93,106} It is understood that all the molecular properties and the structure are all one thing defined by the linear combination of wave functions for each particle. Structure and properties are just how the molecule interacts with different things, so talking about it as a cause-and-effect relationship is silly because quantum mechanics is real. But the physical organic principals that explain reactivity and reaction mechanisms are also real. It all fits together, so it really doesn't matter, you can explain it both ways.

2.2 The Heterocycle Effect

The *s*-indacene scaffold can be tuned through 2 major methods, tuning by addition and tuning through fusion. Step 5 (Scheme 1) is tolerant of a variety of alkyl and phenyl lithiates.^{116,117,118} The reactivity of at the apical carbons requires sterically bulky protecting groups, so mesityl-like R groups are most kinetically stabilizing, and TIPS ethynyl-like groups facilitate the best solid-state packing for the conducting layer of organic electronic devices.^{36,119} Tuning by addition does not have a significant impact on the magnetic or electronic molecular properties, other than fluorinated phenyl groups, which were reported to have reduced the electrochemical gap by up to 0.2 eV.¹²⁰ Tuning through fusion described several different synthetic modifications including π -extension of the *s*-indacene core, π -extension of peripheral aromatics, and the inclusion of heterocycles in the core and peripheral aromatics. The most effective of which is the fusion of heterocycles as the peripheral aromatics. The complete collection of benzoheterocycle-fused-*s*-indacenes published by the Haley lab, can be seen below in Figure 2.1. The defining molecular property

of antiaromatic molecules is the energetically destabilizing paratropic ring current. The relative strength of the ring current (antiaromatic character/antiaromaticity) can be approximated by the shielding effect on the protons on the periphery of the ring caused by the ring current's induced magnetic field. The shielding effect can be measured experimentally by ^1H NMR and accurately predicted and ranked by NICS plots. When NICS plots are computed at B97-2/6-311+G**//M11/6-311+G**^{73,93}

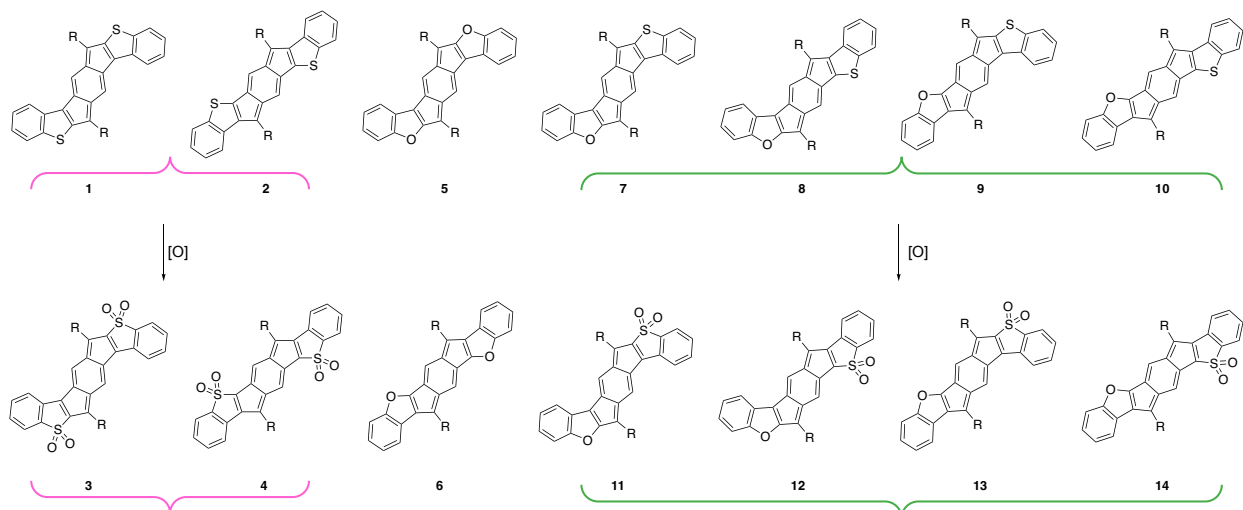


Figure 2.1. All 14 reported benzoheterocycle-fused-s-indacene hybrids by the Haley lab. Pink brackets highlight the symmetric IDBTs (**1** and **2**) and oxidized IDBTs analogs (**3** and **4**). Green brackets highlight the asymmetric IBFBTs (**7 - 10**) and oxidized IBFBTs analogs (**11 - 14**).

The effect of the fusion orientation heterocycles (**1-14**) on the antiaromatic character has been partially explained with reference to Gimarc's rule of topological charge stabilization, which can be summarized as: In a non-isoelectronic structure, there is a preferred (lowest energy) arrangement of topological charge.¹²¹ Natural population analysis (NPA) charges provided by the Wu group in a collaborative publications with the Haley lab reported the points of highest topological charge are at 2 and 6 positions of *s*-indacene.^{62,79} The original NPA calculations of the IDBT (**1** and **2**) and IDBF (**5** and **6**) suggested that the *syn*-fusion (for this subset) was more destabilizing because it enforced a less negative partial charge on the 2 and 6 carbons of the *s*-indacene core, which agreed with the experimental data and NICS calculations for all four molecules. It was thought that the *syn*-IDBF (**5**) was more destabilizing than the *syn*-IDBT(**1**) because oxygen is a better donor than sulfur due to

atomic size and orbital alignment with sp^2 hybridized carbon atoms. Everything was great and made sense until Justin oxidized the IDBTs. The IDBTs (**3** and **4**) flipped trend in fusion orientation effect and made no sense with the topological charge rational. The benzothiophene-*S,S*-dioxide heterocycles should be less donating than benzothiophene, so the IDBTs should have just had less antiaromatic character than the IDBTs but the reason for the trend reversal written off as “being dominated by the clar-sextet effect”.⁷⁹In a more recent computational study, Warren et. al., explain that when fused in the *syn* orientation, O,S, and N-containing heterocycles follow a trend of increasing paratropic ring current strength (antiaromaticity) with increasing donor strength ($N > O > S$). With π -extension of the peripheral benzenes of the fused heterocycles, the strength of the donor effect of the heteroatoms decreases.¹⁰⁶ Elaborating on this explanation, I would agree that the *syn*-fusion of heterocycles to the *s*-indacene core are better oriented to donate, but I would add that the *anti*-fusion of the same heterocycle is better oriented to withdraw from/donate holes to the paratropic ring current, because the current is directional. Electrons and holes each flow in one direction, so depending on whether electrons or holes are being donated, either the *syn* or *anti* fusion orientation accelerates the ring current. Strong π -donors primarily donate electron density, regardless of fusion, and strong π -acceptors primarily withdraw electron density (donate holes), regardless of fusion orientation. These structure property relationships are depicted by calculated benzocyclopentadiene-anion-fused-*s*-indacenes (isoelectronic analogs, IDCPDAs **19**, **20**)

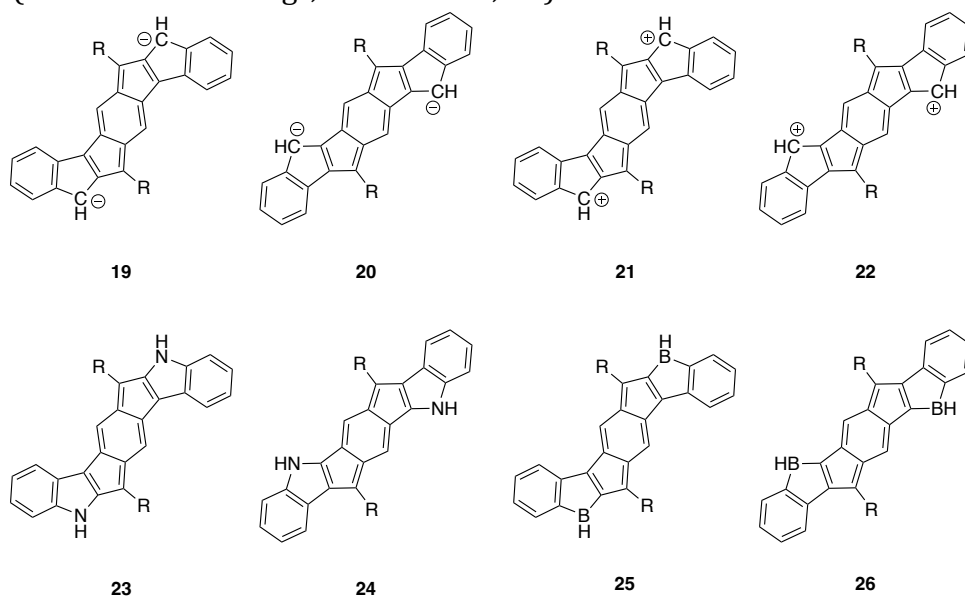


Figure 2.2. Top row, imaginary isoelectronic analogs left to right; *syn*-IDCPDA (**19**), *anti*-IDCPDA (**20**), *syn*-IDCPDC (**21**), *anti*-IDCPDC (**22**). Bottom row left to right; unreported indole-fused *s*-indacenes *syn*-IDI (**23**), *anti*-IDI (**24**), and imaginary borole-fused-*s*-indacenes *syn*-IDB (**25**), *anti*-IDB (**26**).

indacenes (isoelectronic analogs, IDCPDAs **19**, **20**) for the π -donating-heterocycle-fused molecules (**1,2,5,6,7-10**, **23** and **24**), and benzocyclopentadiene-cation-fused-*s*-indacenes (isoelectronic analogs, IDCPDCs **21**, **22**) for the π -accepting-heterocycle-fused molecules (**3,4**, **11-14**, **25** and **26**) seen above in Figure 2.2.

The impact of these effects on the ring current are illustrated by the Gauge-Including Magnetically Induced Current (GIMIC) plots, NICS(1)_{ZZ} ring values, and Natural Population Analysis (NPA) backed resonance structures below (Figure 2.3e).

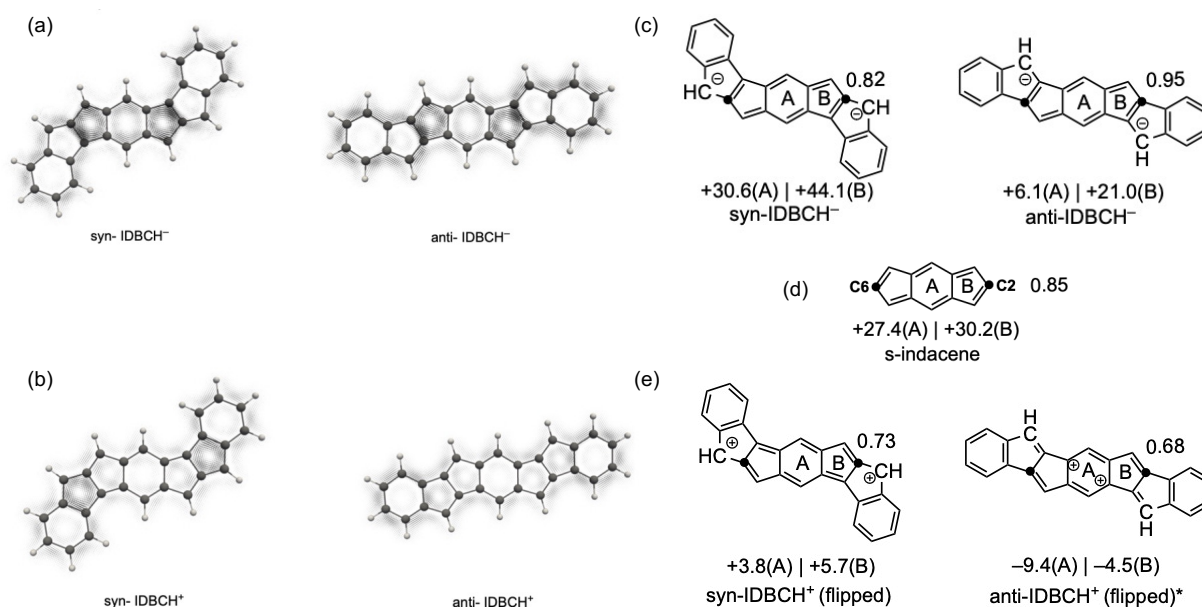


Figure 2.3. (a) GIMIC plots of π -donating isoelectronic analogs (*syn*-IDBCH⁻ and *anti*-IDBCH⁻) and (b) GIMIC plots of π -accepting isoelectronic analogs (*syn*-IDBCH⁺ and *anti*-IDBCH⁺) computed at M11/6-311G** level of theory. (c) NICS(1)_{ZZ} values of π -donating isoelectronic analogs and (d) *s*-indacene and (e) π -accepting isoelectronic analogs computed at the B97-2/6-311+G(d,p) level of theory based on M11/6-311+G** optimized structures, with resonance structures supported by NPA calculations. π -Electron density at the 2 and 6 carbons in (c), (d), and (e) are calculated using extended Hückel theory.

GIMIC plots generated using M11/6-311G** geometry optimized structures, which when placed in an integration plane, produce directional current flow to the left or right of each

grid point. Because tropicity is a non-local property, and every molecule with a ring current contains a paratropic (negative by convention) and diatropic (positive by convention), the streamlines (spaghetti plots which are the basis of the GIMIC plots) illustrate the dominant current.¹²² *Syn*-fusion of CH⁻ induces the strongest paratropic ring current (ring A NICS value) in the *s*-indacene core, followed by *anti*-fusion of CH⁻, followed by *anti*-fusion of CH⁺, then finally *syn*-fusion of CH⁺. Fusion of CH⁻ (π -donors) donates electron density to the *s*-indacene core, accelerating the paratropic ring current. The effect is stronger in the *syn*-fused orientation and weaker in the *anti*-fused orientation, which can be rationalized with the ideas of linear vs cross conjugation for π -donating heterocycles and arrow pushing rational proposed by Warren et. al.⁹⁸ Conversely, *anti*-fusion of CH⁺ (π -withdrawing/hole-donor) accelerates and globalizes the ring current, which is backed by the NPA-generated resonance structure (Figure 2.3e) and highly negative NICS value for ring A. *Syn*-fusion of CH⁺ results in localized ring current on the 5-membered ring of the heterocycle (to stabilize the positive charge), which reduces ring current strength of the *s*-indacene core. NICS(1)_{zz} values for rings A and B are interpreted as ring current strength, where positive values indicate a paratropic ring current and negative values indicate a diatropic ring current, with unsubstituted *s*-indacene for reference (Figure 2.3d). The π -Electron density at the 2 and 6 carbons in (c), (d), and (e) relates to a topological charge stabilization argument discussed further in the following section.

2.3 The Donor-Acceptor Topological Charge Argument

The difference in fusion-dependent magnetic property trends for the π -donating heterocycle-fused *s*-indacene derivatives is explained by an arrow pushing and resonance structure rational, but the effects of the π -withdrawing/hole-donating heterocycle-fused *s*-indacene derivatives are not. Both can be explained by applying donor/acceptor assignments to the *s*-indacene core and both peripheral heterocycles, in combination with the rules of topological charge stabilization. The symmetrically fused π -donating heterocycles act as donors, and the *s*-indacene-core acts as an acceptor in a D-A-D triad. Increased electron density (donated by the heterocycles) is pulled by the π -accepting *s*-indacene core toward its points of preferred highest topological charge (C2 and C6

positions). When the π -donating heterocycles are *syn*-fused, the preferred topological charge arrangement for *s*-indacene is obstructed by the topological charge preferences of the heterocycle, increasing the strength of the paratropic (counterclockwise) current toward the C2 and C6 positions of *s*-indacene. When the π -donating heterocycles are fused *anti*, the preferred topological charge arrangement for *s*-indacene is enforced, which does not induce a pull, and is relatively stabilizing. The symmetrically fused π -accepting heterocycles act as acceptors, and the *s*-indacene-core acts as a donor in a A-D-A triad. When the π -accepting heterocycles are *syn*-fused, the preferred topological charge arrangement for *s*-indacene is obstructed by the topological charge preferences of the heterocycle, but the reversed bond dipole between the heteroatom and C2/6 atom pulls electron density from the *s*-indacene ring current decreasing the strength of the paratropic (counterclockwise) current. When the π -accepting heterocycles are *anti*-fused, the preferred topological charge arrangement for *s*-indacene is enforced by the topological charge preferences of the heterocycle, but the reversed bond dipole between the heteroatom donates holes to the *s*-indacene ring current increasing the strength of the diatropic (clockwise) current (Figure 2.4).

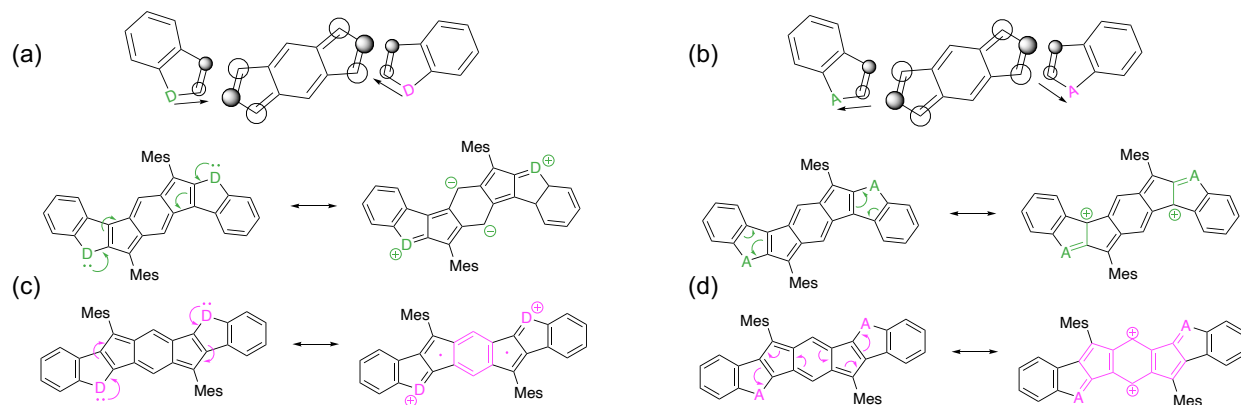


Figure 2.4. (a) and (b) Topological charge points of high electron density (C2/6 of *s*-indacene) are marked with black circles, *syn*-fusions are highlighted in green and *anti*-fusions are highlighted in magenta, and bond dipoles represented by arrows to and from π -donor and acceptor heteroatoms. (c) Top, *syn*-fusion of π -donor heterocycles result in an antiaromatic resonance structure. Bottom, *anti*-fusion of π -donor heterocycles result in an aromatic resonance structure. (d) Top, *syn*-fusion of π -acceptor heterocycles result in an antiaromatic resonance structure with electron deficient *s*-indacene core. Bottom, *anti*-fusion of π -acceptor heterocycles result in a globally antiaromatic resonance structure with double fulvalene-like rings.

The proposed arrow pushing and resulting resonance structures for the π -donating heterocycles above and those found in the computational study by Warren et. al both agree with previously published experimental and computational results (for **1**, **2**, **5**, **6**) and unpublished results for **19** and **20**. However, the above proposed rationalizations above differ in that they include donation from both heteroatoms to the core in a D-A-D triad, are backed by Gimarc's rule of topological charge stabilization, GIMIC plots, and calculations of π -electron density at C2/6 using extended Hückel theory (Figure 2.3). Additionally, this expansion includes the π -accepting heterocycles and can be extrapolated to include the asymmetric heterocycle-fused-*s*-indacene derivatives (**7-14**) as well (Figure 2.6). A final argument in favor of this expanded rational is provided by further arrow pushing of the resonance structures for the π -accepting heterocycles to the "bond-flipped" structures found in the crystal XRD data for **3** and **4**, and geometry optimizations of **11-14** (Figure 2.5).^{79,123}

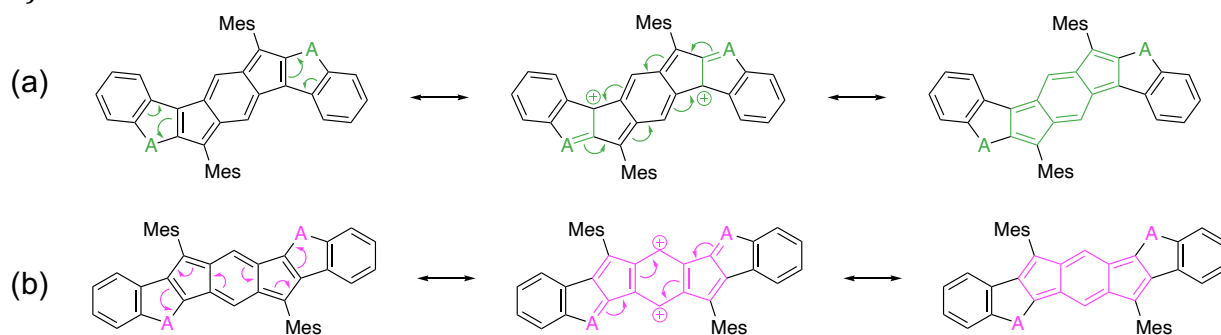


Figure 2.5. Arrow pushing through to bond-localized ground state structures reflected in the previously published data for all *s*-indacene derivatives with fused π -acceptor heterocycles, (a) *syn*-fusion and (b) *anti*-fusion.

To quote Gimarc, "From a pattern of charge densities once can see immediately what is favorable of destabilizing about a particular arrangement of atoms." The resonance structures from the initial arrow push (Figures 2.4 and 2.5) are representative of the delocalized excited state, and reflect the ring current densities depicted in the GIMIC plots because the delocalized (antiaromatic) state is stabilized by a magnetic field. π -Electron density at the 2 and 6 carbons (C2/6) calculated using extended Hückel theory, can be used to explain the relative strength of each fusion type and donor type. *Syn*-fusion of the π -donating heterocycles opposes the preferred topological charge arrangement for *s*-indacene, which destabilizes the molecule and increases the strength of the paratropic ring current in

the delocalized state. The negative charge preferentially held at C2/6 by native *s*-indacene is decreased (opposed) by the *syn*-fusion of π -donating heterocycles in order with donating character (N>O>CH>S), and increased (enforced) by the *anti*-fusion of π -donating heterocycles in order with electronegativity (O>N>S>CH⁻) (Figure S34, appendix). The negative charge preferentially held at C2/6 by native *s*-indacene is decreased (opposed) by the *syn*-fusion and *anti*-fusion of π -accepting heterocycles in order with π -accepting ability. CH⁺ is the strongest π -acceptor with a formal positive charge, followed by BH with an empty p-orbital and trigonal planar geometry (well situated to withdraw from the sp² hybridized carbons). SO₂ is the weakest π -acceptor because it is larger than the carbon atoms and further bent out of orbital alignment with the planar ring by its tetrahedral geometry. These statements are corroborated by previously reported NICS_{1.7} π_{zz} calculations, which as previously mentioned, are representative of the p_z orbital contributions to the ring current and magnetic properties of the molecules. They are also reflected in the NICS(1)_{zz} calculations, which include more of the sigma contributions, which is relevant because inductive effects occur through sigma bonds.

The arrow pushing rationale for the donor-acceptor-fused-*s*-indacenes (**11-14**) in seen below in Figure 2.6, can be related to bipolar junction transistors through a figurative analogy. The relative energy levels of the calculated HOMO (π -electron donation) and LUMO (π -electron accepting) for the heterocycles and *s*-indacene core can be thought of as a

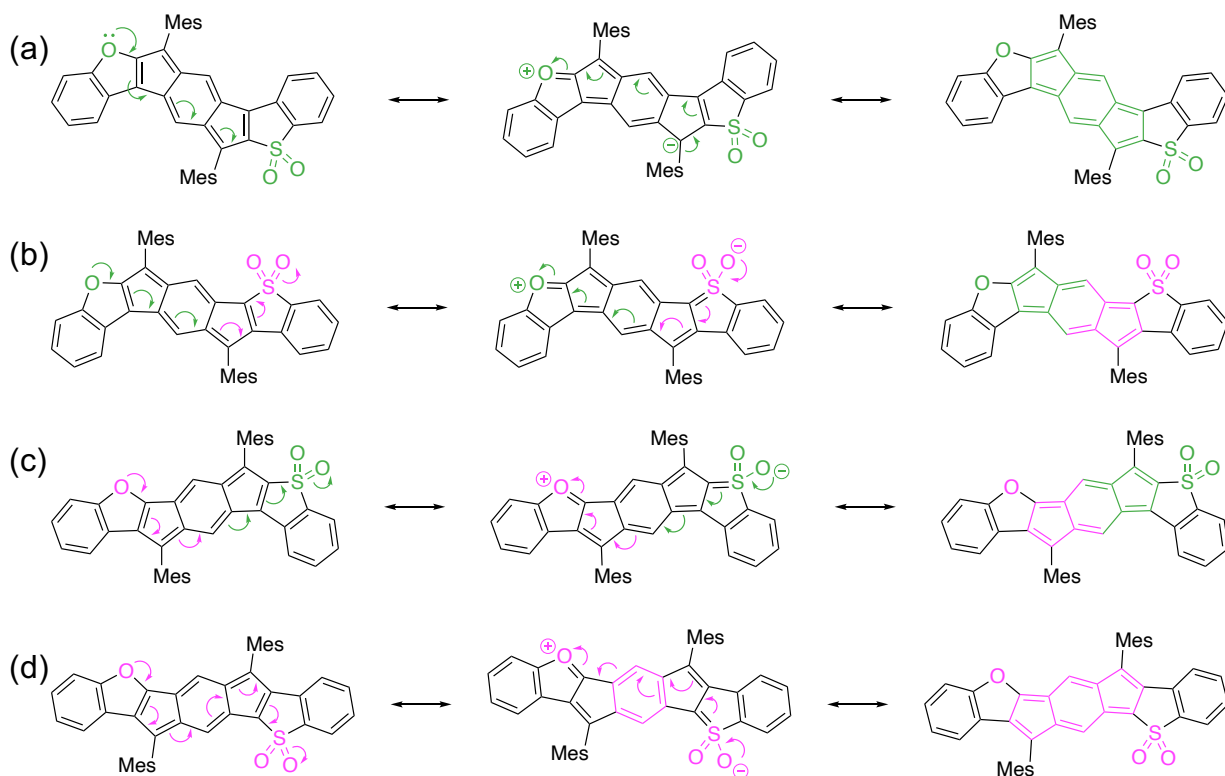


Figure 2.6. (a) syn-syn IBFBTS (**11**) has the least favorable zwitterionic resonance structure with the negative charge localized on the apical carbon because the alternative is to break the aromaticity of the outer benzene ring on the sulfone side. (b) syn-anti IBFBTS (**12**), and (c) anti-syn IBFBTS (**13**). (d) anti-anti IBFBTS (**14**) passes through the most favorable center zwitterionic resonance structure. The right most resonance structure for all four isomers is reflected in the bond length alternation calculations found in the appendix. Syn-fusions are highlighted in green, and anti-fusions are highlighted in pink.

potential energy gradient in across a transistor. In this analogy, the donor heterocycle is always *syn*-fused and it donates from the HOMO, the acceptor heterocycle is always *anti*-fused, and accepts from the LUMO. The *s*-indacene core is either a donor or acceptor depending on the fusion of the heterocycles, so **11** is a D-A-D triad from the furan to sulfone, **12** is a D-A-A, **13** is A-D-D, and **14** is A-D-A.

The transistor analogy would be **11** as a N-P-N junction, with a steeper potential energy gradient on one side, but would not transfer charge well from N to N. **12** would be a N-P junction with a constant negative potential gradient and would transfer charge well from N to P. **13** would be a reversible P-N junction, and would transfer charge well if the sulfone could π -donate (increased e- doping of the N, or increased hole doping of the P side). There is some experimental evidence to suggest charge transfer is induced with the addition of acid or water in DMF for **13**. Addition water could provide additional electron density to the syn-fused sulfone through dipole-dipole interactions (additional e- doping of the N side of the junction), facilitating charge transfer from the core to the furan side, which is stabilized by hydrogen bonding between the oxygen of the furan moiety and water (additional hole doping of the P side). Addition of acid in this analogy would be reversing the P and N sides of the junction. Hole doping of the formerly N side (*syn*-fused sulfone) to induce e- donation from the formerly P side of the junction (*anti*-fused furan) facilitates inductive withdraw stabilized by H⁺ in solution at the partial negative charge on the oxygen atom of the sulfone (Figure 2.7).

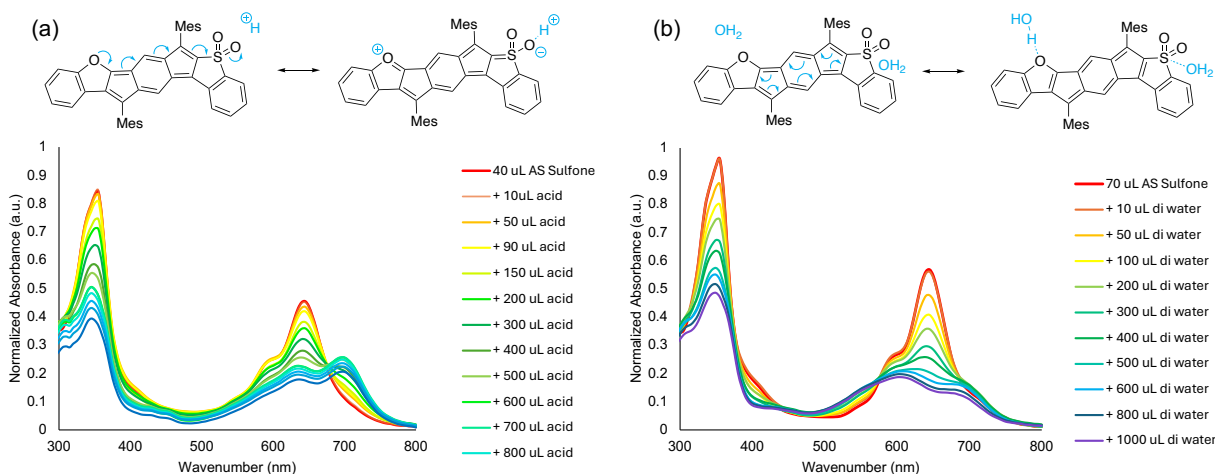


Figure 2.7. (a) addition of formic acid in DMF induces a solvatochromic shift, reminiscent of those in **12** and **14**. (b) addition of water in DMF induces a bathochromic shift, presumably in the opposite direction across the molecule (sulfone to furan).

14 would be a P-N-P junction, with a steeper potential energy gradient to one side, which could induce a steady gradient from P to P. This analogy is reasonable because the amphoteric redox properties of *s*-indacene based molecules imply the core could act as either a donor (N-type) or acceptor (P-type), but the trend of decreasing reduction potentials

with increasing antiaromaticity imply they are better acceptors than donors. This offers a possible explanation for the lack of charge transfer observed in **11**, if the N part of the junction offers a local energy well (strong binding energy) charge donated from the heterocycles will collect in the core instead of transferring across the molecule. And rationalizes the strength of the charge transfer observed in **14** (along with the pro-aromatic resonance structure), which has an *anti*-fused (withdrawing in the analogy) donor moiety. The remainder of the experimentally observed properties of these molecules (**11-14**) and their unoxidized asymmetric precursors (**7-10**) are discussed at length in the following chapter.

If we think about structure property relationships in the context of Hammett values, we could think of it as a cause-and-effect relationship, and maybe we can relate all of this to pKa values at some point in the future. If the defining characteristic of antiaromatic molecules is the magnetic properties (paratropic ring current), and the property is the effect, then the structure is the cause.

CHAPTER III

DONOR/ACCEPTOR-FUSED-S-INDACENE DERIVATIVES

This chapter includes previously published and co-authored materials from Demachkie, I. S.; Miller, M. P.; Warren, G. I.; Barker, J. E.; Strand, E. T.; Zakharov, L. N.; Haley, M. M. Intramolecular Charge Transfer in Antiaromatic Donor/Acceptor-Fused *s*-Indacenes. *Angew. Chem. Int. Ed.* **2024**, e202420989. This manuscript was written by me with editorial assistance from Dr. Josh Barker, Dr. Gabrielle Warren, and Prof. Michael M. Haley. The project in this chapter was initially conceived by Dr. Josh Barker. The synthetic adaptation to make isolation of the target molecules possible and investigative methods were conceived and carried out by me, along with the entirety of published and unpublished experimental work. The computational work in this chapter was performed by Michael Miller and me, crystallographic measurements were performed by Lev N. Zakharov.

3.1 Introduction

Antiaromaticity refers to a class of organic molecules with $4n$ π -electrons in a planar, conjugated ring.^{24,25,124,125} *s*-Indacene (12 π -electrons in a planar, conjugated 3-ring scaffold) can be effectively stabilized through aromatic ring fusion to the outer five-membered rings, and the reactive apical carbons can be kinetically blocked with bulky substituents. A general modification (oxidation).¹²⁶ Previous studies have incorporated heterocycles (benzothiophene, benzofuran) as part of the outer aromatic rings, e.g., **1-6** (Figure 3.1c).^{62,79,127} By varying the fusion orientation (Figure 3.1b) from *anti*- (where the heteroatom is fused on the opposite side of the scaffold from the apical carbon of the five-membered ring) to *syn*- (where the heteroatom is on the same side as the apical carbon), we could further tune molecular properties within a set of regioisomers. synthetic method for *s*-indacene derivatives permits fine-tuning of molecular properties through early-stage (identity of the fused peripheral aromatics) or late-stage synthetic modification (oxidation).¹²⁶ Previous studies have incorporated heterocycles (benzothiophene, benzofuran) as part of the outer aromatic rings, e.g., **1-6** (Figure 3.1c).^{62,79,127} By varying the fusion orientation (Figure 3.1b) from *anti*- (where the heteroatom is fused on the opposite side of the scaffold from the apical carbon of the five-membered ring) to *syn*- (where the

heteroatom is on the same side as the apical carbon), we could further tune molecular properties within a set of regioisomers.

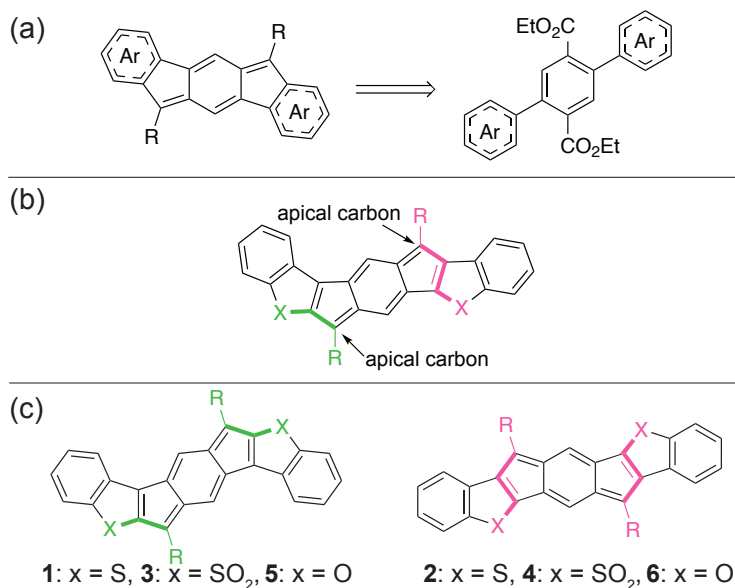


Figure 3.1. (a) Generic and abbreviated *s*-indacene retrosynthesis for tuning by fusion. (b) Generic benzoheterocycle-fused *s*-indacene with labelled apical carbons; syn-fusion is highlighted in blue and anti-fusion is highlighted in red. (c) Previously reported symmetric benzoheterocycle-fused *s*-indacenes.

Many of the same properties that make antiaromatic compounds attractive for organic electronics are also associated with donor-acceptor (D/A) molecules. Incorporation of D/A motifs is a popular design strategy in improving aromatic scaffolds for use in organic electronics because it can facilitate intramolecular charge transfer (ICT),^{128,129} which is the functional basis for many semiconducting and optoelectronic devices.^{130,131} ICT is a fundamental process in photochemistry where upon excitation, electron density flows from a donor group through a covalently linked σ - or π -bridge to an acceptor group.¹³² ICT results in molecular properties such as an extension of the absorption spectrum, a decrease in the HOMO-LUMO energy gap, and amphoteric redox behavior. ICT can be tuned by the identity and strength of the donor and acceptor groups, the length of the π -bridge, bond length alternation in the π -bridge, and the ways in which the donor, bridge, and acceptor are connected.^{133,134} Conductivity is defined as the ratio of current density in a material to the electric field. ICT is the flow of electron density from a donor group through a covalently

linked σ - or π -bridge to an acceptor group within a molecule. The correlation between antiaromaticity and conductivity has been investigated via single molecule conductance measurements several times across different systems. To the best of our knowledge this is the first study that has been able to correlate increasing antiaromaticity with increasing intramolecular charge transfer.

Several groups have incorporated donor and/or acceptor groups onto antiaromatic scaffolds, but almost always as either a D-A-D or A-D-A triad with the paratropic core as either the acceptor or donor unit.¹³⁵⁻¹⁴¹ Molecular property tuning is limited to the identity of the donor or acceptor groups, and evidence of ICT has been weak. Recently, the London group appended donor and acceptor groups on two isomers of monobenzopentalene and observed some evidence of donor-acceptor character, although this was not the focus of the work.¹⁴² Das and co-workers were able to desymmetrize an indeno[2,1-*c*]fluorene (IF) with donor- and acceptor-functionalized R groups, with one derivative showing modest evidence of charge transfer (~ 10 nm solvatochromic shift), which is noteworthy considering the limited conjugation between the planar core and the orthogonal aryl groups; however, the authors noted the synthesis was difficult.¹⁴³ To the best of our knowledge, there are no published examples of antiaromatic molecules with fused donor and acceptor groups.

Recent studies focused on novel D/A aromatic topologies suggest electronic interactions between the donor and acceptor groups may be greatly enhanced if they are fused coplanar to the π -conjugated bridge; however, such structures have proven elusive.^[36]

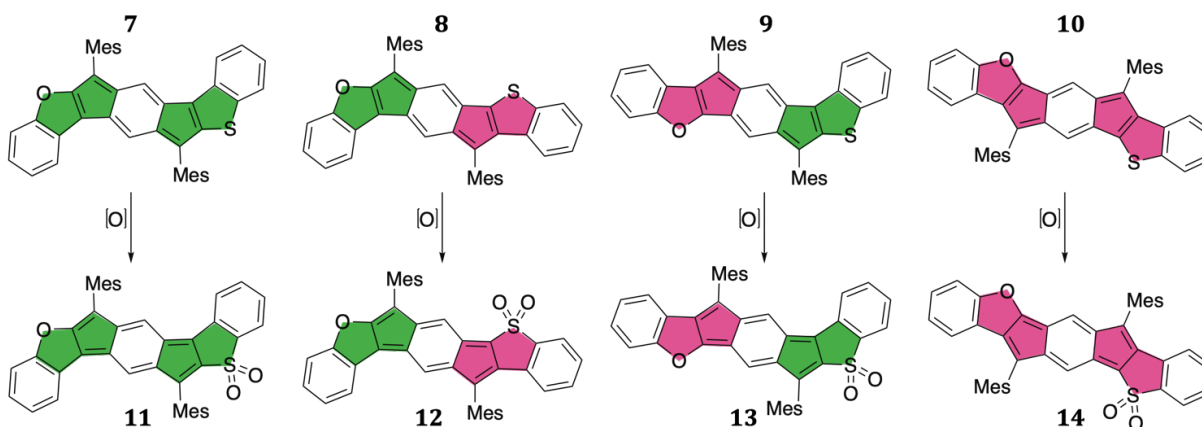


Figure 3.2. Eight new unsymmetrical benzoheterocycle-fused *s*-indacenes, IBFBTs **7-10** and IBFBTSS **11-14**; colored 5-membered rings denote the four possible substitution patterns of asymmetric heterocycle fusion on the *s*-indacene core (green syn-fusion, pink anti-fusion).

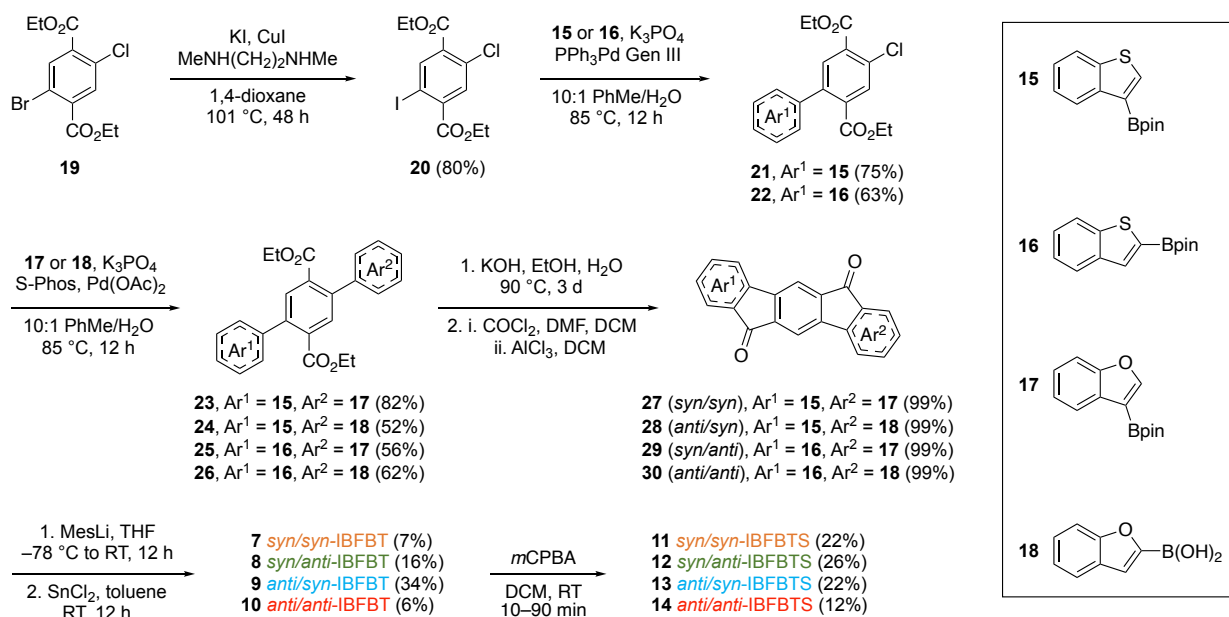
Herein, we report the synthesis and characterization of a family of unsymmetrical, antiaromatic indacenobenzofuran-benzothiophenes (IBFBTs **7-10**, Figure 3.2). Late-stage oxidation transforms the thiophene into an acceptor motif, furnishing all four D/A isomers (IBFBTSs **11-14**) that, depending on the fusion orientation of the benzofuran donor and benzothiophene-S,S-dioxide acceptor, show varying degrees of antiaromaticity and ICT character. The previously reported sets of symmetric benzoheterocycle-fused *s*-indacenes (**1-6**)^{62,79,127} provide standards for the impact of each heterocycle and its fusion orientation on the antiaromaticity and molecular properties of the *s*-indacene scaffold, thus permitting a thorough, rationally designed study of desymmetrization of the paratropic *s*-indacene core, as well as any interplay between antiaromaticity and ICT. Notably, analogous studies with benzoheterocycles fused to *aromatic* motifs such as naphthalene (10 π -electrons) or anthracene (14 π -electrons), most comparable to *s*-indacene, have not been reported. As Anthony showed in 2004, creating heterocycle-fused acenes is a significant synthetic challenge, as the double Aldol condensation to generate the eventual anthracene core leads to an inseparable *syn/anti* mixture.¹⁴⁴ While Tykwinski was able to prepare isomerically-pure *syn*-thiophene¹⁴⁵ and *syn*-benzothiophene regioisomers, their syntheses were considerably more involved.¹⁴⁵ Importantly, none of the routes are amenable to installing *different* heterocycles on either side of the aromatic core, thus highlighting the precision synthetic chemistry used to construct **11-14**.

3.2 Results and Discussion

3.2.1 Molecular Design and Solid-State Structures.

The synthesis of symmetric IFs and their benzoheterocycle analogues (**1-6**, Figure 1a) typically begins with a Pd-mediated Suzuki cross-coupling of arylboronic acids or arylboronate esters to diethyl 2,5-dibromoterephthalate. This modular route is readily adaptable to desymmetrization, as we previously disclosed using diethyl 2-bromo-5-chloroterephthalate (**19**) with Pd(PPh₃)₄ as the catalyst to gain regioselectivity in the initial cross-coupling step with phenylboronic acid.¹⁴⁶ For this current family of molecules, the bromo/chloro reactivity difference in the initial oxidative addition step on **19** was insufficient, as a small amount of double-coupled product was also produced, which proved exceedingly difficult to separate from the desired mono-coupled material. Rather, the

revised synthesis (In 2) begins with an aromatic Finkelstein reaction to convert **19** to the more reactive diethyl 2-chloro-5-iodoterephthalate (**20**). Suzuki cross-coupling with either 3- (**15**) or 2-benzothiopheneboronic acid pinacolate ester (**16**) using third generation Buchwald pre-catalyst yielded chlorides **21** and **22**, respectively, with no evidence of double-coupled material. Each chloride was then cross-coupled with 3-benzofuranboronic acid pinacolate ester (**17**) or 2-benzofuranboronic acid (**18**) to furnish diesters **23-26** in moderate to good yields. Each diester was subsequently saponified and subjected to Friedel-Crafts acylation to afford the poorly soluble diketones **27-30**. Nucleophilic addition of the mesityl units to each dione introduced the protecting groups for the apical carbons, followed by a SnCl₂-mediated reductive dearomatization to give the four asymmetric IBFBT regioisomers **7-10**. Because of the rapid decomposition of *anti*-IDBF **6** to its ring-opened form,⁶² we were unsure of the stability of *anti/anti*-IBFBT **10**; however, inclusion of one benzothiophene provides a stabilizing effect. All four parent isomers are stable for months at -20 °C and up to several weeks at 20 °C. IBFBTs **7-10** were subsequently subjected to *m*CPBA oxidation to yield their sulfone analogues (IBFBTSs) **11-14** in modest yields. All four sulfones are acid sensitive, which is partially responsible for the lowered yields. Similar to *anti*-IDBF **6**, *anti/anti*-IBFBTS **14** began to decompose upon oxidation and is extremely acid sensitive, as the stabilizing effect of the thiophene in **10** is significantly reduced upon oxidation.



Scheme 2. Synthesis of IBFBTs **7-10** and late-stage oxidation to IBFBTSs **11-14**.

Several groups have utilized asymmetry as a means of creating a dipole moment and exploiting this property to influence solubility, solid-state packing, and polarizability;^{147,148} thus, we sought insight into the molecular structures of the asymmetric *s*-indacene derivatives via single-crystal X-ray diffraction (XRD). Slow evaporation of a CHCl₃ solution of **10** gave deep violet crystals, whereas layering pentanes over CH₂Cl₂ provided dark blue crystals of **8**. The XRD structure of **10** (Figure 3.3a) revealed positional disordering of the O/S atoms in a ratio of 58/42; no such disordering was observed in **8** (Figure 3.3b). Whereas **2** packs in a herringbone fashion, the molecules of **10** form a 1-D chain (Figure 3.3c), similar to what was found in **6**. The distance between the mean planes of **10** is 3.48 Å, which is slightly shorter than in **6** (3.55 Å). Molecules of **8** also form a 1-D chain with a slight curvature of the molecule. The distance between the plane of the six-membered rings on the furan side is 3.57 Å and is 3.33 Å on the thiophene side. The *syn/anti*-fusion of **8** results in a weak dipole moment toward the side of the molecule with both heteroatoms, affording an anti-parallel packing pattern (Figure 3.3d). One must often rely on computationally-optimized geometries in the absence of XRD data, such as this study (Table S2, appendix), making the choice of DFT functional critically important (see experimental versus computational comparison in Table S1, appendix).⁷³ Bond length alternation (BLA) is defined as the

difference between the average lengths of adjacent C=C and C-C bonds and is an important parameter in assessing both antiaromaticity and ICT.

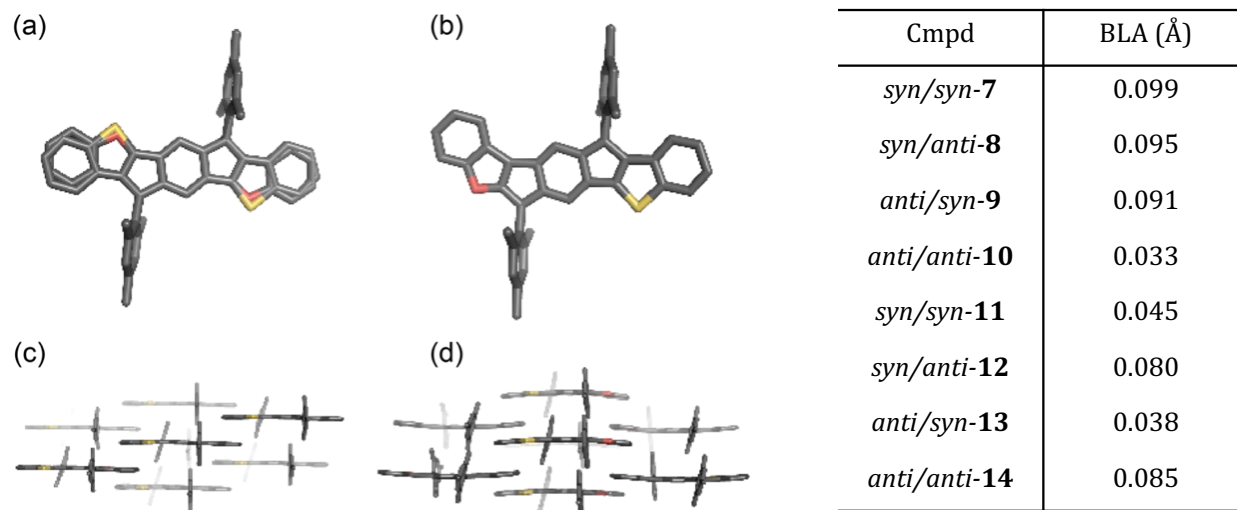


Figure 3.3. Left, X-ray crystal structures of (a) **10** and (b) **8** along with the packing diagrams for (c) **10** and (d) **8**. Right, bond length alternation (BLA) as an average difference between bond lengths from M11 optimized structures.

High degrees of bond length alternation (~ 0.1 Å) are characteristic of a formally antiaromatic ground state. As is explained in detail in section 1.3, structural criteria including π -electron count and bond length alternation describe the ground state, which is not antiaromatic because antiaromaticity is defined by the paratropic ring current strength, found only in the delocalized excited state. Bond length alternation will not be used to rank relative strengths of antiaromatic character in this set of molecules, because the degree of bond alternation corresponds to the depth of the energy well of each valence tautomers, or the size of the activation barrier (E_a) between them. The size of the E_a is proportional to energetic difference between the excited state (LUMO) and both bond alternant valence tautomers, or the size of the activation barrier (E_a) between them. The size of the E_a is proportional to energetic difference between the excited state (LUMO) and both bond alternant valence tautomers (HOMO and HOMO-1) which depends on a multitude of factors

including antiaromaticity of the delocalized state, planarity, symmetry of the molecule itself, aromaticity of the stabilizing aromatic groups, and in this case, charge transfer.

3.2.2 Optical, Electrochemical, and Magnetic Properties

There is no agreed upon (definitive experimental or computational) measure of the relative antiaromaticity (antiaromatic character) of a given set of formally antiaromatic molecules. Antiaromaticity has historically been assessed by four separate criteria, structural, magnetic, energetic, and electrochemical, with the expectation that increasing bond length alternation (structural) is thought to correlate linearly with increasing paratropic ring current strength (magnetic) and decreasing HOMO-LUMO gap (energetic/electrochemical), which can be estimated experimentally with optical and electrochemical gaps.

Amphoteric redox behavior is characteristic of antiaromatic molecules because loss or gain of an electron relieves the energetic strain of antiaromaticity, but the electrochemical gap should not be used to rank relative strengths of antiaromatic character because there are contributing factors other than the instability of the delocalized state. The electrochemical gap ($E_{\text{ox1}} - E_{\text{red1}}$), which is measured for molecules by solution state cyclic voltammetry (CV) is often used as an experimental approximation for the HOMO-LUMO gap. The electrochemical gap is usually larger than the optical gap, which is measured by solution state UV-vis. The optical gap represents the energy of the lowest electronic transition available via absorption of a single photon, and the electrochemical gap represents the difference between the energy required to remove one electron from the highest occupied molecular orbital (ionization potential, IP), and the energy required to inject one electron into the lowest unoccupied molecular orbital (electron affinity), plus the electron-hole binding energy. While neither approximation equates to the HOMO-LUMO gap (especially in molecules where the lowest electronic transition is forbidden), both have been shown to trend linearly with calculated HOMO-LUMO gap values.¹⁵¹⁻¹⁵⁴

As is discussed in section 1.3, a small HOMO-LUMO gap is a characteristic of antiaromatic molecules because of the 1, (pseudo) 2, 1 molecular orbital energy level pattern, and the instability of a bond localized ring system (relative to a delocalized aromatic ring system). Identification of a small HOMO-LUMO gap is a criterion used to assess

antiaromatic character in molecules in the same way amphoteric redox properties and number of π -electron are. All three are molecular properties common to the class of formally antiaromatic molecules. Optical and electrochemical properties are experimentally measurable quantities, and number of π -electrons can be counted from the lewis-dot structure of planar and cyclic organic molecules. The electrochemical gap and optical gap are not criterion that should be used to rank relative antiaromatic character of a set of molecules but should be measured and reported because these properties are extremely valuable for applications in organic electronics. Regardless of the relationship between optical and electrochemical properties and the relative antiaromaticity (paratropic ring strength) of a molecule, experimental (and computational) measure of molecular properties provides valuable information about the impact of different methods of synthetic modification on the valuable molecular properties common to the class of formally antiaromatic molecules.

Optoelectronic properties. All asymmetric parent IBFBTs **7-10** and their corresponding sulfones **11-14** possess strong absorptions in the range of 300-400 nm and low-energy absorptions around 600-700 nm (Figure 3.4). The Optical gap ($^{\text{opt}}E_{\text{gap}}$), which linearly correlates with characteristic small HOMO-LUMO gap of antiaromatic molecules, was determined as the intersection of the x -axis and a tangent line passing through the inflection point of the lowest-energy absorption (Table 1). Based on molecular orbital plots, the LUMO+1 is most spatially similar to the delocalized antiaromatic state (LUMO) of *s*-indacene, which aligns with the theory of the AADC. Calculated gas-phase TD-DFT excitation oscillator strength values indicate the low energy absorption peak is primarily attributed to the HOMO-1 \rightarrow LUMO transition for all isomers except for **11** and **13** (Table S3). Oxidation of the *syn*-fused benzothiophene in **11** and **13** (and **3**) results in a significant drop in antiaromatic character, causing the HOMO and HOMO-1 to invert which has been known to occur in molecules with weak antiaromatic character, making the HOMO \rightarrow LUMO transition the major contributor to the low energy absorbance. Most *s*-indacene derivatives display a hip (shoulder) in the lowest energy excitation peak. The hips of the low energy absorption peaks can be attributed to the next highest oscillator strength transition, which corresponds to the

HOMO \rightarrow LUMO+1 for **8**, HOMO-2 \rightarrow LUMO for **7**, HOMO-1 \rightarrow LUMO for **9**, HOMO \rightarrow LUMO+2 for **10**, and HOMO \rightarrow LUMO for **12** and **14**.¹⁵⁵

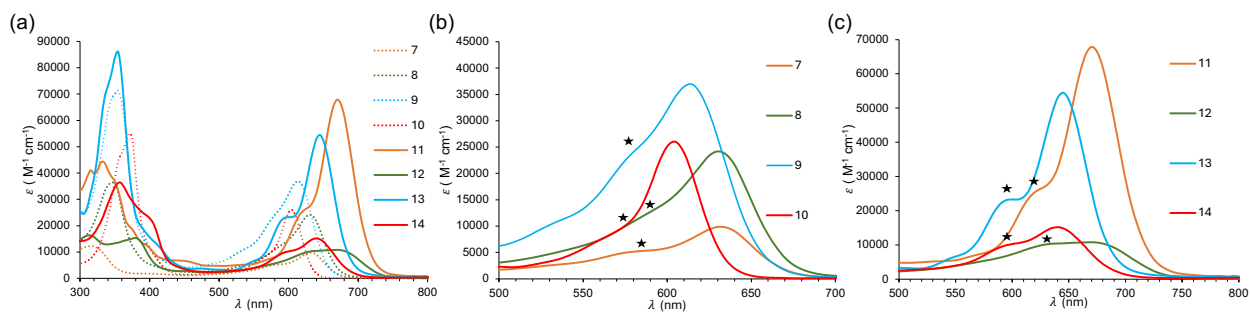


Figure 3.4. (a) Electronic absorption spectra of the asymmetric parent regioisomers (**7-10**, dotted lines) and the corresponding sulfones (**11-14**, solid lines) in CH_2Cl_2 . (b) Spectra of **7-10** low energy absorption with hips indicative of forbidden transitions marked with stars. (c) Spectra of **11-14** low energy absorption with increased hips marked with stars.

The main difference between the parent and sulfone of the same isomer is the low energy absorption band, where a significant bathochromic red-shift (30-40 nm) is observed for all sulfones, indicative of D/A character imparted by the oxidation of the thiophene ring. Molecules **7** and **8** exhibit the largest (40 nm) shift from 630 nm to 670 nm for **11** and **12**, followed by **10** at 605 nm to **14** at 644 nm (39 nm shift). IBFBT **9** (615 nm) shifts by 30 nm to its corresponding sulfone **13** (645 nm). In contrast, the symmetric IDBTs **3** (624 nm) and **4** (587 nm) are hypsochromic blue-shifted relative to their respective unoxidized analogues **1** (626 nm) and **2** (618 nm),^{79,127} which further confirms that the red-shifted absorption in **11-14** is due to ICT across the *s*-indacene core and not merely to the presence of the sulfone moiety. Finally, the molar absorptivity of **11** and **13** is considerably larger than **12** and **14**, which is consistent with the calculated transition dipole moments (Table S3), indicating much stronger charge transfer in **12** and **14**. Plots of the frontier molecular orbitals (Figures S12-S15) illustrate the spatial similarities between the isomers that exhibit charge transfer (**12**, **14**) vs. isomers that do not (**11**, **13**). As noted earlier, the aromatic analogues of **11-14** that possess naphthalene or anthracene as the core motif are unknown. Nonetheless, we computationally investigated both the *syn*- and *anti*-isomers of a linearly benzofuran/benzothiophene-fused naphthalene pre- and post-oxidation and note some

striking differences. Whereas the calculated HOMO- LUMO energy gap in general decreases upon oxidation to **11-14**, this gap increases significantly (~ 0.3 eV) in the naphthalene model compounds (Table S5 and S6), which is reflected in the predicted 30-40 nm *hypsochromic* shift of the lowest energy optical transition. In addition, the calculated frontier molecular orbital plots (Figures S22-S23) show little to no evidence of ICT. Whereas the antiaromatic *s*-indacene core facilitates ICT, an aromatic naphthalene would seem to impede this behavior.

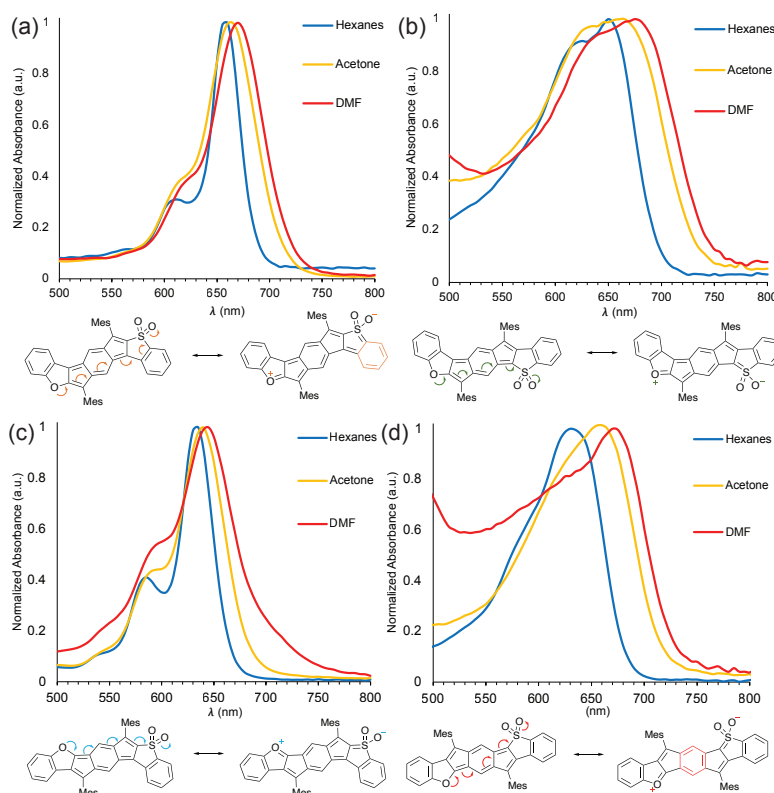


Figure 3.5. Solvatochromic UV-vis absorption data for (a) **11**, (b) **12**, and (c) **13**, and (d) **14** in hexanes, acetone, and DMF. Below each set of spectra are the (formal) neutral and charge transfer resonance structures for the corresponding isomer.

ICT often results in a bathochromic shift in more polar solvents due to the stabilization of the more polar charge-transfer/ zwitterionic state. This can be seen clearly for both isomers with *anti*-fused benzothiophene-*S,S*-dioxides (**12** and **14**, Figure 3.5), which show significant 29 and 41 nm shifts, respectively, from hexanes to DMF ($\Delta\mu = 3.86$ D). IBFBTSs **11** and **13** both exhibit more modest bathochromic shifts of ~ 10 nm in the same solvents.

IBFBTS **11** has significant antiaromatic character but does not exhibit strong ICT. This can be explained by the zwitterionic resonance structure (Figure 3.5a) in which the fused benzene on the benzothiophene-S,S-dioxide would have to sacrifice its aromaticity to facilitate through-bond charge transfer. Conversely, IBFBTS **14** is the most solvatochromic, showing a 25 nm shift just changing from hexanes to DCM ($\Delta\mu = 1.55D$), likely due to the stability of the pro-aromatic charge transfer resonance structure (Figure 3.5d).

Electrochemical Properties. To assess the redox properties of these molecules, cyclic voltammetry (CV) experiments were performed to measure the reduction and oxidation potentials of **7-13**. Scans of solution-state CV measurements of the reduction and oxidation potentials provide approximate experimental values for the HOMO-LUMO gap. Comparison between the TD-DFT predicted HOMO-LUMO gap and electrochemical HOMO-LUMO gap for each compound can be found in Table 2. All four IBFBTs (**7-10**) display amphoteric redox properties typical of antiaromatic molecules, with potentials for each event at approximately the average value of their respective symmetric counterparts (Table S7). Consistent with previous findings, decreasing reduction potentials trend with increasing antiaromaticity.^[12] All four isomers (**7-10**) have a reversible first oxidation and first reduction. The isomer with the strongest antiaromatic character, **7**, is the only molecule without a reversible second oxidation in the DCM solvent window, whereas the isomer with the least antiaromatic character, **9**, is without a second reduction in the DCM solvent window. DCM is not a standard solvent for electrochemistry because it evolves small amounts of HCl, however is the only solvent the majority of the symmetric heterocycle-fused and hydrocarbon *s*-indacene derivatives are soluble in. For consistencies sake, we continue to measure CV in DCM.

Table 1. Electrochemical data, optical gap, and calculated HOMO-LUMO gap for **1-14**.

cmpd	E_{red2} (V)	E_{red1} (V)	E_{ox1} (V)	E_{ox2} (V)	E_{HOMO} (eV)	E_{LUMO} (eV)	E_{gap} (eV) ^[a]	opt. E_{gap} (eV) ^[b]	H→L E_{gap} (eV) ^[c]
7	-1.29	-0.61	0.98	—	-5.67	-4.07	1.59	1.75	1.60
8	-1.36	-0.75	0.89	1.61	-5.57	-3.93	1.63	1.75	1.67
9	—	-0.88	0.73	—	-5.41	-3.80	1.61	1.82	1.65
10	-1.76	-0.83	0.86	1.32	-5.54	-3.84	1.69	2.04	1.62
11	-1.25	-0.24	1.16	—	-5.84	-4.44	1.40	1.63	1.39

12	-1.15	-0.32	1.11	—	-5.79	-4.36	1.43	1.59	1.37
13	—	-0.53	1.12	—	-5.80	-4.15	1.65	1.68	1.59
14	—	—	—	—	—	—	—	1.65	1.65

[a] Electrochemical E_{gap} . [b] Optical E_{gap} determined as the intersection of the x -axis and a tangent line passing through the inflection point of the lowest-energy absorption. [c] HOMO-LUMO gap calculated at the TPSSh/def2-TZVP level of theory.

All electrochemical experiments were conducted with traditional 3-electrode geometry using a Biologic SP-50 potentiostat. Electrolyte solutions (0.1 M) were prepared from anhydrous, degassed HPLC grade CH_2Cl_2 and anhydrous Bu_4NPF_6 . The working electrode was a glassy carbon electrode (3-mm diameter), with a Pt-coil counter electrode and a Ag wire pseudo reference. The ferrocene/ferrocenium (Fc/Fc^+) couple was used as an internal standard following each experiment. Potential values were re-referenced to SCE using a value of 0.46 (V vs. SCE) for the Fc/Fc^+ couple in CH_2Cl_2 . LUMO and HOMO levels were approximated using $\text{SCE} = -4.68$ eV vs. vacuum. CV experiments were conducted in a three-neck flask that had been evacuated and backfilled with N_2 for three cycles using standard Schlenk-line technique. Voltammograms were recorded at sweep rates of 50 mV s^{-1} . $E_{1/2}$ values were calculated assuming $E_{1/2} \approx E_{o'} = (E_{\text{anodic}} + E_{\text{cathodic}})/2$ based on these observations for reversible couples; for irreversible couples, the $E_{o'}$ value is estimated as the potential at peak current. Analyte concentrations were ca. 1-5 mM.

Electrochemical data for **11-13** (Figure 3.5) display an increase in the oxidation and reduction potentials for all isomers post oxidation, a decrease in the electrochemical gap for **11** and **12** (relative to **7** and **8**, respectively), and an increase in the electrochemical gap for **13** relative to **9**. Interestingly, the second oxidation event present for both **7** and **8** disappears post oxidation but is maintained for **9**. It is also worth noting the marked difference between **11-12** and IDBTs **3-4**. Whereas both the oxidation and reduction potentials increase by the same amount for **3** and **4**, affording an E_{gap} similar to that found in **1** and **2**,¹²⁷ the reduction potentials of **11** and **12** increase twice as much as the oxidation potentials relative to **7** and **8** resulting in the observed smaller E_{gap} . Finally, the non-Faradaic capacitance for **11** and **12** is much larger than their unoxidized counterparts, implying an increased ability for the molecules to carry charge in their oxidized forms, assuming concentration was unaffected by sparging and remained constant across all measurements.

As already noted, **14** was too unstable for accurate electrochemical measurement. We should have done differential pulse and square wave voltammetry to investigate conductivity and impedance. The kinetics of charge transfer between molecules in solution could have been investigated by variable scan rate measurements and could have provided valuable information about diffusion rates in a gradient of polar solvents.

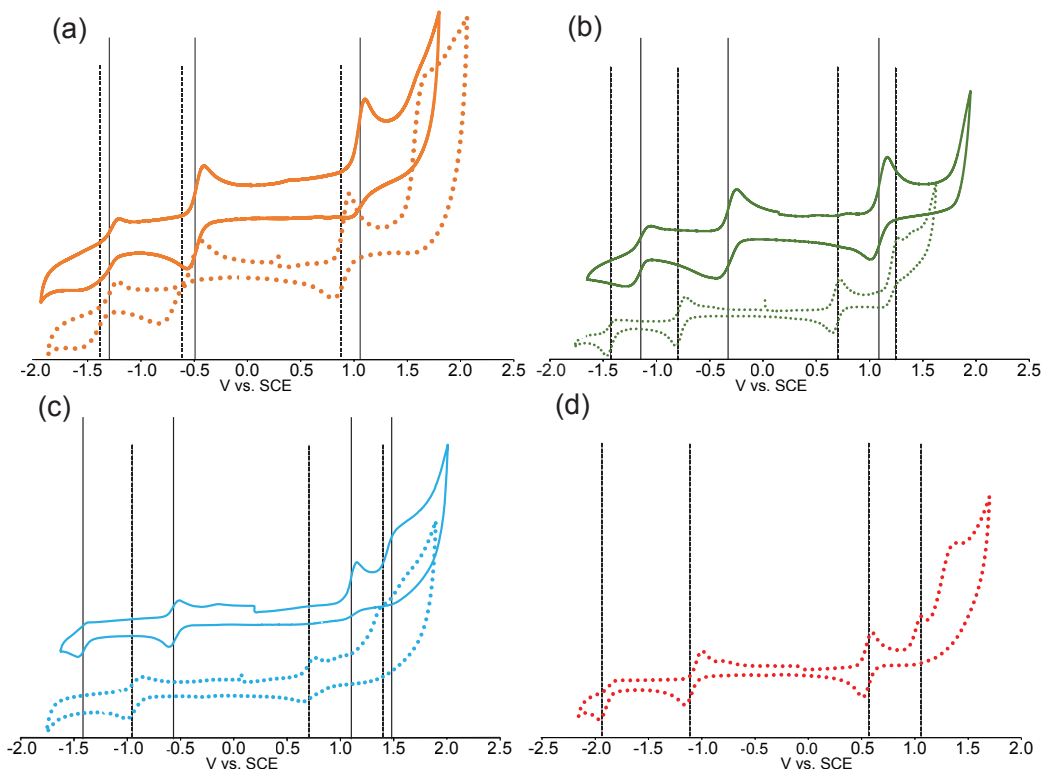


Figure 3.6 Cyclic voltammograms of (a) **7** and **11**, (b) **8** and **12**, (c) **9** and **13**, (a) **10**. Dotted traces are the IBFBTs (**7-10**) and solid traces are the oxidized IBFBTSs (**11-13**). Half-wave potentials for each redox event are marked with dotted grey lines for the IBFBTs (**7-10**), and solid grey lines the IBFBTSs (**11-13**).

3.2.3 Magnetic Properties and Relative Antiaromaticity

For reasons already mentioned, the only reasonable way to rank the antiaromatic character of a group of molecules is by the relative strengths of the paratropic ring current, which we can call the (relative) antiaromaticity of the molecule. This ring current strength can be experimentally measured by the relative deshielding effect of the ring current, which manifests as an upfield-shifted ^1H NMR shift of the protons on center ring of s-indacene.

Importantly, the delocalized paratropic ring current is stabilized by the presence of an applied magnetic field, so molecular properties assessed by NMR are more likely to be representative of the delocalized state. Nucleus Independent Chemical Shift (NICS)-XY scans 1.7 Å above the plane of the molecule, primarily reflect the p_z orbital contributions to the deshielding effect the core protons experience. When calculated at the B972/6-311+G** level of theory based on geometry optimizations at M11/6-311+G**, NICS values for Ring 4 trend with experimental ^1H NMR signals with an R^2 value of .744 (Figure S35), implying approximately 75% of the trend in ring current strength is captured by NICS. The NICS plots provide a convenient visual for the impact of synthetic modification on ring current strength and can be used to identify new synthetic targets.¹⁰⁶

NICS-XY Scans. The magnetic property associated with antiaromaticity is the strength of the paratropic ring current present in an applied magnetic field. The compound with the most antiaromatic character of a set should have the strongest paratropic ring current and therefore the most upfield shifted core protons and most positive NICS value. When comparing NICS values and experimental ^1H NMR shifts, we typically focus on the NICS value of the center 6-membered ring (R4) because that is the ring with the core protons and is the center of the paratropic ring current; however, averaging the NICS values of the whole *s*-indacene core (R 3-5) trends the same way (Table 3). The trends in the structural and magnetic properties for IBFBTs **7-10** align with predicted relative paratropicities based on previously synthesized symmetric analogues **1**, **2**, **5**, and **6**. We anticipated *syn/syn* isomer **7** to be the most antiaromatic based on prior experimental^{62,79,156} and computational work,⁹³ which showed that *syn*-fusion results in increased antiaromaticity of the *s*-indacene compared to *anti*-fusion of the same heterocycle for π -donors. We expected *syn/anti*-**8** to be more antiaromatic than *anti/syn*-**9** because benzofuran-fused **5** is significantly more antiaromatic than benzothiophene-fused **1**, and **10** to be the least antiaromatic with both heterocycles *anti*-fused. The relative antiaromaticities of **7-10** are illustrated by the NICS-XY plots (Figure 3.6a) and agree with our expectations, with all but IBFBT **10** having greater deshielding effects than the ring current strength of *s*-indacene itself.¹⁵⁷ Due to the overlapping electronic effects of antiaromaticity and ICT through the *s*-indacene core, interpretation of the NICS plots for **11-14** (Figure 3.6b) is convoluted. Based on prior studies,

we expected **12** to be the most antiaromatic and **13** to be the least antiaromatic. IBFBTS **11** and **14** were expected to fall in between **12** and **13**, but the strengths of the effect of the *syn*-furan vs. the *anti*-benzothiophene-S,S-dioxide, combined with the potential for ICT in **14**, made the exact order more difficult to predict.

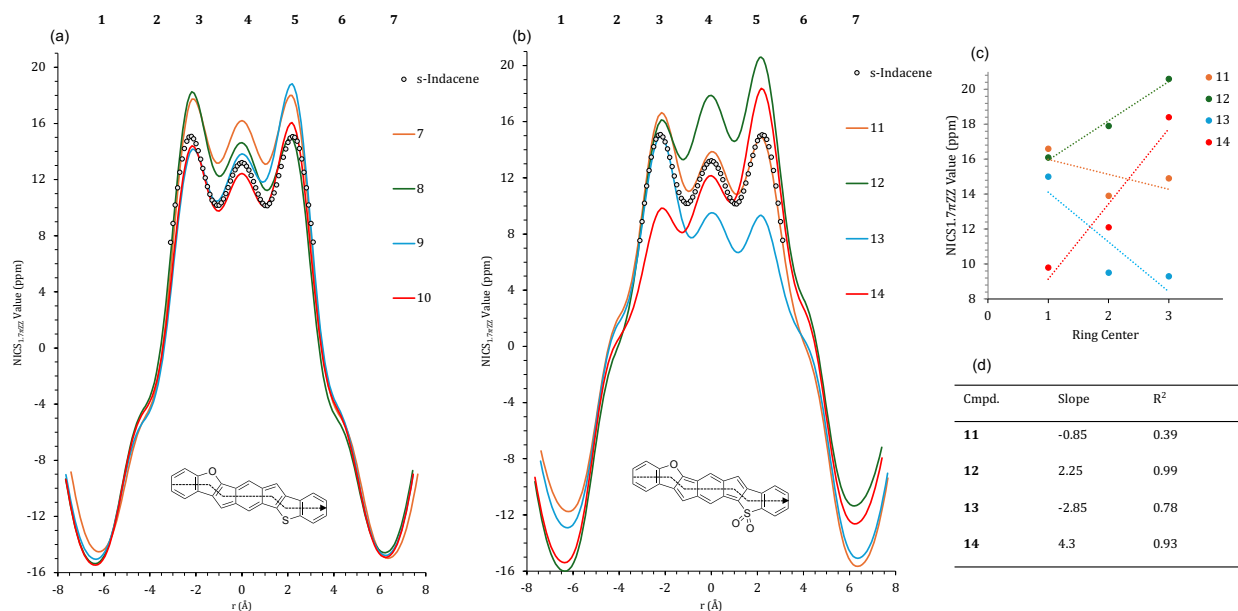


Figure 3.7. NICS-XY scans of (a) **7*–10*** vs. s-indacene and (b) **11*–14*** vs. s-indacene. The dashed line represents the path of the dummy atoms used in the NICS calculations. Calculations were performed on structures optimized using M11 without mesityl groups (**7*–14***) to reduce computational cost. For consistency, ring 2 is always the furan ring, and ring 6 is always the thiophene/thiophene-dioxide ring. (c) Plot of ring center values (ppm) for the core of each IBFBTS (**11–14**); electron density within the s-indacene core should trend with increasing ring current strength/NICS values. (d) Slope and R² values of trend lines for each isomer in (c).

The NICS data as well as ¹H NMR shifts in general corroborate this predicted order; however, they do not perfectly agree with each other. Ring 4 (R4) of **11** is more positive than R4 of **14** in the NICS calculations, but the core proton signals for **14** are significantly more upfield than for **11** (Table 3). NICS scans, when interpreted through the assumption that the absolute value of each ring center linearly correlates with relative electron density (i.e., the larger the value (ppm), the greater the electron density), illustrate the relative ICT character strength across the four sulfones (Figures 3.6c, d). The R² values for **12** and **14** are much higher than **11** or **13**, indicating a much more linear distribution of charge in the two isomers that exhibit charge transfer. The slope of the core (R3→R5) indicates strength of the charge

transfer, and trends with decreasing transition dipole moments (**11**>**13**>**12**>**14**, Table S3) and observed solvatochromic shift (Figure 3.5). While this trend does not align perfectly with the trend in increasing NICS values (**13**<**11**<**14**<**12**) or decreasing ¹H NMR ppm (**13**>**11**>**14**>**12**). All three trends rank **12** and **14** as first and second greatest antiaromatic character, in alignment with trends in ICT character (observed and predicted) across the four isomers (Figure S32). IBFBTs **12** and **14** both display a positive slope from R3→R5, due to the pull of the *anti*-fused benzothiophenesulfone acceptor (R6) from the furan donor (R2). The slope of **14** is greater because the furan is *anti*-fused (better donation, less antiaromatic R3 vs *syn*-fused in **12**, larger R3 value; see resonance structures in Figure 3.5. Regardless, the similar values of R5→R7 of **12** and **14** imply *anti*-fusion of the benzothiophene-S,S-dioxide acceptor is the driving force behind the ICT in these molecules. This is corroborated by DFT generated molecular orbitals, which show clear orbital overlap from the *s*-indacene core to the sulfone moiety in the LUMO of **12** and **14**, but not **11** and **13** (Figures S12-S15). Compounds **11** and **13** both display a negative slope from R3→R5, implying the furan can still donate into the core, but the *syn*-fused sulfones do not withdraw. The steeper negative slope from R3→R5 of **13** is explained by the stronger donation of the *anti*-fused furan relative to the *syn*-fusion in **11**. Additional NICS comparison plots of each isomer pre- and post-oxidation can be found in Figures S24-S28.

Table 2. Comparison of the NICS values (ppm) of the rings based on their optimized M11 geometries and experimental ¹H NMR core proton shifts (ppm)

cmpd	Ring ^[a,b] (ppm)							Core Avg. (ppm)	1H NMR (ppm)
	1	2	3	4	5	6	7		
<i>s</i> -Indacene			15.1	13.2	15.1			14.5	6.59 ^[d]
<i>syn</i> -IDBT 1	-15.0	-4.2	16.3	14.3	16.3	-4.2	-15.0	15.6	6.06 ^[e]
<i>anti</i> -IDBT 2	-15.5	-4.0	14.1	11.7	14.1	-4.0	-15.5	13.3	6.11 ^[e]
<i>syn</i> -IDBTS 3	-15.0	0.8	10.0	8.5	10.0	0.8	-15.0	9.5	6.91 ^[f]
<i>anti</i> -IDBTS	-15.7	0.4	13.3	14.0	13.3	0.4	-15.7	13.5	6.01 ^[g]
<i>syn</i> -IDBF 5	-14.4	-4.0	19.6	18.2	19.6	-4.0	-14.4	19.1	5.60 ^[h]
<i>anti</i> -IDBF 6	-14.8	-3.7	16.4	13.1	16.4	-3.7	-14.8	15.3	6.14 ^[h]
<i>syn/syn</i> - 7	-14.5	-4.3	17.7	16.2	18.0	-4.3	-15.0	17.3	5.85
<i>syn/anti</i> - 8	-15.4	-3.5	18.3	14.6	15.0	-4.9	-14.6	15.9	5.87
<i>anti/syn</i> - 9	-15.1	-4.6	14.2	13.8	18.8	-3.7	-14.8	15.6	6.05

<i>anti/anti-10</i>	-15.5	-3.8	14.4	12.4	16.1	-3.7	-14.9	14.3	6.10
<i>syn/syn-11</i>	-11.8	2.1	16.6	13.9	14.9	0.3	-15.7	15.1	6.17
<i>syn/anti-12</i>	-16.0	0.3	16.1	17.9	20.6	3.4	-11.4	18.2	5.64
<i>anti/syn-13</i>	-12.9	1.8	15.0	9.5	9.3	0.5	-15.1	11.2	6.50
<i>anti/anti-14</i>	-15.4	0.7	9.8	12.1	18.4	2.7	-12.6	13.4	5.99

[a] Throughout this dissertation we have adopted the convention where ring 2 is always the furan ring and ring 6 is always the thiophene or thiophene-S,S-dioxide ring for unsymmetrical structures **7-10** and **11-14**, respectively, as illustrated in Figure 5. [b] Rings 1 & 7, 2 & 6, and 3 & 5 are equivalent in the symmetrical structures **1-6**; rings 3 & 5 are equivalent in *s*-indacene. [c] Experimental core proton shift (ring 4) in CD₂Cl₂; mesityl R group unless otherwise noted. In the case of two core proton signals, the value reported is the average. [d] Compound **1f** in reference [58]. [e] Reference [17]. [f] Reference [18]; NMR in CDCl₃ and 4-*t*-butyl-2,6-dimethylphenyl R group. [g] Reference [18], NMR in CDCl₃. [h] Reference [19].

¹H NMR. Although the identity of the R groups on the apical carbons can affect the shift of the protons on the central six-membered ring of the *s*-indacene core, we can compare the ¹H NMR data of **7-14** with the symmetric IDBF, IDBT, and IDBTS derivatives (**1-6**) since all 14 compounds bear mesityl or “mesityl-like” 4-*t*-butyl-2,6-dimethylphenyl substitution.

In prior studies, we ranked relative ring current strength by comparing the chemical shift of the two-proton core singlet on similarly substituted molecules (e.g., *syn*-fused vs *anti*-fused). Because of the IDFBT isomers are unsymmetrical, the two core protons now appear as individual singlets in the NMR spectra (Figure 3.7). This illustrates the importance of comparing molecules with similar structures or at least understanding how to account for the differences. Heteroatoms in conjugated ring systems also effect the shift of the nearby ¹H signals in NMR spectrometry. The fact that the asymmetric isomers (**7-10**) have two unique ¹H signals on the same (in theory) delocalized *s*-indacene core indicate the heteroatom effects are more significant than previously thought.⁶² If the *s*-indacene core delocalizes uniformly in the presence of a magnetic field, then the *para*-protons on the center 6-membered ring should experience the same deshielding effect from the ring current which occurs in the π -orbitals, but the deshielding contributions from the heteroatoms are proximity dependent inductive withdrawing effects that occur primarily in the σ -bonds. The core protons on the asymmetric heterocycle-fused *s*-indacenes (**7-10**) have separate signals because the total deshielding effect on each is the sum of the contribution from the shared

paratropic ring current, and the inductive withdrawal of the most closely conjugated heteroatom.

The midpoint between the two core peaks for IBFBTs **7-10** falls approximately halfway between each of the two symmetric analogues **1, 2, 5, and 6** (Figure S33), implying the ring current strength of the asymmetric molecules is an average of strengths of both symmetric halves. The difference in magnetic response (ΔHz) between two *para*-H's across the core each isomers can be attributed to differences in proximity to the heteroatoms, and the differences in conjugation across the core (π -bridge).^{150,158} **10** has the least antiaromatic character and has the smallest ΔHz (12 Hz), followed by **8** which supports the *anti*-fusion resonance structure theory proposed in chapter 2. The core proton peaks of IBFBTS isomers shift further upfield for isomers with *anti*-fused sulfones (**12** and **14**) and downfield for the isomers with *syn*-fused sulfones (**11** and **13**), consistent with the observed behavior in symmetric IDBTSs **3** and **4**.^[18] The difference between core peaks in **7** and **9** increases by 0.23 and 0.08 ppm upon oxidation to **11** and **13** respectively, but the two core proton peaks in **8** and **10** converge to a singlet (2H) for **12** (5.64 ppm) and **14** (5.99 ppm), that at low concentrations resolve extremely finely split doublets with J-coupling values of <1 Hz (comparable to the spin-coupling in highly delocalized aromatic molecules) indicating the coupling across the core increases with the introduction of a donor acceptor system, when the acceptor (benzothiophene-S,S-dioxide) is *anti*-fused. Variable temperature NMR studies of **12** in CH_2Cl_2 illustrate the temperature dependant magnetic response. Decreasing temperature resolves a broad singlet at 0 °C, which expands to a tight doublet that expands

and shifts further upfield (5 Hz from 0 to -20 °C) and then begins to look paramagnetic at -30 °C (Figure 3.8).

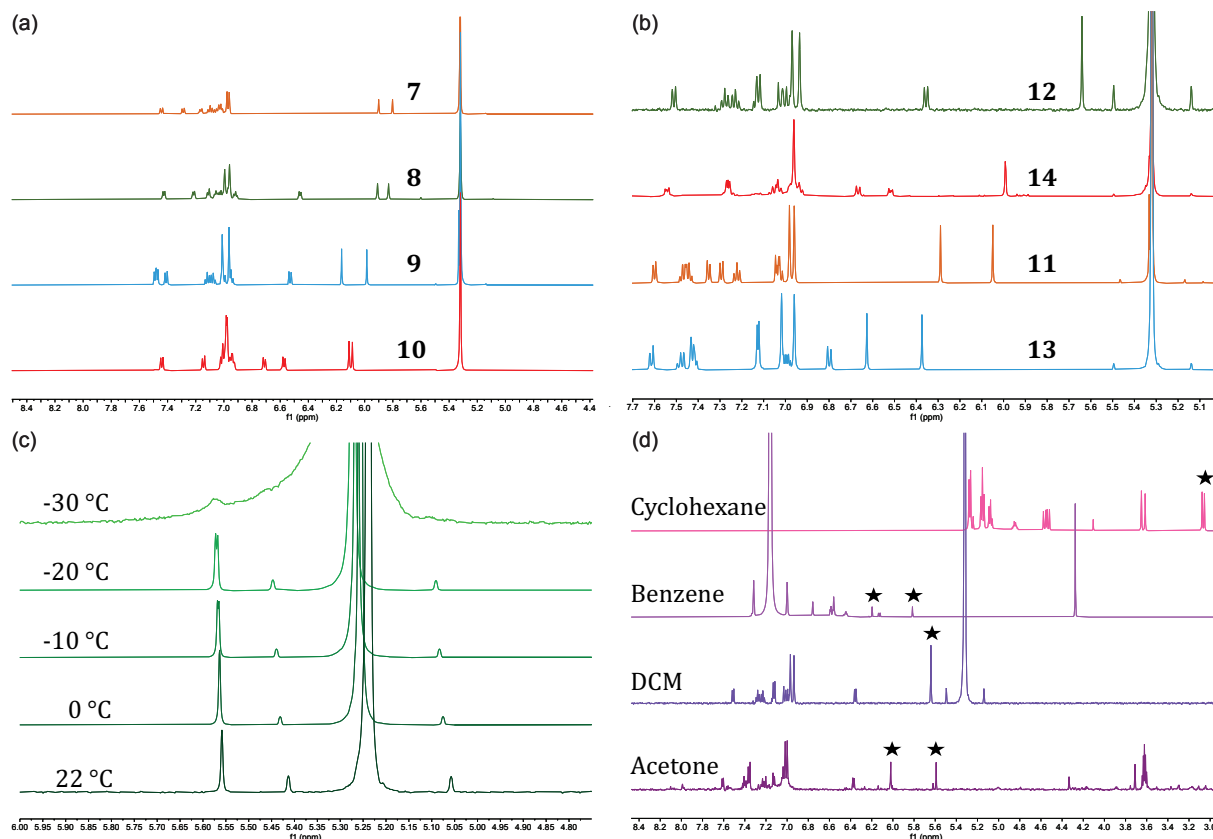


Figure 3.8. (a) Aromatic region of ¹H NMR spectra (CD₂Cl₂) of IBFBTs **7-10** showing upfield-shifted core singlets given in ppm. (b) Aromatic region of ¹H NMR spectra (CD₂Cl₂) of IBFBTs **11-14** showing upfield-shifted core singlets given in ppm. Both sets of spectra are ordered bottom to top in increasing upfield shift of the s-indacene core proton signals. (c) Variable temperature NMR spectra of **12** in DCM, referenced to TMS. (d) NMR solvent study of **12** in decreasingly polar solvents from acetone to apolar cyclohexane.

Encouraged by the variable temperature study, I investigated possible solvent effects in case the increased coupling strength at low temperatures was due to residual water freezing or something. Acetone ($\mu = 2.85$ D) and Benzene ($\mu = 0$ D) bookend the dielectric constant of DCM ($\mu = 1.55$ D), and in both solvents **12** resolves as two separate singlets. In acetone the core proton signals split, one upfield and one downfield of the DCM singlet, indicating a more polarized state was stabilized by the more polar solvent, which aligns with the results of the solvatochromic UV-vis study. In quadrupolar benzene, the two singlets both

shift downfield relative to the DCM singlet, suggesting the effect of the ring current strength decreased. In a-polar cyclohexane, all peaks shift upfield, and the DCM singlet splits into a

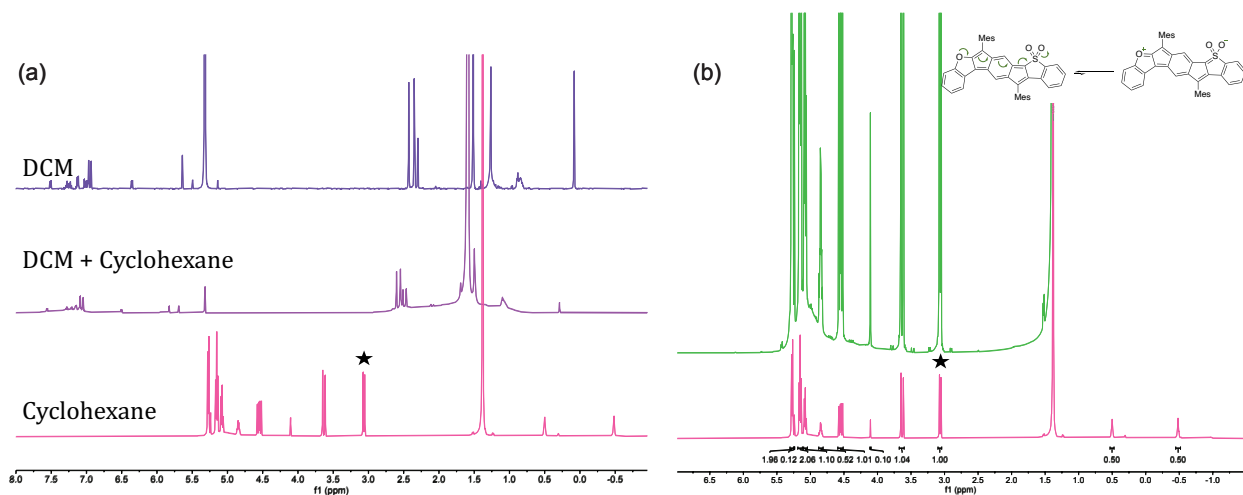


Figure 3.9. (a) NMR solvent study of **12** in Cyclohexane, Cyclohexane and a couple drops of DCM, and DCM. (b) Aromatic and zwitterionic formal resonance structures and NMR spectra of **12** in cyclohexanes (pink), scrolling the baseline up reveals satellite peaks (green).

tight doublet, and the mesityl protons disappear. The methyls could be under the cyclohexane peak, but scrolling up on the baseline looks like there is strong ^{13}C ^1H coupling (green trace Figure 3.8b) which implies the presence of strong π -stacking interactions in dilute solution. A possible culprit for this strange behavior is again solvent effects, from UV-vis and NMR solvent studies we can conclude that increasingly polar solvents stabilized a zwitterionic-like resonance form, and non-polar solvents stabilize the antiaromatic resonance form. Strong C-H coupling could be the result of strong intermolecular interactions (π -stacking), between paratropic ring currents inducing intermolecular paramagnetic coupling, but this is just speculation. COSY NMR confirmed the identity of the core protons (see appendix), but further investigation is needed.

CHAPTER IV

CONCLUSION

This chapter was written and edited by me.

4.1 Molecular Electronics

London's theory of superconductivity proposes that a superconducting (molecular) ring could be interpreted as a *pure quantum mechanism* of macroscopic scale, which aside from practical applications is fundamentally very exciting.² But I think I would need to do kind of a lot of work in argon matrixes at 0 K to prove that's what these molecules are, and sadly I am out of time for this chapter of my chemistry research journey. However, in the absence of proof, I do have some supporting evidence.

Decreasing temperature decreases molecular motion, which increases conductivity and paramagnetism in conductive metals. Semiconducting materials and organic conductors typically require thermal excited to become conductive or paramagnetic, or extremely low temperatures (much lower than -30 °C).^{8,11,159} There are plenty of stable room temperature organic radicals, but they are all aromatic. As explained in chapter I, antiaromatic ring currents (and concomitant magnetic properties) are much stronger than aromatic ring currents, because of the differences in charge density. Electrical conduction in molecular wires is strongest when it flows along the magnetic field lines produced by induced magnetic flux generated by the ring current. The strength of the magnetic flux (and conductivity in the π -stacking direction) is directly related to the strength of the ring current through Ampere's law. The obvious choice for superconducting molecular wires is antiaromatic molecules, which are notoriously tricky to make. Happily, *s*-Indacene exists at the intersection of strong antiaromatic character and synthetic tunability.

Charge flow occurs in conductive wires when voltage is applied, or it is induced by a magnetic field. The molecular equivalent of voltage is the incorporation of donor-acceptor (polarizable) moieties across a delocalized ring current (molecular wire), which induces intramolecular charge transfer (charge flow). Evidence of intramolecular charge transfer in a family of donor-acceptor-fused *s*-indacene isomers is presented in the solvatochromic UV-vis studies in chapters II and III, and TD-DFT generated excitation calculations found in the

appendix. Evidence of strong paramagnetic coupling at room temperature is presented in the NMR spectra of **12** in cyclohexane, and increased paramagnetic behavior is observed in the NMR spectra of **12** in DCM with decreasing temperature. The heterocycle effect rational described in chapter II, combined with the reported molecular properties of **11-14** indicates cross conjugation (*anti*-fusion) of benzothiophene-S,S-dioxide in combination with a donor group of either fusion orientation facilitates charge transfer through the molecule. This results in behavior and molecular properties similar to what would be expected from a molecular room temperature superconductor.

In 2016, Stoddart, Feringa, and Sauvage were jointly awarded the Nobel prize in chemistry for their pioneering work in the field of molecular machines.¹⁶⁰ The collection of machine pieces developed by the trio have almost limitless potential in energy storage and conversion applications and have inspired exciting synthetic curiosities including a molecular car.¹⁶¹ Feringa was recognized for developing molecular motors, which can convert external stimuli (light) into mechanical energy and do work on a molecular scale.¹⁶² Mechanical and electrical engineering on a macroscopic scale have been combined to produce some of the most impactful advancements in technology including but not limited to cars, airplanes, rockets, wind turbines, solar cells, and nuclear powerplants. Motor-generators such as those found in cars, combine batteries (electrical energy) and mechanical motors (mechanical energy), in what should be an “infinite” energy loop of a battery powered motor, which in turn recharges the battery. On a macroscopic scale, the energy loop is not actually infinite due to the resistivity of the materials involved which dissipate energy as heat, contributing to the degradation of the materials themselves over time. These issues should not be present on a molecular scale using superconducting (resistance free) molecular wires. What if the combination of molecular electronics and molecular motors could generate infinite energy?

As a physical organic chemist, my job is to understand, explain, and figure out how to control the components I can make with synthetic organic chemistry. If the donor-acceptor-fused *s*-indacene derivatives I made are room temperature super conductors, chapter II represents my effort toward understanding and explaining the molecular electronic components I made while working in the Haley lab, which is detailed in chapter III.

4.2 Conclusion

In conclusion, the defining molecular property of antiaromatic molecules is the strength of the paratropic ring current. Formally antiaromatic molecules exist on a spectrum of increasing diradical (paramagnetic) character which increases with increasing conjugation. Antiaromaticity exists in CBD, pentalene, and several indacene isomers (which are outside the scope of this discussion) including *s*-indacene. π -extension of the *s*-indacene core produces DCPN and DCPA, which are formally antiaromatic but are diradical in character. The structure property relationships of heterocycle-fused-*s*-indacenes have been understood and explained. Donor-acceptor functionality of *s*-indacene is uniquely possible through the robust synthetic methods developed by the Haley lab. Intramolecular charge transfer can be measured by STM-break junction measurements, or solvatochromic shifts and calculated transition dipole moments in donor-acceptor molecules. Electrical conduction between molecular wires should be measured by single crystal conductivity measurements in materials along the same axis as π -stacking between molecules.¹⁶³ A very meaningful study would compare the molecular intramolecular charge transfer measurements (bond length alternation and solvatochromic shift), STM-BJ resistivity measurements, and single crystal conductivity measurements in materials composed of 3-coordinate π -stacked aromatic and antiaromatic molecules. The end.

APPENDIX

SUPPLEMENTARY INFORMATION FOR CHAPTERS I AND II

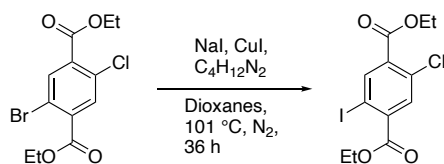
The appendix is the supplementary information for chapters I and II of this dissertation. It includes experimental details, X-ray crystallography details, bond length comparisons, TD-DFT calculations and molecular orbitals, long-range UV-vis experiments, calculations of proposed aromatic analogs, additional NICS XY-plots, additional electrochemistry information, additional plots and comparisons, extended Hückel theory calculations and GIMIC plots, computational details, and copies of NMR spectra

1. Experimental Details

General. All air-sensitive manipulations were carried out under an inert atmosphere using standard Schlenk technique. Silica gel (240-300 mesh) was used for column chromatography. NMR spectra were recorded on a Bruker Avance III HD 500 equipped with a Prodigy multinuclear cryoprobe (^1H : 500 MHz, ^{13}C : 126 MHz) or Bruker Avance III HD 600 equipped with a Prodigy multinuclear cryoprobe (^1H : 600 MHz, ^{13}C : 151 MHz) NMR spectrometer at room temperature (unless otherwise noted). ^1H and ^{13}C NMR chemical shifts (δ) are expressed in ppm relative to the residual non-deuterated solvent reference (CDCl_3 : ^1H 7.26 ppm, ^{13}C 77.16 ppm; CD_2Cl_2 : ^1H 5.32 ppm, ^{13}C 53.84 ppm). UV-vis spectra were recorded on an Agilent Technologies Cary 60 UV-Vis spectrometer in reagent grade DMF, DCM, acetone, and hexanes. HRMS were recorded on a Waters XEVOG2-XS TOF mass spectrometer. Diethyl 2-bromo-5-chloroterephthalate,¹ benzothiophene-2-boronic acid pinacolate ester,² benzothiophene-3-boronic acid pinacolate ester,² and benzofuran-3-boronic acid pinacolate ester² were prepared as previously described. Unless otherwise noted, all other reagents were purchased from commercial sources and used as received.

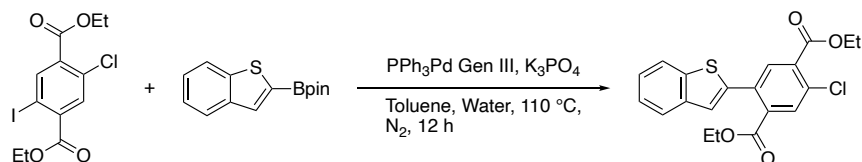
Diethyl 2-chloro-5-iodoterephthalate (15). To a two-neck round-bottom flask was added diethyl 2-bromo-5-chloroterephthalate (4.13 g, 12.31 mmol, 1.0 equiv.), KI (40.8 g, 246.2 mmol, 20 equiv.), and CuI (1.17 g, 6.15 mmol, 0.5 equiv.), which was evacuated and backfilled with N_2 . Dry, sparged dioxane (200 mL) and *N,N'*-dimethylethylenediamine (1.33

mL, 12.31 mmol, 1 equiv.) were added, heated to reflux and stirred overnight. After cooling to room temperature, the crude mixture was washed through celite with DCM, and then extracted with DCM (3 x 50 mL). The combined organics were washed successively with brine and water (1 x 50 mL each), dried (MgSO₄), filtered, and concentrated under vacuum. The residue was purified by recrystallization from EtOH. The resultant off-white solid (3.81 g, 80%) was used without further purification. ¹H NMR (500 MHz, CDCl₃) δ 8.36 (s, 1H), 7.83 (s, 1H), 4.44–4.40 (m, 4H), 1.44–1.40 (m, 6H); ¹³C NMR (126 MHz, CDCl₃) δ 164.94, 163.76, 143.48, 138.86, 133.83, 133.05 (2), 90.72, 62.57, 62.41, 14.30. HRMS (ASAP) (*m/z*), calculated for C₁₂H₁₂ClIO₄ (M)⁺ 381.9469, found 382.9469.



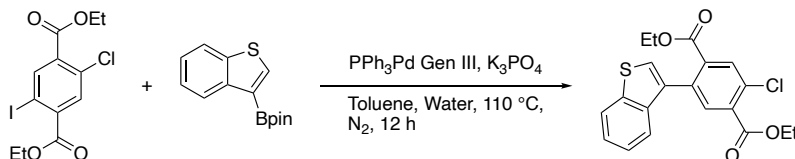
General Procedure for Suzuki cross-couplings to synthesize aryl chlorides 16-17

A two-neck round-bottom flask fitted with a condenser was charged with terephthalate **15** (1.0 equiv.), benzothiophene-2-boronic or benzothiophene-3-boronic acid pinacolate ester (0.95 equiv.), K₃PO₄ (2 equiv.), and PPh₃ Pd Gen III (0.05 equiv.). These solids were then placed under N₂ atmosphere and dissolved in a solution of toluene and water (10:1, 0.1 M) that had been degassed by sparging with N₂. After refluxing overnight and cooling to room temperature, the reaction was quenched with H₂O, poured through celite, and extracted with DCM (3 x 30 mL). The combined organic layer was washed successively with brine and water (1 x 30 mL each), dried (MgSO₄), filtered, and concentrated under vacuum. The residue was purified by column chromatography to yield a viscous, colorless oil.



Chloride 16 (2-benzothiophene). A mixture of terephthalate **15** (1.94 g, 5.07 mmol, 1.0 equiv.), benzothiophene-2-boronic acid pinacolate ester (881 mg, 3.39 mmol, 0.95 equiv.), K₃PO₄ (1.51 g, 7.14 mmol, 2.0 equiv.), and PdPPh₃ Gen. III (66.4 mg, 0.11 mmol, 0.03 equiv.)

yielded diester **16** (881 mg, 63%) as a clear oil. ¹H NMR (500 MHz, CDCl₃) δ 7.98 (s, 1H), 7.85 (s, 1H), 7.84 (d, *J* = 7.6 Hz, 1H), 7.78 (d, *J* = 7.5 Hz, 1H), 7.40–7.34 (m, 2H), 7.27 (s, 1H), 4.43 (q, *J* = 7.1 Hz, 2H), 4.21 (q, *J* = 7.1 Hz, 2H), 1.41 (t, *J* = 7.1 Hz, 3H), 1.08 (t, *J* = 7.1 Hz, 3H); ¹³C NMR (151 MHz, CDCl₃) δ 166.39, 164.66, 140.40, 140.03, 139.79, 135.49, 133.89, 133.57, 132.82, 132.46, 131.96, 124.71, 124.67, 123.83, 123.81, 122.13, 62.12, 61.99, 14.20, 13.74; HMRS (ASAP) (*m/z*), calculated for C₂₀H₁₇ClO₄S (M+H)⁺ 388.0536, found 388.0520.

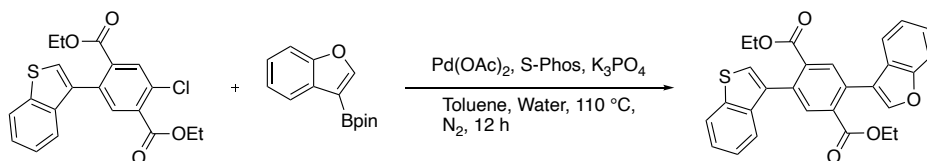


Chloride 17 (3-benzothiophene). A mixture of terephthalate **15** (50 mg, 0.14 mmol, 1.0 equiv.), benzothiophene-3-boronic acid pinacolate ester (36 mg, 0.14 mmol, 1 equiv.), K₃PO₄ (44 mg, 0.28 mmol, 2.0 equiv.), and PdPPh₃ Gen. III (10 mg, 0.014 mmol, 0.1 equiv.) yielded diester **17** (40 mg, 75%) as a clear oil. ¹H NMR (500 MHz, CDCl₃) δ 8.05 (s, 1H), 7.90 (d, *J* = 7.9 Hz, 1H), 7.87 (s, 1H), 7.40–7.32 (m, 4H), 4.42 (q, *J* = 7.1 Hz, 2H), 3.91 (q, *J* = 7.1 Hz, 2H), 1.40 (t, *J* = 7.1 Hz, 3H), 0.71 (t, *J* = 7.1 Hz, 3H); ¹³C NMR (126 MHz, CDCl₃) δ 166.10, 165.05, 139.68, 138.89, 135.45, 135.43, 134.58, 134.25, 133.32, 133.21, 132.76, 124.70, 124.67, 124.20, 122.91, 122.27, 62.20, 61.70, 14.33, 13.35.; HMRS (ASAP) (*m/z*), calculated for C₂₀H₁₇ClO₄S (M+H)⁺ 388.0536, found 388.0529.

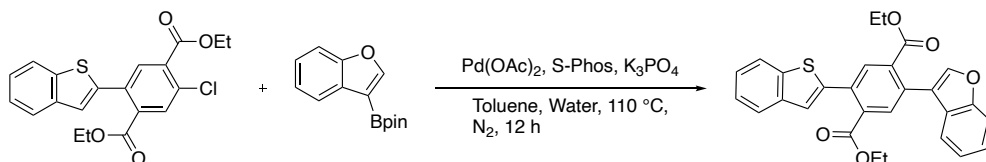
General procedure for Suzuki cross-coupling to synthesize diesters 18-21

A two-neck round-bottom flask fitted with a condenser was charged with chloride **16** or **17** (1 equiv.), benzofuran-3-boronic acid pinacolate ester or benzofuran-2-boronic acid (1.1-1.5 equiv.), K₃PO₄ (1.5-2.2 equiv.), Pd(OAc)₂ (0.05 equiv.), and SPhos (0.13 equiv.). These solids were then placed under N₂ atmosphere and dissolved in a solution of toluene and water (10:1, 0.1M) that had been degassed by sparging with N₂. After refluxing overnight and cooling to room temperature, the reaction was quenched with H₂O, poured through celite, and extracted with DCM (3 x 30 mL). The combined organics were washed successively with brine and water (1 x 30 mL each), dried (MgSO₄), filtered, and

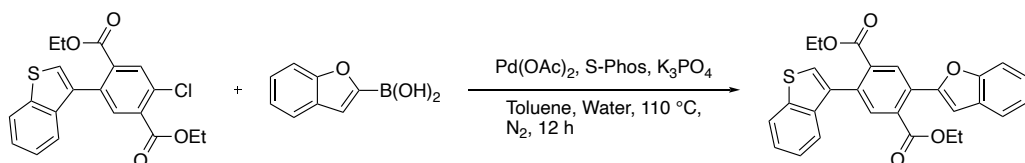
concentrated under vacuum. The residue was recrystallized from EtOH to precipitate the product diester as a grey or white solid.



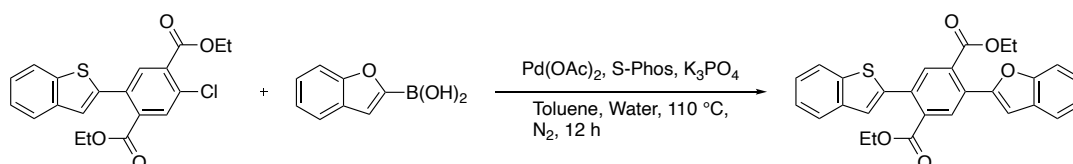
Diester 18 (*syn/syn*). Chloride **17** (400 mg, 1.03 mmol, 1.0 equiv.), benzofuran-3-boronic acid pinacolate ester (276 mg, 1.13 mmol, 1.1 equiv.), K_3PO_4 (327 mg, 1.54 mmol, 1.5 equiv.), $Pd(OAc)_2$ (12.0 mg, 0.053 mmol, 0.05 equiv.), and SPhos (53 mg, 0.13 mmol, 0.13 equiv.) gave diester **18** (400 mg, 82%) as a beige solid. 1H NMR (600 MHz, $CDCl_3$) δ 8.10 (s, 1H), 8.01 (s, 1H), 7.92 (d, $J = 7.6$ Hz, 1H), 7.81 (s, 1H), 7.57 (d, $J = 8.3$ Hz, 1H), 7.51 (d, $J = 7.1$ Hz, 1H), 7.48 (d, $J = 7.8$ Hz, 1H), 7.42 (s, 1H), 7.39–7.34 (m, 3H), 7.28 (t, $J = 7.5$ Hz, 1H), 4.06 (q, $J = 7.1$ Hz, 2H), 3.91 (q, $J = 7.1$ Hz, 2H), 0.90 (t, $J = 7.1$ Hz, 3H), 0.70 (t, $J = 7.1$ Hz, 3H); ^{13}C NMR (151 MHz, $CDCl_3$) δ 167.65, 167.40, 155.36, 142.58, 139.95, 139.25, 136.42, 135.70, 134.98, 134.88, 133.62, 133.39, 131.43, 127.94, 125.03, 124.86, 124.83, 124.28, 123.42, 123.11, 122.67, 121.06, 120.25, 112.10, 62.02, 61.71, 13.82, 13.59; HRMS (ASAP) (m/z), calculated for $C_{28}H_{22}O_5S$ ($M+H$) $^+$ 470.1188, found 470.1186.



Diester 19 (*syn/anti*). Chloride **16** (500 mg, 1.28 mmol, 1 equiv.), benzofuran-3-boronic acid pinacolate ester (344 mg, 1.41 mmol, 1.1 equiv.), K_3PO_4 (408 mg, 1.92 mmol, 1.5 equiv.), $Pd(OAc)_2$ (14 mg, 0.06 mmol, 0.05 equiv.) and SPhos (70 mg, 0.17 mmol, 0.13 equiv.) furnished **19** (310 mg, 52%) as a light tan solid. 1H NMR (500 MHz, $CDCl_3$) δ 8.11 (s, 1H), 7.89 (s, 1H), 7.86 (d, $J = 7.7$ Hz, 1H), 7.81 (d, $J = 7.5$ Hz, 1H), 7.78 (s, 1H), 7.56 (d, $J = 8.2$ Hz, 1H), 7.47–7.33 (m, 6H), 4.22 (q, $J = 7.2$ Hz, 2H), 4.06 (q, $J = 7.1$ Hz, 2H), 1.08 (t, $J = 7.1$ Hz, 3H), 0.90 (t, $J = 7.2$ Hz, 3H); ^{13}C NMR (126 MHz, $CDCl_3$) δ 167.40, 166.91, 154.88, 142.13, 140.73, 140.36, 139.83, 134.82, 133.76, 133.54, 132.89, 132.19, 131.41, 127.43, 124.59, 124.50 (2), 123.70, 123.53, 122.98, 122.04, 120.48, 119.75, 111.62, 61.69, 61.57, 13.66, 13.34; HRMS (ASAP) (m/z), calculated for $C_{28}H_{22}O_5S$ ($M+H$) $^+$ 470.1188, found 470.1169.



Diester 20 (*anti/syn*). Chloride **17** (430 mg, 1.15 mmol, 1.0 equiv.), benzofuran-2-boronic acid (330 mg, 1.26 mmol, 1.5 eq.), K_3PO_4 (336 mg, 1.73 mmol, 1.5 equiv.), $Pd(OAc)_2$ (13 mg, 0.06 mmol, 0.05 equiv.), and SPhos (62 mg, 0.15 mmol, 0.13 equiv.) yielded diester **20** (300 mg, 56%) as a pale yellow solid. 1H NMR (500 MHz, $CDCl_3$) δ 8.38 (s, 1H), 7.90 (d, $J = 7.3$ Hz, 1H), 7.79 (s, 1H), 7.65 (d, $J = 7.6$ Hz, 1H), 7.51 (d, $J = 8.1$ Hz, 1H), 7.47 (d, $J = 7.1$ Hz, 1H), 7.40 (s, 1H), 7.39–7.27 (m, 4H), 7.10 (s, 1H), 4.34 (q, $J = 7.1$ Hz, 2H), 3.92 (q, $J = 7.1$ Hz, 2H), 1.20 (t, $J = 7.1$ Hz, 3H), 0.70 (t, $J = 7.1$ Hz, 3H); ^{13}C NMR (126 MHz, $CDCl_3$) δ 167.94, 166.77, 155.08, 153.25, 139.47, 138.71, 136.00, 135.87, 133.88, 133.69, 132.28, 130.63, 128.84, 128.66, 124.86, 124.40 (2), 123.87, 123.05, 122.63, 122.16, 121.32, 111.14, 105.27, 61.84, 61.27, 13.93, 13.10. HRMS (ASAP) (m/z), calculated for $C_{28}H_{22}O_5S$ ($M+H$) $^+$ 470.1188, found 470.1189.



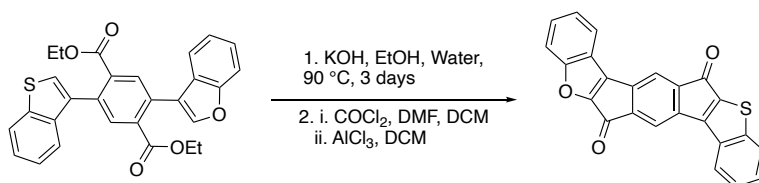
Diester 21 (*anti/anti*). Chloride **16** (1.1 g, 2.82 mmol, 1.0 equiv.), benzofuran-2-boronic acid (687 mg, 4.24 mmol, 1.5 equiv.), K_3PO_4 (1.2 g, 5.66 mmol, 2 equiv.), $Pd(OAc)_2$ (32 mg, 0.14 mmol, 0.05 equiv.), and SPhos (152 mg, 0.37 mmol, 0.13 equiv.) afforded diester **21** (820 mg, 62%) as an off-white solid. 1H NMR (500 MHz, CD_2Cl_2) δ 8.18 (s, 1H), 7.90–7.86 (m, 2H), 7.83 (d, $J = 7.2$ Hz, 1H), 7.67 (d, $J = 7.0$ Hz, 1H), 7.52 (d, $J = 8.8$ Hz, 1H), 7.43–7.34 (m, 4H), 7.29 (t, $J = 7.5$ Hz, 1H), 7.11 (s, 1H), 4.35 (q, $J = 7.1$ Hz, 2H), 4.25 (q, $J = 7.2$ Hz, 2H), 1.21 (t, $J = 7.1$ Hz, 3H), 1.11 (t, $J = 7.1$ Hz, 3H); ^{13}C NMR (126 MHz, CD_2Cl_2) δ 168.18, 167.72, 155.74, 153.69, 141.22, 140.99, 140.53, 134.99, 134.70, 133.75, 132.50, 130.30, 129.56, 129.32, 125.67, 125.27, 125.23, 124.39, 124.35, 123.79, 122.66, 122.01, 111.71, 106.19, 62.57, 62.40,

14.41, 14.17; HRMS (ASAP) (m/z), calculated for $C_{28}H_{22}O_5S$ ($M+H$)⁺ 470.1188, found 470.1189.

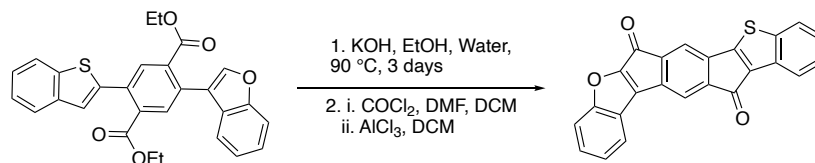
General procedure for synthesis of diones 22-25

A round-bottom flask fitted with a condenser was charged with a diester (1 equiv.), KOH (10 equiv.), and a solution of EtOH and H₂O (4:1, 0.01 M). After refluxing overnight, the mixture was cooled and the EtOH evaporated. Concentrated HCl was slowly added to the aqueous solution and a precipitate formed, which was isolated and washed with H₂O to yield the diacid intermediate as a yellow solid that was carried on without further purification.

To a suspension of the diacid (1 equiv.) in DCM (0.01 M) was added DMF (2 equiv.) followed by oxalyl chloride (4 equiv.). After 12 h, the volatiles were removed under reduced pressure. The crude acid chloride was dissolved in DCM (0.01 M) and solid AlCl₃ (5 equiv.) was added to the flask. The reaction was stirred overnight and then poured into an HCl-ice mixture, precipitating the dione. The solid was filtered and washed successively with H₂O, acetone, and DCM to afford the dione as a green solid which was too insoluble to obtain NMR spectra.

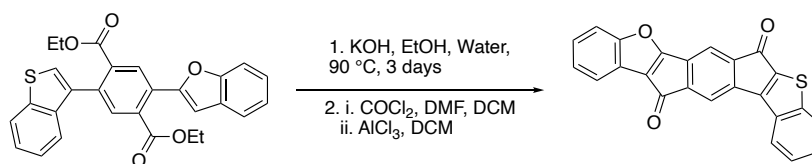


Dione 22 (*syn/syn*). Saponification of diester **18** (300 mg, 0.64 mmol, 1 equiv.) with KOH (358 mg, 6.4 mmol, 10 equiv.) afforded the crude diacid (300 mg, 99%). The *syn-syn*-IBFBT diacid (250 mg, 0.60 mmol, 1 equiv.) was reacted with (COCl)₂ (0.31 ml, 2.41 mmol, 4 equiv.), DMF (0.09 ml, 1.21 mmol, 2 equiv.), and AlCl₃ (400 mg, 3.0 mmol, 5 equiv.). Dione **22** was isolated as an olive-brown powder (75 mg, 33%). HRMS (ASAP) (m/z), calculated for $C_{24}H_{10}O_3S$ ($M+H$)⁺ 379.0430, found 379.0416.

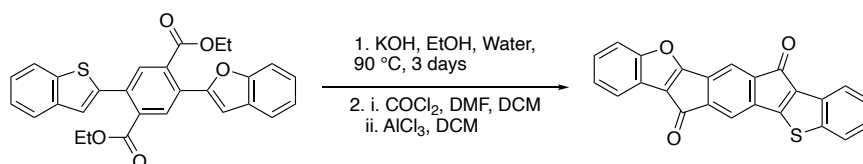


Dione 23 (*syn/anti*). Saponification of diester **19** (310 mg, 0.66 mmol, 1 equiv.) with KOH (370 mg, 6.59 mmol, 10 equiv.) afforded the crude diacid (308 mg, 99%). The *syn-anti*-

IBFBT diacid (308 mg, 0.74 mmol, 1 equiv.) was reacted with (COCl)₂ (0.38 ml, 2.96 mmol, 4 equiv.), DMF (0.11 ml, 1.48 mmol, 2 equiv.), and AlCl₃ (493 mg, 3.7 mmol, 5 equiv.). Dione **23** was isolated as a beige-green powder (130 mg, 46%). HRMS (ASAP) (*m/z*), calculated for C₂₄H₁₀O₃S (M)⁺ 378.0351, found 378.0371.



Dione 24 (anti/syn). Saponification of diester **20** (300 mg, 0.64 mmol, 1 equiv.) with KOH (358 mg, 6.4 mmol, 10 equiv.) afforded the crude diacid (300 mg, 99%). The *anti-syn*-IBFBT diacid (326 mg, 0.79 mmol, 1 equiv.) was reacted with (COCl)₂ (0.36 ml, 4.25 mmol, 4 equiv.), DMF (0.15 ml, 2.12 mmol, 2 equiv.), and AlCl₃ (706 mg, 5.30 mmol, 5 equiv.). Dione **24** was isolated as a green powder (230 mg, 57%). HRMS (ASAP) (*m/z*), calculated for C₂₄H₁₀O₃S (M)⁺ 378.0351, found 378.0369.



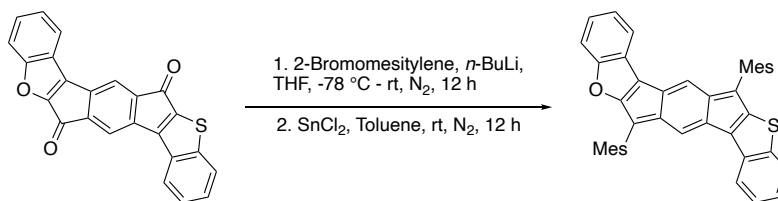
Dione 25 (anti/anti). Saponification of diester **21** (820 mg, 1.74 mmol, 1 equiv.) with KOH (978 mg, 17.4 mmol, 10 equiv.) afforded the crude diacid (720 mg, 99%). The *anti-anti*-IBFBT diacid (720 mg, 1.73 mmol, 1 equiv.) was reacted with (COCl)₂ (0.59 ml, 6.95 mmol, 4 equiv.), DMF (0.27 ml, 3.47 mmol, 2 equiv.), and AlCl₃ (1.15 g, 8.65 mmol, 5 equiv.). Dione **25** was isolated as a dark green powder (430 mg, 66%). HRMS (ASAP) (*m/z*), calculated for C₂₄H₁₀O₃S (M+H)⁺ 379.0430, found 379.0458.

General procedure for synthesis of heterocycle-fused *s*-indacenes 7-10

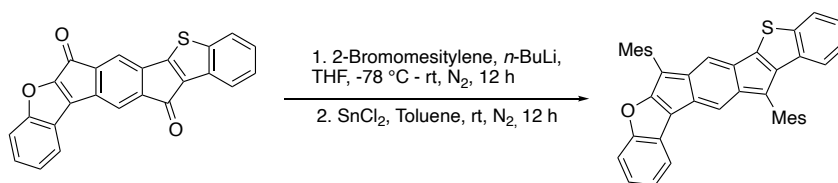
To a flame-dried round-bottom flask was added dione (1 equiv.) and dry THF (0.02 M) and the mixture cooled to -78 °C while stirring under N₂. In a second flame-dried round-bottom flask, 2-bromomesitylene (8 equiv.) and dry THF (50 ml) were added and the mixture cooled to -78 °C while stirring. To the second flask, *n*-butyllithium (7.5 equiv.) was added dropwise at -78 °C. After stirring for 30 min, the lithiate was slowly cannula transferred to the suspension of dione and stirred at -78 °C for 2 hours and then warmed to room temperature

overnight. The reaction was quenched with aq. NH₄Cl soln and extracted with DCM (3 x 30 mL). The combine organic layer was washed with brine and water (1 x 30 mL each), dried (MgSO₄), filtered, and concentrated under vacuum. The residue was suspended in hexanes, sonicated, and filtered to yield the diol which was carried on without further purification.

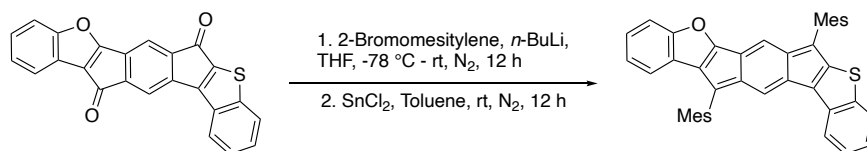
In a single-neck round-bottom flask the crude diol (1 equiv.) and anhydrous SnCl₂ (4 equiv.) were dissolved in dry degassed toluene (0.005 M) and stirred overnight at room temperature. The reaction mixture was filtered through a plug of celite and the solvent was evaporated. The crude product dissolved in minimal DCM before layering MeOH on top, and then left at -20 °C for 4-6 h to crystallize out polar impurities. The suspension was then filtered and the resulting filtrate was dried under reduced pressure, dissolved in hexanes, and then left at -20 °C to crystallize out non-polar impurities. The suspension was again filtered and the filtrate evaporated under reduced pressure. The residue was purified by column chromatography using a mixture of hexanes and EtOAc as the eluent (see each compound for specific details).



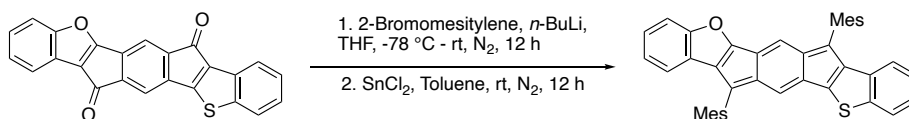
***syn/syn*-IBFBT (7).** Dione **22** (75 mg, 0.19 mmol, 1.0 equiv.) was reacted with the lithiate generated from MesBr (0.23 mL, 1.47 mmol, 8 equiv.) and *n*-BuLi (0.84 mL, 2.5 M, 7.5 equiv.) to yield the crude diol (20 mg, 16%) as a light brown solid. Diol (20 mg, 0.03 mmol, 1.0 equiv.) and SnCl₂ (25 mg, 0.13 mmol, 4.0 equiv.) afforded the crude indacene, which was purified by flash column chromatography (5% EtOAc/hexanes) to give **7** (8 mg, 46%) as a deep blue solid with a purple sheen. ¹H NMR (500 MHz, CD₂Cl₂) δ 7.44 (d, *J* = 7.9 Hz, 1H), 7.29 (d, *J* = 7.8 Hz, 1H), 7.16 (d, *J* = 8.9 Hz, 1H), 7.11–7.00 (m, 5H), 6.97 (d, *J* = 8.0 Hz, 4H), 5.90 (s, 1H), 5.80 (s, 1H), 2.41 (s, 6H), 2.40 (s, 6H), 2.34 (s, 3H), 2.33 (s, 3H); ¹³C NMR (126 MHz, CD₂Cl₂) δ 166.72, 161.88, 149.42, 146.88, 146.40, 142.43, 139.09, 138.62, 138.39, 137.96, 136.98, 136.80, 136.53, 134.94, 133.32, 130.93, 129.21, 128.69, 128.53, 127.12, 126.69, 126.45, 125.49, 125.35, 124.85, 124.15, 124.00, 123.90, 121.97, 119.93, 112.44, 96.29, 29.88, 21.06, 20.62, 20.48; HRMS (ASAP) (*m/z*), calculated for C₄₂H₃₂OS (M)⁺ 584.2174, found 584.2158



***syn/anti*-IBFBT (8).** Dione **23** (385 mg, 1.01 mmol, 1.0 equiv.) was reacted with the lithiate generated from MesBr (1.25 mL, 8.13 mmol, 8 equiv.) and *n*-BuLi (4.75 mL, 2.5 M, 7.5 equiv.) to yield the crude diol (300 mg, 48 %) as a tan solid. Diol (300 mg, 0.48 mmol, 1.0 equiv.) and SnCl₂ (364 mg, 1.92 mmol, 4.0 equiv.) in toluene (30 mL) afforded the crude indacene, which was purified by flash column chromatography (15% EtOAc/hexanes) to give **8** (100 mg, 35%) as a deep blue solid with a purple sheen. ¹H NMR (600 MHz, CD₂Cl₂) δ 7.43 (d, *J* = 8.0 Hz, 1H), 7.21 (d, *J* = 7.6 Hz, 1H), 7.11 (d, *J* = 8.1 Hz, 1H), 7.07–7.02 (m, 2H), 7.00–6.95 (m, 5H), 6.92 (t, *J* = 7.5 Hz, 1H), 6.46 (d, *J* = 7.9 Hz, 1H), 5.91 (s, 1H), 5.83 (s, 1H), 2.37 (s, 15H), 2.32 (s, 3H); ¹³C NMR (151 MHz, CD₂Cl₂) δ 166.01, 162.23, 151.36, 149.30, 144.05, 143.03, 138.59, 138.19, 137.36, 137.10, 136.94, 136.65, 136.49, 133.29, 133.12, 129.71, 129.09, 128.59, 128.46, 128.27, 127.27, 126.88, 126.74, 125.81, 125.36, 124.05, 123.97, 123.92, 123.84, 120.49, 120.33, 112.46, 21.14, 21.07, 20.60, 20.42; HRMS (ASAP) (*m/z*), calculated for C₄₂H₃₂OS (M+H)⁺ 585.2253, found 585.2305.



***anti/syn*-IBFBT (9).** Dione **9** (200 mg, 0.53 mmol, 1.0 equiv.) was reacted with the lithiate generated from MesBr (0.65 mL, 4.22 mmol, 8 equiv.) and *n*-BuLi (2.47 mL, 1.6 M, 7.5 equiv.) to yield the crude diol (222 mg, 68 %) as a light orange solid. Diol (222 mg, 0.36 mmol, 1.0 equiv.) and SnCl₂ (272 mg, 1.43 mmol, 4.0 equiv.) afforded the crude indacene, which was purified by layered evaporation of acetonitrile in DCM to give **13** (107 mg, 51%) as a sparkly purple solid. ¹H NMR (500 MHz, CDCl₃) δ 7.45 (d, *J* = 9.0 Hz, 1H), 7.37 (d, *J* = 9.0 Hz, 1H), 7.13 (d, *J* = 8.2 Hz, 1H), 7.11–7.05 (m, 2H), 7.00–6.91 (m, 6H), 6.66 (d, *J* = 7.8 Hz, 1H), 6.13 (s, 1H),

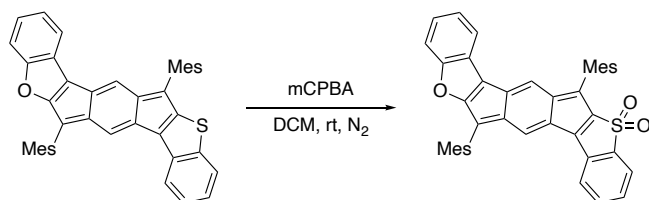


5.96 (s, 1H), 2.42 (s, 6H), 2.35 (s, 9H), 2.32 (s, 3H); ^{13}C NMR (126 MHz, CD_2Cl_2) δ 168.59, 161.65, 149.08, 147.51, 147.39, 145.43, 144.23, 138.53, 138.41, 137.93, 136.85, 136.64, 133.80, 133.45, 132.06, 130.06, 129.53, 129.10, 128.93, 128.69, 127.14, 126.31, 125.69, 125.61, 125.37, 124.48, 124.39, 124.12, 124.10, 122.71, 119.37, 112.40, 21.30, 21.24, 20.80, 20.68. HRMS (ASAP) (m/z), calculated for $\text{C}_{42}\text{H}_{32}\text{OS}$ (M) $^+$ 584.2174, found 584.2174.

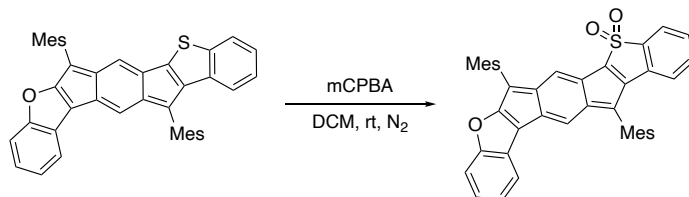
***anti/anti*-IBFBT (10).** Dione **10** (230 mg, 0.6 mmol, 1.0 equiv.) was reacted with the lithiate generated from MesBr (0.74 mL, 4.86 mmol, 8 equiv.) and n-BuLi (1.8 mL, 2.5 M, 7.5 equiv.) to yield the crude diol (130 mg, 35%) as a tan solid. Diol (130 mg, 0.21 mmol, 1.0 equiv.) and SnCl_2 (159 mg, 0.84 mmol, 4.0 equiv.) afforded the crude indacene, which was purified flash column chromatography (5% EtOAc/hexanes) to give **10** (20 mg, 16%) as a deep blue solid with a reddish sheen. ^1H NMR (500 MHz, CD_2Cl_2) δ 7.44 (d, $J = 7.9$ Hz, 1H), 7.14 (d, $J = 8.2$ Hz, 1H), 7.02–6.93 (m, 8H), 6.71 (d, $J = 7.6$ Hz, 1H), 6.57 (d, $J = 7.8$ Hz, 1H), 6.11 (s, 1H), 6.09 (s, 1H), 2.37 (s, 6H), 2.36 (s, 3H), 2.34 (s, 3H), 2.30 (s, 6H); ^{13}C NMR (126 MHz, CD_2Cl_2) δ 168.99, 162.04, 150.41, 148.54, 146.74, 144.70, 143.45, 138.54, 138.49, 137.50, 136.99, 136.95, 134.39, 133.53, 130.78, 130.37, 130.35, 130.14, 129.47, 128.99, 128.81, 128.64, 126.37, 126.17, 124.88, 124.64, 124.22, 124.20, 122.90, 121.24, 119.86, 112.56, 21.50, 21.47, 20.93, 20.78; HRMS (ASAP) (m/z), calculated for $\text{C}_{42}\text{H}_{32}\text{OS}$ ($\text{M}+\text{H}$) $^+$ 585.2253, found 585.2210.

General procedure for synthesis of sulfones 11-14

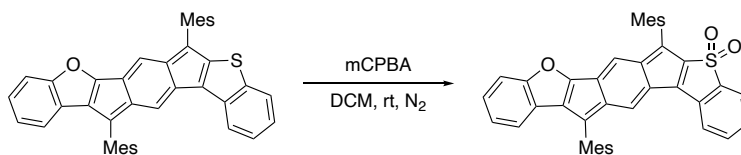
A flame-dried, foil-wrapped round bottom flask equipped with a Claisen head was charged with the parent indacene compound (1 equiv.) and sparged DCM (0.002 M). To this m-CPBA (3-4 equiv.) was added in 3 portions over a 30 min period. Immediately following the third addition of m-CPBA, reaction progress was closely monitored by TLC. Once the starting material had been consumed (10-90 min), the reaction was quenched with a 10% KOH solution and the organics were extracted using DCM (3 x 10 mL). The combined organic layers were washed with 10% KOH solution (3 x 10 mL), brine (1 x 10 mL), water (1 x 10 mL), dried (NaSO_4), and then concentrated to dryness. The crude residue was suspended in hexanes filtered through a 0.45 micron filter and the precipitate was washed with hexanes until the eluent was clear. The filtrate was then concentrated to dryness to afford the crude product. Column chromatography using a mixture of hexanes and DCM as mobile phase (see each compound for specific details) afforded the purified sulfones.



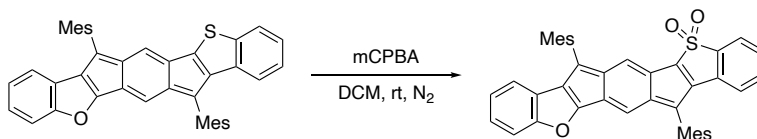
Sulfone 11 (*syn/syn*-IBFBTS). Parent IBFBT **7** (15 mg, 0.026 mmol, 1 equiv.) and mCPBA (13 mg, 0.077 mmol, 3 equiv.) in DCM (10 mL) were reacted to afford the crude sulfone, which was purified by flash column chromatography (1:1 DCM/hexanes) to give **11** (3.5 mg, 22%) as a dark green solid. ^1H NMR (600 MHz, CD_2Cl_2) δ 7.60 (d, $J = 7.2$ Hz, 1H), 7.49–7.43 (m, 2H), 7.35 (d, $J = 7.1$ Hz, 1H), 7.29 (d, $J = 7.9$ Hz, 1H), 7.25–7.21 (m, 1H), 7.04 (d, $J = 8.4$ Hz, 1H), 7.03 (t, $J = 8.0$ Hz, 2H), 6.98 (s, 2H), 6.96 (s, 2H), 6.29 (s, 1H), 6.05 (s, 1H), 2.43 (s, 6H), 2.39 (s, 6H), 2.34 (s, 6H); ^{13}C NMR (151 MHz, CD_2Cl_2) δ 166.19, 164.32, 147.73, 146.15, 145.61, 143.73, 142.17, 139.29, 139.22, 138.82, 137.44, 137.09, 137.00, 134.23, 133.08, 132.23, 131.18, 130.73, 130.60, 129.01, 128.45, 127.97, 127.87, 126.52, 126.09, 124.87, 123.78 (2), 123.05, 122.00, 113.15 (2), 21.29, 20.93, 20.36; HRMS (ASAP) (m/z), calculated for $\text{C}_{42}\text{H}_{32}\text{O}_3\text{S}$ (M) $^+$ 616.2072, found 617.2072.



Sulfone 12 (*syn/anti*-IBFBTS). Parent IBFBT **8** (25 mg, 0.043 mmol, 1 equiv.) and mCPBA (22 mg, 0.128 mmol, 3 equiv.) in DCM (10 mL) were reacted to afford the crude sulfone, which was purified by flash column chromatography (DCM/hexanes, 2:3) to give **12** (7 mg, 26%) as a teal solid. ^1H NMR (500 MHz, CD_2Cl_2) δ 7.51 (d, $J = 7.4$ Hz, 1H), 7.28, (t, $J = 7.7$ Hz, 1H), 7.23 (t, $J = 7.7$ Hz, 1H), 7.12 (d, $J = 7.6$ Hz, 2H), 7.05–6.98 (m, 2H), 6.97 (s, 2H), 6.94, (s, 2H), 6.36 (d, $J = 7.5$ Hz, 1H), 5.64 (s, 2H), 2.43 (s, 6H), 2.35 (s, 6H), 2.34, (s, 3H), 2.30 (s, 3H); ^{13}C NMR (151 MHz, CD_2Cl_2) δ 166.01, 162.23, 151.36, 149.30, 144.05, 143.03, 138.59, 138.19, 137.36, 137.10, 136.94, 136.65, 136.49, 133.29, 133.12, 129.71, 129.09, 128.59, 128.46, 128.27, 127.27, 126.88, 126.74, 125.81, 125.36, 124.05, 123.97, 123.92, 123.84, 120.49, 120.33, 112.46, 21.14, 21.07, 20.60, 20.42; HRMS (ASAP) (m/z), calculated for $\text{C}_{42}\text{H}_{32}\text{O}_3\text{S}$ (M) $^+$ 616.2072, found 617.2072.



Sulfone 13 (anti/syn-IBFBTS). Parent IBFBT **9** (15 mg, 0.026 mmol, 1 equiv.) and mCPBA (13 mg, 0.077 mmol, 3 equiv.) were reacted to afford the sulfone. No purification was required as the product was pure after work up, giving **13** (3.5 mg, 22%) as a dark teal solid. ^1H NMR (500 MHz, CD_2Cl_2) δ 7.61 (d, $J = 7.0$ Hz, 1H), 7.48 (t, $J = 7.2$ Hz, 1H), 7.45–7.40 (m, 2H), 7.13 (d, $J = 4.0$ Hz, 2H), 7.04–6.94 (m, 5H), 6.80 (d, $J = 7.6$ Hz, 1H), 6.63 (s, 1H), 6.37 (s, 1H), 2.37–2.32 (m, 18H); ^{13}C NMR (126 MHz, CD_2Cl_2) δ 176.23, 164.03, 148.72, 145.62, 143.74, 142.25, 141.66, 139.08, 138.79, 138.61, 137.23, 136.94, 136.83, 133.36, 133.18, 132.03, 130.27, 129.77, 129.59, 129.10, 128.95, 128.40, 127.97, 127.64, 125.98, 125.50, 123.79, 122.62, 122.13, 121.89, 115.99, 112.73, 21.34, 21.28, 20.77, 20.39; HRMS (ASAP) (m/z), calculated for $\text{C}_{42}\text{H}_{32}\text{O}_3\text{S}$ (M) $^+$ 616.2072, found 616.2074.



Sulfone 14 (anti/anti-IBFBTS). Parent IF **10** (16 mg, 0.024 mmol, 1 equiv.) and mCPBA (13 mg, 0.072 mmol, 3 equiv.) were reacted to afford the crude sulfone, which was purified via flash column chromatography (DCM/hexanes, 1:1 + 1% TEA) to give **14** (1.8 mg, 12%) as a teal solid. The molecule is rather unstable, as well as the very small amount of material, precluded obtaining its ^{13}C NMR spectrum. ^1H NMR (500 MHz, CD_2Cl_2) δ 7.56–7.53 (m, 1H), 7.28–7.25 (m, 2H), 7.04 (m, 2H), 6.96 (m, 5H), 6.67 (d, $J = 7.6$ Hz, 1H), 6.54–6.50 (m, 1H), 5.99 (d, $J = 1.5$ Hz, 2H), 2.42 (s, 6H), 2.33 (2 s, 6H), 2.27 (s, 6H); (ASAP) (m/z), calculated for $\text{C}_{42}\text{H}_{32}\text{O}_3\text{S}$ (M) $^+$ 616.2072, found 617.2076.

2. X-ray Crystallography Details

General. Diffraction intensities for **8**, **10**, and over-oxidized **12** were collected at 173 K on a Bruker Apex2 single crystal diffractometer using CuK α radiation, 1.54178 Å. Space groups were determined based on intensity statistics. Absorption corrections were applied by SADABS.³ Structures were solved by direct methods and Fourier techniques and refined on F^2 using full matrix least-squares procedures. All non-H atoms were refined with anisotropic thermal parameters. H atoms in all structures were refined in calculated positions in a rigid group model. Crystals of **8** were very thin plates and the diffraction data at high angles are very weak. The diffraction data for **8** were collected up to $2\theta_{\max} = 99.36^\circ$ and the ratio of the number of the measured reflections per the number of the refined parameters is close to 8 (3174/397). Solvent molecules CH₂Cl₂ in **8** are highly disordered around an inversion center and were treated by SQUEEZE.⁴ The structure of **8** is determined with low resolution but it provides the clear chemical results. The structure of **10** was determined in space group $P1$ and the crystals used for data collection were a racemic twin. The Flack parameter is 0.36(2). The terminal 5- and 6-membered rings in **10** are disordered. All calculations were performed by the Bruker SHELXL-2014/7 package.⁵

Crystallographic Data for 8: C₄₃H₃₄Cl₂OS, M = 669.66, 0.123 x 0.110 x 0.005 mm, T = 173(2) K, Triclinic, space group $P-1$, $a = 8.073(5)$ Å, $b = 8.667(5)$ Å, $c = 24.104(17)$ Å, $\alpha = 92.34(3)^\circ$, $\beta = 90.98(3)^\circ$, $\gamma = 97.42(3)^\circ$, $V = 1670.6(19)$ Å³, $Z = 2$, $D_c = 1.331$ Mg/m³, $\mu(\text{Cu}) = 2.591$ mm⁻¹, $F(000) = 700$, $2\theta_{\max} = 99.36^\circ$, 5706 reflections, 3174 independent reflections [$R_{\text{int}} = 0.0530$], $R1 = 0.1079$, $wR2 = 0.2983$ and $\text{GOF} = 1.088$ for 3174 reflections (397 parameters) with $I > 2\sigma(I)$, $R1 = 0.1321$, $wR2 = 0.3136$ and $\text{GOF} = 1.088$ for all reflections, max/min residual electron density +0.377/-0.477 eÅ⁻³. CCDC 2350802.

Crystallographic Data for 10: C₄₃H₃₃Cl₃OS, M = 704.10, 0.28 x 0.13 x 0.02 mm, T = 173(2) K, Triclinic, space group $P1$, $a = 8.0663(2)$ Å, $b = 8.7799(28)$ Å, $c = 13.2154(3)$ Å, $\alpha = 98.9320(10)^\circ$, $\beta = 105.9590(10)^\circ$, $\gamma = 96.8910(10)^\circ$, $V = 875.81(4)$ Å³, $Z = 1$, $D_c = 1.335$ Mg/m³, $\mu(\text{Cu}) = 3.183$ mm⁻¹, $F(000) = 366$, $2\theta_{\max} = 133.64^\circ$, 9141 reflections, 4678 independent reflections [$R_{\text{int}} = 0.0315$], $R1 = 0.0449$, $wR2 = 0.1218$ and $\text{GOF} = 1.030$ for 4678 reflections (561 parameters) with $I > 2\sigma(I)$, $R1 = 0.0452$, $wR2 = 0.1222$ and $\text{GOF} = 0.983$ for all reflections, the Flack = 0.36(2), max/min residual electron density +0.354/-0.264 eÅ⁻³. CCDC 2350801.

Crystallographic Data for 12': C₄₂H₃₂O₄S, M = 632.73, 0.12 x 0.09 x 0.05 mm, T = 173(2) K, Triclinic, space group *P*-1, *a* = 7.8275(4) Å, *b* = 10.1495(5) Å, *c* = 22.2592(12) Å, α = 78.253(3)°, β = 85.000(3)°, γ = 69.082(3)°, *V* = 1617.04(15) Å³, *Z* = 2, *D*_c = 1.300 Mg/m³, μ (Cu) = 1.235 mm⁻¹, *F*(000) = 664, $2\theta_{\max}$ = 140.24°, 27950 reflections, 5966 independent reflections [*R*_{int} = 0.0465], *R*₁ = 0.0575, *wR*₂ = 0.1527 and *GOF* = 1.061 for 5966 reflections (425 parameters) with *I* > 2σ(*I*), *R*₁ = 0.0649, *wR*₂ = 0.1583 and *GOF* = 1.061 for all reflections, max/min residual electron density +0.433/-0.376 eÅ⁻³. CCDC 2350800.

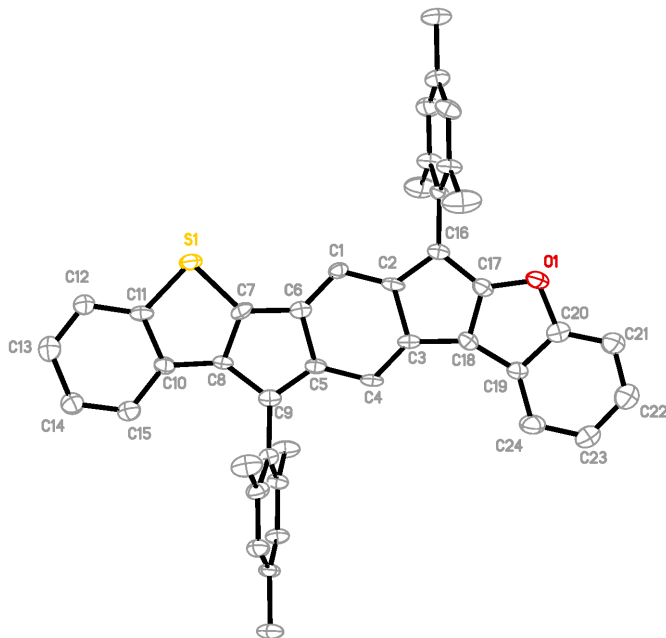


Figure S1. Molecular structure of indacene **8**; ellipsoids drawn at the 50% probability level.

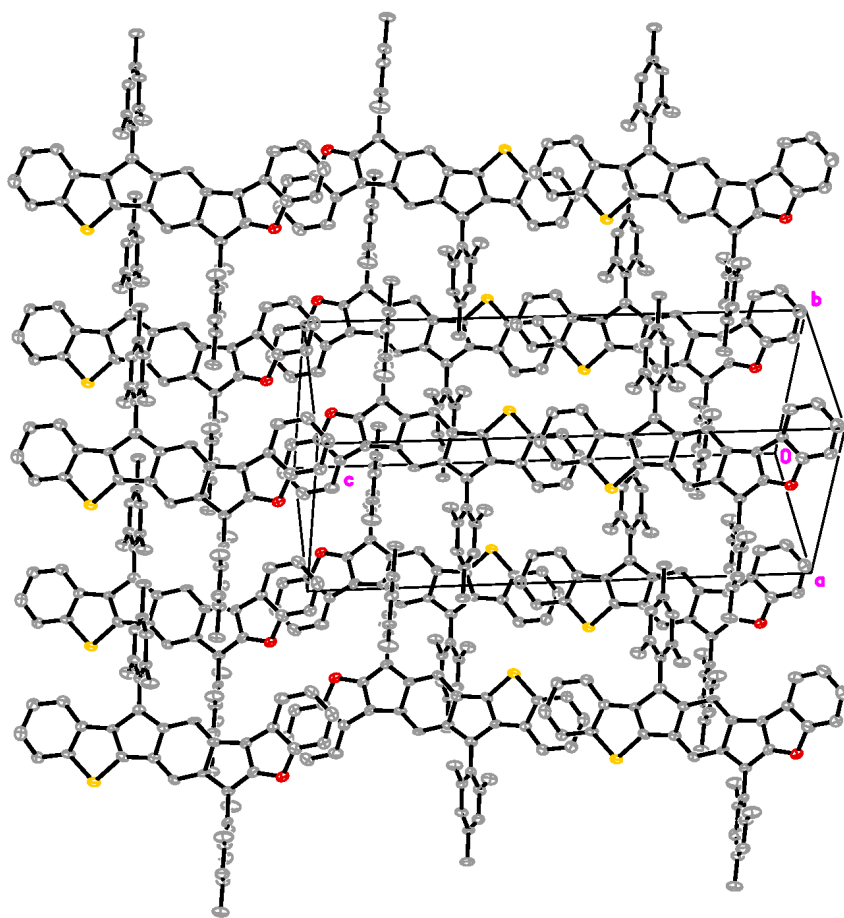


Figure S2. Molecular packing of indacene **8**.

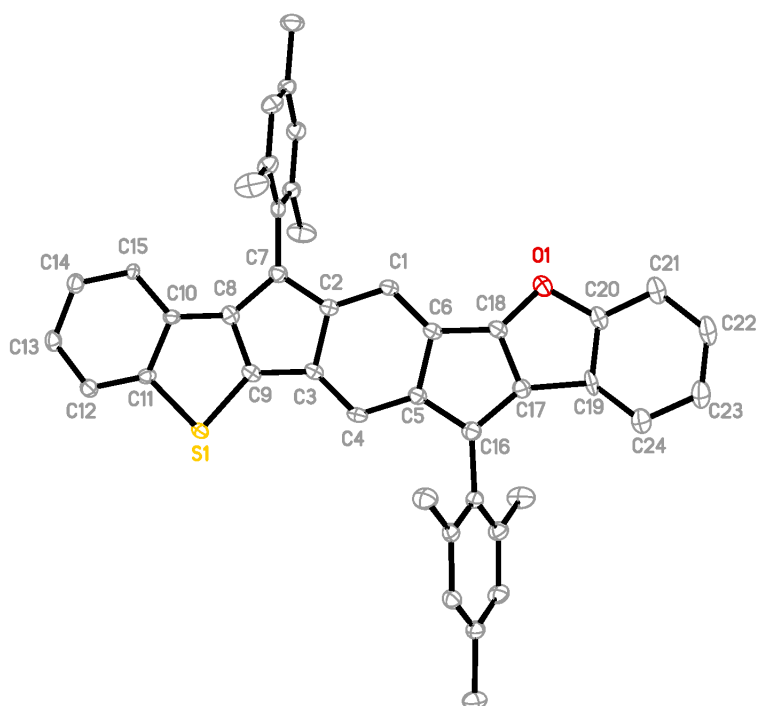


Figure S3. Molecular structure of indacene **10**; ellipsoids drawn at the 50% probability level.

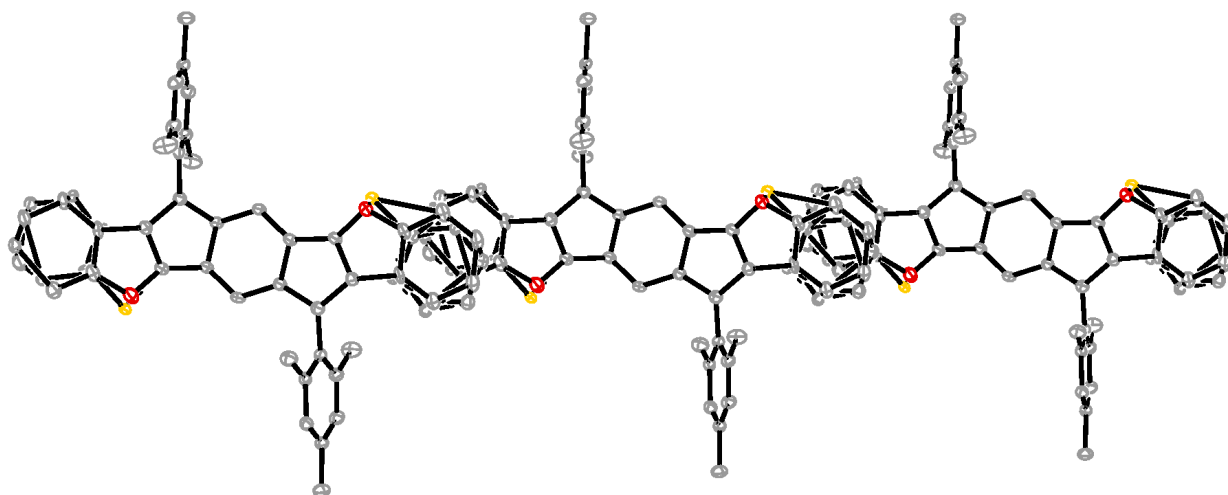


Figure S4. Molecular packing of indacene **10**. Model reflects the positional disorder of the O and S atoms.

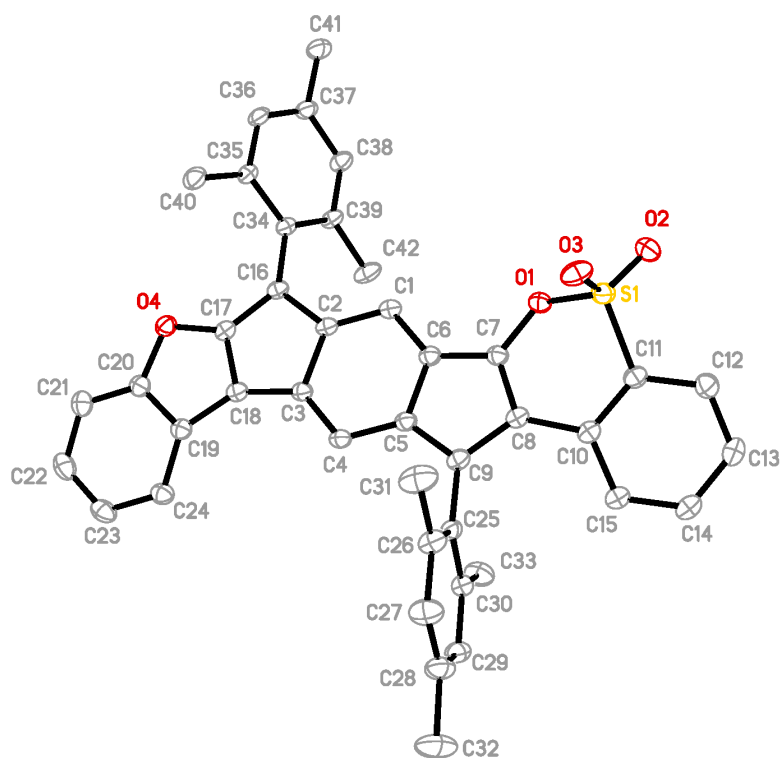


Figure S5. Molecular structure of an unexpected decomposition/side product in the over-oxidation of **12**; ellipsoids drawn at the 50% probability level.

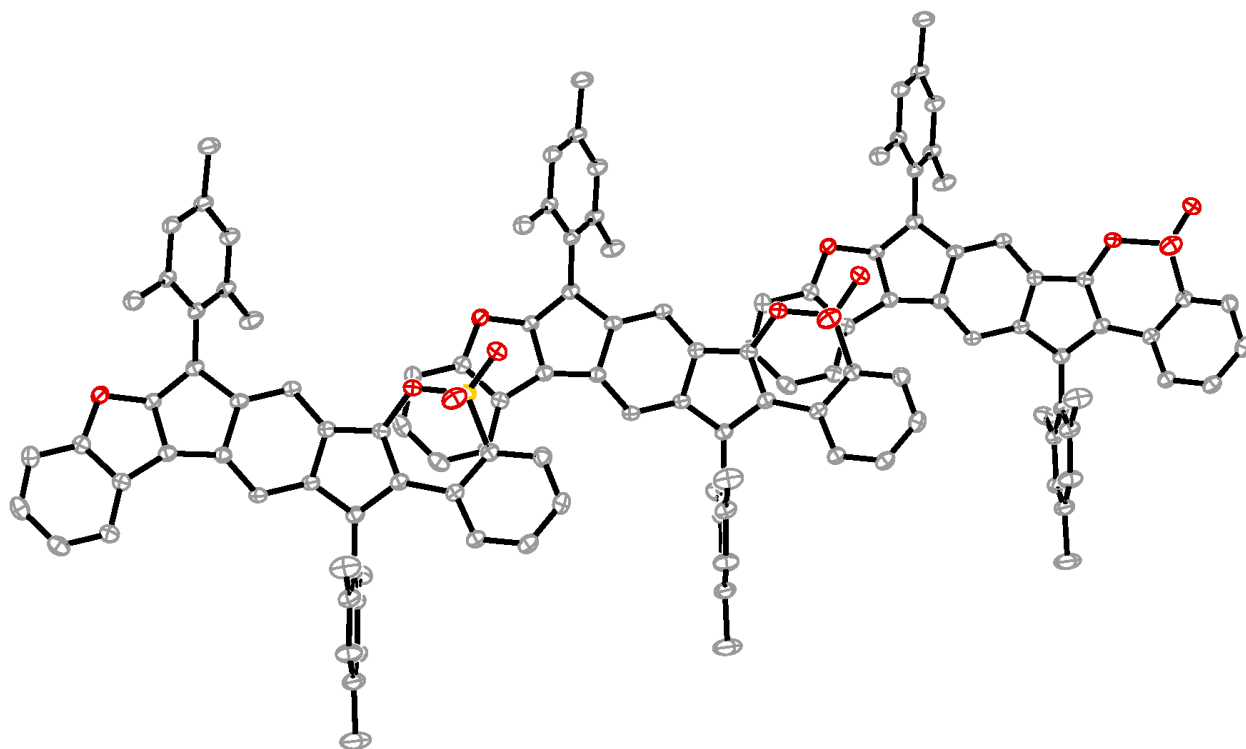
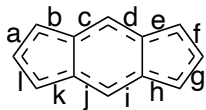


Figure S6. Molecular packing of an unexpected decomposition/side product.

3. Bond Length Comparisons

Table S1. Comparison of bond lengths in the XRD crystal structures of **8** and **10** vs. their



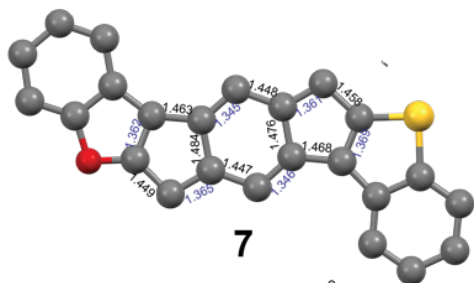
M11-optimized structures. Bond labels for *s*-indacene core are shown below.

bond	a	b	c	d	e	f	g	h	i	j	k	l
cmp d												
10 crystal	1.40	1.43	1.37	1.40	1.42	1.43	1.39	1.43	1.37	1.41	1.40	1.426
	0	4	8	1	1	1	4	1	5	3	8	
10 M11 opt	1.38	1.44	1.37	1.40	1.41	1.41	1.39	1.44	1.37	1.40	1.42	1.419
	5	1	4	7	5	9	3	7	6	5	0	
Difference	0.01	0.00	0.00	0.00	0.00	0.01	0.00	0.01	0.00	0.00	0.01	0.007
	5	7	4	6	6	2	1	6	1	8	2	
8 crystal	1.37	1.46	1.33	1.43	1.37	1.44	1.34	1.44	1.34	1.40	1.38	1.410
	4	1	1	1	7	9	4	3	6	3	4	
8 M11 opt	1.35	1.41	1.34	1.44	1.36	1.46	1.37	1.46	1.34	1.44	1.36	1.445
	4	6	7	5	2	1	0	2	7	4	8	
Difference	0.02	0.04	0.01	0.01	0.01	0.01	0.02	0.01	0.00	0.04	0.01	0.035
	0	5	6	4	5	2	6	9	1	1	6	

Table S2. Comparison of calculated bond lengths for M11-optimized structures **7-14** and *s*-indacene for reference.

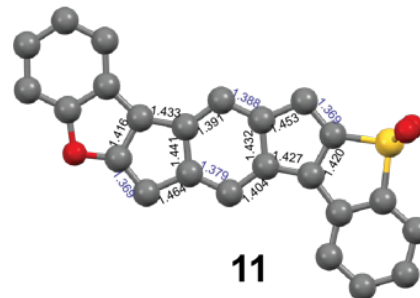
bo	a	b	c	d	e	f	g	h	i	j	k	l
nd												
cmp d.												
s-indacene	1.465	1.362	1.446	1.349	1.465	1.354	1.465	1.362	1.446	1.349	1.465	1.354
7	1.362	1.463	1.345	1.448	1.361	1.458	1.369	1.468	1.346	1.447	1.365	1.449
8	1.364	1.461	1.347	1.445	1.362	1.461	1.370	1.468	1.347	1.447	1.368	1.445
9	1.363	1.453	1.346	1.443	1.365	1.451	1.373	1.463	1.350	1.448	1.367	1.445
10	1.385	1.441	1.374	1.407	1.415	1.411	1.393	1.447	1.376	1.405	1.421	1.419

11	1.4 16	1.43 3	1.39 1	1.38 8	1.45 3	1.36 9	1.42 0	1.42 7	1.40 4	1.37 9	1.46 4	1.36 9
12	1.4 47	1.39 3	1.41 8	1.36 7	1.46 4	1.36 1	1.44 6	1.37 2	1.43 3	1.35 7	1.47 9	1.35 0
13	1.4 15	1.41 7	1.39 4	1.38 4	1.44 8	1.37 1	1.41 9	1.42 2	1.40 2	1.38 1	1.45 6	1.38 3
												1. 3
14	1.456	1.37 4	1.42 1	1.36 4	1.45 5	1.36 4	1.44 3	1.36 4	1.43 8	1.35 2	1.47 7	1.35 5



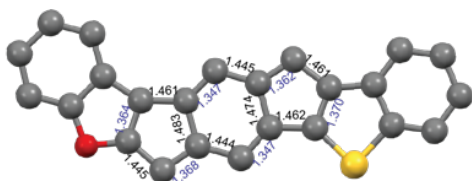
7

BLA = 0.099 Å
Dipole = 0.389 D



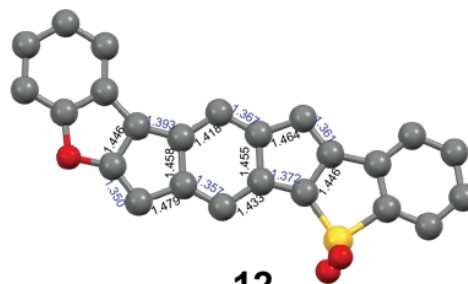
11

BLA = 0.045 Å
Dipole = 6.753 D



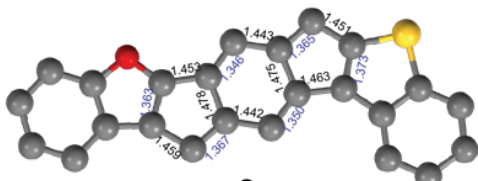
8

BLA = 0.095 Å
Dipole = 1.455 D



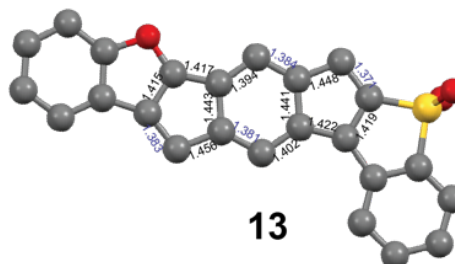
12

BLA = 0.080 Å
Dipole = 7.632 D



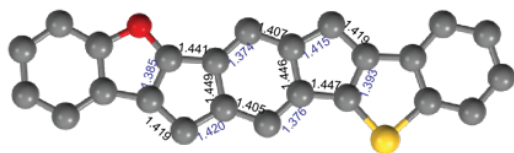
9

BLA = 0.091 Å
Dipole = 1.180 D



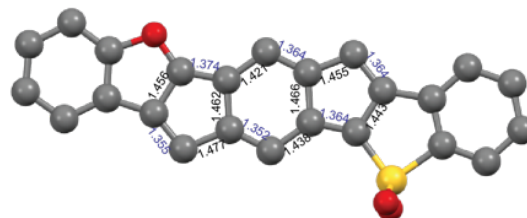
13

BLA = 0.038 Å
Dipole = 8.605 D



10

BLA = 0.033 Å
Dipole = 0.075 D



14

BLA = 0.085 Å
Dipole = 6.972 D

Figure S7. Calculated BLA and dipole moment values for **7-14**. Long bonds in black, short bonds in blue.

4. TD-DFT Calculations and Molecular Orbitals

Charge transfer and solvatochromic behavior are difficult to model accurately because of the more complicated molecular orbital due to charge localized resonance structures, resulting in less computationally straightforward solvation.⁶ A popular solution is to run the calculations in the gas phase,⁷⁻⁹ which we did, resulting in much more agreeable computational and experimental results.

Next, different density functionals were tested in order to evaluate which one would furnish the best match of orbital energies and predicted vertical excitation energies (TDDFT) with experimental values from UV-vis absorption spectra. Each structures geometry was optimized at functional M11/6-311+G** level of theory, then the vertical excitation energies were calculated using TDDFT at CAM-B3LYP/6-311G with variable dispersion and polarization corrections do determine the optimal basis set.¹⁰ The best match to experimental results came from TDDFT predicted vertical excitation energies at CAMB3LYP/6-311+G**. Varying the functional using the 6-311+G** basis set did not result in a significant improvement, so we went back to basis set optimization and tried def2-TZVP.¹¹ We found that at the TPSSh¹² level of theory we were able to model low energy excitations within 20% of the experimental values for the low energy absorption.

The major difference between the experimental and predicted absorption data is an additional weak transition predicted to be in the near IR for each sulfone. We searched extensively for this absorbance via long range UV-vis in DCM and DMF for **12** and **14** (the two largest oscillator strengths; see Figures S16-S17 in SI Section 5) and have concluded that we are unlikely to see it because the transition is too weak.

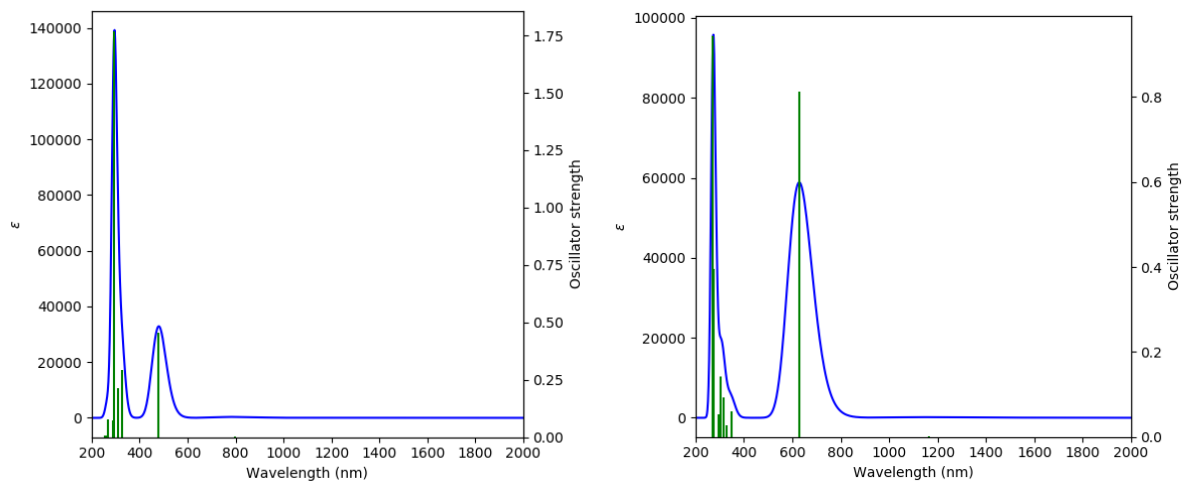


Figure S8. Gas phase TD-DFT predicted UV-Vis spectra for (left) *syn/syn*-IBFBT (**7**) and for (right) *syn/syn*-IBFBTS (**11**) calculated at the TPSSh/def2-TZVP level of theory.

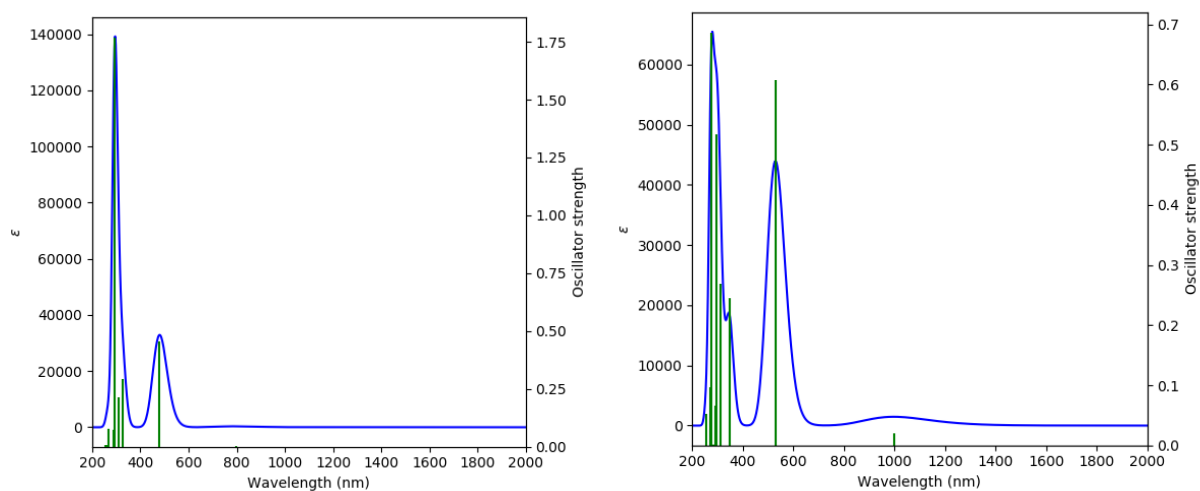


Figure S9. Gas phase TD-DFT predicted UV-Vis spectra for (left) *syn/anti*-IBFBT (**8**) and for (right) *syn/anti*-IBFBTS (**12**) calculated at the TPSSh/def2-TZVP level of theory.

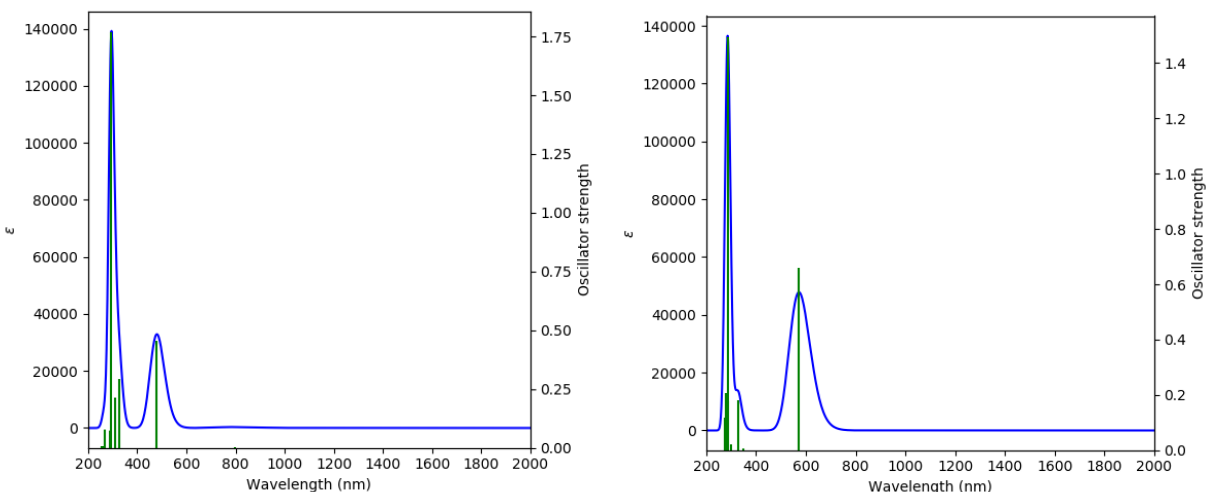


Figure S10. Gas phase TD-DFT predicted UV-Vis spectra for (left) *anti/syn*-IBFBT (**9**) and for (right) *anti/syn*-IBFBTS (**13**) calculated at the TPSSh/def2-TZVP level of theory.

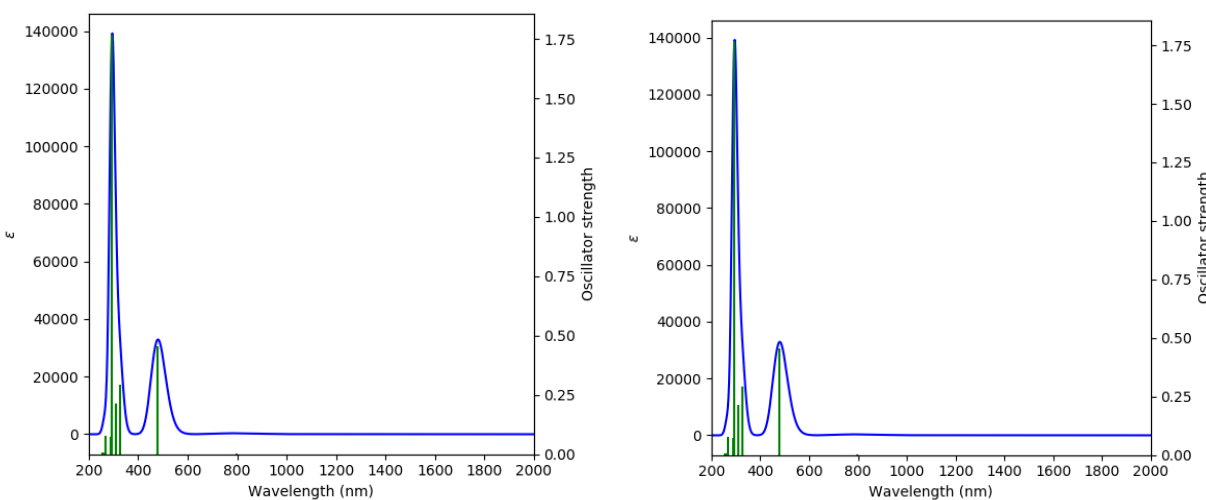


Figure S11. Gas phase TD-DFT predicted UV-Vis spectra for (left) *anti/anti*-IBFBT (**10**) and for (right) *anti/anti*-IBFBTS (**14**) calculated at the TPSSh/def2-TZVP level of theory.

Table S3. Calculated optical data and HOMO-LUMO energy gaps for compounds **7-14** at the TPSSh/def2-TZVP level of theory.

Cmp	Excite d state	λ_{\max}	Contributions	ν (D)	μ (D)	HO	LUM	E _{ga}
						f	O	p
						(eV)	(eV)	(eV)

7	2	572	H-1→L (67%), H→L+2 (10%), H-2→L (17%)	0.0 44 0.5	7.096	0.414	- 4.98 6	- 3.38 6	1.6
	1	944	H→L (70%)	54	0.902	0.004			
8	2	571	H-1→L (68%), H→L+1 (12%), H-2→L (10%), L→H (-10%)	0.0 51 0.5	6.984	0.402	- 5.00 8	- 3.33 4	1.6 7
	1	919	H→L (70%)	46	1.065	0.006			
9	2	545	H-1→L (66%), H-2→L (19%), H→L+2 (-13%)	0.0 25 0.4	6.070	0.317	- 4.98 8	- 3.33 2	1.6 5
	1	928	H→L (70%)	98	0.453	0.001			
10	2	584	H-1→L (64%), H→L+2 (20%), H→L(19%), H-3→L (10%), L→H (-13%)	0.0 25 0.4	6.275	0.316 6	- 4.99	- 3.36 2	1.6 2
	1	983	H→L (70%), H-1→L (-20%)	79	0.395	0.000 7			
11	2	628	H→L (68%), H-1→L (-16%), H-1→L+1 (10%)	0.0 25 0.6	9.535	0.812	- 7.68 1	- - 2.84	4.8 4
	1	1163	H-1→L (67%), H→L (16%)	81	0.748	0.002			
12	2	529	H-1→L (63%), H→L (-26%), H→L+1 (-10%)	0.0 57 0.5	7.117	0.607	- 5.30 2	- 3.93 1	1.3 7
	1	997	H→L (63%), H-1→L (27%)	62	1.494	0.020 3			
13	2	572	H→L (68%), H-1→L (-12%), H-1→L+1 (-14%)	0 0.5	7.754	0.66	- 5.44 6	- 3.85 3	1.5 9
	1	955	H-1→L (68%), H→L (13%)	87	0.137	0.000 1			
14	2	479	H-1→L (66%), H→L (14%), H→L+1 (-16%)	0 0.4	5.382	0.454	- 5.37 1	- - 3.72	1.6 5
	1	795	H→L (67%), H-1→L (-14%), H-6→L (11%)	56	0.288	0.005			

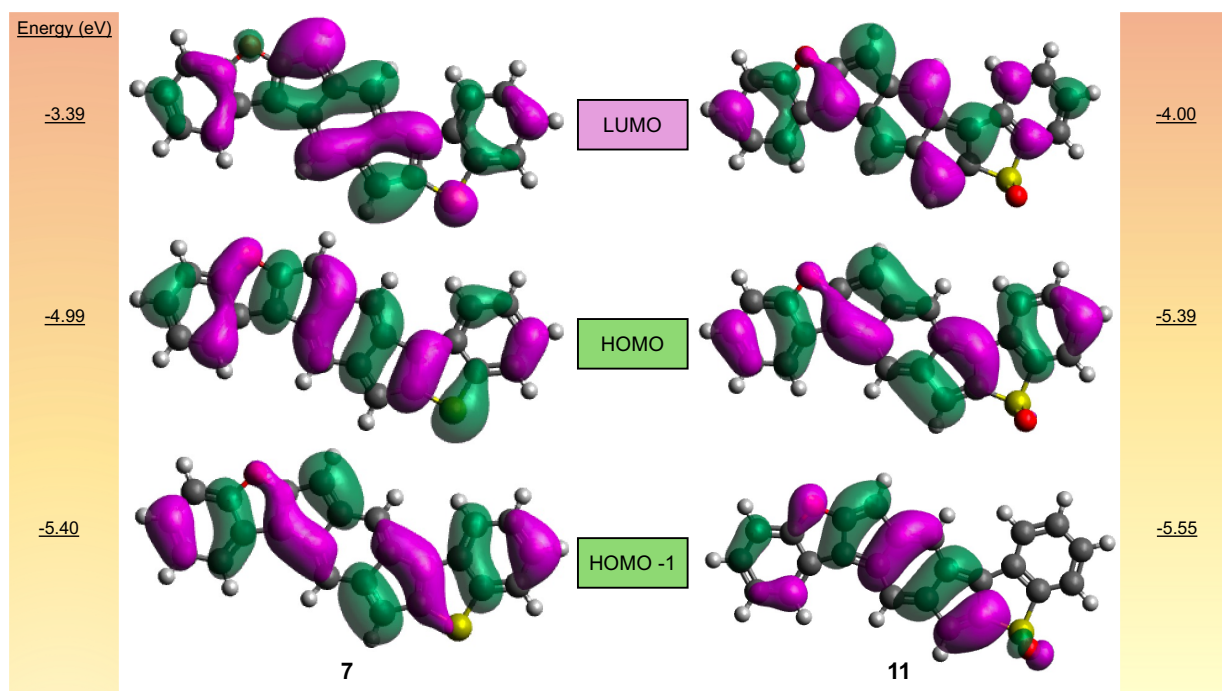


Figure S12. Comparison of pre and post oxidation molecular orbitals of the HOMO-1, HOMO, and LUMO at the TPSSh/def2-TZVP level for (left) *syn/syn*-IBFBT (**7**) and for (right) *syn/syn*-IBFBTS (**11**). Pink and green isosurfaces with contour values of ± 0.015 a.u.

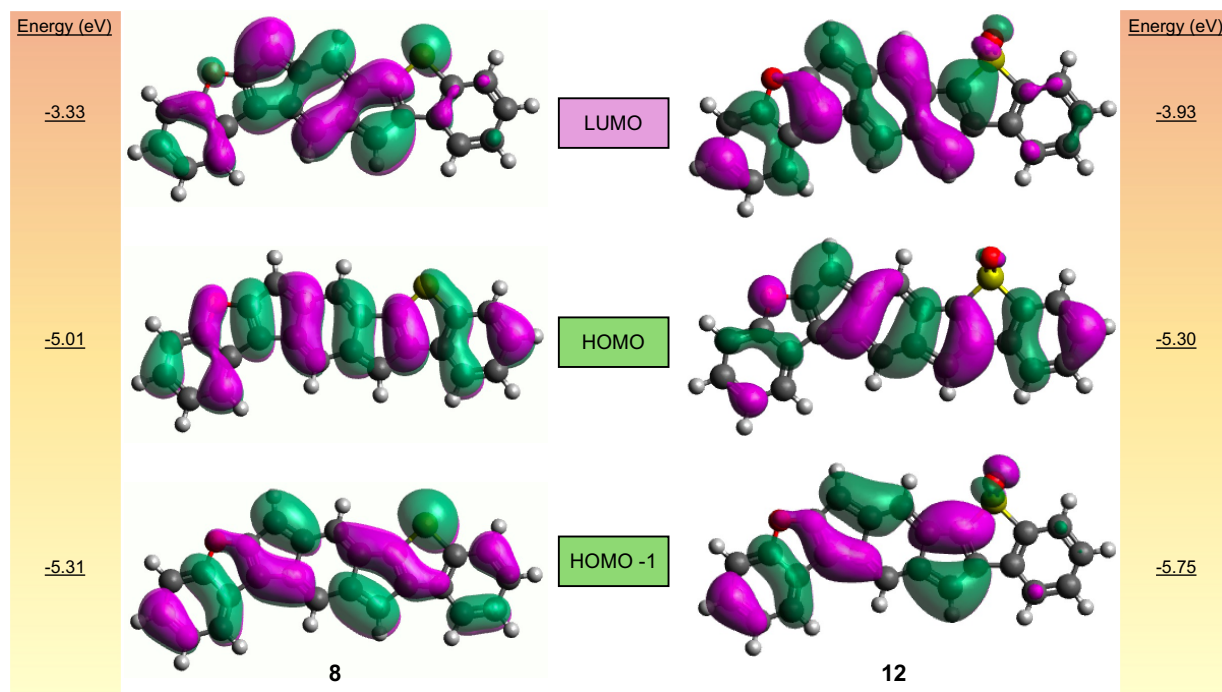


Figure S13. Comparison of pre and post oxidation molecular orbitals of the HOMO-1, HOMO, and LUMO at the TPSSh/def2-TZVP level for (left) *syn/anti*-IBFBT (**8**) and for (right) *syn/anti*-IBFBTS (**12**). Pink and green isosurfaces with contour values of ± 0.015 a.u.

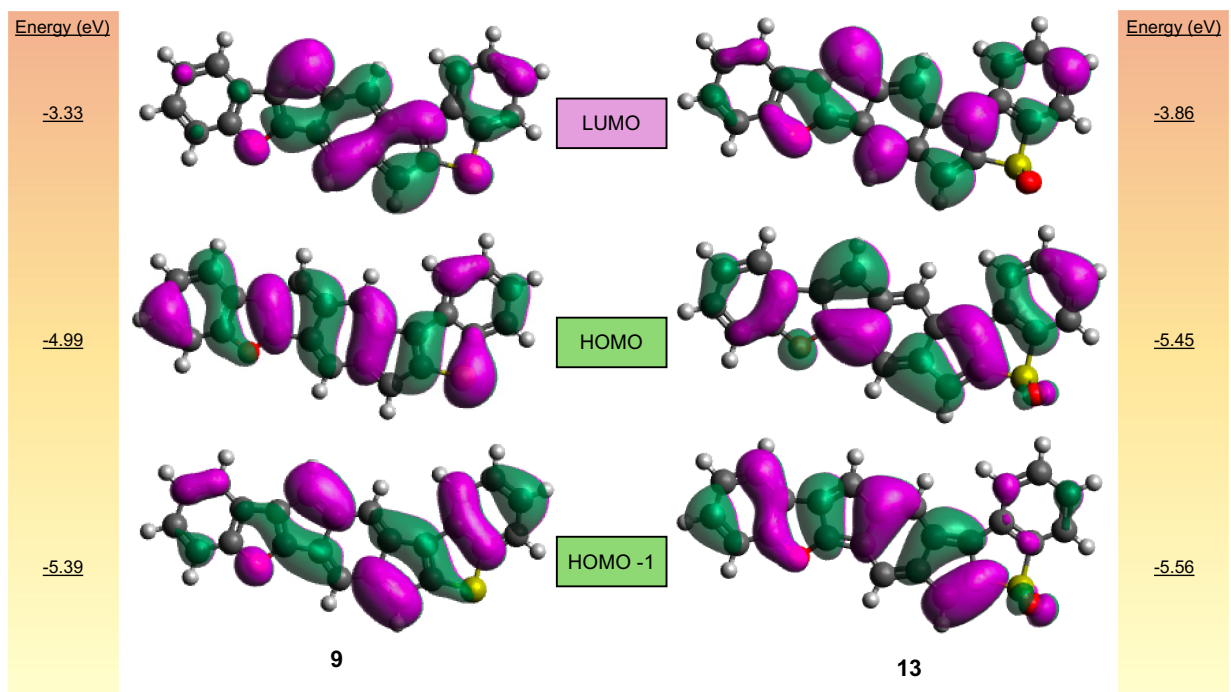


Figure S14. Comparison of pre and post oxidation molecular orbitals of the HOMO-1, HOMO, and LUMO at the TPSSh/def2-TZVP level for (left) *anti/syn*-IBFBT (**9**) and for (right) *anti/syn*-IBFBTS (**13**). Pink and green isosurfaces with contour values of ± 0.015 a.u.

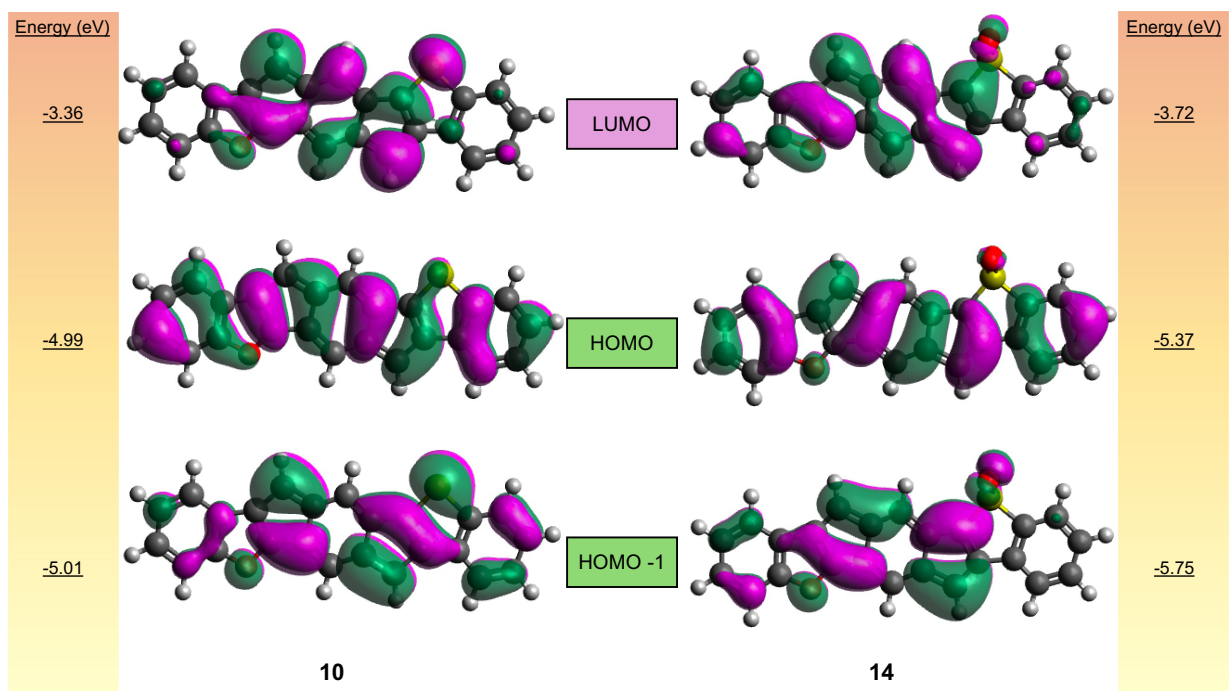


Figure S15. Comparison of pre and post oxidation molecular orbitals of the HOMO-1, HOMO, and LUMO at the TPSSh/def2-TZVP level for (left) *anti/anti*-IBFBT (**10**) and for (right) *anti/anti*-IBFBTS (**14**). Pink and green isosurfaces with contour values of ± 0.015 a.u.

The unexpected TD-DFT results which predicted primarily HOMO \rightarrow LUMO contributions for the low energy excitation for **11** and **13** and HOMO and HOMO-1 inversion for **7** \rightarrow **11** (Figure S12) and **9** \rightarrow **13** (Figure S14) prompted us to examine orbital contributions for the symmetric analogues **1-4**, which we did not do in the initial publications.^{14,15} Indeed, the predicted orbital contributions for the low energy transition for the symmetric *syn*-sulfone (**3**) is also primarily HOMO \rightarrow LUMO. The HOMO/HOMO-1 inversion can be seen in Figure S16. In agreement with the molecules in this study (**12** and **14**), the symmetric *anti*-sulfone (**4**) is primarily HOMO-1 \rightarrow LUMO, and does not show the HOMO/HOMO-1 inversion associated with weakly antiaromatic molecules.

Table S4. Calculated optical data and HOMO-LUMO energy gaps for compounds **1-4** at the TPSSh/def2-TZVP level of theory.

Cmpd	Excited state	λ_m (ax)	Contributions	f	HOM	LUM	Egap (eV)
					O (eV)	O (eV)	
1	1	932	H \rightarrow L(70%)	0.00			
				0	-5.01	-3.83	1.18

				0.39			
	2	568	H-2→L(23%), H-1→L(66%),	6			
<hr/>							
2	1	873	H→L(70%)	0.00			
				9			
					-5.04	-3.29	1.75
	2	567	H-4→L(12%), H-1→L(67%), H→L+1(-16%), L→H-1 (-10%)	0.32			
				5			
<hr/>							
3	1	807	H-1→L(70%)	0.00			
				0			
					-6.03	-4.25	1.78
	2	564	H-1→L+1(15%), H→L(69%), L→H(- 14%)	0.69			
				1			
<hr/>							
4	1	943	H→L(70%)	0.00			
				0			
					-5.82	-4.20	1.62
	2	498	H-2→L(-40%), H-1→L(57%)	0.09			
				4			

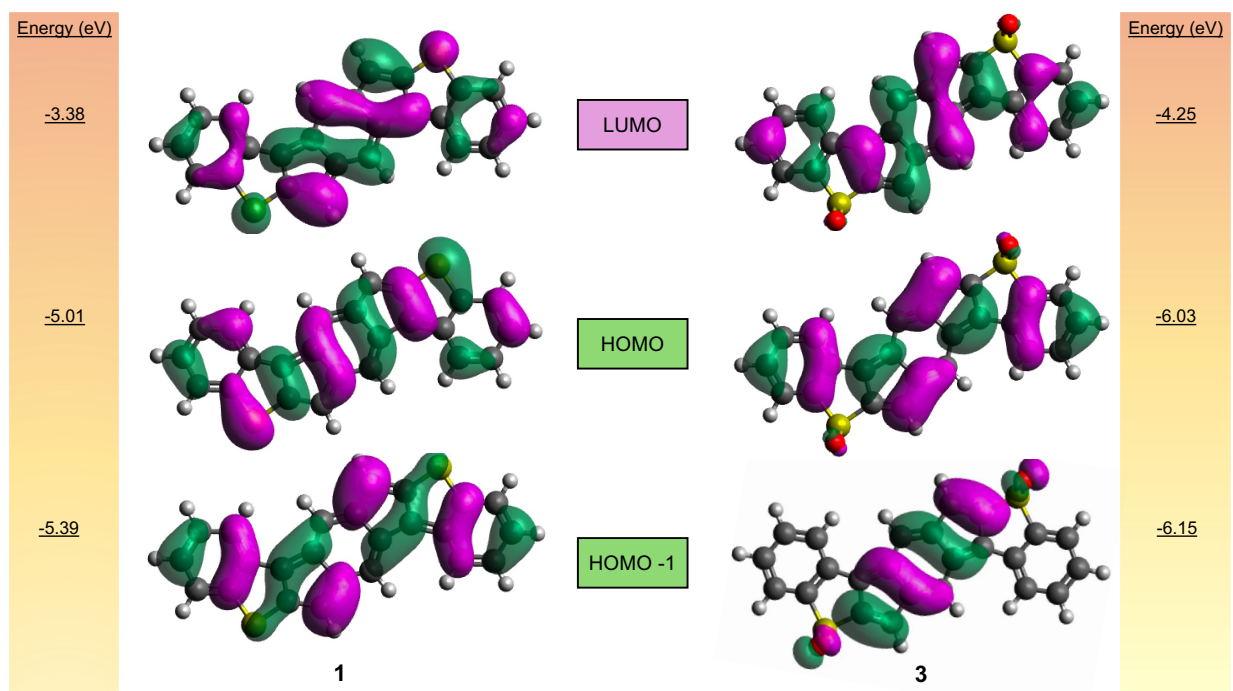


Figure S16. Comparison of pre and post oxidation molecular orbitals of the HOMO-1, HOMO, and LUMO at the TPSSh/def2-TZVP level for (left) *syn*-IDBT (**1**) and for (right) *syn*-IDBTS (**3**). Pink and green isosurfaces with contour values of ± 0.015 a.u.

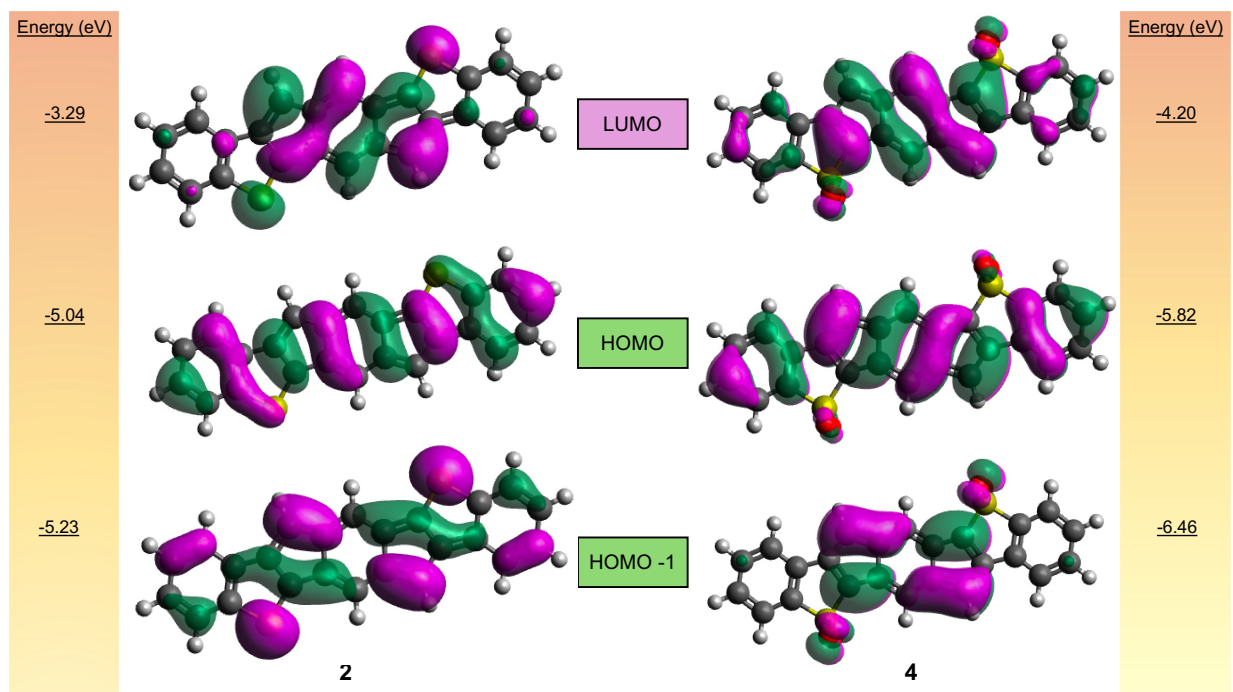


Figure S17. Comparison of pre and post oxidation molecular orbitals of the HOMO-1, HOMO, and LUMO at the TPSSh/def2-TZVP level for (left) *anti*-IDBT (**2**) and for (right) *anti*-IDBTS (**4**). Pink and green isosurfaces with contour values of ± 0.015 a.u.

5. Long-range UV-vis Experiments

Long-range UV-vis spectra were recorded on a Perkin Elmer Lambda-1050 UV/Vis/NIR spectrophotometer in reagent grade DCM and DMF. All spectra show only minimal changes in the data.

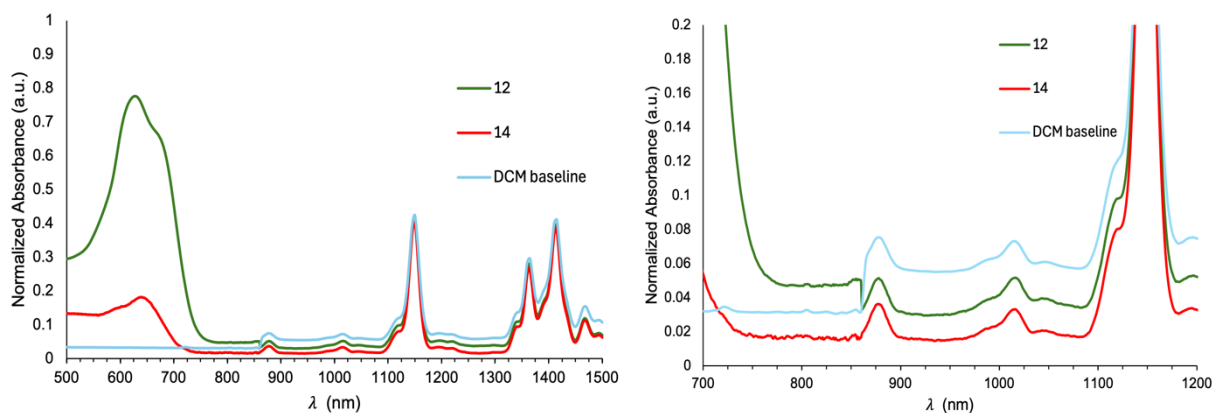


Figure S18. Long range UV-Vis spectra of **12** and **14** in DCM; (left) full scan and (right) zoomed in with background .

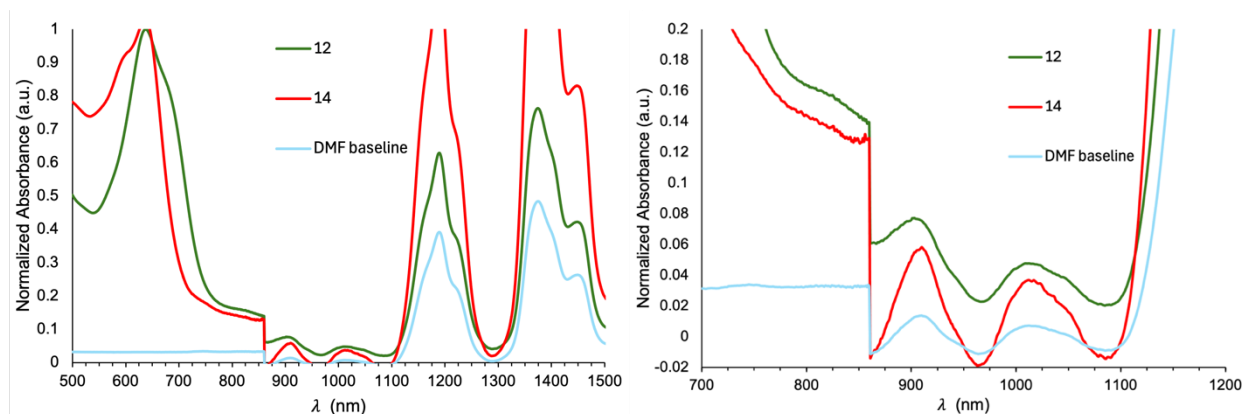


Figure S19. Long range UV-Vis spectra of **12** and **14** in DMF; (left) full scan and (right) zoomed in baseline view.

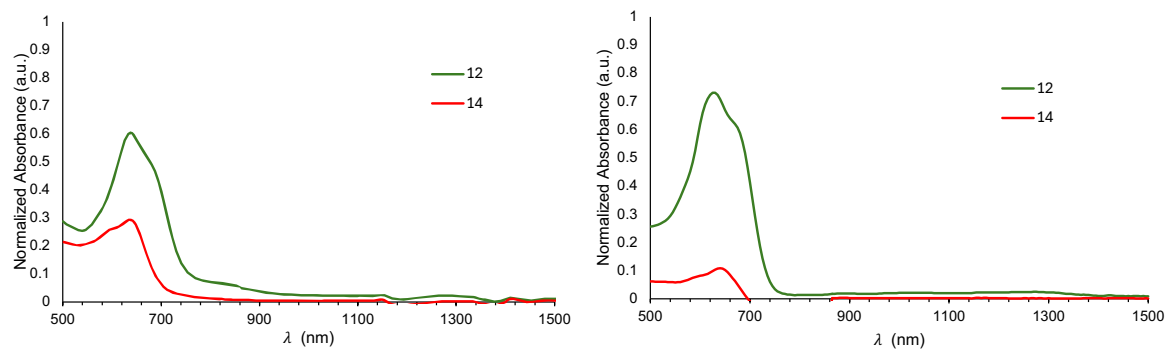


Figure S20. Long range UV-Vis spectra of **12** and **14** in DCM and DMF with baseline correction; (left) DMF (right) DCM.

6. Calculations of Proposed Aromatic D/A Analogues

We ran additional computations on aromatic naphthalene core analogues for the *syn*- and *anti*-fused D/A *s*-indacene systems (Figure S20) for comparison. Geometries were optimized at M11/6-311+G** and B3LYP/6-311+G** and then TD-DFT was calculated at TPSSh/def2-TZVP and B3LYP/def2-TZVP in an effort to account for bias in using functionals/basis sets commonly used in aromatic molecules and antiaromatic molecules. Both sets of calculated excitation energies and HOMO-LUMO energy gaps display the same trends (Tables S5-S6). These calculations are not discussed in the body of the paper because the optimized functional/basis set for the antiaromatic compounds (**7-14**) had a range of ~6-18% difference from experimental values, and we have no way of determining the accuracy of these computations on the aromatic analogues (**A-D**) as these molecules are unknown in the literature. That said, both sets of data show an increase in the HOMO-LUMO energy gap from the unoxidized (**A, B**) to the oxidized analogues (**C, D**), indicating the aromatic bridge would not facilitate charge transfer between the same donor and acceptor. It is worth noting that **C** probably is not capable of ICT for the same reason **11** is not. The zwitterionic charge transfer resonance structure would have to sacrifice the aromaticity of the outer benzene ring on the thiophene side, making it energetically unfavorable. However, both sets of calculations show a slight red shift for one of the high energy excitations for **D** (the *anti*-fused analogue).

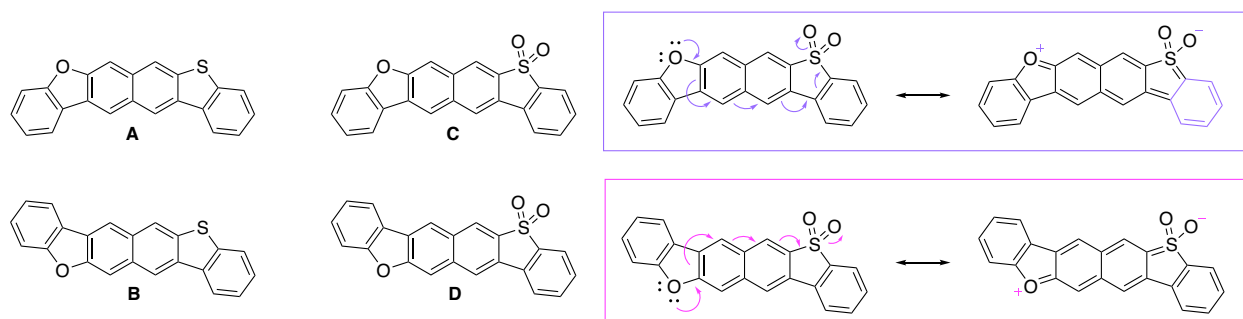


Figure S21. Aromatic analogues (*syn*-fusion **A**, *anti*-fusion **B**) of IBFBTs (**7-10**), aromatic analogues (*syn*-fusion **C**, *anti*-fusion **D**) of IBFBTSs (**11-14**), and theoretical charge resonance structures of **C** (purple) and **D** (pink).

Table S5. Calculated optical data and HOMO-LUMO energy gaps for compounds **A-D** at the TPSSh/def2-TZVP level of theory.

Cmpd	Excited state	λ_{max}	Contributions	f	HOMO (eV)	LUMO (eV)	E _{gap} (eV)
A	1	405	H→L(69%)	0.029	-	-	3.10
	4	308	H-2→L(42%), H-1→L(-30%), H-1→L+1(13%), H→L+1(37%), H→L+2(19%)	0.914	5.224	2.119	5
C	1	373	H-1→L(16%), H-2→L+1(10%), H→L(64%), H-1→L+1(-18%)	0.009	-	-	3.38
	6	295	H-2→L(30%), H-1→L(-22%), H- 1→L+1 (-15%), H→L+1(- 16%),H→L+2 (53%)	0.457	5.877	2.494	3
B	1	418	H-1→L(11%), H→L(69%)	0.317	-	-	3.02
	5	291	H-4→L(19%), H-3→L(24%), H- 2→L(-12%), H-1→L(20%), H→L+2(47%), H→L+3(-33%)	0.660	5.215	2.188	7
D	1	372	H-2→L(19%), H-1→L(-12%), H→L(62%)	0.145	-	-	3.35
	3	315	H-2→L(-11%), H-1→L(45%), H- 1→L+1(20%), H→L+1 (-44%), H→L+3 (-13%)	0.746	5.872	2.521	1

Table S6. Calculated optical data and HOMO-LUMO energy gaps for compounds **A-D** at the B3LYP/def2-TZVP level of theory.

Cmpd	Excited state	λ_{max}	Contributions	f	HOMO (eV)	LUMO (eV)	E _{gap} (eV)
A	1	394	H→L(69%)	0.03			
	3	310	H-2→L(54%), H-1→L(-27%), H→L+1(-33%)	0.23			3.55
					5.547	1.990	7
	4	305	H-2→L(41%), H-1→L(-28%), H→L+2(-33%)	1.12			
C	1	366	H-1→L(20%), H-1→L+1(11%), H→L(63%), H→L+1(-20%)	0.010			
	3	302	H-1→L(43%), H-1→L+1(27%), H→L+1(45%)	1.479			3.84
					-6.23	2.381	9
	4	297	H-2→L(-11%), H-1→L(-20%), H-1→L+1(58%), H→L(- 10%)H→L+1(-20%),H→L+2 (15%)	0.266			
B	1	408	H-1→L(11%), H→L(69%)	0.061			
	2	345	H-1→L(64%), H→L(-13%), H→L+2(-25%)	0.457			3.47
					5.542	2.070	2
	5	282	H-4→L(21%), H-3→L(21%), H- 2→L(-16%), H-1→L(23%), H→L+2(54%), H→L+3(-13%)	1.113			
D	1	364	H-2→L(-17%), H-1→L+1(13%), H→L(67%)	0.233			
	2	348	H-1→L(48%), H→L(16%), H→L+1(-47%)	0.076			3.78
					6.208	2.421	7
	3	309	H-1→L(44%), H-1→L+1(21%), H→L+1(47%), H-4→L(11%), H-1→L(-12%), H- 1→L+1(62%), H→L(-14%), H→L+1(-18%)	0.693			
	4	286		0.645			

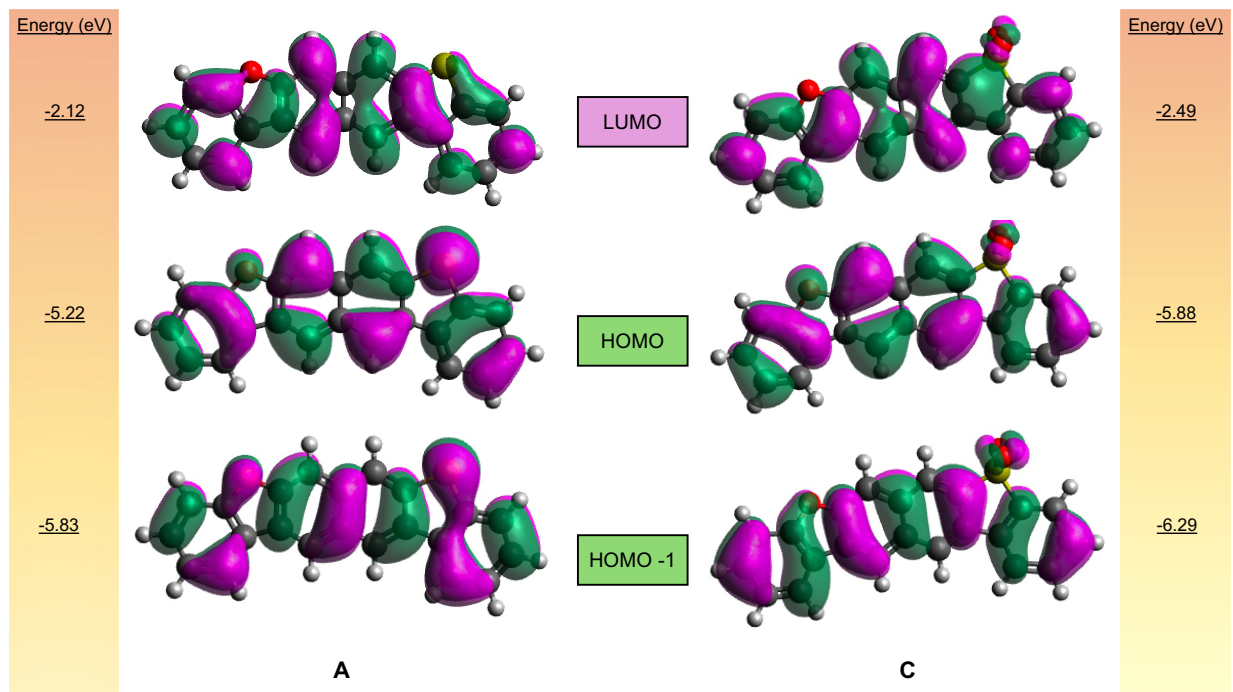


Figure S22. Comparison of pre- and post-oxidation molecular orbitals of the HOMO-1, HOMO, and LUMO at the TPSSh/def2-TZVP level for *syn*-fused aromatic analogues **A** (left) and **C** (right), respectively. Pink and green isosurfaces with contour values of ± 0.015 a.u.

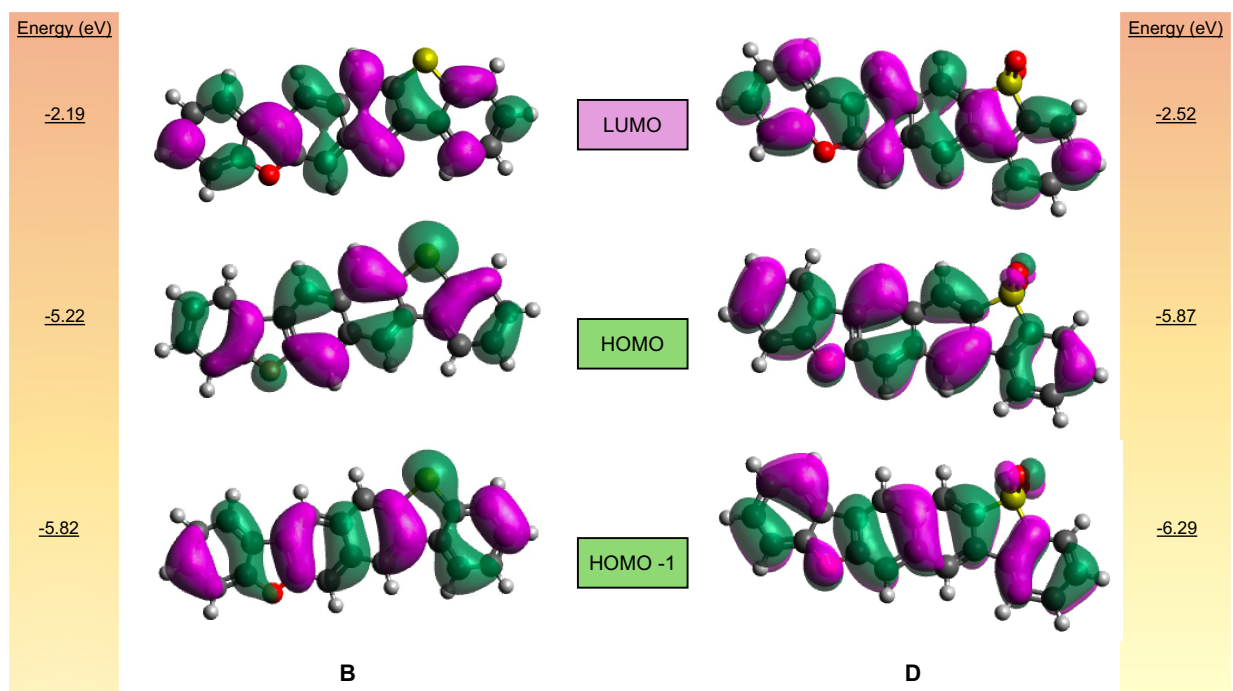


Figure S23. Comparison of pre- and post-oxidation molecular orbitals of the HOMO-1, HOMO, and LUMO at the TPSSh/def2-TZVP level for *anti*-fused aromatic analogues **B** (left) and **D** (right), respectively. Pink and green isosurfaces with contour values of ± 0.015 a.u.

7. Additional NICS-XY Plots

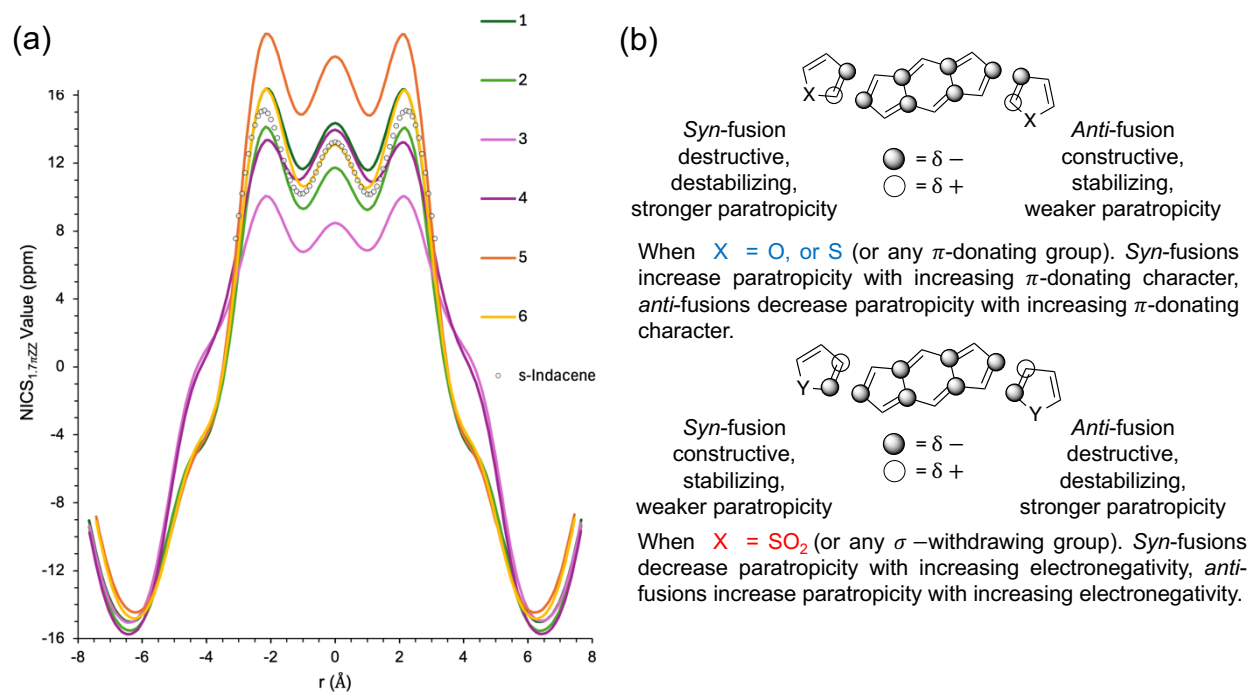


Figure S24. (a) NICS-XY scans at the B972/6-311+G** level of theory of *s*-indacene and the symmetrically-fused heterocycles **1-6**. Calculations were performed on structures optimized using the M11/6-311+G** level of theory without mesityl groups to reduce cost. (b) Trends in the NICS scans rationalized by Gimarc's topological charge stabilization principle.¹³

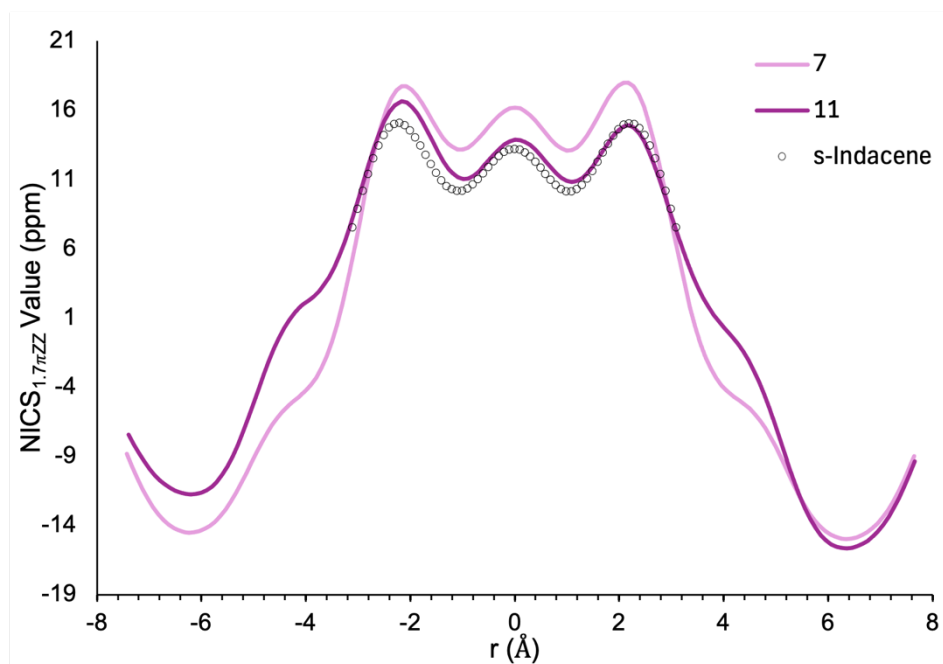


Figure S25. NICS-XY scans of *syn/syn*-IBFBT (**7**) and *syn/syn*-IBFBTS (**11**). Calculations were performed on structures optimized using the M11/6-311+G** level of theory without mesityl groups to reduce cost.

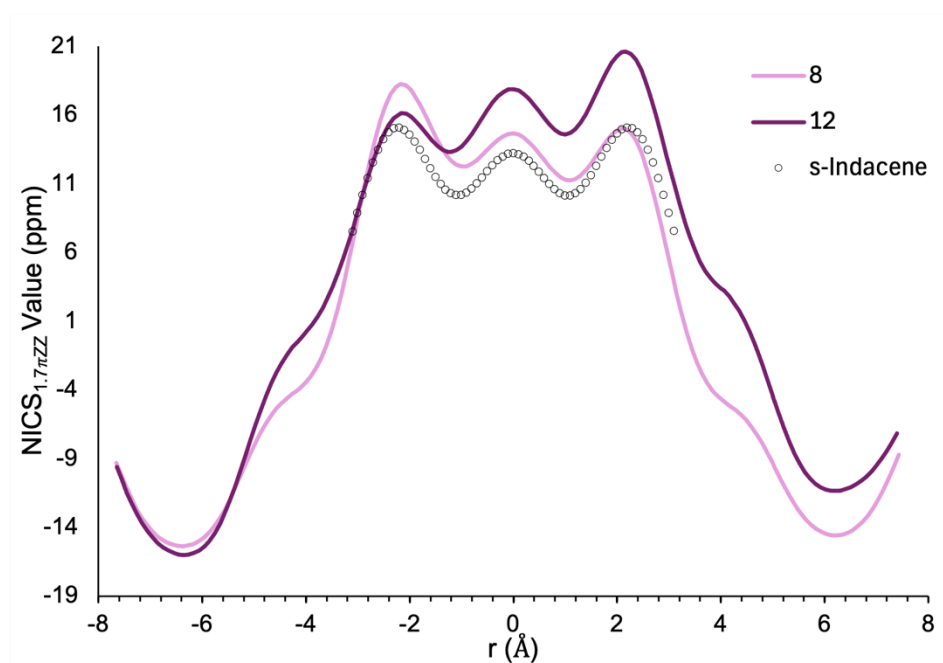


Figure S26. NICS-XY scans of *syn/anti*-IBFBT (**8**) and *syn/anti*-IBFBTS (**12**). Calculations were performed on structures optimized using the M11/6-311+G** level of theory without mesityl groups to reduce cost.

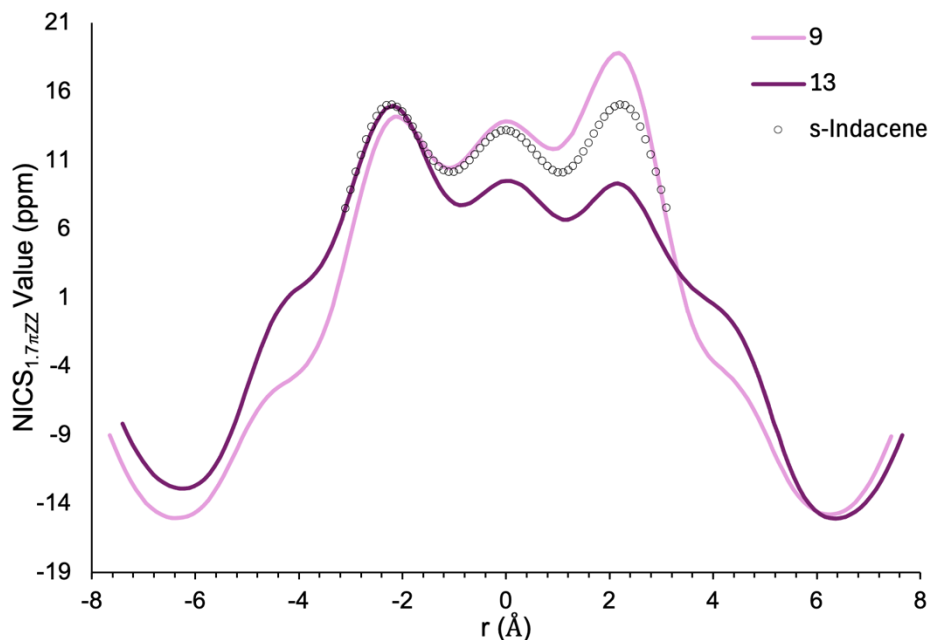


Figure S27. NICS-XY scans of *anti/syn*-IBFBT (**9**) and *anti/syn*-IBFBTS (**13**). Calculations were performed on structures optimized using the M11/6-311+G** level of theory without mesityl groups to reduce cost.

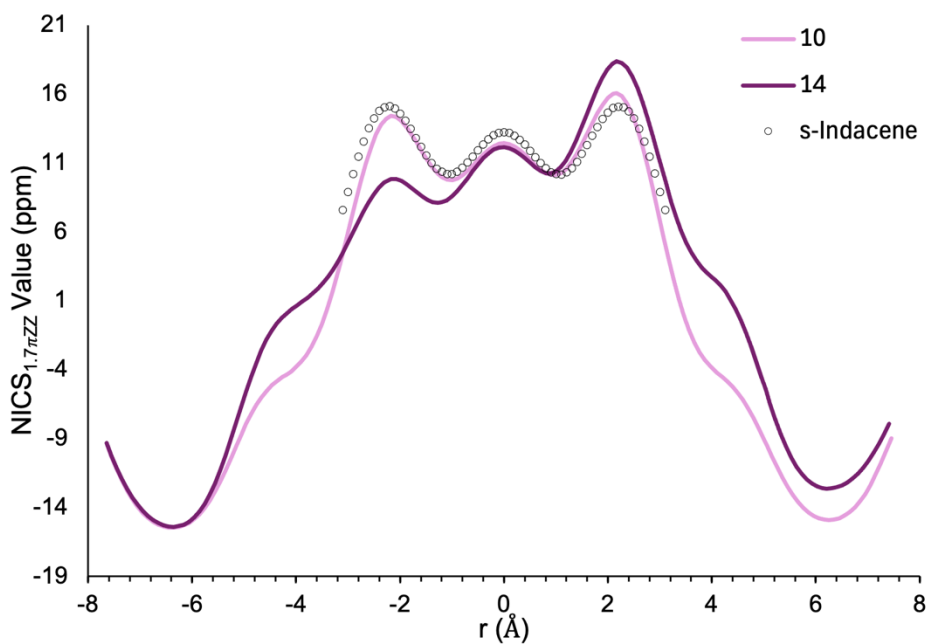


Figure S28. NICS-XY scans of *anti/anti*-IBFBT (**10**) and *anti/anti*-IBFBTS (**14**). Calculations were performed on structures optimized using the M11/6-311+G** level of theory without mesityl groups to reduce cost.

8. Electrochemistry

All electrochemical experiments were conducted with traditional 3-electrode geometry using a Biologic SP-50 potentiostat. Electrolyte solutions (0.1 M) were prepared from anhydrous, degassed HPLC grade CH₂Cl₂ and anhydrous Bu₄NPF₆. The working electrode was a glassy carbon electrode (3-mm diameter), with a Pt-coil counter electrode and a Ag wire pseudo reference. The ferrocene/ferrocenium (Fc/Fc⁺) couple was used as an internal standard following each experiment. Potential values were re-referenced to SCE using a value of 0.46 (V vs. SCE) for the Fc/Fc⁺ couple in CH₂Cl₂. LUMO and HOMO levels were approximated using SCE = -4.68 eV vs. vacuum. CV experiments were conducted in a three-neck flask that had been evacuated and backfilled with N₂ for three cycles using standard Schlenk-line technique. Voltammograms were recorded at sweep rates of 50 mV s⁻¹. E_{1/2} values were calculated assuming E_{1/2} ≈ E_{o'} = (E_{anodic} + E_{cathodic})/2 based on these observations for reversible couples; for irreversible couples, the E_{o'} value is estimated as the potential at peak current. Analyte concentrations were ca. 1-5 mM.

Table S7. Electrochemical for compounds **1-14**.

cmpd	E _{red2}	E _{red1}	E _{ox1}	E _{ox2} (V)	E _{HOMO}	E _{LUMO}	E _{gap}	E _{gap}
1 ^[d]	-1.37	-0.75	0.86	1.57	-5.54	-3.93	1.61	1.77
2 ^[d]	-1.72	-0.87	0.84	1.32	-5.52	-3.81	1.71	1.83
3 ^[e]	-0.96	-0.17	1.60	—	-6.28	-4.51	1.77	1.79
4 ^[f]	-1.08	-0.22	1.44	—	-6.12	-4.46	1.67	1.76
5 ^[g]	-1.40	-0.71	0.87	1.73	-5.55	-3.97	1.58	1.77
7	-1.29	-0.61	0.98	—	-5.67	-4.07	1.59	1.75
8	-1.36	-0.75	0.89	1.61	-5.57	-3.93	1.63	1.75
9	—	-0.88	0.73	—	-5.41	-3.80	1.61	1.82
10	-1.76	-0.83	0.86	1.32	-5.54	-3.84	1.69	2.04
11	-1.25	-0.24	1.16	—	-5.84	-4.44	1.40	1.63
12	-1.15	-0.32	1.11	—	-5.79	-4.36	1.43	1.59
13	—	-0.53	1.12	—	-5.80	-4.15	1.65	1.68
14	—	—	—	—	—	—	—	1.65

[a] CVs were recorded at a scan rate of 50 mV s⁻¹ with a glassy carbon working electrode, Pt coil counter electrode and Ag wire pseudo-reference. All data were collected in degassed CH₂Cl₂ and ferrocene was used as an internal reference. Potentials were referenced to SCE by using the Fc/Fc⁺ half-wave potential (Fc/Fc⁺ = 0.46 C vs. SCE). [b] Electrochemical E_{gap}. [c] Optical E_{gap} determined as the intersection of the x-axis and a tangent line passing through the inflection point of the lowest-energy absorption. [d] Reference [14]. [e] Reference [15], in CHCl₃; 4-*t*-butyl-2,6-dimethylphenyl R group. [f] Reference [15]. [g] Reference [16], in CHCl₃.

While **1** and **5** have almost identical redox properties, **7** has higher reduction and oxidation potentials. The reduction potential of **8** is comparable to **5** and higher than **2**. The E_{gap} of both **7** and **8** is considerably closer to **5** than **1** or **2**, respectively. IBFBTSs **11** and **12** have reduction potentials similar to **3** and **4**, with oxidation potentials roughly between the furan and sulfone counterpart of each molecule, resulting in one of the smallest E_{gap} measurements for any benzoheterocycle-fused *s*-indacene derivative to date. As already noted, **14** (and **6**) was too unstable for accurate electrochemical measurement.

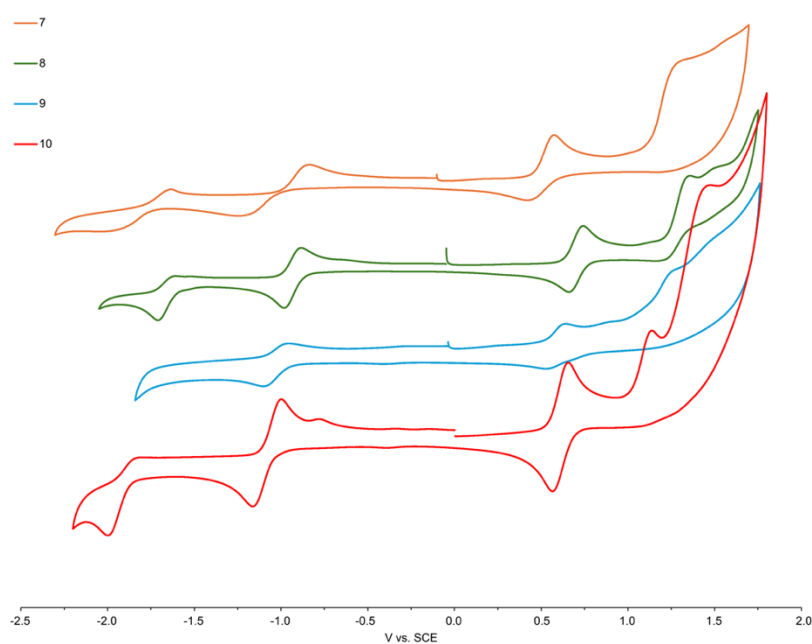


Figure S29. Cyclic voltammograms of IBFBTs **7-10**.

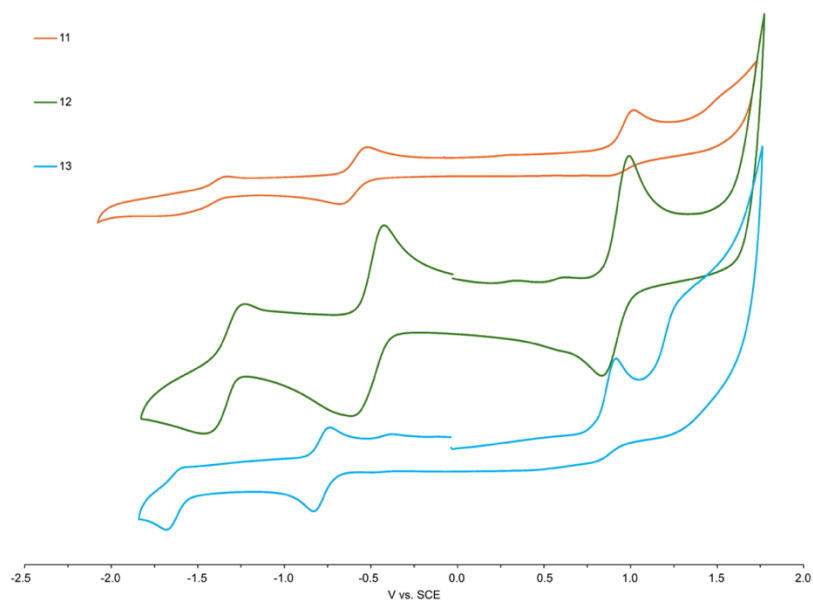


Figure S30. Cyclic voltammograms of IBFBTs **11-13**.

9. Additional Plots and Comparisons

Plotted comparisons of antiaromaticity and intramolecular charge transfer can be seen below in Figure S30. This data is best analyzed by comparing two isomers at a time. Isomers with a common heterocycle fusion (ie, *syn-syn* IBFBTS (**11**) vs *syn-anti* IBFBTS (**12**)) can be compared because of the common *syn*-fused benzofuran moiety, however *anti-syn* IBFBTS (**13**) and (**12**) cannot be compared because there is no common heterocycle fusion.

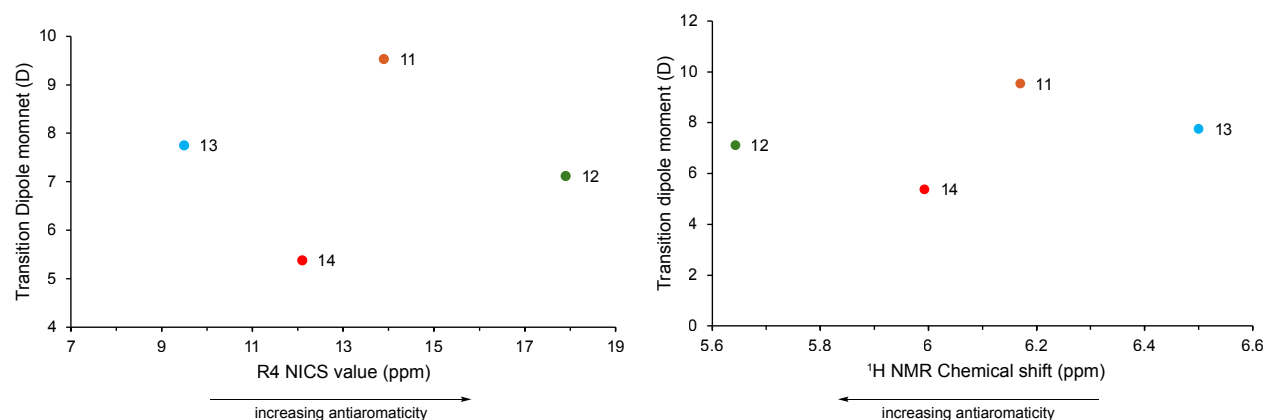


Figure S31. Left: Transition dipole moment (μ) plotted vs. NICS value of R4 of each of the sulfone isomers (**11-14**). Right: Transition dipole moment (μ) plotted vs. ¹H NMR chemical shift of the core protons on each of the sulfone isomers (**11-14**).

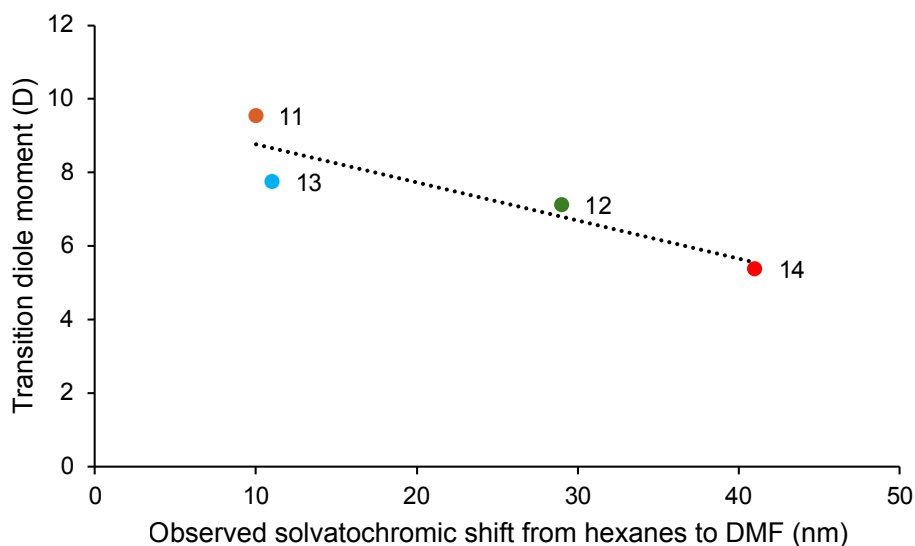


Figure S32. Comparison of calculated ICT strength (transition dipole moment) and experimentally observed ICT strength (observed solvatochromic shift from hexanes to DMF in nm) each of the sulfone isomers (**11-14**).

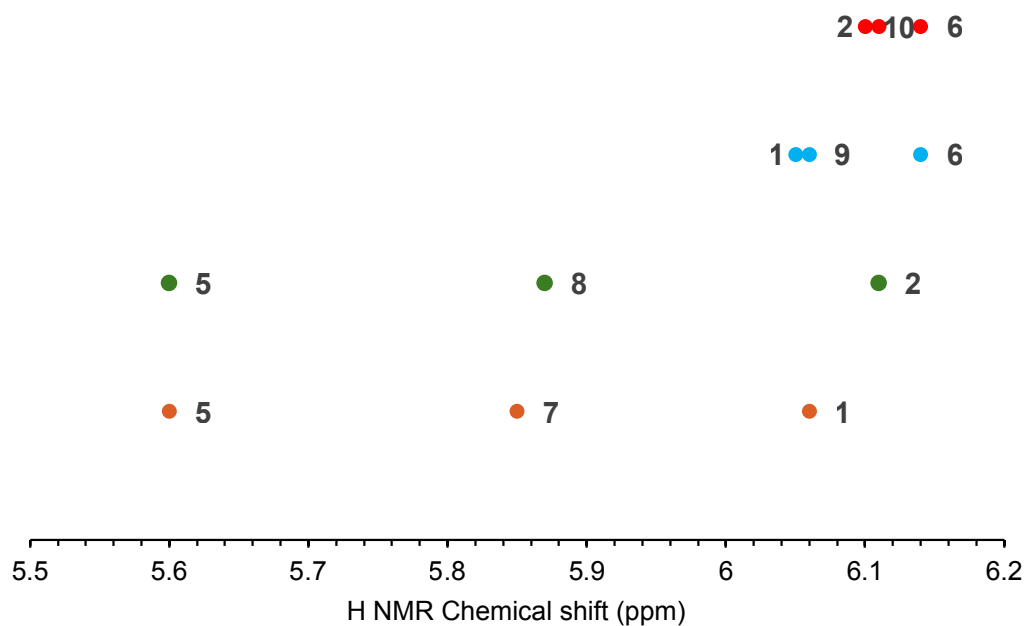


Figure S33. ^1H NMR chemical shift of each of the parent isomers (**7-10**) and their respective symmetric components (**1-6**).

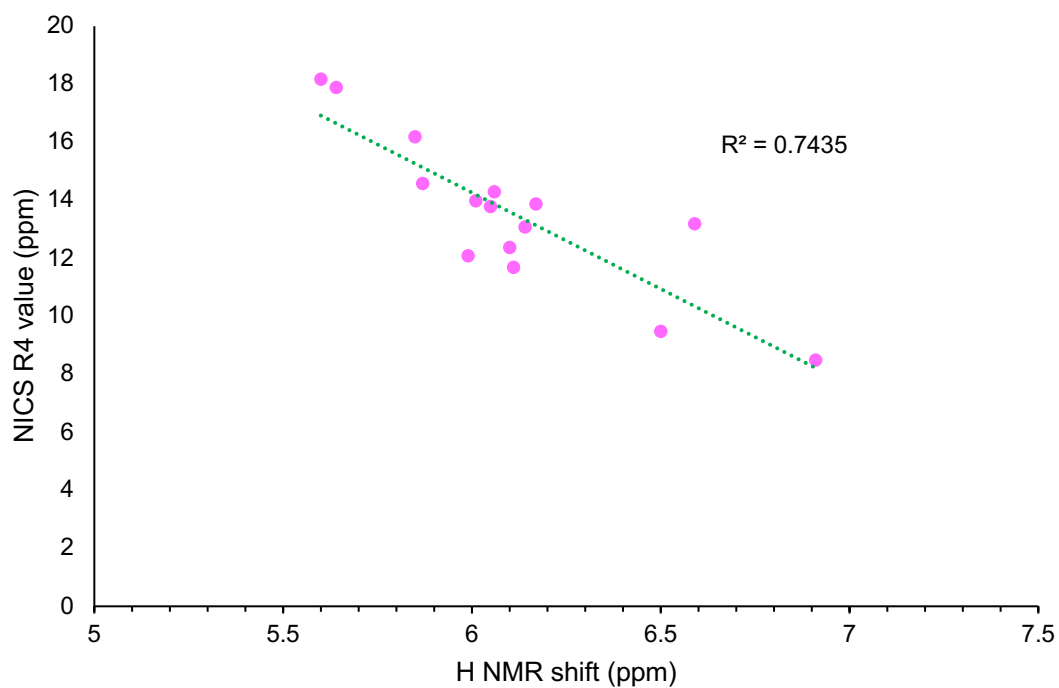


Figure S34. ^1H NMR chemical shift of each of the parent isomers (**1-14**) plotted against NICS R4 value.

10. Extended Hückel theory calculations and GIMIC plots

The following calculations were performed by Dr. Dr. Said Jalifo Jacobo with assistance from Prof. Judy Wu.

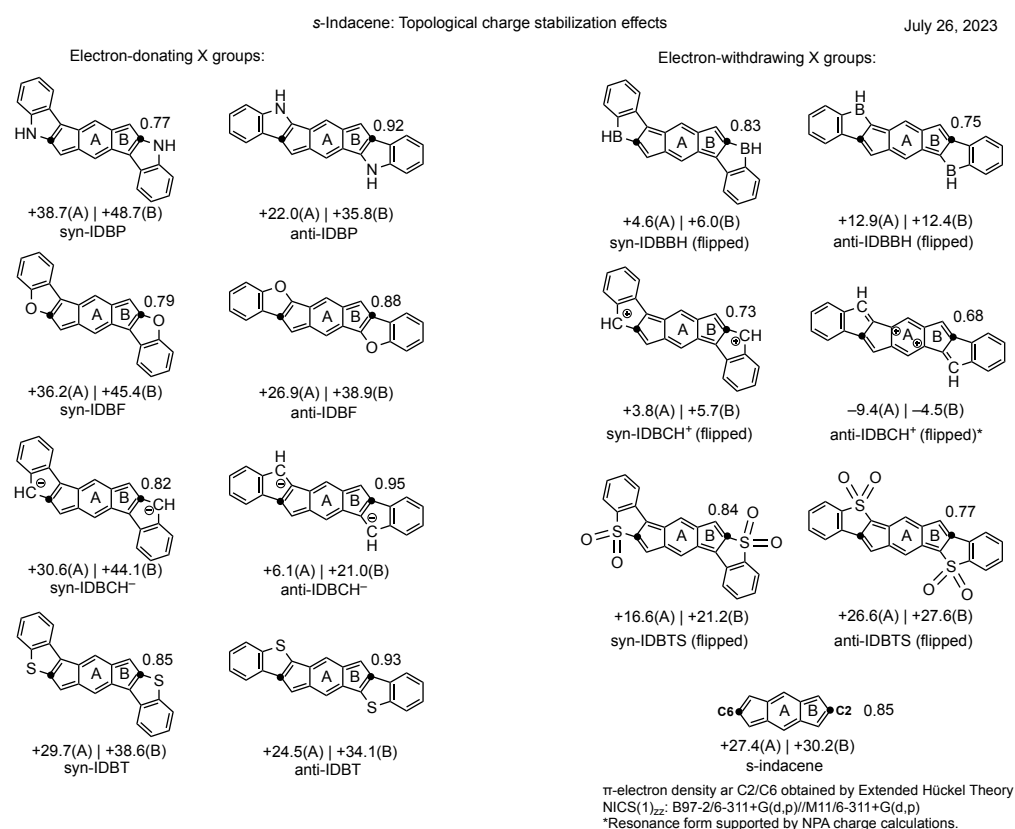
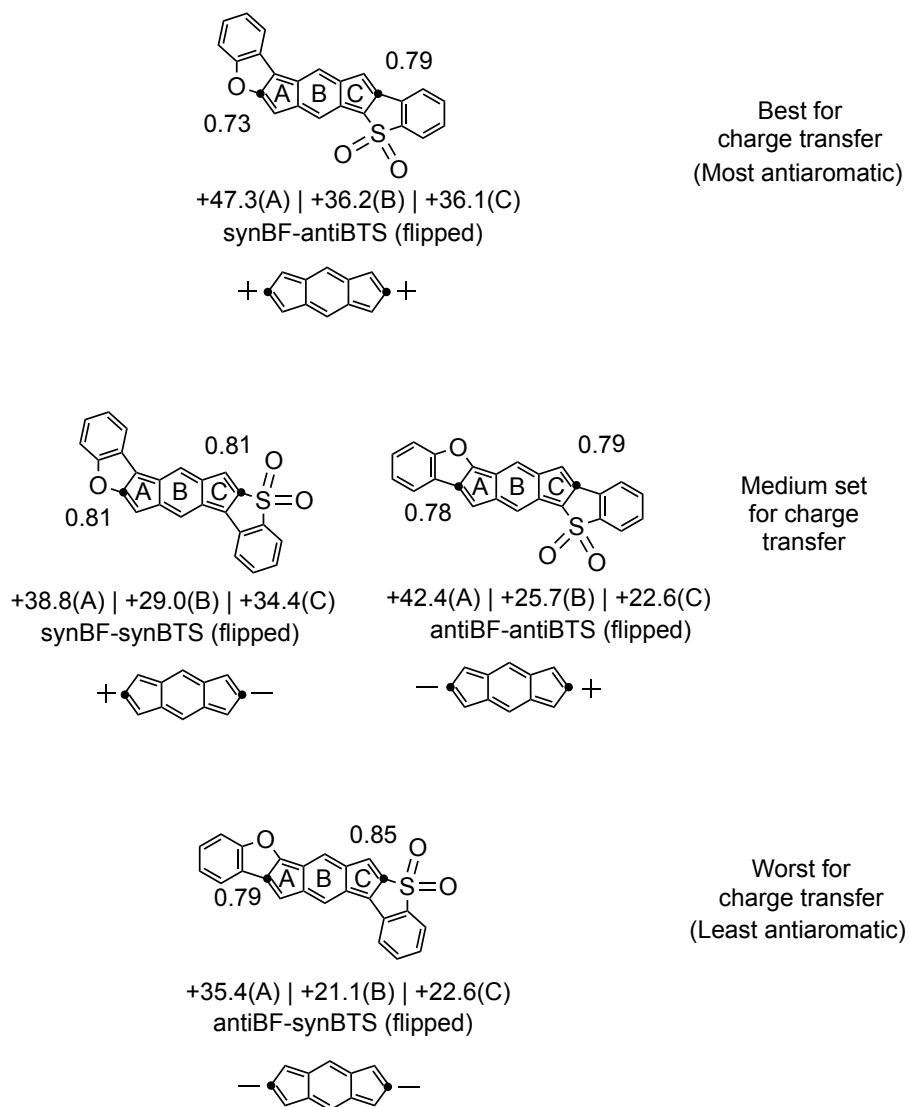


Figure S34. Symmetric heterocycles-fused s-indace π -electron density at C2/6 obtained by extended Hückel theory, NICS(1)_{zz} values for rings A and B were computed at the B97-2/6-311G** based in geometry optimizations at M11/6-311G**



π -electron density at C2/C6: Extended Hückel Calculations
NICS(1)_{zz}: B97-2/6-311+G(d,p)//M11/6-311+G(d,p)

Figure S35. Symmetric heterocycles-fused s-indacene π -electron density at C2/6 obtained by extended Hückel theory, NICS(1)_{zz} values for rings A and B were computed at the B97-2/6-311G** based in geometry optimizations at M11/6-311G**

10. Computational Details

All calculations were carried out using Gaussian 09.¹⁷ Structure geometries represent simplified models of compounds X-X(R-groups omitted). Geometry optimizations were performed on all structures with M11/6-311+G** level of theory. These geometries were checked and confirmed to have stable wavefunctions. Recently, Wu and co-workers showed that workhorse functional B3LYP tends to over-delocalize antiaromatic structures, and that geometry optimization with the M11 functional is more accurate.¹⁸ Previous reports from our group have included NICS-XY scans¹⁹⁻²¹ of molecules optimized at B3LYP. We computationally reassessed our prior work using M11 and found that, outside of the *s*-indacene reference, the previously determined order of antiaromaticities remained valid.²² We therefore performed NICS-XY scans of **7-14** (Figure 6) using M11-optimized geometries. For reference, Figure S23 shows the M11 NICS-XY scans of **1-6**.²² NICS-XY scans utilized the Aroma software package²³ and were generated with B972/6-311+G** level of theory.

Calculated Structures

anti/anti-IBFBT (10)

Zero-point correction = 0.279564 (Hartree/Particle)

Thermal correction to Energy = 0.297502

Thermal correction to Enthalpy = 0.298446

Thermal correction to Gibbs Free Energy = 0.233399

Sum of electronic and zero-point Energies = -1394.497423

Sum of electronic and thermal Energies = -1394.479485

Sum of electronic and thermal Enthalpies = -1394.478540

Sum of electronic and thermal Free Energies = -1394.543587

C	1.52174	-0.43659	0.00000
C	0.52472	-1.38201	-0.00000
C	-0.80568	-0.92512	-0.00000
C	-2.02698	-1.63886	0.00000
C	-3.08724	-0.69629	0.00000
C	-2.53969	0.58472	-0.00000
S	-3.71963	1.84157	-0.00000
C	-5.01938	0.63910	0.00000
C	-4.53257	-0.68168	0.00000
C	-5.44876	-1.73677	0.00000
C	-6.80525	-1.46391	0.00000
C	-7.27069	-0.14463	0.00000
C	-6.38199	0.91824	0.00000
C	-1.09538	0.49106	-0.00000
C	-0.09466	1.43549	0.00000
C	1.23619	0.98389	0.00000
C	2.45616	1.71046	0.00000
C	3.51914	0.77006	0.00000
C	2.96125	-0.49724	0.00000
O	3.87263	-1.48355	0.00000
C	5.10209	-0.84384	0.00000
C	4.95227	0.55444	0.00000
C	6.10012	1.34498	0.00000
C	7.33942	0.72015	0.00000
C	7.45182	-0.67395	0.00000
C	6.32393	-1.48559	0.00000
H	0.75327	-2.44723	-0.00000
H	-2.12594	-2.72062	0.00000
H	-5.09091	-2.76514	0.00000
H	-7.51998	-2.28458	0.00000
H	-8.34103	0.05110	0.00000
H	-6.74102	1.94550	0.00000

H	-0.31967	2.50210	0.00000
H	2.53981	2.79277	0.00000
H	6.02572	2.43035	0.00000
H	8.24343	1.32586	0.00000
H	8.43840	-1.13255	-0.00000
H	6.38730	-2.57069	-0.00000

anti/anti-IBFBTs (14)

Zero-point correction = 0.288661 (Hartree/Particle)

Thermal correction to Energy = 0.308636

Thermal correction to Enthalpy = 0.309581

Thermal correction to Gibbs Free Energy = 0.239530

Sum of electronic and zero-point Energies = -1544.843525

Sum of electronic and thermal Energies = -1544.823551

Sum of electronic and thermal Enthalpies = -1544.822606

Sum of electronic and thermal Free Energies = -1544.892657

O	-3.46574	-2.25526	-1.25478
S	-3.44213	-1.50795	0.00000
C	-2.16197	-0.28107	-0.00000
C	-2.71848	1.05070	0.00000
C	-1.69566	1.95290	0.00000
C	-0.79851	-0.23326	-0.00000
C	-0.45577	1.19172	-0.00000
C	0.84961	1.58592	0.00000
C	0.21512	-1.25375	-0.00000
C	1.50500	-0.84719	-0.00000
C	1.84787	0.57439	0.00000
C	3.22172	0.58765	0.00000
O	4.17563	1.52369	0.00000
C	5.39639	0.83765	-0.00000
C	5.22200	-0.55322	-0.00000
C	6.34549	-1.36835	0.00000
C	7.60254	-0.77111	0.00000
C	7.73956	0.61578	0.00000
C	6.62556	1.45391	0.00000
C	3.77936	-0.75706	0.00000
C	2.75118	-1.63995	0.00000
C	-4.72339	-0.23267	0.00000
C	-4.18685	1.05611	0.00000
C	-5.05976	2.13813	0.00000
C	-6.43009	1.90368	0.00000
C	-6.94018	0.60704	0.00000
C	-6.07955	-0.48641	0.00000

O	-3.46574	-2.25526	1.25478
H	-1.76838	3.03582	0.00000
H	1.13133	2.63858	0.00000
H	-0.06534	-2.30645	-0.00000
H	6.24381	-2.45134	0.00000
H	8.49290	-1.39595	0.00000
H	8.73430	1.05650	-0.00000
H	6.71189	2.53713	0.00000
H	2.79297	-2.72432	-0.00000
H	-4.67084	3.15479	0.00000
H	-7.11692	2.74809	-0.00000
H	-8.01630	0.44759	0.00000
H	-6.45561	-1.50786	0.00000

anti-IDBF (6)

Zero-point correction = 0.283006 (Hartree/Particle)

Thermal correction to Energy = 0.300225

Thermal correction to Enthalpy = 0.301169

Thermal correction to Gibbs Free Energy = 0.237850

Sum of electronic and zero-point Energies = -1071.507754

Sum of electronic and thermal Energies = -1071.490534

Sum of electronic and thermal Enthalpies = -1071.489590

Sum of electronic and thermal Free Energies = -1071.552910

C	1.31321	-0.43467	0.00000
C	0.32917	-1.40431	0.00000
C	-1.00210	-0.97789	0.00000
C	-2.21790	-1.73187	-0.00000
C	-3.28651	-0.81432	-0.00000
C	-2.74604	0.46936	0.00000
O	-3.67620	1.43800	0.00000
C	-4.89563	0.77611	0.00000
C	-4.72401	-0.61907	-0.00000
C	-5.85812	-1.42771	-0.00000
C	-7.10818	-0.82318	-0.00000
C	-7.24241	0.56821	-0.00000
C	-6.12698	1.39803	0.00000
C	-1.31321	0.43467	0.00000
C	-0.32917	1.40431	0.00000
C	1.00210	0.97789	0.00000
C	2.21790	1.73187	-0.00000
C	3.28651	0.81432	-0.00000
C	2.74604	-0.46936	0.00000
O	3.67620	-1.43800	0.00000

C	4.89563	-0.77611	0.00000
C	4.72401	0.61907	-0.00000
C	5.85812	1.42771	-0.00000
C	7.10818	0.82318	-0.00000
C	7.24241	-0.56821	-0.00000
C	6.12698	-1.39803	0.00000
H	0.58117	-2.46425	0.00000
H	-2.28074	-2.81544	-0.00000
H	-5.76565	-2.51168	-0.00000
H	-8.00221	-1.44348	-0.00000
H	-8.23602	1.01141	-0.00000
H	-6.20774	2.48196	0.00000
H	-0.58117	2.46425	-0.00000
H	2.28074	2.81544	-0.00000
H	5.76565	2.51168	-0.00000
H	8.00221	1.44348	-0.00000
H	8.23602	-1.01141	0.00000
H	6.20774	-2.48196	0.00000

anti-IDBT (2)

Zero-point correction = 0.276184 (Hartree/Particle)

Thermal correction to Energy = 0.294872

Thermal correction to Enthalpy = 0.295816

Thermal correction to Gibbs Free Energy = 0.228955

Sum of electronic and zero-point Energies = -1717.487404

Sum of electronic and thermal Energies = -1717.468716

Sum of electronic and thermal Enthalpies = -1717.467771

Sum of electronic and thermal Free Energies = -1717.534633

C	-1.30512	0.49588	-0.00000
C	-0.29415	1.41460	-0.00000
C	1.03939	0.93263	0.00000
C	2.25779	1.61802	0.00000
C	3.31596	0.65123	-0.00000
C	2.75446	-0.61352	-0.00000
S	3.91531	-1.88891	-0.00000
C	5.22913	-0.70689	0.00000
C	4.75863	0.62070	0.00000
C	5.68888	1.66511	0.00000
C	7.04078	1.37512	0.00000
C	7.49015	0.04908	0.00000
C	6.58945	-1.00232	0.00000
C	1.30512	-0.49588	-0.00000
C	0.29415	-1.41460	-0.00000

C	-1.03939	-0.93263	-0.00000
C	-2.25779	-1.61802	-0.00000
C	-3.31596	-0.65123	-0.00000
C	-2.75446	0.61352	-0.00000
S	-3.91531	1.88891	-0.00000
C	-5.22913	0.70689	-0.00000
C	-4.75863	-0.62070	0.00000
C	-5.68888	-1.66511	0.00000
C	-7.04078	-1.37512	0.00000
C	-7.49015	-0.04908	0.00000
C	-6.58945	1.00232	0.00000
H	-0.49497	2.48598	0.00000
H	2.37694	2.69795	0.00000
H	5.34415	2.69796	0.00000
H	7.76602	2.18654	0.00000
H	8.55808	-0.15944	0.00000
H	6.93596	-2.03387	0.00000
H	0.49497	-2.48598	-0.00000
H	-2.37693	-2.69795	0.00000
H	-5.34415	-2.69796	0.00000
H	-7.76602	-2.18654	0.00000
H	-8.55808	0.15944	0.00000
H	-6.93596	2.03387	0.00000

anti-IDBTS (4)

Zero-point correction = 0.295778 (Hartree/Particle)

Thermal correction to Energy = 0.318310

Thermal correction to Enthalpy = 0.319254

Thermal correction to Gibbs Free Energy = 0.242874

Sum of electronic and zero-point Energies = -2018.175963

Sum of electronic and thermal Energies = -2018.153431

Sum of electronic and thermal Enthalpies = -2018.152486

Sum of electronic and thermal Free Energies = -2018.228867

O	-4.02936	-2.31317	-1.25661
S	-3.99850	-1.57411	0.00000
C	-2.68245	-0.37416	0.00000
C	-3.21886	0.98680	0.00000
C	-2.18594	1.85865	0.00000
C	-1.33292	-0.36417	0.00000
C	-0.94885	1.06189	0.00000
C	0.34770	1.42497	0.00000
C	-0.34770	-1.42497	0.00000
C	0.94885	-1.06190	0.00000

C	1.33292	0.36417	0.00000
C	2.68245	0.37416	0.00000
S	3.99850	1.57411	0.00000
C	5.24439	0.26722	-0.00000
C	4.68529	-1.01206	-0.00000
C	5.53721	-2.11154	-0.00000
C	6.91042	-1.90279	-0.00000
C	7.44415	-0.61481	-0.00000
C	6.60631	0.49479	-0.00000
O	4.02936	2.31316	1.25661
O	4.02936	2.31317	-1.25661
C	3.21886	-0.98680	0.00000
C	2.18594	-1.85865	0.00000
C	-5.24439	-0.26722	-0.00000
C	-4.68529	1.01206	-0.00000
C	-5.53721	2.11154	-0.00000
C	-6.91042	1.90279	-0.00000
C	-7.44415	0.61481	-0.00000
C	-6.60631	-0.49479	-0.00000
O	-4.02936	-2.31316	1.25661
H	-2.22731	2.94292	0.00000
H	0.66881	2.46595	0.00000
H	-0.66881	-2.46595	0.00000
H	5.12883	-3.12040	-0.00000
H	7.58162	-2.75942	-0.00000
H	8.52307	-0.47589	-0.00000
H	7.00297	1.50833	-0.00000
H	2.22731	-2.94292	0.00000
H	-5.12883	3.12040	-0.00000
H	-7.58162	2.75942	-0.00000
H	-8.52307	0.47589	-0.00000
H	-7.00297	-1.50833	-0.00000

anti/syn-IBFBT (9)

Zero-point correction = 0.281895 (Hartree/Particle)

Thermal correction to Energy = 0.299658

Thermal correction to Enthalpy = 0.300602

Thermal correction to Gibbs Free Energy = 0.235828

Sum of electronic and zero-point Energies = -1394.494036

Sum of electronic and thermal Energies = -1394.476273

Sum of electronic and thermal Enthalpies = -1394.475329

Sum of electronic and thermal Free Energies = -1394.540103

C	-1.47265	-0.68904	0.00000
---	----------	----------	---------

C	-0.63383	-1.74195	0.00000
C	0.78339	-1.46932	0.00000
C	1.84315	-2.33027	0.00000
C	3.05114	-1.52703	-0.00000
C	2.74348	-0.18899	0.00000
C	3.90618	0.65342	0.00000
C	4.02222	2.05106	0.00000
C	5.27362	2.63315	0.00000
C	6.43293	1.84410	-0.00000
C	6.34855	0.46440	-0.00000
C	5.08476	-0.12461	-0.00000
S	4.75600	-1.85178	-0.00000
C	1.28437	-0.08174	0.00000
C	0.43548	0.96749	0.00000
C	-0.98286	0.70569	0.00000
C	-2.04500	1.56639	0.00000
C	-3.27239	0.77706	0.00000
C	-2.91832	-0.53955	0.00000
O	-3.96656	-1.38501	0.00000
C	-5.07980	-0.57108	-0.00000
C	-4.71636	0.78947	-0.00000
C	-5.73080	1.74931	-0.00000
C	-7.04887	1.32258	-0.00000
C	-7.37563	-0.04013	-0.00000
C	-6.38922	-1.01546	-0.00000
H	-0.99712	-2.76910	0.00000
H	1.79464	-3.41501	-0.00000
H	3.12879	2.67191	0.00000
H	5.36416	3.71764	0.00000
H	7.41053	2.32199	-0.00000
H	7.24697	-0.14961	-0.00000
H	0.78922	1.99781	0.00000
H	-1.97999	2.65084	0.00000
H	-5.49035	2.81035	-0.00000
H	-7.84970	2.05937	-0.00000
H	-8.42155	-0.33967	-0.00000
H	-6.62046	-2.07758	-0.00000

***anti/syn*-IBFBTS (13)**

Zero-point correction = 0.288380 (Hartree/Particle)

Thermal correction to Energy = 0.308267

Thermal correction to Enthalpy = 0.309211

Thermal correction to Gibbs Free Energy = 0.239439

Sum of electronic and zero-point Energies = -1544.846383

Sum of electronic and thermal Energies = -1544.826496
Sum of electronic and thermal Enthalpies = -1544.825551
Sum of electronic and thermal Free Energies = -1544.895323

O	4.95439	-1.94968	-1.25605
S	4.45102	-1.40395	0.00000
C	2.68057	-1.27519	0.00000
C	1.60316	-2.12268	-0.00000
C	0.42438	-1.28143	-0.00000
C	-0.91686	-1.62284	-0.00000
C	-1.84273	-0.58044	-0.00000
C	-3.25822	-0.51710	-0.00000
O	-4.25253	-1.41156	-0.00000
C	-5.42985	-0.66494	0.00000
C	-5.16971	0.71420	-0.00000
C	-6.24604	1.59481	0.00000
C	-7.53395	1.07231	0.00000
C	-7.75612	-0.30600	0.00000
C	-6.69596	-1.20748	0.00000
C	-3.71909	0.82096	-0.00000
C	-2.61435	1.65314	-0.00000
C	-1.43283	0.80268	-0.00000
C	-0.09280	1.13790	-0.00000
C	0.84640	0.09649	-0.00000
C	2.26840	0.08280	0.00000
C	3.36809	1.03725	0.00000
C	4.61444	0.39837	0.00000
C	5.81093	1.07793	0.00000
C	5.76228	2.47118	0.00000
C	4.53749	3.13403	-0.00000
C	3.33841	2.43055	-0.00000
O	4.95439	-1.94968	1.25605
H	1.61729	-3.20740	-0.00000
H	-1.23951	-2.66310	-0.00000
H	-6.08285	2.67031	0.00000
H	-8.38596	1.74883	0.00000
H	-8.77590	-0.68501	0.00000
H	-6.84621	-2.28381	0.00000
H	-2.59930	2.73828	-0.00000
H	0.21445	2.18239	0.00000
H	6.75745	0.54052	0.00000
H	6.68754	3.04336	0.00000
H	4.51848	4.22213	-0.00000
H	2.39177	2.96504	-0.00000

syn/anti-IBFBT (8)

Zero-point correction = 0.281738 (Hartree/Particle)

Thermal correction to Energy = 0.299554

Thermal correction to Enthalpy = 0.300498

Thermal correction to Gibbs Free Energy = 0.235497

Sum of electronic and zero-point Energies = -1394.495450

Sum of electronic and thermal Energies = -1394.477633

Sum of electronic and thermal Enthalpies = -1394.476689

Sum of electronic and thermal Free Energies = -1394.541691

C	-1.06352	-0.72659	-0.00000
C	-0.18925	-1.75068	-0.00000
C	1.22080	-1.43938	-0.00000
C	2.30133	-2.27778	0.00000
C	3.46416	-1.42002	-0.00000
C	3.13794	-0.09550	-0.00000
C	4.38905	0.61538	-0.00000
C	4.80621	1.94947	-0.00000
C	6.16394	2.22058	0.00000
C	7.11417	1.18949	0.00000
C	6.73006	-0.14294	0.00000
C	5.36996	-0.39752	0.00000
O	4.79902	-1.64712	0.00000
C	1.67858	-0.02836	-0.00000
C	0.79677	0.98938	-0.00000
C	-0.61433	0.67732	-0.00000
C	-1.70568	1.49287	-0.00000
C	-2.90682	0.66104	-0.00000
C	-2.52400	-0.65463	-0.00000
S	-3.84512	-1.76624	0.00000
C	-4.98365	-0.42146	0.00000
C	-4.33537	0.83075	0.00000
C	-5.11427	1.99494	0.00000
C	-6.49136	1.89288	0.00000
C	-7.11914	0.63922	0.00000
C	-6.37364	-0.52547	0.00000
H	-0.51610	-2.79048	0.00000
H	2.29125	-3.36271	0.00000
H	4.07863	2.75838	-0.00000
H	6.50374	3.25435	0.00000
H	8.17325	1.43884	0.00000
H	7.45082	-0.95662	0.00000
H	1.12091	2.02978	-0.00000
H	-1.68918	2.57984	-0.00000

H	-4.63093	2.97065	0.00000
H	-7.09927	2.79553	0.00000
H	-8.20566	0.58045	0.00000
H	-6.85936	-1.49923	-0.00000

syn/anti-IBFBTS (12)

Zero-point correction = 0.287756 (Hartree/Particle)

Thermal correction to Energy = 0.307845

Thermal correction to Enthalpy = 0.308789

Thermal correction to Gibbs Free Energy = 0.238575

Sum of electronic and zero-point Energies = -1544.840846

Sum of electronic and thermal Energies = -1544.820757

Sum of electronic and thermal Enthalpies = -1544.819813

Sum of electronic and thermal Free Energies = -1544.890028

O	3.62262	-2.15132	1.25583
S	3.51519	-1.41513	0.00000
C	2.09552	-0.34744	0.00000
C	2.49401	1.04288	0.00000
C	1.37150	1.81251	0.00000
C	0.72845	-0.46217	0.00000
C	0.22495	0.90290	0.00000
C	-1.12092	1.13998	0.00000
C	-1.99475	0.02307	0.00000
C	-3.38345	-0.08306	0.00000
C	-4.64306	0.60868	0.00000
C	-5.04697	1.94508	-0.00000
C	-6.40234	2.22864	-0.00000
C	-7.34970	1.19771	-0.00000
C	-6.97554	-0.14059	-0.00000
C	-5.62037	-0.40801	-0.00000
O	-5.07895	-1.67022	-0.00000
C	-3.72354	-1.48902	0.00000
C	-2.63125	-2.28157	0.00000
C	-1.48711	-1.34365	0.00000
C	-0.15286	-1.59225	0.00000
C	4.63523	0.00280	-0.00000
C	3.95104	1.21961	0.00000
C	4.69105	2.39669	0.00000
C	6.07922	2.32444	-0.00000
C	6.73812	1.09657	-0.00000
C	6.01204	-0.09017	-0.00000
O	3.62262	-2.15132	-1.25583
H	1.31213	2.89637	0.00000

H	-1.51949	2.15427	0.00000
H	-4.31025	2.74559	0.00000
H	-6.73861	3.26286	-0.00000
H	-8.40849	1.44970	-0.00000
H	-7.70310	-0.94762	-0.00000
H	-2.57166	-3.36307	0.00000
H	0.25141	-2.60369	0.00000
H	4.18596	3.36088	0.00000
H	6.66233	3.24352	-0.00000
H	7.82548	1.06460	-0.00000
H	6.50541	-1.06039	-0.00000

syn-IDBF (5)

Zero-point correction = 0.284865 (Hartree/Particle)

Thermal correction to Energy = 0.302072

Thermal correction to Enthalpy = 0.303017

Thermal correction to Gibbs Free Energy = 0.239470

Sum of electronic and zero-point Energies = -1071.505960

Sum of electronic and thermal Energies = -1071.488753

Sum of electronic and thermal Enthalpies = -1071.487809

Sum of electronic and thermal Free Energies = -1071.551355

C	1.41385	0.14960	0.00000
C	0.69071	1.28281	0.00000
C	-0.75375	1.17940	0.00000
C	-1.69774	2.16408	0.00000
C	-2.97929	1.48501	0.00000
C	-2.85159	0.12960	0.00000
C	-4.19326	-0.39011	0.00000
C	-4.80289	-1.64816	0.00000
C	-6.18563	-1.71542	-0.00000
C	-6.97354	-0.55531	-0.00000
C	-6.39719	0.70571	-0.00000
C	-5.01435	0.75626	-0.00000
O	-4.26420	1.90766	-0.00000
C	-1.41385	-0.14960	0.00000
C	-0.69071	-1.28281	0.00000
C	0.75375	-1.17940	0.00000
C	1.69774	-2.16408	0.00000
C	2.97929	-1.48501	0.00000
C	2.85159	-0.12960	0.00000
C	4.19326	0.39011	0.00000
C	4.80289	1.64816	0.00000
C	6.18563	1.71542	-0.00000

C	6.97354	0.55531	-0.00000
C	6.39719	-0.70571	-0.00000
C	5.01435	-0.75626	-0.00000
O	4.26420	-1.90766	-0.00000
H	1.16089	2.26569	0.00000
H	-1.52967	3.23608	0.00000
H	-4.20271	-2.55559	0.00000
H	-6.67432	-2.68770	-0.00000
H	-8.05779	-0.64580	-0.00000
H	-6.99013	1.61674	-0.00000
H	-1.16089	-2.26569	0.00000
H	1.52967	-3.23608	0.00000
H	4.20271	2.55559	0.00000
H	6.67432	2.68770	-0.00000
H	8.05779	0.64580	-0.00000
H	6.99013	-1.61674	-0.00000

syn-IDBT (1)

Zero-point correction = 0.278636 (Hartree/Particle)

Thermal correction to Energy = 0.297082

Thermal correction to Enthalpy = 0.298026

Thermal correction to Gibbs Free Energy = 0.231526

Sum of electronic and zero-point Energies = -1717.484659

Sum of electronic and thermal Energies = -1717.466214

Sum of electronic and thermal Enthalpies = -1717.465270

Sum of electronic and thermal Free Energies = -1717.531770

C	1.41596	0.11171	0.00000
C	0.72078	1.26461	0.00000
C	-0.72414	1.19286	0.00000
C	-1.65139	2.19073	-0.00000
C	-2.96541	1.56321	-0.00000
C	-2.84963	0.19795	0.00000
C	-4.11801	-0.47363	0.00000
C	-4.42973	-1.84119	0.00000
C	-5.75067	-2.24081	0.00000
C	-6.78767	-1.29654	-0.00000
C	-6.51007	0.05744	-0.00000
C	-5.17581	0.46225	-0.00000
S	-4.60543	2.12528	-0.00000
C	-1.41596	-0.11171	0.00000
C	-0.72078	-1.26461	0.00000
C	0.72414	-1.19286	0.00000
C	1.65139	-2.19073	-0.00000

C	2.96541	-1.56321	-0.00000
C	2.84963	-0.19795	0.00000
C	4.11801	0.47363	0.00000
C	4.42973	1.84119	0.00000
C	5.75067	2.24081	0.00000
C	6.78767	1.29654	-0.00000
C	6.51007	-0.05744	-0.00000
C	5.17581	-0.46225	-0.00000
S	4.60543	-2.12528	-0.00000
H	1.20871	2.23831	0.00000
H	-1.45313	3.25834	-0.00000
H	-3.63248	-2.58152	0.00000
H	-5.99308	-3.30173	0.00000
H	-7.82269	-1.63230	-0.00000
H	-7.31324	0.79168	-0.00000
H	-1.20871	-2.23831	0.00000
H	1.45313	-3.25834	-0.00000
H	3.63248	2.58152	0.00000
H	5.99308	3.30173	0.00000
H	7.82269	1.63230	-0.00000
H	7.31324	-0.79168	-0.00000

syn-IDBTS (3)

Zero-point correction = 0.293827 (Hartree/Particle)

Thermal correction to Energy = 0.316402

Thermal correction to Enthalpy = 0.317347

Thermal correction to Gibbs Free Energy = 0.241059

Sum of electronic and zero-point Energies = -2018.183215

Sum of electronic and thermal Energies = -2018.160640

Sum of electronic and thermal Enthalpies = -2018.159696

Sum of electronic and thermal Free Energies = -2018.235984

O	-5.30597	-2.13242	1.25709
S	-4.85096	-1.55146	0.00000
C	-3.09211	-1.28956	-0.00001
C	-1.96133	-2.04585	-0.00001
C	-0.84227	-1.10696	-0.00002
C	0.51371	-1.34515	-0.00001
C	1.37241	-0.23182	-0.00001
C	2.78384	-0.10726	-0.00000
C	3.95381	-0.96850	0.00000
C	4.03145	-2.36106	0.00001
C	5.28047	-2.96887	0.00001
C	6.45020	-2.21173	0.00001

C	6.39223	-0.81919	0.00001
C	5.14686	-0.23340	0.00001
S	4.85096	1.55146	0.00000
O	5.30597	2.13242	1.25709
O	5.30598	2.13241	-1.25708
C	3.09211	1.28956	-0.00000
C	1.96133	2.04585	-0.00001
C	0.84227	1.10696	-0.00001
C	-0.51371	1.34515	-0.00002
C	-1.37241	0.23182	-0.00002
C	-2.78384	0.10726	-0.00001
C	-3.95381	0.96850	0.00000
C	-5.14686	0.23340	0.00001
C	-6.39223	0.81919	0.00001
C	-6.45020	2.21173	0.00002
C	-5.28047	2.96887	0.00001
C	-4.03145	2.36106	0.00001
O	-5.30598	-2.13241	-1.25708
H	-1.88859	-3.12825	-0.00002
H	0.89847	-2.36313	-0.00000
H	3.12937	-2.96755	0.00001
H	5.34638	-4.05497	0.00001
H	7.41696	-2.71057	0.00002
H	7.29495	-0.21117	0.00001
H	1.88859	3.12825	-0.00001
H	-0.89847	2.36313	-0.00003
H	-7.29495	0.21117	0.00002
H	-7.41696	2.71057	0.00002
H	-5.34639	4.05497	0.00002
H	-3.12937	2.96755	0.00000

syn/syn-IBFBT (7)

Zero-point correction = 0.281722 (Hartree/Particle)

Thermal correction to Energy = 0.299556

Thermal correction to Enthalpy = 0.300500

Thermal correction to Gibbs Free Energy = 0.235439

Sum of electronic and zero-point Energies = -1394.495378

Sum of electronic and thermal Energies = -1394.477545

Sum of electronic and thermal Enthalpies = -1394.476601

Sum of electronic and thermal Free Energies = -1394.541662

C	-1.60361	-0.16398	-0.00000
C	-0.89346	-1.30567	-0.00001
C	0.55148	-1.21536	-0.00001

C	1.49062	-2.20078	-0.00001
C	2.79828	-1.55691	-0.00000
C	2.66504	-0.19392	-0.00000
C	3.92461	0.49372	-0.00000
C	4.21895	1.86522	-0.00000
C	5.53462	2.28140	0.00000
C	6.58359	1.35025	0.00001
C	6.32337	-0.00702	0.00001
C	4.99419	-0.42876	0.00000
S	4.44474	-2.09856	0.00000
C	1.22637	0.09753	-0.00001
C	0.51778	1.24207	-0.00000
C	-0.92668	1.15694	-0.00000
C	-1.85910	2.15401	-0.00001
C	-3.14726	1.49081	-0.00000
C	-3.03647	0.13314	-0.00000
C	-4.38455	-0.36987	-0.00000
C	-5.00974	-1.62019	0.00000
C	-6.39332	-1.67049	0.00001
C	-7.16676	-0.50084	0.00001
C	-6.57466	0.75301	0.00001
C	-5.19141	0.78653	0.00000
O	-4.42732	1.92880	-0.00000
H	-1.37430	-2.28339	-0.00001
H	1.30562	-3.27083	-0.00000
H	3.41245	2.59544	-0.00000
H	5.76366	3.34528	0.00000
H	7.61423	1.69920	0.00001
H	7.13577	-0.73100	0.00001
H	0.99494	2.22107	0.00000
H	-1.67799	3.22381	-0.00001
H	-4.42075	-2.53495	0.00000
H	-6.89387	-2.63672	0.00001
H	-8.25205	-0.57781	0.00001
H	-7.15626	1.67134	0.00001

syn/syn-IBFBTS (11)

Zero-point correction = 0.287934 (Hartree/Particle)

Thermal correction to Energy = 0.307860

Thermal correction to Enthalpy = 0.308804

Thermal correction to Gibbs Free Energy = 0.238969

Sum of electronic and zero-point Energies = -1544.845200

Sum of electronic and thermal Energies = -1544.825274

Sum of electronic and thermal Enthalpies = -1544.824330

Sum of electronic and thermal Free Energies = -1544.894165

O	4.61417	-2.23434	-1.25608
S	4.18178	-1.63103	-0.00000
C	2.44195	-1.28367	0.00000
C	1.26621	-1.98575	0.00001
C	0.19966	-0.99894	0.00001
C	-1.17813	-1.16796	-0.00000
C	-1.97096	-0.02483	-0.00001
C	-3.38980	0.17732	-0.00000
C	-4.68629	-0.42513	-0.00000
C	-5.19147	-1.73074	0.00000
C	-6.56246	-1.90980	0.00000
C	-7.43465	-0.81112	0.00000
C	-6.96353	0.49467	0.00000
C	-5.59115	0.66078	-0.00000
O	-4.95175	1.87223	-0.00000
C	-3.61783	1.57519	-0.00000
C	-2.45245	2.29386	-0.00000
C	-1.38581	1.29169	-0.00000
C	-0.01677	1.45880	0.00001
C	0.78653	0.30696	0.00001
C	2.20095	0.11614	0.00000
C	3.40822	0.92611	0.00000
C	4.56660	0.13769	0.00000
C	5.83732	0.66473	0.00000
C	5.96016	2.05365	-0.00000
C	4.82649	2.86300	-0.00000
C	3.55004	2.31308	-0.00000
O	4.61418	-2.23434	1.25608
H	1.14242	-3.06359	0.00001
H	-1.62171	-2.16294	-0.00001
H	-4.51765	-2.58471	-0.00000
H	-6.97495	-2.91624	0.00000
H	-8.50874	-0.98599	0.00000
H	-7.62965	1.35321	0.00000
H	-2.32435	3.36996	-0.00000
H	0.41843	2.45655	0.00002
H	6.71062	0.01513	0.00000
H	6.94889	2.50744	-0.00000
H	4.94213	3.94506	-0.00000
H	2.67618	2.95962	-0.00000

Syn-fused aromatic analog (A)

Zero-point correction= 0.270667 (Hartree/Particle)
 Thermal correction to Energy= 0.287059
 Thermal correction to Enthalpy= 0.288003
 Thermal correction to Gibbs Free Energy= 0.226508
 Sum of electronic and zero-point Energies= -1318.414530
 Sum of electronic and thermal Energies= -1318.398137
 Sum of electronic and thermal Enthalpies= -1318.397193
 Sum of electronic and thermal Free Energies= -1318.458688

C	-4.60609	-0.30712	-0.11292
O	-5.92426	-0.24153	-0.14322
C	-6.36389	-1.48547	-0.11754
C	-5.31561	-2.38	-0.06961
C	-5.51976	-3.75801	-0.03506
C	-6.84859	-4.22007	-0.05072
C	-7.92597	-3.30646	-0.09984
C	-7.68738	-1.91961	-0.13388
C	-4.17637	-1.61607	-0.06662
C	-2.82726	-1.95647	-0.02791
C	-1.88318	-0.90801	-0.03727
C	-0.5056	-1.19866	0.00056
C	0.41453	-0.14323	-0.0096
C	1.8155	-0.23385	0.02297
C	2.59672	-1.39664	0.07262
C	3.99576	-1.27383	0.09905
C	4.60257	-0.00438	0.07606
C	3.81691	1.15624	0.02639
C	2.43116	1.01635	0.00072
S	1.27565	2.24373	-0.05878
C	-0.0315	1.17591	-0.05653
C	-1.38382	1.50179	-0.09477
C	-2.32788	0.46011	-0.08556
C	-3.70752	0.75518	-0.12361
H	-4.68875	-4.45029	0.00246
H	-7.04703	-5.28361	-0.02496
H	-8.94306	-3.67601	-0.11139
H	-8.50607	-1.21299	-0.17156
H	-2.52148	-2.99518	0.00806
H	-0.16605	-2.22595	0.03693
H	2.14583	-2.37942	0.09081
H	4.61203	-2.1627	0.13741
H	5.68156	0.07701	0.09682
H	4.27741	2.13551	0.00848
H	-1.69187	2.53991	-0.1308

H -4.06922 1.77562 -0.16029

Anti-fused aromatic analog (B)

Zero-point correction= 0.270658 (Hartree/Particle)

Thermal correction to Energy= 0.287038

Thermal correction to Enthalpy= 0.287982

Thermal correction to Gibbs Free Energy= 0.226571

Sum of electronic and zero-point Energies= -1318.414238

Sum of electronic and thermal Energies= -1318.397859

Sum of electronic and thermal Enthalpies= -1318.396914

Sum of electronic and thermal Free Energies= -1318.458325

C	-4.79848	-0.28293	-0.12742
C	-6.17	-0.29831	-0.13912
C	-7.113	0.60394	-0.62748
C	-8.47178	0.27318	-0.473
C	-8.84975	-0.93434	0.15698
C	-7.87329	-1.82573	0.6401
C	-6.53462	-1.4773	0.47604
O	-5.47215	-2.16345	0.85243
C	-4.4186	-1.4533	0.49394
C	-3.07849	-1.77648	0.68339
C	-2.10218	-0.86839	0.21968
C	-0.73395	-1.15558	0.39067
C	0.2184	-0.24149	-0.07648
C	1.6161	-0.35222	0.00216
C	2.36124	-1.39839	0.56355
C	3.76357	-1.32015	0.54285
C	4.40928	-0.20981	-0.032
C	3.65964	0.83453	-0.5925
C	2.27006	0.74089	-0.56351
S	1.15277	1.85239	-1.1647
C	-0.18681	0.93578	-0.70187
C	-1.52858	1.25369	-0.88867
C	-2.50429	0.35228	-0.42849
C	-3.8737	0.64306	-0.60133
H	-6.81449	1.52628	-1.10852
H	-9.23339	0.94899	-0.83958
H	-9.89868	-1.17592	0.26899
H	-8.15354	-2.75234	1.12367
H	-2.80511	-2.70245	1.17462
H	-0.4261	-2.07219	0.87749
H	1.88024	-2.2584	1.00909

H	4.35225	-2.12029	0.9725
H	5.49039	-0.16127	-0.04176
H	4.15013	1.69123	-1.03615
H	-1.80462	2.17922	-1.37969
H	-4.20364	1.5543	-1.0856

Syn-fused D/A-aromatic analog (C)

Zero-point correction= 0.279670 (Hartree/Particle)

Thermal correction to Energy= 0.298067

Thermal correction to Enthalpy= 0.299011

Thermal correction to Gibbs Free Energy= 0.232800

Sum of electronic and zero-point Energies= -1468.751401

Sum of electronic and thermal Energies= -1468.733004

Sum of electronic and thermal Enthalpies= -1468.732060

Sum of electronic and thermal Free Energies= -1468.798271

O	3.36733	-0.32663	-1.35574
S	3.04693	0.06344	0.09466
C	3.25403	1.7843	0.42063
C	2.57406	2.85201	-0.1556
C	2.89984	4.15652	0.25391
C	2.22997	5.26341	-0.30983
C	2.58516	6.53635	0.12555
O	2.08172	7.68923	-0.27467
C	2.7124	8.63062	0.4016
C	3.64421	8.08438	1.25878
C	4.44202	8.87366	2.08481
C	4.26775	10.26824	2.01919
C	3.31372	10.83218	1.14189
C	2.52239	10.00814	0.31958
C	3.56162	6.72697	1.07974
C	4.24933	5.66724	1.66418
C	3.91881	4.35971	1.24996
C	4.58505	3.25246	1.81011
C	4.24419	1.96361	1.38717
C	4.83622	0.68127	1.86284
C	4.28185	-0.44175	1.24643
C	4.69909	-1.73427	1.55297
C	5.7083	-1.89765	2.51258
C	6.27781	-0.77613	3.14347
C	5.8441	0.52053	2.82137
O	1.64325	-0.45837	0.43501
H	1.81176	2.6688	-0.90306

H	1.45943	5.13862	-1.06094
H	5.17007	8.43322	2.75354
H	4.86917	10.91405	2.64559
H	3.19036	11.90658	1.10182
H	1.78963	10.43121	-0.35499
H	5.01184	5.84998	2.41177
H	5.35263	3.39653	2.55972
H	4.25546	-2.59087	1.06277
H	6.05084	-2.89167	2.76916
H	7.0562	-0.91368	3.88275
H	6.28981	1.37418	3.31333

Anti-fused D/A-aromatic analog (D)

Zero-point correction= 0.279723 (Hartree/Particle)

Thermal correction to Energy= 0.298124

Thermal correction to Enthalpy= 0.299068

Thermal correction to Gibbs Free Energy= 0.232784

Sum of electronic and zero-point Energies= -1468.751758

Sum of electronic and thermal Energies= -1468.733358

Sum of electronic and thermal Enthalpies= -1468.732413

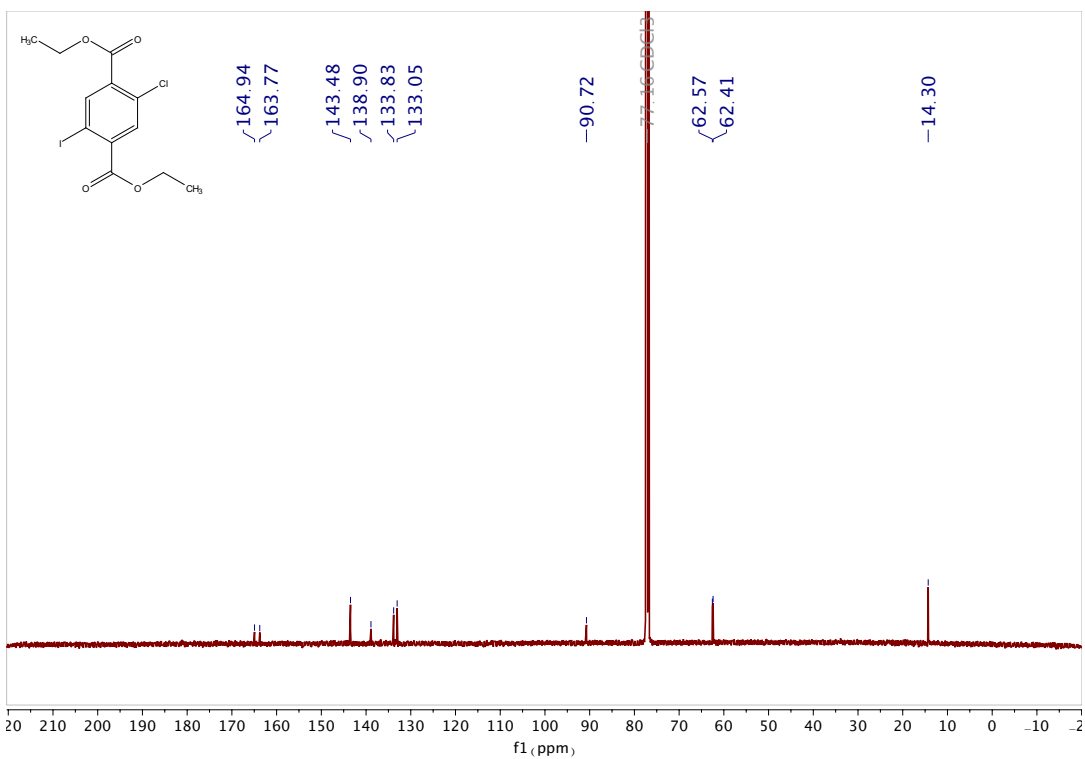
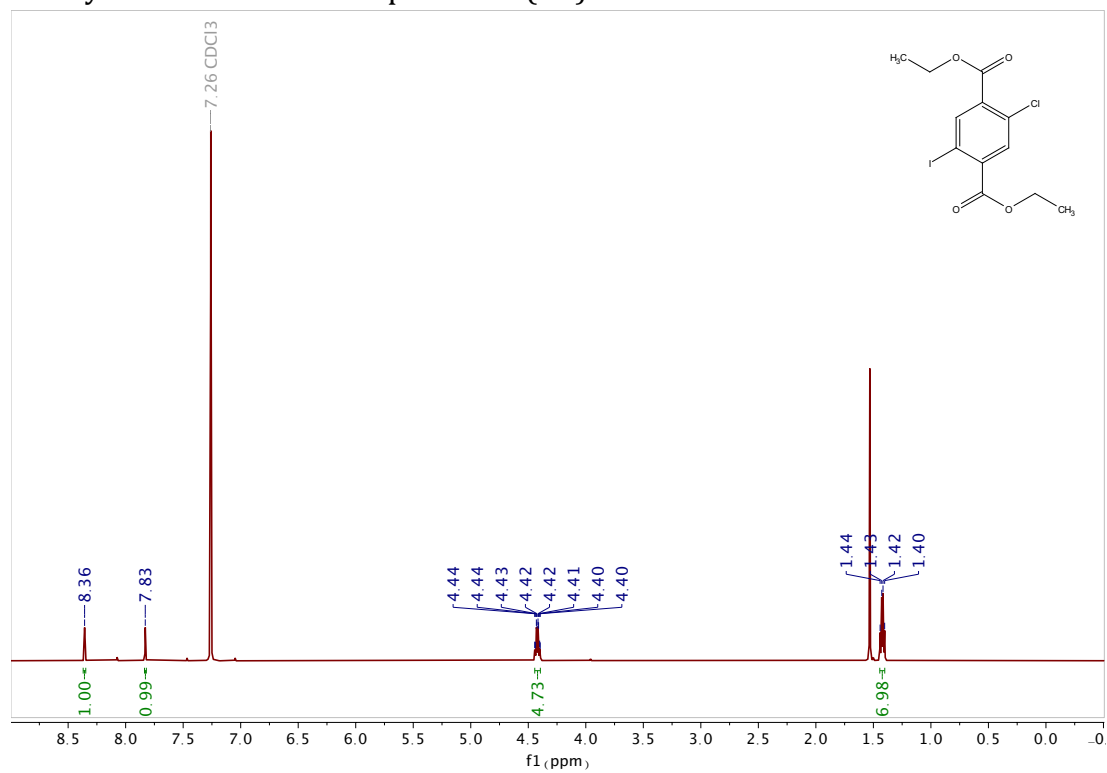
Sum of electronic and thermal Free Energies= -1468.798698

O	1.50731	0.51022	-1.16604
S	2.88605	0.02789	-0.69182
C	3.13649	-1.70429	-0.90922
C	2.42553	-2.75058	-0.33119
C	2.79622	-4.06953	-0.6449
C	2.09721	-5.15512	-0.07707
C	2.50507	-6.44061	-0.42124
C	2.04537	-7.6789	-0.05142
C	1.0137	-8.08112	0.79454
C	0.8056	-9.46317	0.95636
C	1.62222	-10.39653	0.27827
C	2.6569	-9.95894	-0.56992
C	2.84422	-8.58624	-0.71472
O	3.74759	-7.97049	-1.45371
C	3.55326	-6.67565	-1.28513
C	4.26758	-5.63215	-1.8658
C	3.89142	-4.30932	-1.54753
C	4.58701	-3.22277	-2.11263
C	4.20043	-1.91886	-1.78601
C	4.8135	-0.65429	-2.2822
C	4.20082	0.49086	-1.77064

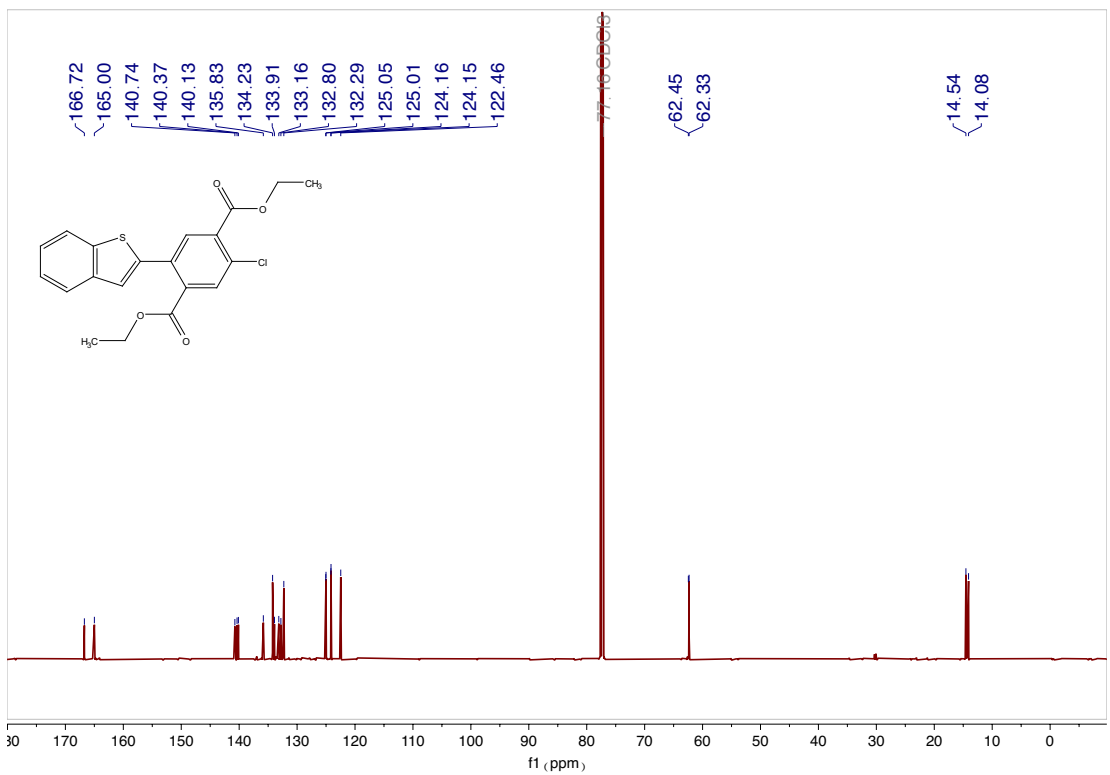
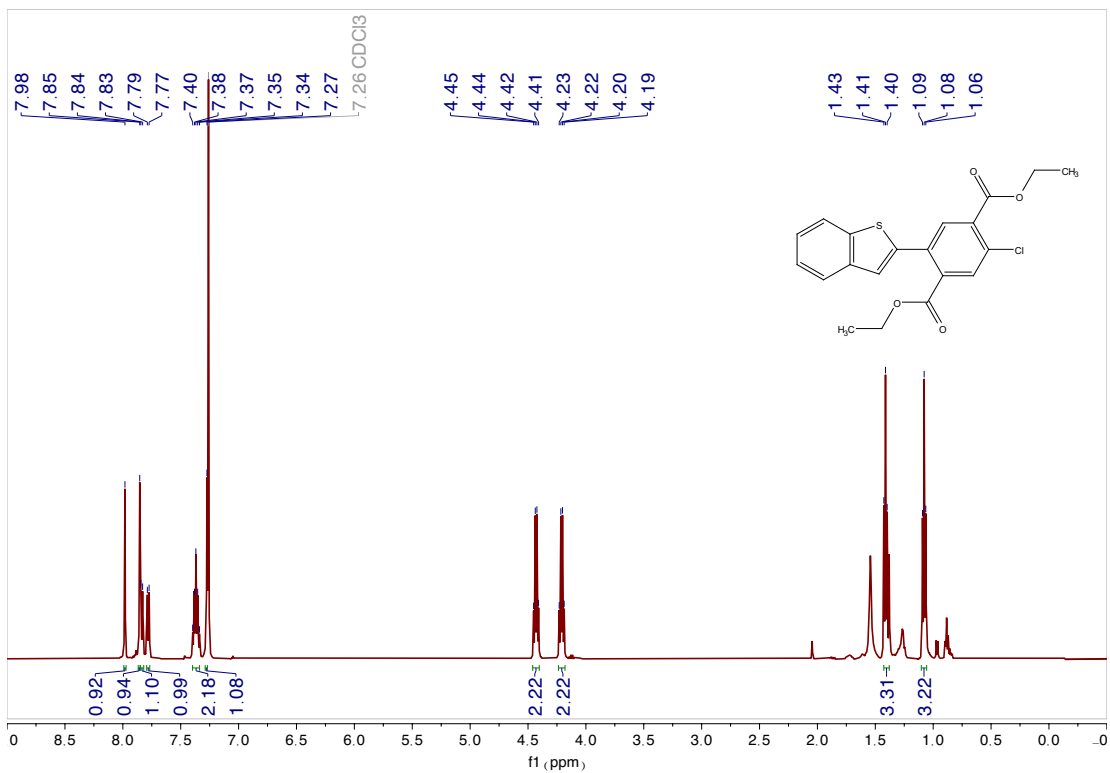
C	4.62633	1.77178	-2.11249
C	5.70493	1.90008	-2.99918
C	6.33382	0.75589	-3.52406
C	5.89072	-0.5286	-3.16776
O	3.08897	0.49765	0.75615
H	1.60564	-2.54019	0.34474
H	1.26938	-5.00266	0.60497
H	0.39331	-7.35938	1.30976
H	0.01382	-9.81404	1.6053
H	1.45079	-11.45666	0.4121
H	3.2869	-10.66639	-1.09297
H	5.08752	-5.84237	-2.54178
H	5.41185	-3.39411	-2.79241
H	4.13672	2.64599	-1.70397
H	6.05536	2.88442	-3.28118
H	7.16553	0.86641	-4.20772
H	6.38249	-1.39993	-3.57807

11. Copies of NMR Spectra

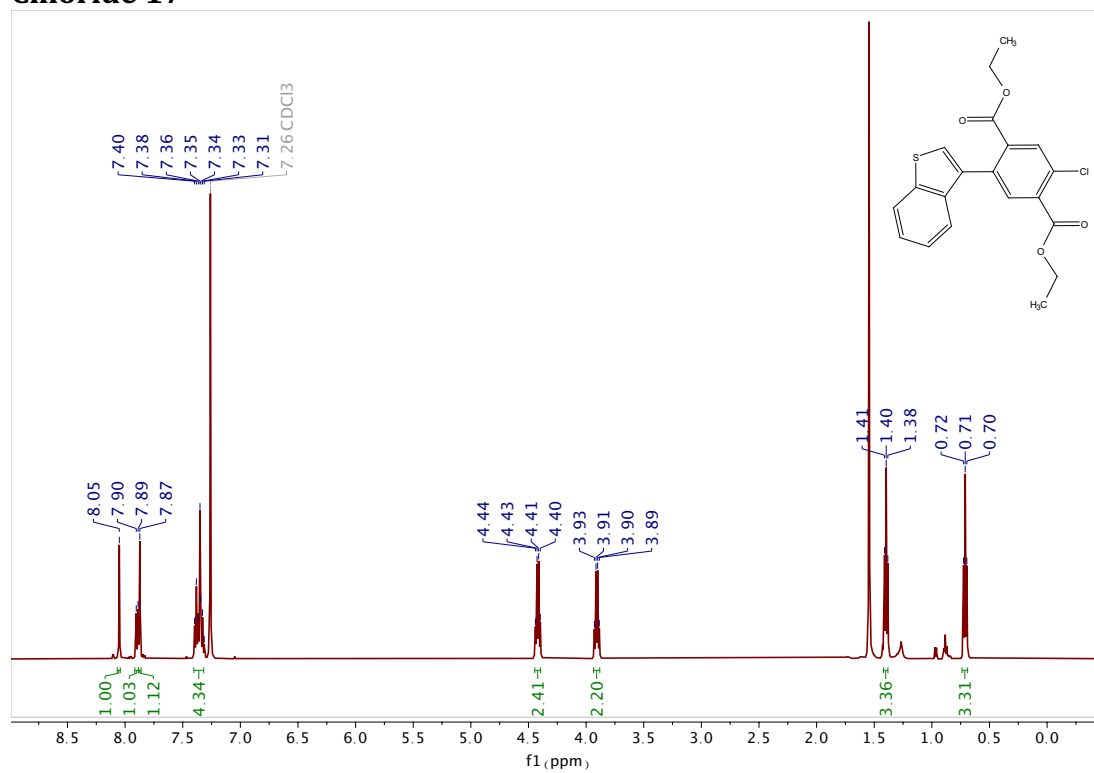
Diethyl 2-chloro-5-iodoterephthalate (15)

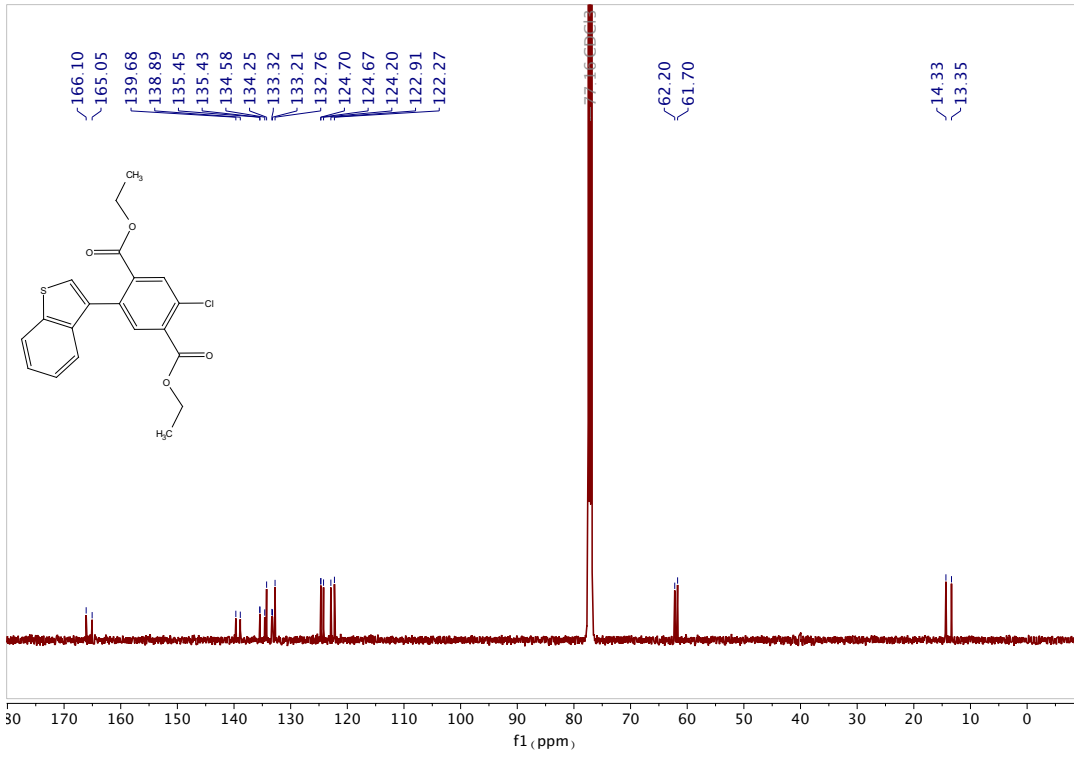


Chloride 16

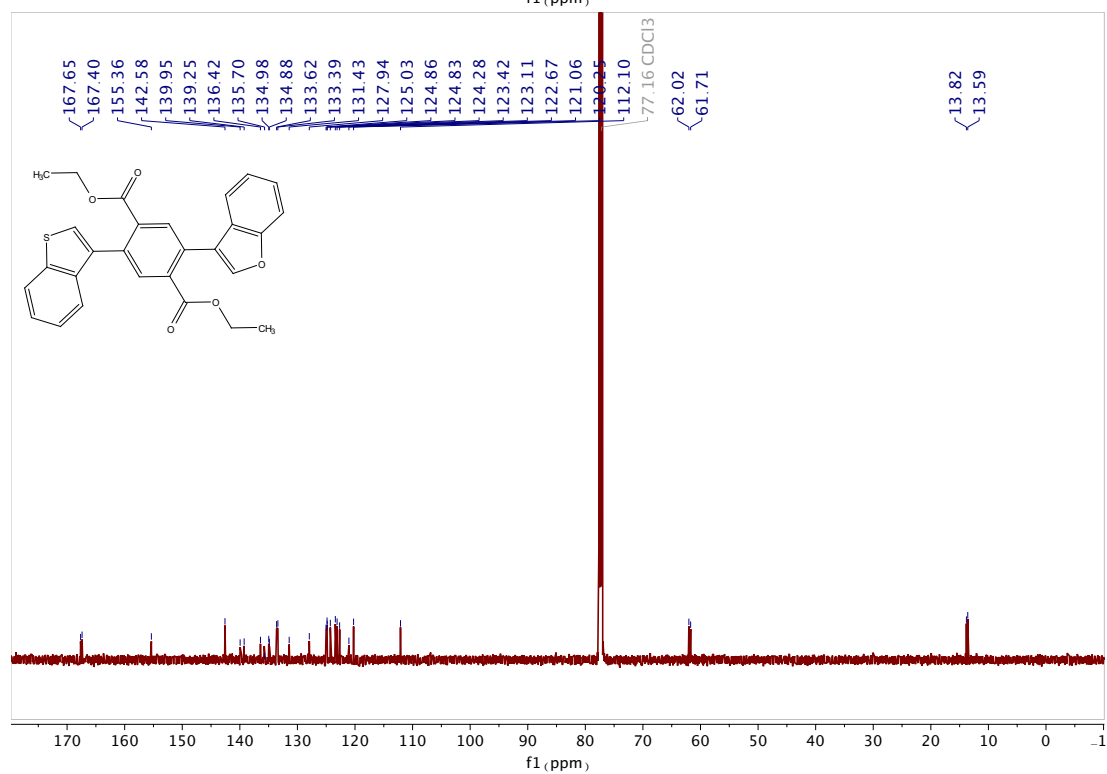
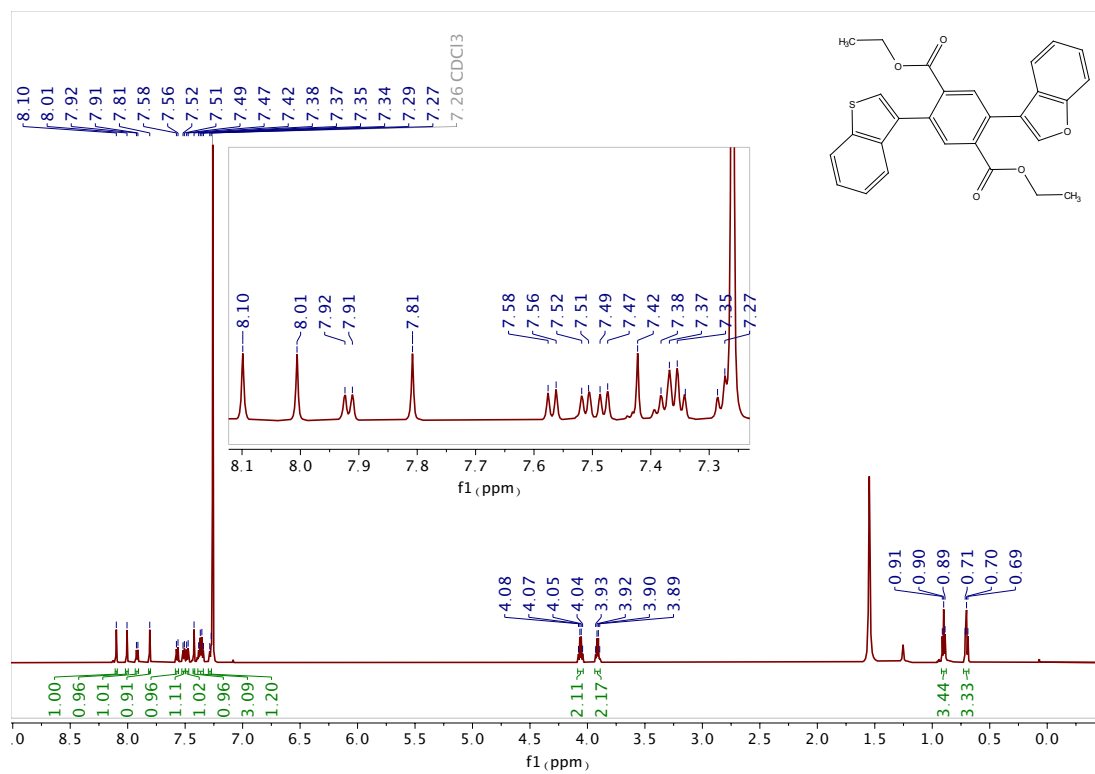


Chloride 17

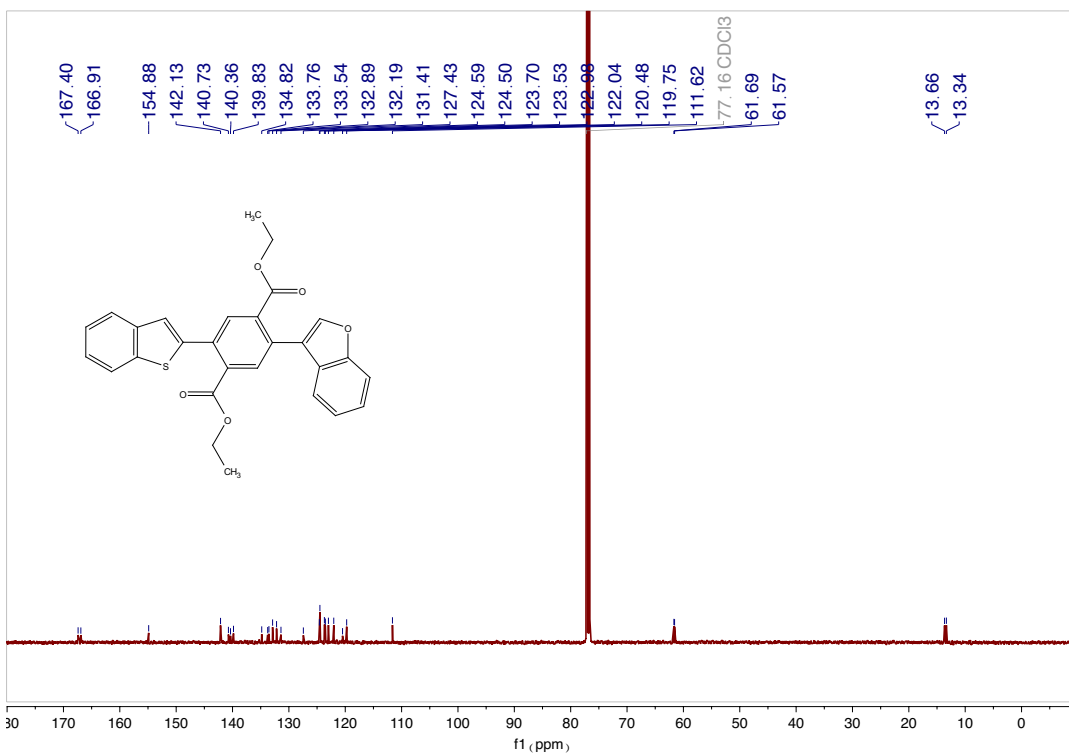
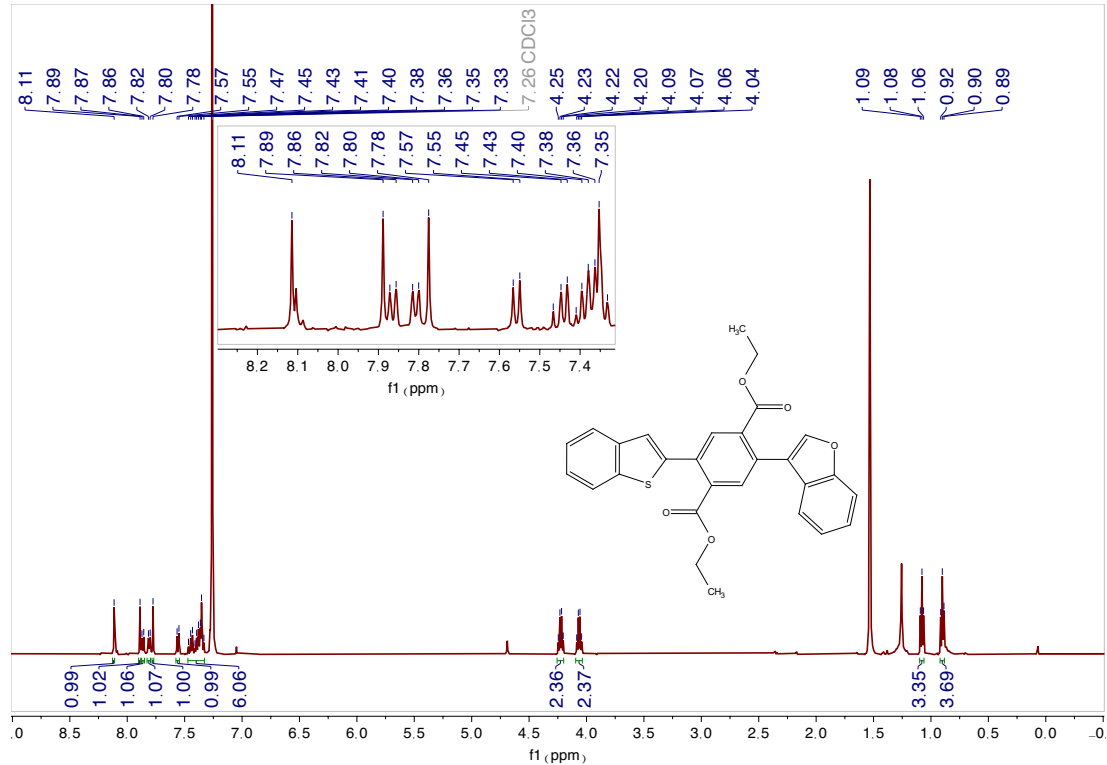




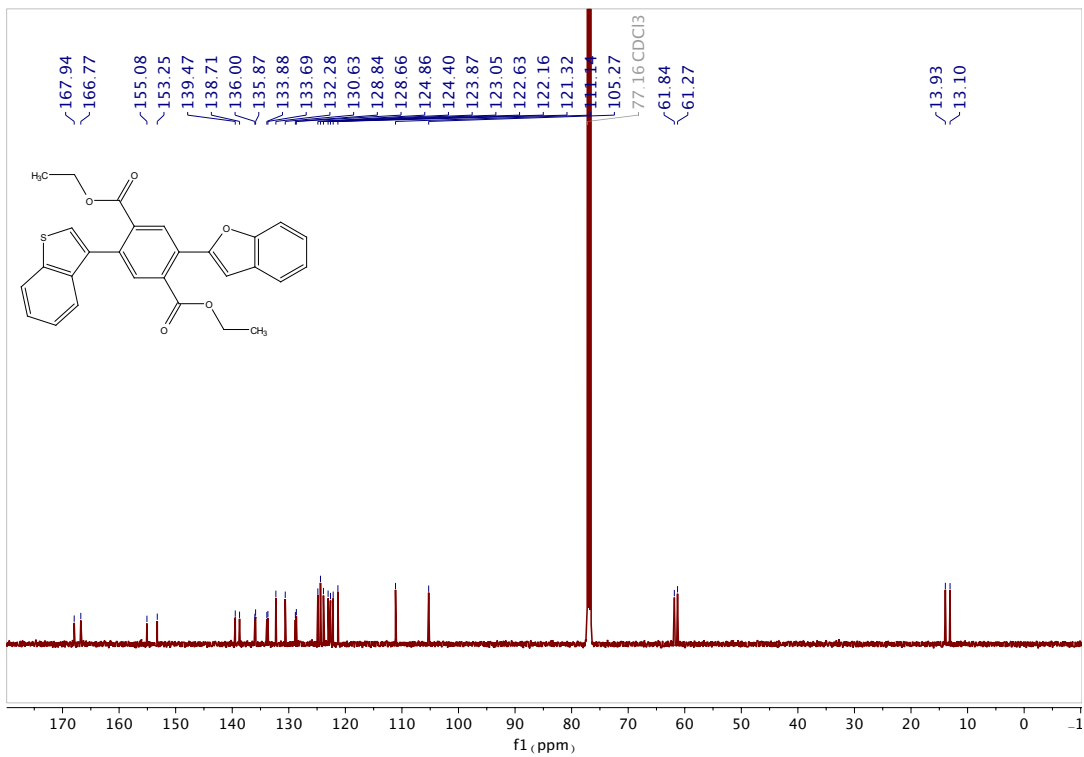
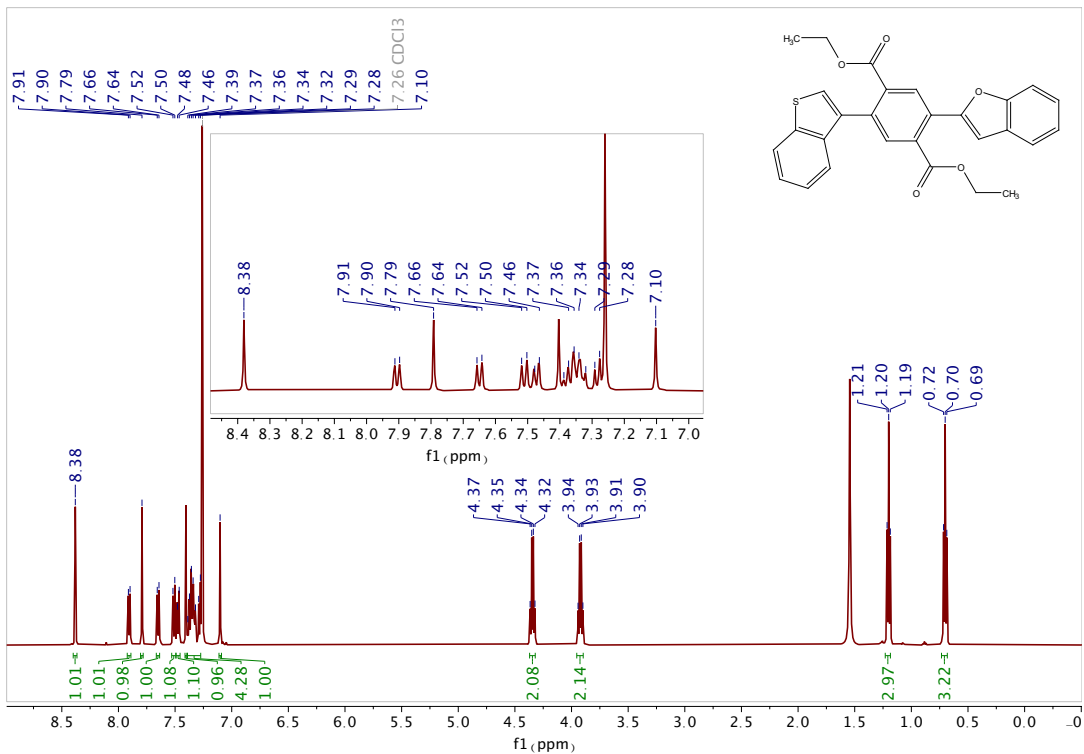
Diester 18



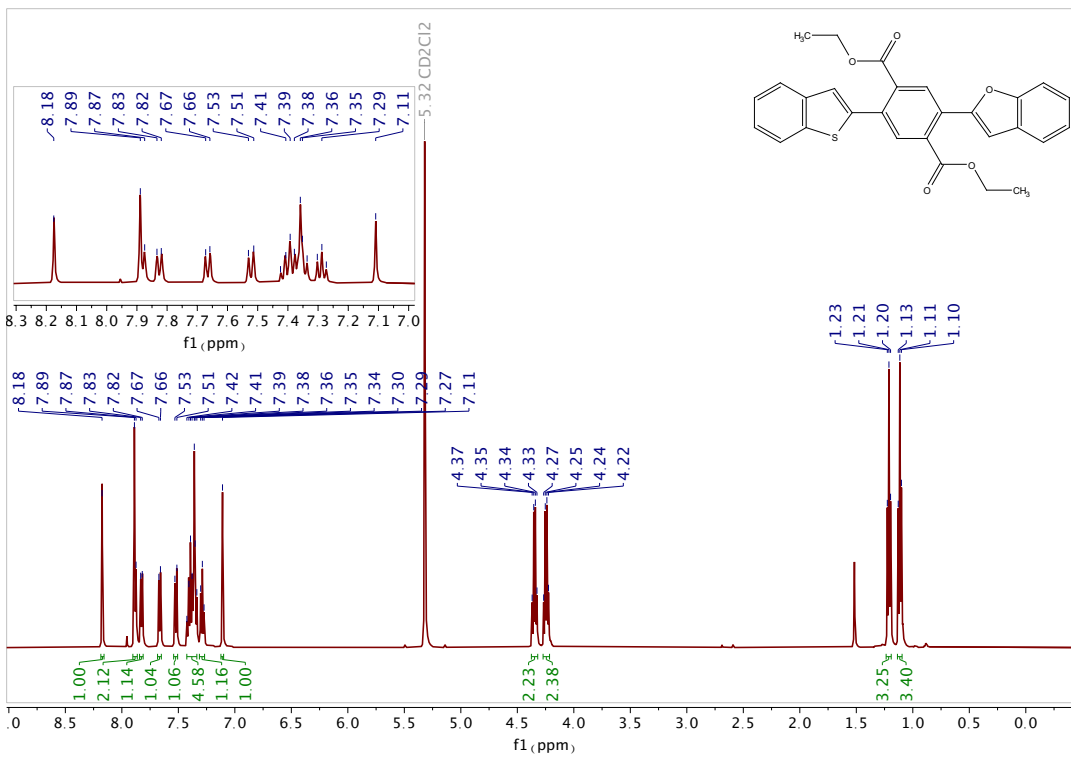
Diester 19

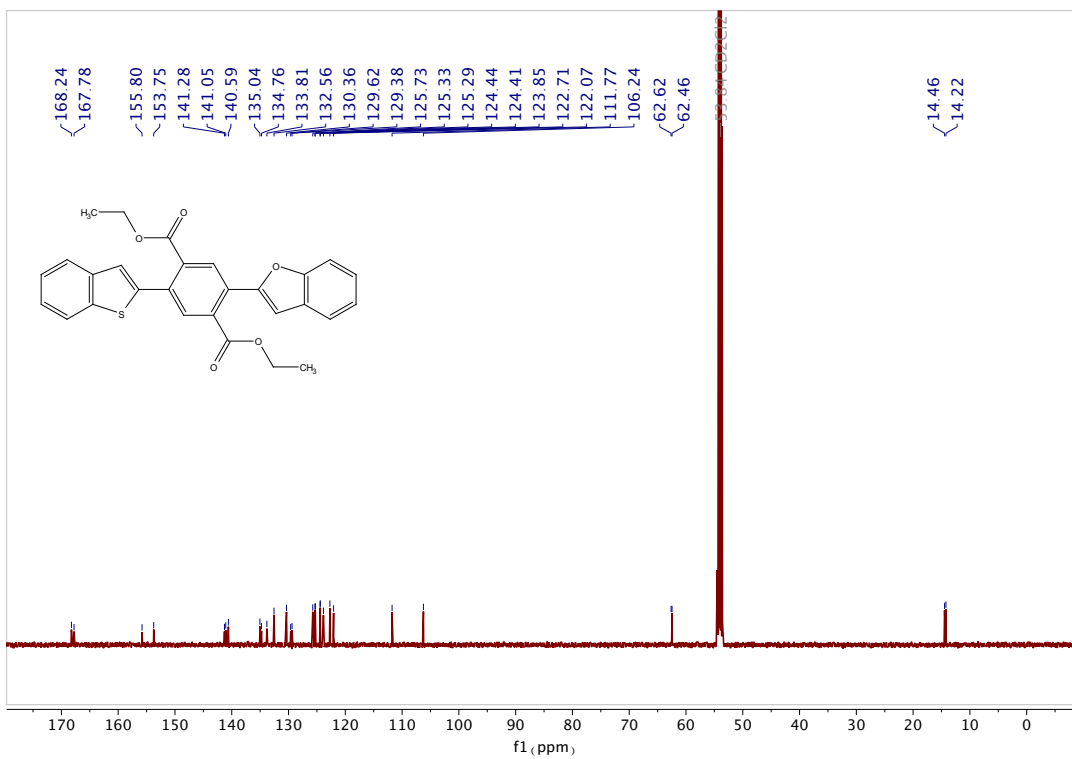


Diester 20

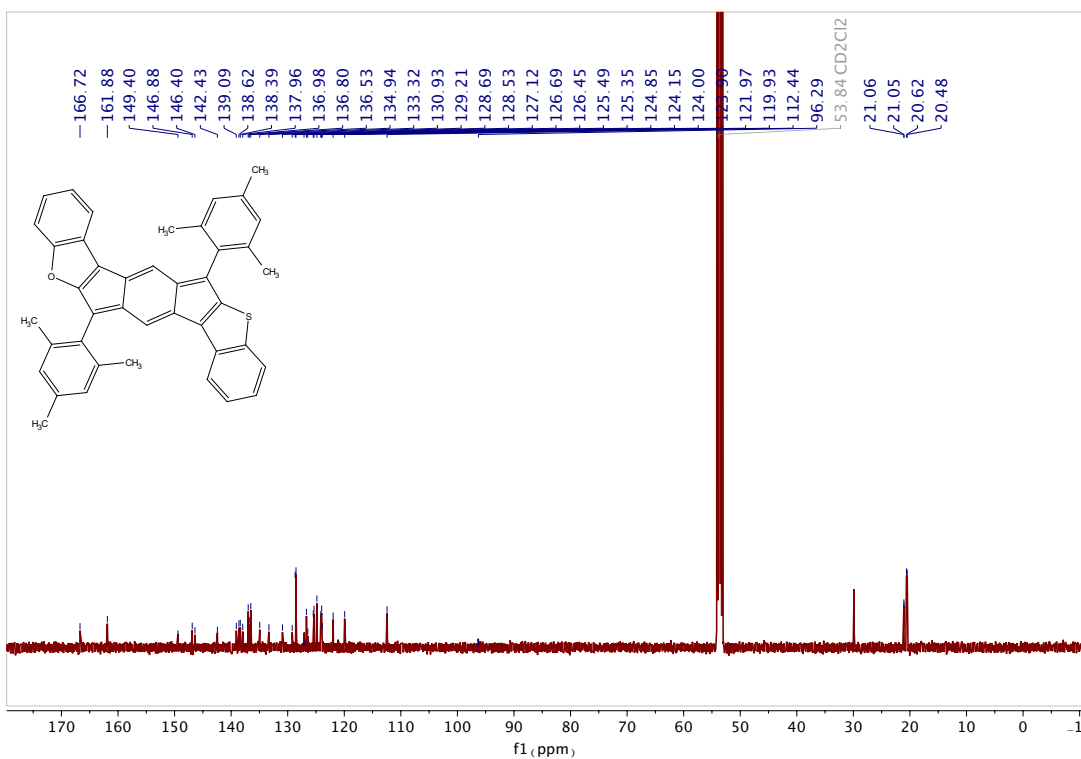
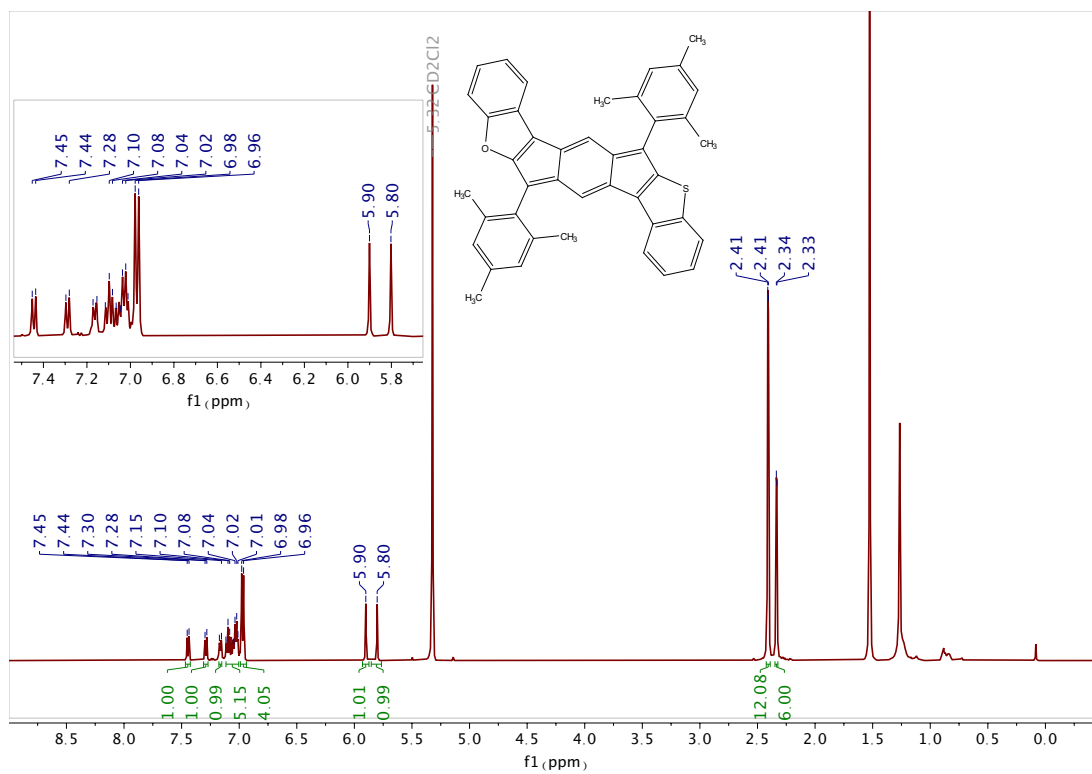


Diester 21

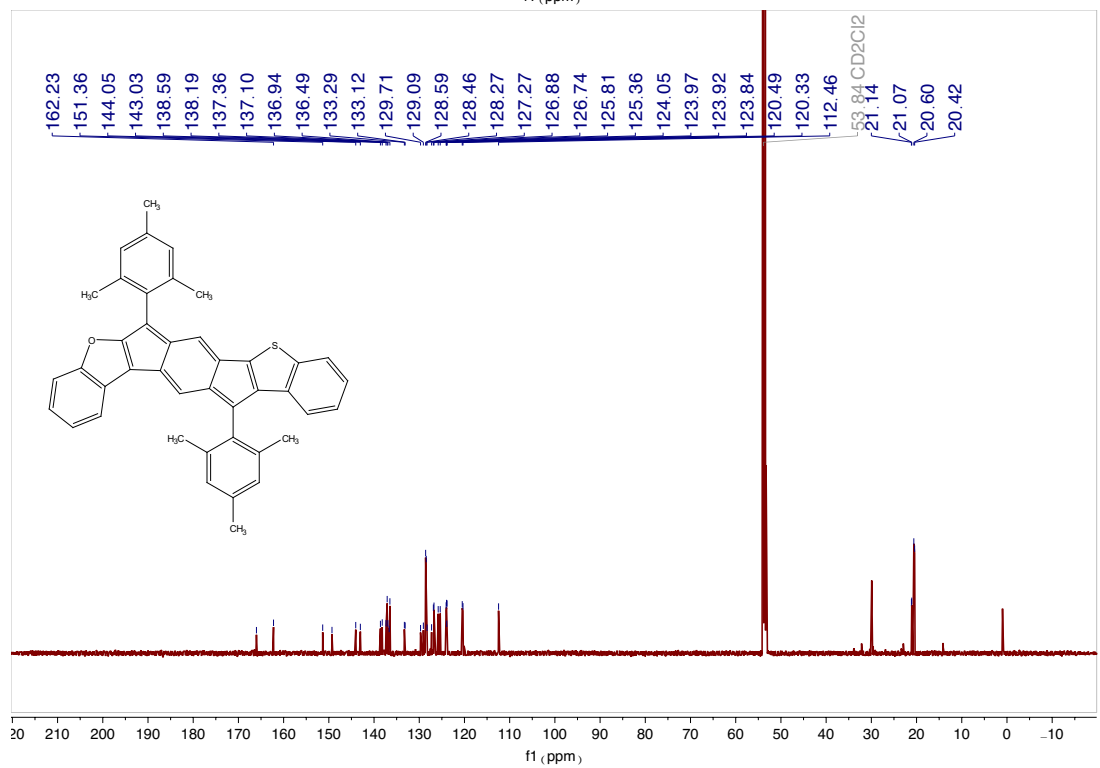
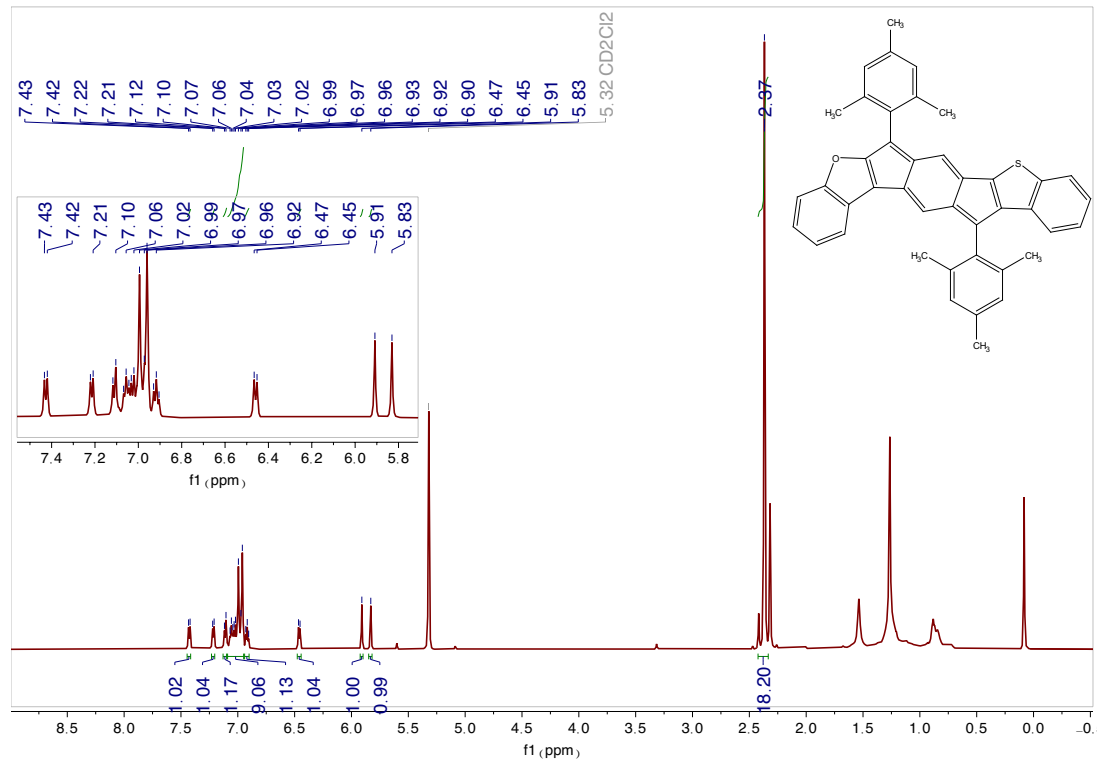




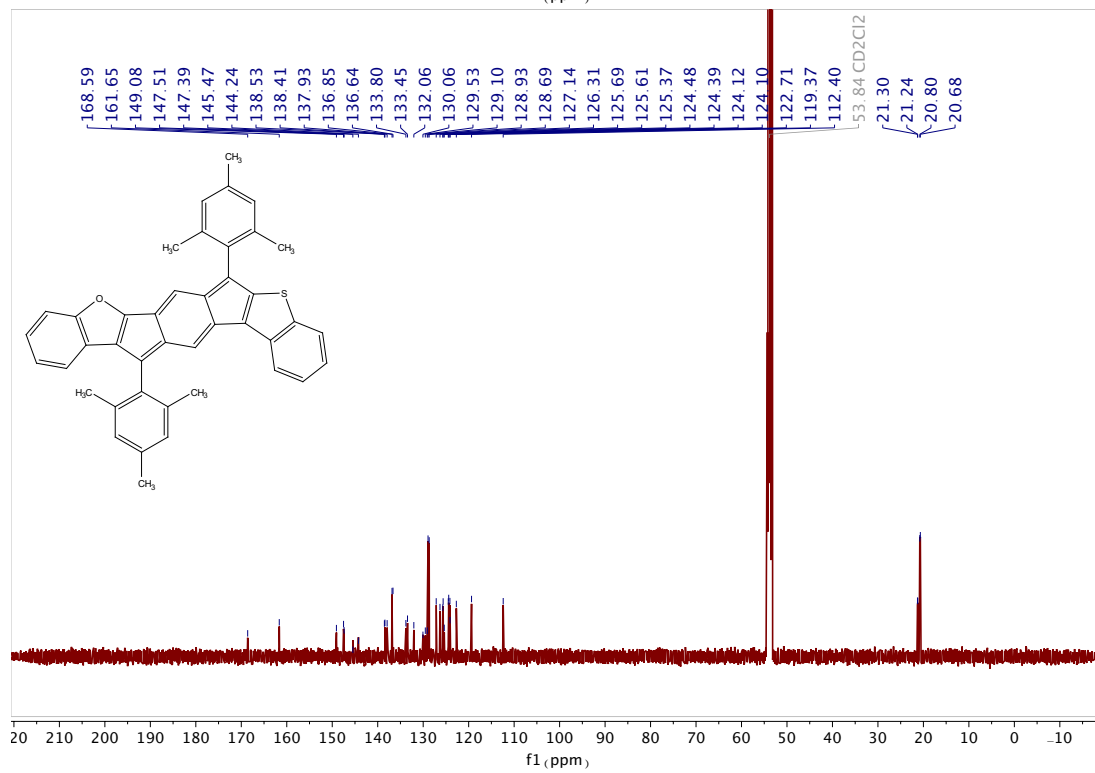
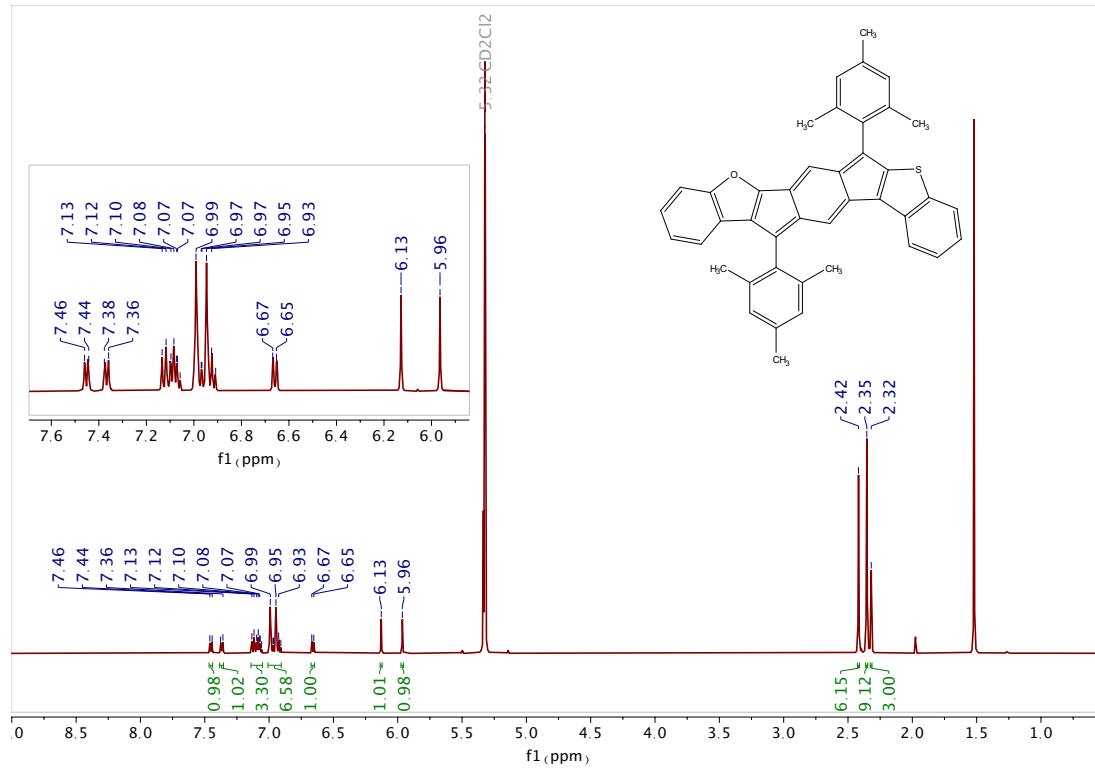
IBFBT 7



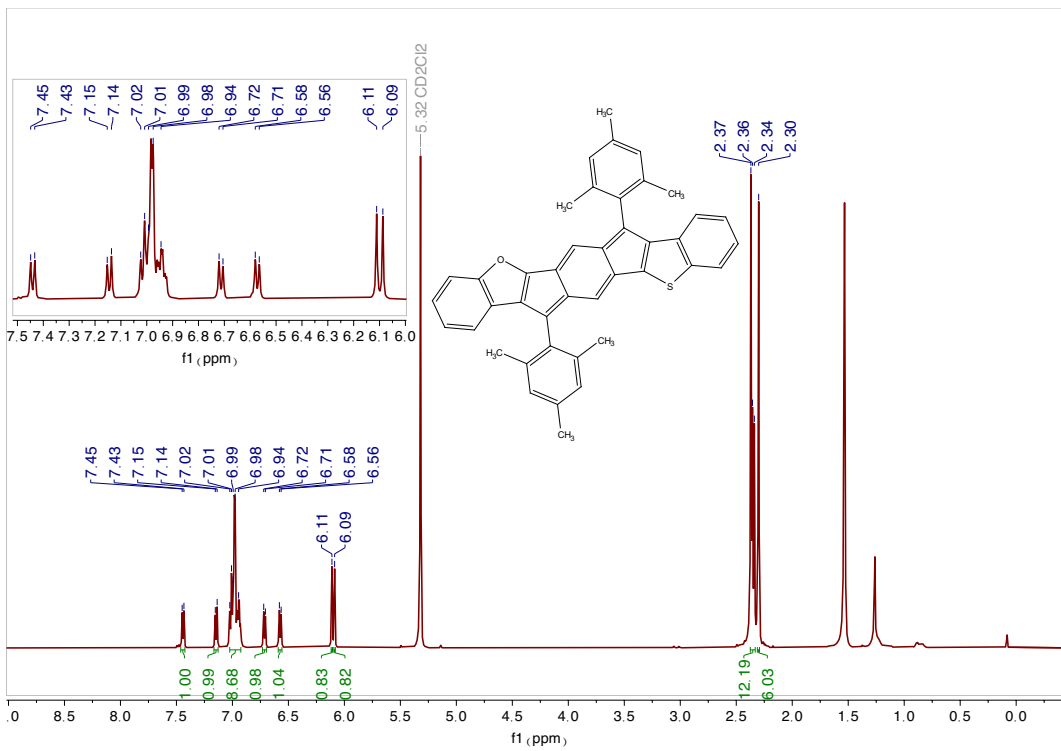
IBFBT 8

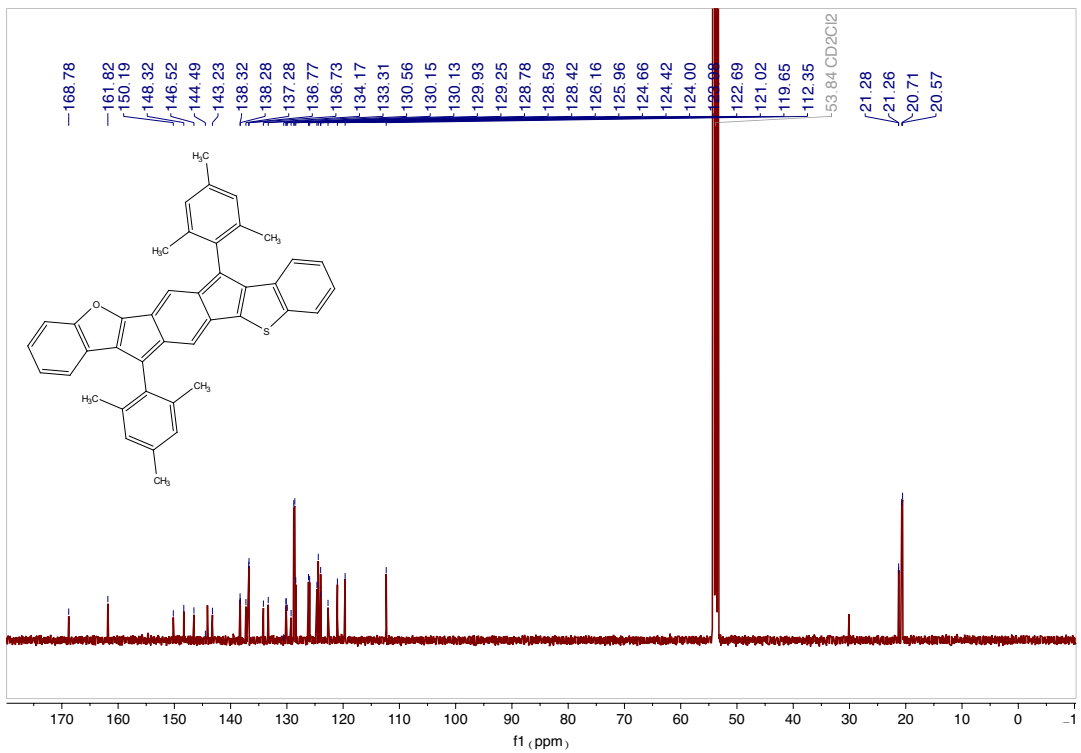


IBFBT 9

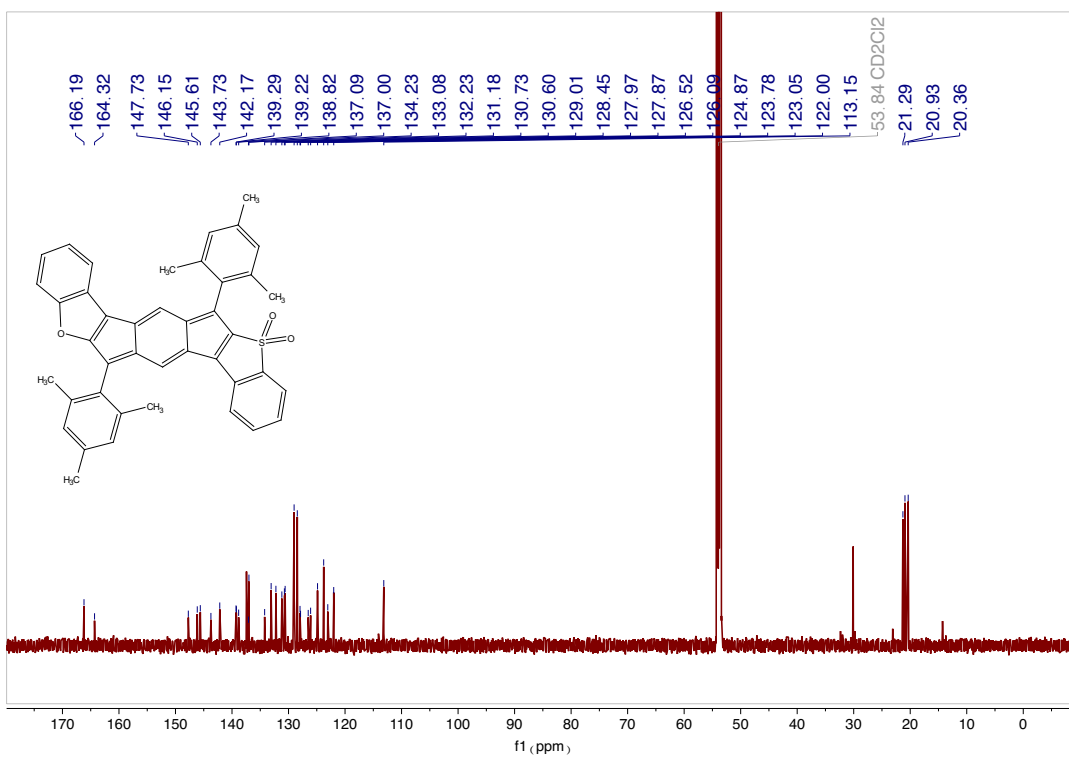
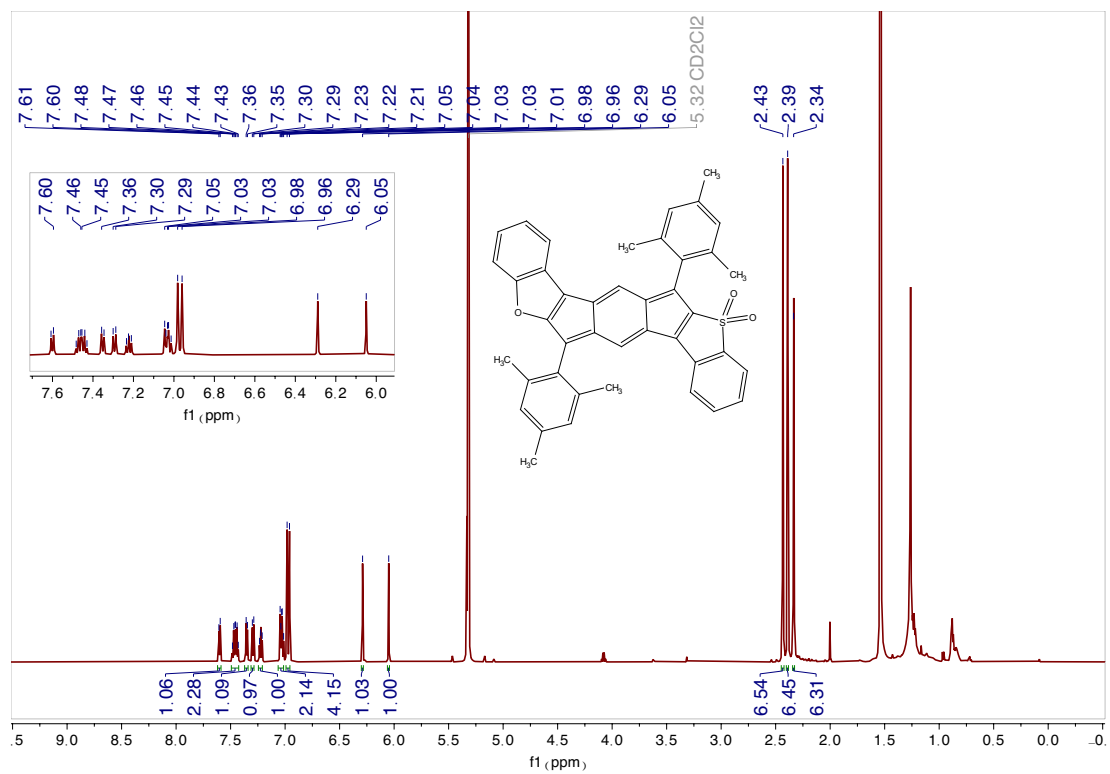


IBFBT 10

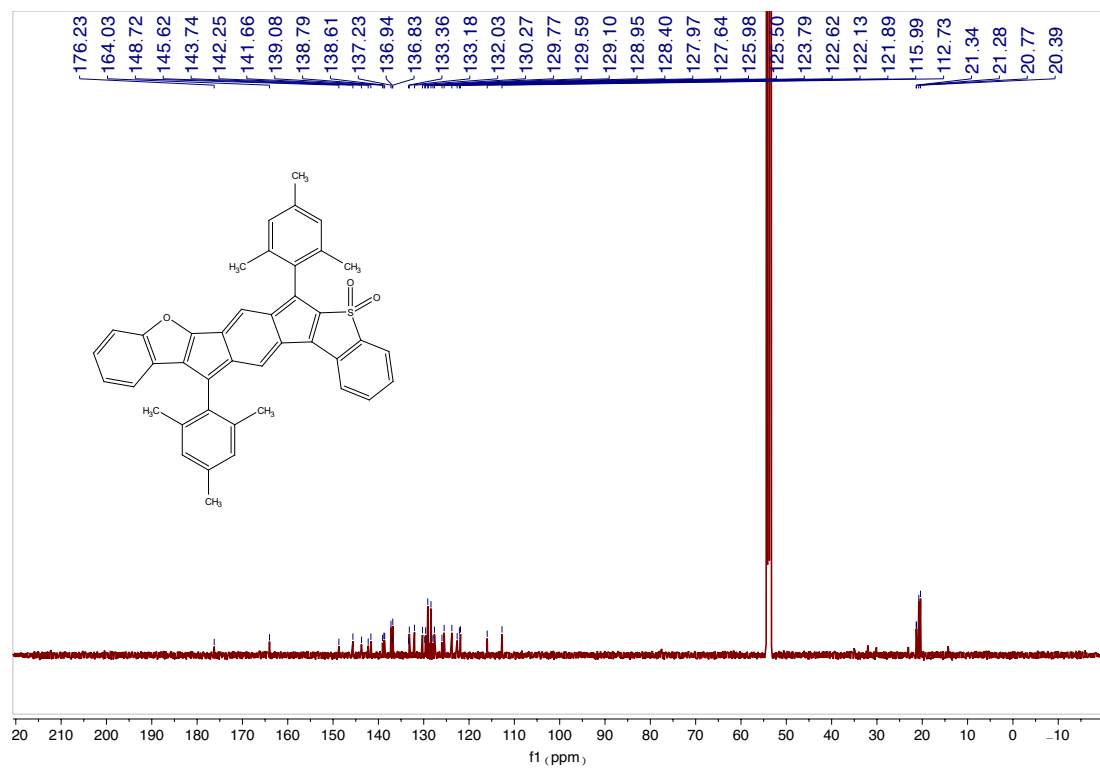
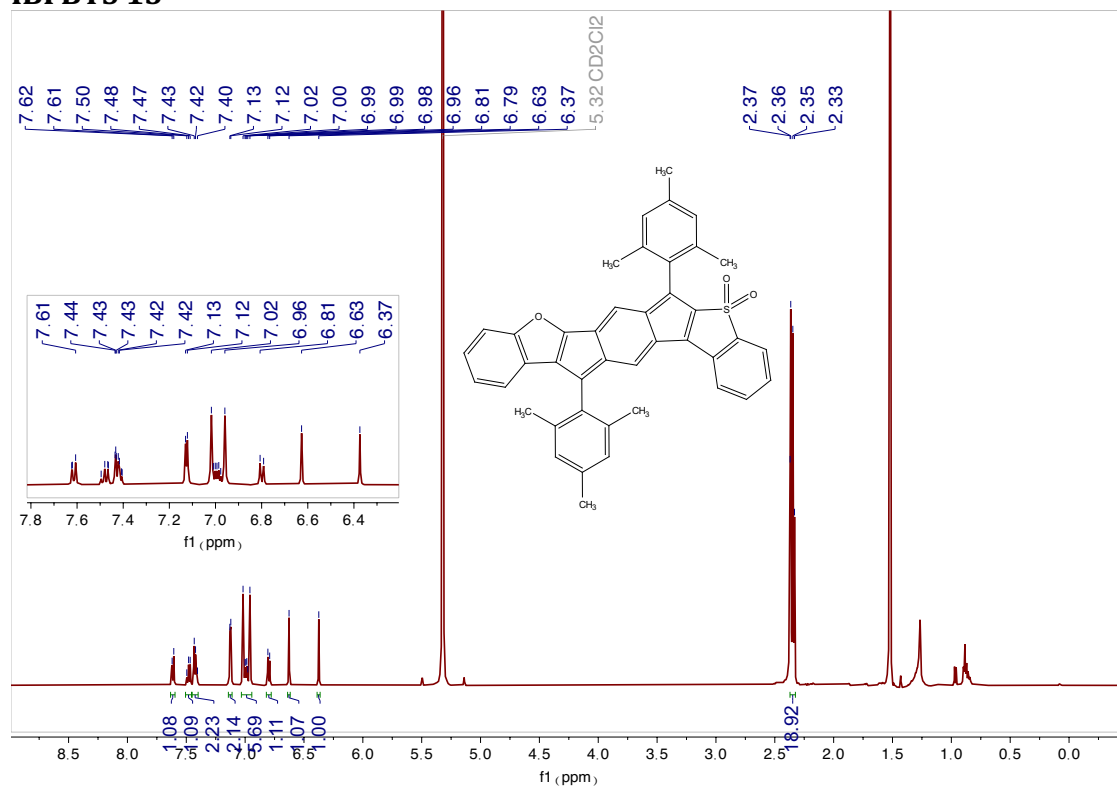




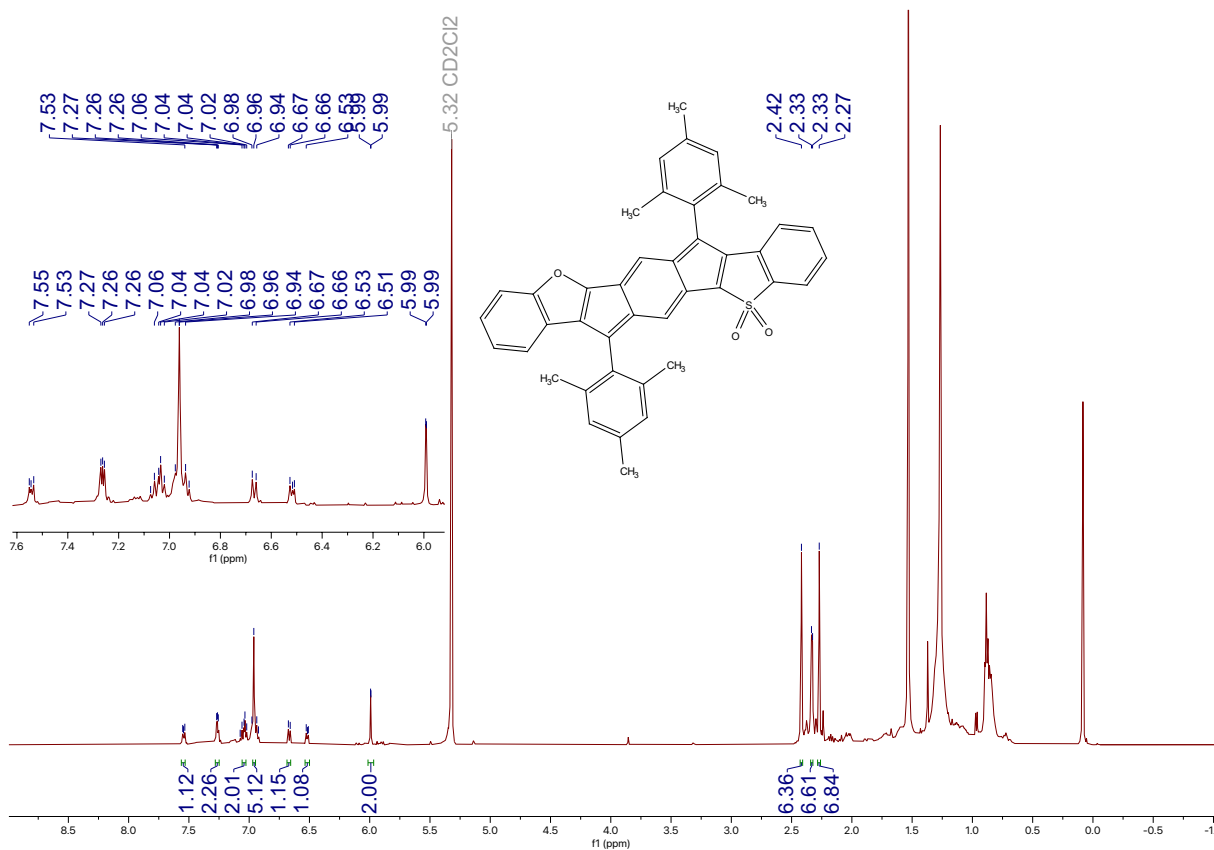
IBFBTS 11



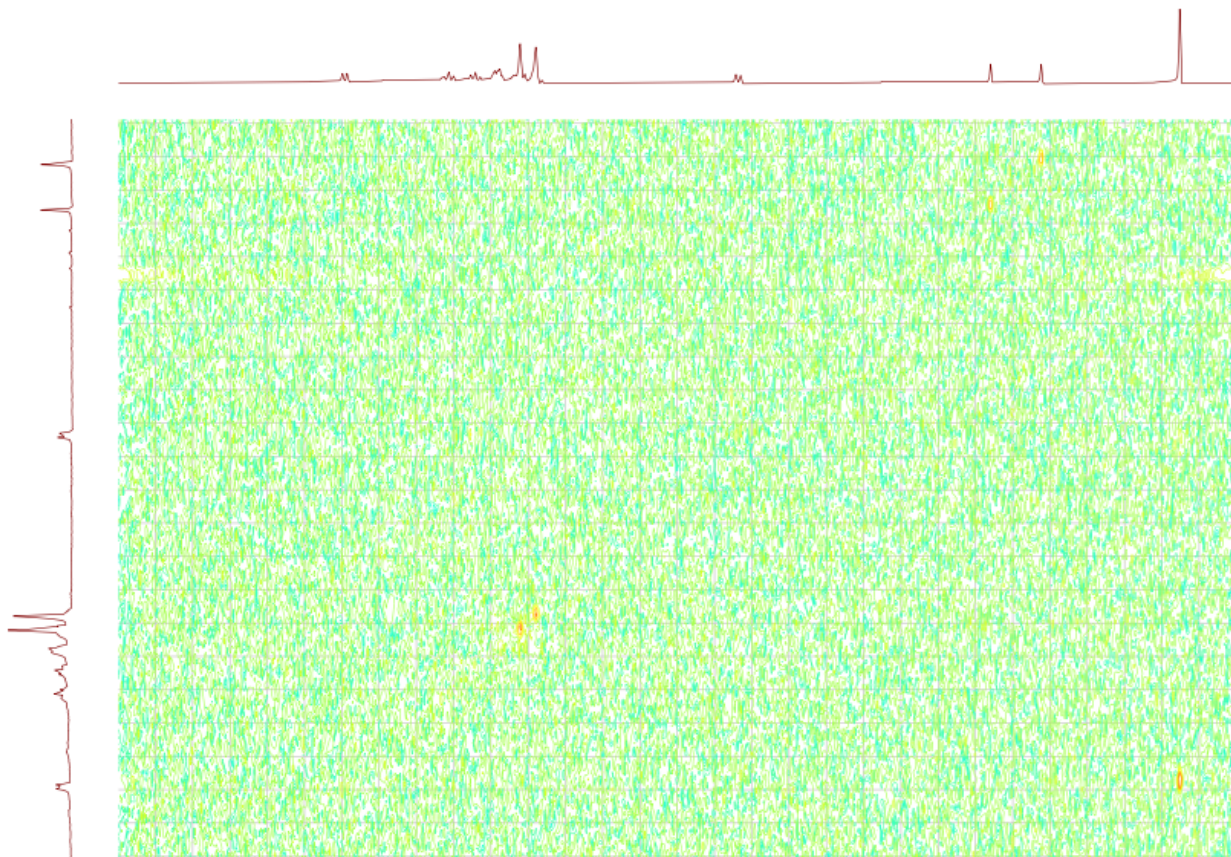
IBFBTS 13



IBFBTS 14



COSEY NMR of 12 in cyclohexane



REFERENCES CITED

- (1) Heisenberg, W. Zur Theorie der Supraleitung. In *Original Scientific Papers / Wissenschaftliche Originalarbeiten*; Blum, W., Dürr, H.-P., Rechenberg, H., Eds.; Springer Berlin Heidelberg: Berlin, Heidelberg, 1993; pp 28–44. https://doi.org/10.1007/978-3-642-70079-8_2.
- (2) London, F. On the Problem of the Molecular Theory of Superconductivity. *Phys. Rev.* **1948**, *74* (5), 562–573. <https://doi.org/10.1103/PhysRev.74.562>.
- (3) London, F. Théorie Quantique Des Courants Interatomiques Dans Les Combinaisons Aromatiques. *J. Phys. Radium* **1937**, *8* (10), 397–409. <https://doi.org/10.1051/jphysrad:01937008010039700>.
- (4) Shirakawa, H.; Louis, E. J.; MacDiarmid, A. G.; Chiang, C. K.; Heeger, A. J. Synthesis of Electrically Conducting Organic Polymers: Halogen Derivatives of Polyacetylene, (CH) x. *J. Chem. Soc. Chem. Commun.* **1977**, No. 16, 578. <https://doi.org/10.1039/c39770000578>.
- (5) Nezakati, T.; Seifalian, A.; Tan, A.; Seifalian, A. M. Conductive Polymers: Opportunities and Challenges in Biomedical Applications. *Chem. Rev.* **2018**, *118* (14), 6766–6843. <https://doi.org/10.1021/acs.chemrev.6b00275>.
- (6) K, N.; Rout, C. S. Correction: Conducting Polymers: A Comprehensive Review on Recent Advances in Synthesis, Properties and Applications. *RSC Adv.* **2024**, *14* (25), 17467–17470. <https://doi.org/10.1039/D4RA90058H>.
- (7) K, N.; Rout, C. S. Conducting Polymers: A Comprehensive Review on Recent Advances in Synthesis, Properties and Applications. *RSC Adv.* **2021**, *11* (10), 5659–5697. <https://doi.org/10.1039/D0RA07800J>.
- (8) Little, W. A. Possibility of Synthesizing an Organic Superconductor. *Phys. Rev.* **1964**, *134* (6A), A1416–A1424. <https://doi.org/10.1103/PhysRev.134.A1416>.
- (9) Ai, Q.; Bhat, V.; Ryno, S. M.; Jarolimek, K.; Sornberger, P.; Smith, A.; Haley, M. M.; Anthony, J. E.; Risko, C. OCELOT: An Infrastructure for Data-Driven Research to Discover and Design Crystalline Organic Semiconductors. *J. Chem. Phys.* **2021**, *154* (17), 174705. <https://doi.org/10.1063/5.0048714>.
- (10) Melby, L. R.; Harder, R. J.; Hertler, W. R.; Mahler, W.; Benson, R. E.; Mochel, W. E. **Substituted Quinodimethans. II. Anion-Radical Derivatives and Complexes of 7,7,8,8-Tetracyanoquinodimethan.** *J. Am. Chem. Soc.* **1962**, *84* (17), 3374–3387. <https://doi.org/10.1021/ja00876a029>.
- (11) Poehler, T. O. Organic Conductors. *APL Tech. Dig.* **1976**, *15* (4), 13–21.
- (12) Bloch, A. N.; Cowan, D. O.; Bechgaard, K.; Pyle, R. E.; Banks, R. H.; Poehler, T. O. Low-Temperature Metallic Behavior and Resistance Minimum in a New Quasi One-Dimensional Organic Conductor. *Phys. Rev. Lett.* **1975**, *34* (25), 1561–1564. <https://doi.org/10.1103/PhysRevLett.34.1561>.
- (13) Dong, S.; Xiang, H.; Dagotto, E. Magnetoelectricity in Multiferroics: A Theoretical Perspective. *Natl. Sci. Rev.* **2019**, *6* (4), 629–641. <https://doi.org/10.1093/nsr/nwz023>.
- (14) Moore, J. E. The Birth of Topological Insulators. *Nature* **2010**, *464* (7286), 194–198. <https://doi.org/10.1038/nature08916>.
- (15) Pizzi, R. A. This Icon of Modern Physics Was, in Reality, a Chemist by Training and Profession. *Today's Chem. Work* **2004**.

- (16) *Electromagnetism - Induction, Faraday, Magnetism / Britannica*. <https://www.britannica.com/science/electromagnetism/Faradays-discovery-of-electric-induction> (accessed 2025-02-08).
- (17) XX. On New Compounds of Carbon and Hydrogen, and on Certain Other Products Obtained during the Decomposition of Oil by Heat. *Philos. Trans. R. Soc. Lond.* **1825**, *115*, 440–466. <https://doi.org/10.1098/rstl.1825.0022>.
- (18) Robinson, A. Chemistry's Visual Origins. *Nature* **2010**, *465* (7294), 36–36. <https://doi.org/10.1038/465036a>.
- (19) Hückel, E. Quantentheoretische Beiträge zum Benzolproblem: I. Die Elektronenkonfiguration des Benzols und verwandter Verbindungen. *Z. Für Phys.* **1931**, *70* (3–4), 204–286. <https://doi.org/10.1007/BF01339530>.
- (20) Dewar, M. J. S. The Determination of Resonance Energies from Thermal Data. *Trans. Faraday Soc.* **1946**, *42*, 767. <https://doi.org/10.1039/tf9464200767>.
- (21) Pople, J. A. Molecular Orbital Theory of Aromatic Ring Currents. *Mol. Phys.* **1958**, *1* (2), 175–180. <https://doi.org/10.1080/00268975800100211>.
- (22) Schleyer, P. V. R. Introduction: Aromaticity. *Chem. Rev.* **2001**, *101* (5), 1115–1118. <https://doi.org/10.1021/cr0103221>.
- (23) Labes, M. M. Conductivity in Polymeric Solids. *Pure Appl. Chem.* **1966**, *12* (1–4), 275–286. <https://doi.org/10.1351/pac196612010275>.
- (24) Breslow, R. Aromatic Character: One Hundred Years after Kekulé, Chemists Are Still Trying to Understand Aromatic Character. Modern Techniques and the Increasing Application of Quantum Mechanics to Organic Chemistry Have Led to the Preparation of Many New Aromatic Systems and to a Deeper Understanding of Conjugated Systems Generally. *Chem. Eng. News Arch.* **1965**, *43* (26), 90–100. <https://doi.org/10.1021/cen-v043n026.p090>.
- (25) Breslow, R. Antiaromaticity. *Acc. Chem. Res.* **1973**, *6* (12), 393–398. <https://doi.org/10.1021/ar50072a001>.
- (26) Breslow, Ronald.; Murayama, D. R.; Murahashi, Shunichi.; Grubbs, Robert. Quantitative Assessment of the Antiaromatic City of Cyclobutadiene by Electrochemical Studies on Quinone Derivatives. *J. Am. Chem. Soc.* **1973**, *95* (20), 6688–6699. <https://doi.org/10.1021/ja00801a027>.
- (27) Breslow, R. Quantitative Studies on Aromaticity and Antiaromaticity. *Pure Appl. Chem.* **1971**, *28* (2–3), 111–130. <https://doi.org/10.1351/pac197128020111>.
- (28) Goldstein, H. *Classical Mechanics*, 2d ed.; Addison-Wesley series in physics; Addison-Wesley Pub. Co: Reading, Mass, 1980.
- (29) Brophy, J. J. *Basic Electronics for Scientists*, 2. ed.; McGraw-Hill: New York Düsseldorf, 1972.
- (30) Gershoni-Poranne, R.; Stanger, A. Magnetic Criteria of Aromaticity. *Chem Soc Rev* **2015**, *44* (18), 6597–6615. <https://doi.org/10.1039/C5CS00114E>.
- (31) Dewar, M. J. S. The Determination of Resonance Energies from Thermal Data. *Trans. Faraday Soc.* **1946**, *42*, 767. <https://doi.org/10.1039/tf9464200767>.
- (32) Charistos, N. D.; Papadopoulos, A. G.; Sigalas, M. P. Interpretation of Electron Delocalization in Benzene, Cyclobutadiene, and Borazine Based on Visualization of Individual Molecular Orbital Contributions to the Induced Magnetic Field. *J. Phys. Chem. A* **2014**, *118* (6), 1113–1122. <https://doi.org/10.1021/jp411410r>.

- (33) Schmidt, M.; Abellán Vicente, L.; González, M. T.; Zotti, L. A.; Esser, B.; Leary, E. Low-lying LUMO Boosts Conductance in Antiaromatic Dibenzopentalene Versus Aromatic Analogues. *Chem. – Eur. J.* **2024**, *30* (40), e202400935. <https://doi.org/10.1002/chem.202400935>.
- (34) Schneebeli, S. T.; Kamenetska, M.; Cheng, Z.; Skouta, R.; Friesner, R. A.; Venkataraman, L.; Breslow, R. Single-Molecule Conductance through Multiple Π - π -Stacked Benzene Rings Determined with Direct Electrode-to-Benzene Ring Connections. *J. Am. Chem. Soc.* **2011**, *133* (7), 2136–2139. <https://doi.org/10.1021/ja111320n>.
- (35) Wang, C.; Wei, Y.; Chang, K.; Chou, P.; Wu, Y. Indeno[1,2- *b*]fluorene-Based [2,2]Cyclophanes with $4n/4n$ and $4n/[4n+2]$ π Electrons: Syntheses, Structural Analyses, and Excitonic Coupling Properties. *Angew. Chem. Int. Ed.* **2019**, *58* (30), 10158–10162. <https://doi.org/10.1002/anie.201903561>.
- (36) Zeidell, A. M.; Jennings, L.; Frederickson, C. K.; Ai, Q.; Dressler, J. J.; Zakharov, L. N.; Risko, C.; Haley, M. M.; Jurchescu, O. D. Organic Semiconductors Derived from Dinaphtho-Fused *s*-Indacenes: How Molecular Structure and Film Morphology Influence Thin-Film Transistor Performance. *Chem. Mater.* **2019**, *31* (17), 6962–6970. <https://doi.org/10.1021/acs.chemmater.9b01436>.
- (37) Quinn, J. R.; Foss, F. W.; Venkataraman, L.; Breslow, R. Oxidation Potentials Correlate with Conductivities of Aromatic Molecular Wires. *J. Am. Chem. Soc.* **2007**, *129* (41), 12376–12377. <https://doi.org/10.1021/ja0745097>.
- (38) Chen, W.; Li, H.; Widawsky, J. R.; Appayee, C.; Venkataraman, L.; Breslow, R. Aromaticity Decreases Single-Molecule Junction Conductance. *J. Am. Chem. Soc.* **2014**, *136* (3), 918–920. <https://doi.org/10.1021/ja411143s>.
- (39) Schneebeli, S.; Kamenetska, M.; Foss, F.; Vazquez, H.; Skouta, R.; Hybertsen, M.; Venkataraman, L.; Breslow, R. The Electrical Properties of Biphenylenes. *Org. Lett.* **2010**, *12* (18), 4114–4117. <https://doi.org/10.1021/ol1017036>.
- (40) Frederickson, C. K.; Zakharov, L. N.; Haley, M. M. Modulating Paratropicity Strength in Diareno-Fused Antiaromatics. *J. Am. Chem. Soc.* **2016**, *138* (51), 16827–16838. <https://doi.org/10.1021/jacs.6b11397>.
- (41) Demuth, M. C.; Hendon, C. H. Linker Aromaticity Reduces Band Dispersion in 2D Conductive Metal–Organic Frameworks. *ACS Mater. Lett.* **2023**, *5* (5), 1476–1480. <https://doi.org/10.1021/acsmaterialslett.3c00122>.
- (42) Park, G.; Demuth, M. C.; Hendon, C. H.; Park, S. S. Acid-Dependent Charge Transport in a Solution-Processed 2D Conductive Metal–Organic Framework. *J. Am. Chem. Soc.* **2024**, *jacs.4c02326*. <https://doi.org/10.1021/jacs.4c02326>.
- (43) Hendon, C. H.; Tiana, D.; Walsh, A. Conductive Metal–Organic Frameworks and Networks: Fact or Fantasy? *Phys. Chem. Chem. Phys.* **2012**, *14* (38), 13120. <https://doi.org/10.1039/c2cp41099k>.
- (44) Skorupskii, G.; Chanteux, G.; Le, K. N.; Stassen, I.; Hendon, C. H.; Dincă, M. Electrical Conductivity through π - π Stacking in a Two-dimensional Porous Gallium Catecholate Metal–Organic Framework. *Ann. N. Y. Acad. Sci.* **2022**, *1518* (1), 226–230. <https://doi.org/10.1111/nyas.14906>.
- (45) Apostol, P.; Gali, S. M.; Su, A.; Tie, D.; Zhang, Y.; Pal, S.; Lin, X.; Bakuru, V. R.; Rambabu, D.; Beljonne, D.; Dincă, M.; Vlad, A. Controlling Charge Transport in 2D Conductive

- MOFs—The Role of Nitrogen-Rich Ligands and Chemical Functionality. *J. Am. Chem. Soc.* **2023**, jacs.3c07503. <https://doi.org/10.1021/jacs.3c07503>.
- (46) Kadota, K.; Chen, T.; Gormley, E. L.; Hendon, C. H.; Dincă, M.; Brozek, C. K. Electrically Conductive [Fe₄ S₄]-Based Organometallic Polymers. *Chem. Sci.* **2023**, *14* (41), 11410–11416. <https://doi.org/10.1039/D3SC02195E>.
- (47) Skorupskii, G.; Le, K. N.; Cordova, D. L. M.; Yang, L.; Chen, T.; Hendon, C. H.; Arguilla, M. Q.; Dincă, M. Porous Lanthanide Metal–Organic Frameworks with Metallic Conductivity. *Proc. Natl. Acad. Sci.* **2022**, *119* (34), e2205127119. <https://doi.org/10.1073/pnas.2205127119>.
- (48) Chen, T.; Dou, J.-H.; Yang, L.; Sun, C.; Oppenheim, J. J.; Li, J.; Dincă, M. Dimensionality Modulates Electrical Conductivity in Compositionally Constant One-, Two-, and Three-Dimensional Frameworks. *J. Am. Chem. Soc.* **2022**, *144* (12), 5583–5593. <https://doi.org/10.1021/jacs.2c00614>.
- (49) Bajaj, A.; Ali, Md. E. Anti-Ohmic Nanoconductors: Myth, Reality and Promise. *Phys. Chem. Chem. Phys.* **2023**, *25* (13), 9607–9616. <https://doi.org/10.1039/D3CP00366C>.
- (50) Lawson, B.; Vidal, E.; Luna, S.; Haley, M. M.; Kamenetska, M. Extreme Anomalous Conductance Enhancement in Neutral Diradical Acene-like Molecular Junctions. *ACS Nano* **2024**, *18* (42), 29059–29066. <https://doi.org/10.1021/acsnano.4c10183>.
- (51) Schmidt, M.; Wassy, D.; Hermann, M.; González, M. T.; Agrait, N.; Zotti, L. A.; Esser, B.; Leary, E. Single-Molecule Conductance of Dibenzopentalenes: Antiaromaticity and Quantum Interference. *Chem. Commun.* **2021**, *57* (6), 745–748. <https://doi.org/10.1039/D0CC06810A>.
- (52) Ji, L.; Shi, J.; Wei, J.; Yu, T.; Huang, W. Air-Stable Organic Radicals: New-Generation Materials for Flexible Electronics? *Adv. Mater.* **2020**, *32* (32), 1908015. <https://doi.org/10.1002/adma.201908015>.
- (53) *The IUPAC Compendium of Chemical Terminology: The Gold Book*, 4th ed.; Gold, V., Ed.; International Union of Pure and Applied Chemistry (IUPAC): Research Triangle Park, NC, 2019. <https://doi.org/10.1351/goldbook>.
- (54) Minkin, V. I. Glossary of Terms Used in Theoretical Organic Chemistry. *Pure Appl. Chem.* **1999**, *71* (10), 1919–1981. <https://doi.org/10.1351/pac199971101919>.
- (55) Cram, D. J.; Tanner, M. E.; Thomas, R. The Taming of Cyclobutadiene. *Angew. Chem. Int. Ed. Engl.* **1991**, *30* (8), 1024–1027. <https://doi.org/10.1002/anie.199110241>.
- (56) Masamune, S.; Souto-Bachiller, F. A.; Machiguchi, T.; Bertie, J. E. Cyclobutadiene Is Not Square. *J. Am. Chem. Soc.* **1978**, *100* (15), 4889–4891. <https://doi.org/10.1021/ja00483a043>.
- (57) Maier, G. Tetrahedrane and Cyclobutadiene. *Angew. Chem. Int. Ed. Engl.* **1988**, *27* (3), 309–332. <https://doi.org/10.1002/anie.198803093>.
- (58) Wu, J. I.; Fernández, I.; Mo, Y.; Schleyer, P. V. R. Why Cyclooctatetraene Is Highly Stabilized: The Importance of “Two-Way” (Double) Hyperconjugation. *J. Chem. Theory Comput.* **2012**, *8* (4), 1280–1287. <https://doi.org/10.1021/ct3000553>.
- (59) Kroeger, A. A.; Karton, A. Graphene-induced Planarization of Cyclooctatetraene Derivatives. *J. Comput. Chem.* **2022**, *43* (2), 96–105. <https://doi.org/10.1002/jcc.26774>.
- (60) Hopf, H. Pentalenes—From Highly Reactive Antiaromatics to Substrates for Material Science. *Angew. Chem. Int. Ed.* **2013**, *52* (47), 12224–12226. <https://doi.org/10.1002/anie.201307162>.

- (61) Konishi, A.; Okada, Y.; Nakano, M.; Sugisaki, K.; Sato, K.; Takui, T.; Yasuda, M. Synthesis and Characterization of Dibenzo[*a, f*]Pentalene: Harmonization of the Antiaromatic and Singlet Biradical Character. *J. Am. Chem. Soc.* **2017**, *139* (43), 15284–15287. <https://doi.org/10.1021/jacs.7b05709>.
- (62) Barker, J. E.; Price, T. W.; Karas, L. J.; Kishi, R.; MacMillan, S. N.; Zakharov, L. N.; Gómez-García, C. J.; Wu, J. I.; Nakano, M.; Haley, M. M. A Tale of Two Isomers: Enhanced Antiaromaticity/Diradical Character versus Deleterious Ring-Opening of Benzofuran-fused *s*-Indacenes and Dicyclopenta[*b, g*]Naphthalenes. *Angew. Chem. Int. Ed.* **2021**, *60* (41), 22385–22392. <https://doi.org/10.1002/anie.202107855>.
- (63) Berger, R. J. F.; Viel, A. The Symmetry Principle of Antiaromaticity. *Z. Für Naturforschung B* **2020**, *75* (4), 327–339. <https://doi.org/10.1515/znb-2020-0024>.
- (64) Charistos, N. D.; Papadopoulos, A. G.; Sigalas, M. P. Interpretation of Electron Delocalization in Benzene, Cyclobutadiene, and Borazine Based on Visualization of Individual Molecular Orbital Contributions to the Induced Magnetic Field. *J. Phys. Chem. A* **2014**, *118* (6), 1113–1122. <https://doi.org/10.1021/jp411410r>.
- (65) Barker, J. E.; Dressler, J. J.; Cárdenas Valdivia, A.; Kishi, R.; Strand, E. T.; Zakharov, L. N.; MacMillan, S. N.; Gómez-García, C. J.; Nakano, M.; Casado, J.; Haley, M. M. Molecule Isomerism Modulates the Diradical Properties of Stable Singlet Diradicaloids. *J. Am. Chem. Soc.* **2020**, *142* (3), 1548–1555. <https://doi.org/10.1021/jacs.9b11898>.
- (66) Hayashi, H.; Barker, J. E.; Cárdenas Valdivia, A.; Kishi, R.; MacMillan, S. N.; Gómez-García, C. J.; Miyauchi, H.; Nakamura, Y.; Nakano, M.; Kato, S.; Haley, M. M.; Casado, J. Monoradicals and Diradicals of Dibenzo[fluoreno[3,2-*b*]]fluorene Isomers: Mechanisms of Electronic Delocalization. *J. Am. Chem. Soc.* **2020**, *142* (48), 20444–20455. <https://doi.org/10.1021/jacs.0c09588>.
- (67) Dressler, J. J.; Cárdenas Valdivia, A.; Kishi, R.; Rudebusch, G. E.; Ventura, A. M.; Chastain, B. E.; Gómez-García, C. J.; Zakharov, L. N.; Nakano, M.; Casado, J.; Haley, M. M. Diindenoanthracene Diradicaloids Enable Rational, Incremental Tuning of Their Singlet-Triplet Energy Gaps. *Chem* **2020**, *6* (6), 1353–1368. <https://doi.org/10.1016/j.chempr.2020.02.010>.
- (68) Dressler, J. J.; Haley, M. M. Learning How to Fine-tune Diradical Properties by Structure Refinement. *J. Phys. Org. Chem.* **2020**, *33* (11), e4114. <https://doi.org/10.1002/poc.4114>.
- (69) Barker, J. E.; Frederickson, C. K.; Jones, M. H.; Zakharov, L. N.; Haley, M. M. Synthesis and Properties of Quinoidal Fluorenofluorenes. *Org. Lett.* **2017**, *19* (19), 5312–5315. <https://doi.org/10.1021/acs.orglett.7b02605>.
- (70) Frederickson, C. K.; Zakharov, L. N.; Haley, M. M. Modulating Paratropicity Strength in Diareno-Fused Antiaromatics. *J. Am. Chem. Soc.* **2016**, *138* (51), 16827–16838. <https://doi.org/10.1021/jacs.6b11397>.
- (71) Frederickson, C. K.; Rose, B. D.; Haley, M. M. Explorations of the Indenofluorenes and Expanded Quinoidal Analogues. *Acc. Chem. Res.* **2017**, *50* (4), 977–987. <https://doi.org/10.1021/acs.accounts.7b00004>.
- (72) Dressler, J. J.; Cárdenas Valdivia, A.; Kishi, R.; Rudebusch, G. E.; Ventura, A. M.; Chastain, B. E.; Gómez-García, C. J.; Zakharov, L. N.; Nakano, M.; Casado, J.; Haley, M. M. Diindenoanthracene Diradicaloids Enable Rational, Incremental Tuning of Their

- Singlet-Triplet Energy Gaps. *Chem* **2020**, *6* (6), 1353–1368. <https://doi.org/10.1016/j.chempr.2020.02.010>.
- (73) Karas, L. J.; Jalife, S.; Viesser, R. V.; Soares, J. V.; Haley, M. M.; Wu, J. I. Tetra- *Tert* -butyl- *S*-Indacene Is a Bond-Localized C_{2h} Structure and a Challenge for Computational Chemistry. *Angew. Chem. Int. Ed.* **2023**, *62* (36), e202307379. <https://doi.org/10.1002/anie.202307379>.
- (74) Barker, J. E.; Kodama, T.; Song, M. K.; Frederickson, C. K.; Jousselin-Oba, T.; Zakharov, L. N.; Marrot, J.; Frigoli, M.; Johnson, R. P.; Haley, M. M. Serendipitous Rediscovery of the Facile Cyclization of *Z*, *Z* -3,5-Octadiene-1,7-diyne Derivatives to Afford Stable, Substituted Naphthocyclobutadienes. *ChemPlusChem* **2019**, *84* (6), 665–672. <https://doi.org/10.1002/cplu.201800605>.
- (75) Bergman, H. M.; Beattie, D. D.; Handford, R. C.; Rossomme, E.; Suslick, B. A.; Head-Gordon, M.; Cundari, T. R.; Liu, Y.; Tilley, T. D. Copper(III) Metallacyclopentadienes via Zirconocene Transfer and Reductive Elimination to an Isolable Phenanthrocyclobutadiene. *J. Am. Chem. Soc.* **2022**, *144* (22), 9853–9858. <https://doi.org/10.1021/jacs.2c02581>.
- (76) Bergman, H. M.; Beattie, D. D.; Handford, R. C.; Rossomme, E.; Suslick, B. A.; Head-Gordon, M.; Cundari, T. R.; Liu, Y.; Tilley, T. D. Copper(III) Metallacyclopentadienes via Zirconocene Transfer and Reductive Elimination to an Isolable Phenanthrocyclobutadiene. *J. Am. Chem. Soc.* **2022**, *144* (22), 9853–9858. <https://doi.org/10.1021/jacs.2c02581>.
- (77) Bergman, H. M.; Fan, A.; Jones, C. G.; Rothenberger, A. J.; Jha, K. K.; Handford, R. C.; Nelson, H. M.; Liu, Y.; Tilley, T. D. A New Topological Class of Interlocked and Interwoven Nanocarbons via Dynamic C-C Bond Formation. *Chemistry* March 20, 2024. <https://doi.org/10.26434/chemrxiv-2024-bvxjg-v2>.
- (78) Mizuno, Y.; Nogata, A.; Suzuki, M.; Nakayama, K.; Hisaki, I.; Kishi, R.; Konishi, A.; Yasuda, M. Synthesis and Characterization of Dibenzothieno[*a*, *f*]Pentalenes Enabling Large Antiaromaticity and Moderate Open-Shell Character through a Small Energy Barrier for Bond-Shift Valence Tautomerization. *J. Am. Chem. Soc.* **2023**, *145* (37), 20595–20609. <https://doi.org/10.1021/jacs.3c07356>.
- (79) Dressler, J. J.; Barker, J. E.; Karas, L. J.; Hashimoto, H. E.; Kishi, R.; Zakharov, L. N.; MacMillan, S. N.; Gomez-Garcia, C. J.; Nakano, M.; Wu, J. I.; Haley, M. M. Late-Stage Modification of Electronic Properties of Antiaromatic and Diradicaloid Indeno[1,2- *b*]Fluorene Analogues via Sulfur Oxidation. *J. Org. Chem.* **2020**, *85* (16), 10846–10857. <https://doi.org/10.1021/acs.joc.0c01387>.
- (80) Dressler, J. J.; Haley, M. M. Learning How to Fine-tune Diradical Properties by Structure Refinement. *J. Phys. Org. Chem.* **2020**, *33* (11), e4114. <https://doi.org/10.1002/poc.4114>.
- (81) Dressler, J. J.; Barker, J. E.; Karas, L. J.; Hashimoto, H. E.; Kishi, R.; Zakharov, L. N.; MacMillan, S. N.; Gomez-Garcia, C. J.; Nakano, M.; Wu, J. I.; Haley, M. M. Late-Stage Modification of Electronic Properties of Antiaromatic and Diradicaloid Indeno[1,2- *b*]Fluorene Analogues via Sulfur Oxidation. *J. Org. Chem.* **2020**, *85* (16), 10846–10857. <https://doi.org/10.1021/acs.joc.0c01387>.
- (82) Moles Quintero, S.; Haley, M. M.; Kertesz, M.; Casado, J. Polycyclic Hydrocarbons from [4 *n*]Annulenes: Correlation versus Hybridization Forces in the Formation of

- Diradicaloids. *Angew. Chem. Int. Ed.* **2022**, *61* (44), e202209138. <https://doi.org/10.1002/anie.202209138>.
- (83) Rose, B. D.; Vonnegut, C. L.; Zakharov, L. N.; Haley, M. M. Fluoreno[4,3-*c*]Fluorene: A Closed-Shell, Fully Conjugated Hydrocarbon. *Org. Lett.* **2012**, *14* (9), 2426–2429. <https://doi.org/10.1021/ol300942z>.
- (84) Rudebusch, G. E.; Zafra, J. L.; Jorner, K.; Fukuda, K.; Marshall, J. L.; Arrechea-Marcos, I.; Espejo, G. L.; Ponce Ortiz, R.; Gómez-García, C. J.; Zakharov, L. N.; Nakano, M.; Ottosson, H.; Casado, J.; Haley, M. M. Diindeno-Fusion of an Anthracene as a Design Strategy for Stable Organic Biradicals. *Nat. Chem.* **2016**, *8* (8), 753–759. <https://doi.org/10.1038/nchem.2518>.
- (85) Rudebusch, G. E.; Espejo, G. L.; Zafra, J. L.; Peña-Alvarez, M.; Spisak, S. N.; Fukuda, K.; Wei, Z.; Nakano, M.; Petrukhina, M. A.; Casado, J.; Haley, M. M. A Biradical Balancing Act: Redox Amphoterism in a Diindenoanthracene Derivative Results from Quinoidal Acceptor and Aromatic Donor Motifs. *J. Am. Chem. Soc.* **2016**, *138* (38), 12648–12654. <https://doi.org/10.1021/jacs.6b07882>.
- (86) Zhou, Q.; Carroll, P. J.; Swager, T. M. Synthesis of Diacetylene Macrocycles Derived from 1,2-Diethynyl Benzene Derivatives: Structure and Reactivity of the Strained Cyclic Dimer. *J. Org. Chem.* **1994**, *59* (6), 1294–1301. <https://doi.org/10.1021/jo00085a016>.
- (87) Dressler, J. J.; Zhou, Z.; Marshall, J. L.; Kishi, R.; Takamuku, S.; Wei, Z.; Spisak, S. N.; Nakano, M.; Petrukhina, M. A.; Haley, M. M. Synthesis of the Unknown Indeno[1,2-*a*]Fluorene Regioisomer: Crystallographic Characterization of Its Dianion. *Angew. Chem. Int. Ed.* **2017**, *56* (48), 15363–15367. <https://doi.org/10.1002/anie.201709282>.
- (88) Fix, A. G.; Deal, P. E.; Vonnegut, C. L.; Rose, B. D.; Zakharov, L. N.; Haley, M. M. Indeno[2,1-*c*]Fluorene: A New Electron-Accepting Scaffold for Organic Electronics. *Org. Lett.* **2013**, *15* (6), 1362–1365. <https://doi.org/10.1021/ol400318z>.
- (89) Chase, D. T.; Rose, B. D.; McClintock, S. P.; Zakharov, L. N.; Haley, M. M. Indeno[1,2-*b*]Fluorenes: Fully Conjugated Antiaromatic Analogues of Acenes. *Angew. Chem. Int. Ed.* **2011**, *50* (5), 1127–1130. <https://doi.org/10.1002/anie.201006312>.
- (90) Chase, D. T.; Fix, A. G.; Kang, S. J.; Rose, B. D.; Weber, C. D.; Zhong, Y.; Zakharov, L. N.; Lonergan, M. C.; Nuckolls, C.; Haley, M. M. 6,12-Diarylindeno[1,2-*b*]Fluorenes: Syntheses, Photophysics, and Ambipolar OFETs. *J. Am. Chem. Soc.* **2012**, *134* (25), 10349–10352. <https://doi.org/10.1021/ja303402p>.
- (91) Rose, B. D.; Chase, D. T.; Weber, C. D.; Zakharov, L. N.; Lonergan, M. C.; Haley, M. M. Synthesis, Crystal Structures, and Photophysical Properties of Electron-Accepting Diethynylindeno[1,2-*b*]fluorenediones. *Org. Lett.* **2011**, *13* (8), 2106–2109. <https://doi.org/10.1021/ol200525g>.
- (92) Frederickson, C. K.; Rose, B. D.; Haley, M. M. Explorations of the Indeno[1,2-*b*]fluorenes and Expanded Quinoidal Analogues. *Acc. Chem. Res.* **2017**, *50* (4), 977–987. <https://doi.org/10.1021/acs.accounts.7b00004>.
- (93) Miller, M. P.; Haley, M. M. Computational Comparison of Paratropicity Trends in Antiaromatic *s*-indacene Derivatives: Does the Functional “Make All the Difference”? *J. Phys. Org. Chem.* **2025**, *38* (2), e4648. <https://doi.org/10.1002/poc.4648>.
- (94) Rose, B. D.; Shoer, L. E.; Wasielewski, M. R.; Haley, M. M. Unusually Short Excited State Lifetimes of Indeno[1,2-*b*]fluorene and Fluoreno[1,2-*b*]fluorene Derivatives Result from a Conical

- Intersection. *Chem. Phys. Lett.* **2014**, *616–617*, 137–141. <https://doi.org/10.1016/j.cplett.2014.10.031>.
- (95) Rudebusch, G. E.; Zafra, J. L.; Jorner, K.; Fukuda, K.; Marshall, J. L.; Arrechea-Marcos, I.; Espejo, G. L.; Ponce Ortiz, R.; Gómez-García, C. J.; Zakharov, L. N.; Nakano, M.; Ottosson, H.; Casado, J.; Haley, M. M. Diindeno-Fusion of an Anthracene as a Design Strategy for Stable Organic Biradicals. *Nat. Chem.* **2016**, *8* (8), 753–759. <https://doi.org/10.1038/nchem.2518>.
- (96) Rudebusch, G. E.; Espejo, G. L.; Zafra, J. L.; Peña-Alvarez, M.; Spisak, S. N.; Fukuda, K.; Wei, Z.; Nakano, M.; Petrukhina, M. A.; Casado, J.; Haley, M. M. A Biradical Balancing Act: Redox Amphoterism in a Diindenoanthracene Derivative Results from Quinoidal Acceptor and Aromatic Donor Motifs. *J. Am. Chem. Soc.* **2016**, *138* (38), 12648–12654. <https://doi.org/10.1021/jacs.6b07882>.
- (97) Dressler, J. J.; Teraoka, M.; Espejo, G. L.; Kishi, R.; Takamuku, S.; Gómez-García, C. J.; Zakharov, L. N.; Nakano, M.; Casado, J.; Haley, M. M. Thiophene and Its Sulfur Inhibit Indenoindenodibenzothiophene Diradicals from Low-Energy Lying Thermal Triplets. *Nat. Chem.* **2018**, *10* (11), 1134–1140. <https://doi.org/10.1038/s41557-018-0133-5>.
- (98) Barker, J. E.; Dressler, J. J.; Cárdenas Valdivia, A.; Kishi, R.; Strand, E. T.; Zakharov, L. N.; MacMillan, S. N.; Gómez-García, C. J.; Nakano, M.; Casado, J.; Haley, M. M. Molecule Isomerism Modulates the Diradical Properties of Stable Singlet Diradicaloids. *J. Am. Chem. Soc.* **2020**, *142* (3), 1548–1555. <https://doi.org/10.1021/jacs.9b11898>.
- (99) Hayashi, H.; Barker, J. E.; Cárdenas Valdivia, A.; Kishi, R.; MacMillan, S. N.; Gómez-García, C. J.; Miyauchi, H.; Nakamura, Y.; Nakano, M.; Kato, S.; Haley, M. M.; Casado, J. Monoradicals and Diradicals of Dibenzofluoreno[3,2-*b*]Fluorene Isomers: Mechanisms of Electronic Delocalization. *J. Am. Chem. Soc.* **2020**, *142* (48), 20444–20455. <https://doi.org/10.1021/jacs.0c09588>.
- (100) Dressler, J. J.; Cárdenas Valdivia, A.; Kishi, R.; Rudebusch, G. E.; Ventura, A. M.; Chastain, B. E.; Gómez-García, C. J.; Zakharov, L. N.; Nakano, M.; Casado, J.; Haley, M. M. Diindenoanthracene Diradicaloids Enable Rational, Incremental Tuning of Their Singlet-Triplet Energy Gaps. *Chem* **2020**, *6* (6), 1353–1368. <https://doi.org/10.1016/j.chempr.2020.02.010>.
- (101) Dressler, J. J.; Teraoka, M.; Espejo, G. L.; Kishi, R.; Takamuku, S.; Gómez-García, C. J.; Zakharov, L. N.; Nakano, M.; Casado, J.; Haley, M. M. Thiophene and Its Sulfur Inhibit Indenoindenodibenzothiophene Diradicals from Low-Energy Lying Thermal Triplets. *Nat. Chem.* **2018**, *10* (11), 1134–1140. <https://doi.org/10.1038/s41557-018-0133-5>.
- (102) Hayashi, H.; Barker, J. E.; Cárdenas Valdivia, A.; Kishi, R.; MacMillan, S. N.; Gómez-García, C. J.; Miyauchi, H.; Nakamura, Y.; Nakano, M.; Kato, S.; Haley, M. M.; Casado, J. Monoradicals and Diradicals of Dibenzofluoreno[3,2-*b*]Fluorene Isomers: Mechanisms of Electronic Delocalization. *J. Am. Chem. Soc.* **2020**, *142* (48), 20444–20455. <https://doi.org/10.1021/jacs.0c09588>.
- (103) Moles Quintero, S.; Haley, M. M.; Kertesz, M.; Casado, J. Polycyclic Hydrocarbons from [4 *n*]Annulenes: Correlation versus Hybridization Forces in the Formation of Diradicaloids. *Angew. Chem. Int. Ed.* **2022**, *61* (44), e202209138. <https://doi.org/10.1002/anie.202209138>.

- (104) Warren, G. I.; Barker, J. E.; Zakharov, L. N.; Haley, M. M. Enhancing the Antiaromaticity of *s*-Indacene through Naphthothiophene Fusion. *Org. Lett.* **2021**, *23* (13), 5012–5017. <https://doi.org/10.1021/acs.orglett.1c01514>.
- (105) Warren, G. I.; Zocchi, L. J.; Zakharov, L. N.; Haley, M. M. Comparison of Antiaromatic Properties in a Series of Structurally Isomeric Naphthothiophene-Fused *s*-Indacenes. *Chem. – Eur. J.* **2023**, *29* (40), e202301153. <https://doi.org/10.1002/chem.202301153>.
- (106) Warren, G. I.; Młodzikowska-Pieńko, K.; Jalife, S.; Demachkie, I. S.; Wu, J. I.; Haley, M. M.; Gershoni-Poranne, R. Effects of Benzoheterocyclic Annulation on the *s*-Indacene Core: A Computational Analysis. *Chem. Sci.* **2025**, *16* (2), 575–583. <https://doi.org/10.1039/D4SC06812B>.
- (107) Jin, Z.; Yao, Z.; Barker, K. P.; Pei, J.; Xia, Y. Dinaphthobenzo[1,2:4,5]Dicyclobutadiene: Antiaromatic and Orthogonally Tunable Electronics and Packing. *Angew. Chem.* **2019**, *131* (7), 2056–2061. <https://doi.org/10.1002/ange.201812581>.
- (108) Teo, Y. C.; Jin, Z.; Xia, Y. Synthesis of Cyclobutadienoid-Fused Phenazines with Strongly Modulated Degrees of Antiaromaticity. *Org. Lett.* **2018**, *20* (11), 3300–3304. <https://doi.org/10.1021/acs.orglett.8b01190>.
- (109) Dai, G.; Chang, J.; Zhang, W.; Bai, S.; Huang, K.-W.; Xu, J.; Chi, C. Dianthraceno[a,e]Pentalenes: Synthesis, Crystallographic Structures and Applications in Organic Field-Effect Transistors. *Chem. Commun.* **2015**, *51* (3), 503–506. <https://doi.org/10.1039/C4CC07630C>.
- (110) Gazdag, T.; Mayer, P. J.; Kalapos, P. P.; Holczbauer, T.; El Bakouri, O.; London, G. Unsymmetrical Thienopentalenes: Synthesis, Optoelectronic Properties, and (Anti)Aromaticity Analysis. *ACS Omega* **2022**, *7* (10), 8336–8349. <https://doi.org/10.1021/acsomega.1c05618>.
- (111) Nakano, M.; Osaka, I.; Takimiya, K.; Koganezawa, T. Novel Dibenz[a,e]Pentalene-Based Conjugated Polymers. *J Mater Chem C* **2014**, *2* (1), 64–70. <https://doi.org/10.1039/C3TC31630K>.
- (112) Saha, H. K.; Mallick, D.; Das, S. Dibenzoheterole-Fused *s*-Indacenes. *J. Org. Chem.* **2023**, *88* (23), 16248–16258. <https://doi.org/10.1021/acs.joc.3c01719>.
- (113) Gershoni-Poranne, R.; Stanger, A. Magnetic Criteria of Aromaticity. *Chem Soc Rev* **2015**, *44* (18), 6597–6615. <https://doi.org/10.1039/C5CS00114E>.
- (114) Chase, D. T.; Rose, B. D.; McClintock, S. P.; Zakharov, L. N.; Haley, M. M. Indeno[1,2-*b*]Fluorenes: Fully Conjugated Antiaromatic Analogues of Acenes. *Angew. Chem. Int. Ed.* **2011**, *50* (5), 1127–1130. <https://doi.org/10.1002/anie.201006312>.
- (115) Warren, G. I. Enhancing the Antiaromaticity of *s*-Indacenes Through Heterocycle Fusion. Dissertation, Univeristy of Oregon, 2024. <https://scholarsbank.uoregon.edu/items/5b1b6e61-2ce4-4fb6-bd6c-3fd37b53f98c>.
- (116) Rose, B. D.; Chase, D. T.; Weber, C. D.; Zakharov, L. N.; Lonergan, M. C.; Haley, M. M. Synthesis, Crystal Structures, and Photophysical Properties of Electron-Accepting Diethynylindenofluorenediones. *Org. Lett.* **2011**, *13* (8), 2106–2109. <https://doi.org/10.1021/ol200525g>.
- (117) Rose, B. D.; Santa Maria, P. J.; Fix, A. G.; Vonnegut, C. L.; Zakharov, L. N.; Parkin, S. R.; Haley, M. M. Scalable Synthesis of 5,11-Diethynylated Indeno[1,2-*b*]Fluorene-6,12-Diones and Exploration of Their Solid State Packing. *Beilstein J. Org. Chem.* **2014**, *10*, 2122–2130. <https://doi.org/10.3762/bjoc.10.219>.

- (118) Chase, D. T.; Fix, A. G.; Rose, B. D.; Weber, C. D.; Nobusue, S.; Stockwell, C. E.; Zakharov, L. N.; Lonergan, M. C.; Haley, M. M. Electron-Accepting 6,12-Diethynylindeno[1,2- *b*]Fluorenes: Synthesis, Crystal Structures, and Photophysical Properties. *Angew. Chem. Int. Ed.* **2011**, *50* (47), 11103–11106. <https://doi.org/10.1002/anie.201104797>.
- (119) Dressler, J. J.; Teraoka, M.; Espejo, G. L.; Kishi, R.; Takamuku, S.; Gómez-García, C. J.; Zakharov, L. N.; Nakano, M.; Casado, J.; Haley, M. M. Thiophene and Its Sulfur Inhibit Indenoindenodibenzothiophene Diradicals from Low-Energy Lying Thermal Triplets. *Nat. Chem.* **2018**, *10* (11), 1134–1140. <https://doi.org/10.1038/s41557-018-0133-5>.
- (120) Rose, B. D.; Chase, D. T.; Weber, C. D.; Zakharov, L. N.; Lonergan, M. C.; Haley, M. M. Synthesis, Crystal Structures, and Photophysical Properties of Electron-Accepting Diethynylindeno[1,2-*b*]fluorenediones. *Org. Lett.* **2011**, *13* (8), 2106–2109. <https://doi.org/10.1021/ol200525g>.
- (121) Gimarc, B. M. Topological Charge Stabilization. *J. Am. Chem. Soc.* **1983**, *105* (7), 1979–1984. <https://doi.org/10.1021/ja00345a053>.
- (122) *GIMIC interpretation*. Github. <https://gimic.readthedocs.io/en/latest/interpretation.html> (accessed 2025-02-17).
- (123) Demachkie, I. S.; Miller, M. P.; Warren, G. I.; Barker, J. E.; Strand, E. T.; Zakharov, L. N.; Haley, M. M. Intramolecular Charge Transfer in Antiaromatic Donor/Acceptor-Fused *s*-Indacenes. *Angew. Chem. Int. Ed.* **2024**, e202420989. <https://doi.org/10.1002/anie.202420989>.
- (124) Krygowski, T. M.; Cyrański, M. K.; Czarnocki, Z.; Häfelinger, G.; Katritzky, A. R. Aromaticity: A Theoretical Concept of Immense Practical Importance. *Tetrahedron* **2000**, *56* (13), 1783–1796. [https://doi.org/10.1016/S0040-4020\(99\)00979-5](https://doi.org/10.1016/S0040-4020(99)00979-5).
- (125) Breslow, Ronald.; Brown, John.; Gajewski, J. J. Antiaromaticity of Cyclopropenyl Anions. *J. Am. Chem. Soc.* **1967**, *89* (17), 4383–4390. <https://doi.org/10.1021/ja00993a023>.
- (126) Frederickson, C. K.; Rose, B. D.; Haley, M. M. Explorations of the Indeno[1,2-*b*]fluorenes and Expanded Quinoidal Analogues. *Acc. Chem. Res.* **2017**, *50* (4), 977–987. <https://doi.org/10.1021/acs.accounts.7b00004>.
- (127) Marshall, J. L.; Uchida, K.; Frederickson, C. K.; Schütt, C.; Zeidell, A. M.; Goetz, K. P.; Finn, T. W.; Jarolimek, K.; Zakharov, L. N.; Risko, C.; Herges, R.; Jurchescu, O. D.; Haley, M. M. Indacenodibenzothiophenes: Synthesis, Optoelectronic Properties and Materials Applications of Molecules with Strong Antiaromatic Character. *Chem. Sci.* **2016**, *7* (8), 5547–5558. <https://doi.org/10.1039/C6SC00950F>.
- (128) Leliège, A.; Régent, C.-H. L.; Allain, M.; Blanchard, P.; Roncali, J. Structural Modulation of Internal Charge Transfer in Small Molecular Donors for Organic Solar Cells. *Chem. Commun.* **2012**, *48* (71), 8907. <https://doi.org/10.1039/c2cc33921h>.
- (129) Panahi, F.; Mahmoodi, A.; Ghodrati, S.; Eshghi, F. A Novel Donor- π -Acceptor Halochromic 2,6-Distyrylnaphthalene Chromophore: Synthesis, Photophysical Properties and DFT Studies. *RSC Adv.* **2021**, *11* (1), 168–176. <https://doi.org/10.1039/D0RA08508A>.
- (130) Zhang, J.; Xu, W.; Sheng, P.; Zhao, G.; Zhu, D. Organic Donor-Acceptor Complexes as Novel Organic Semiconductors. *Acc. Chem. Res.* **2017**, *50* (7), 1654–1662. <https://doi.org/10.1021/acs.accounts.7b00124>.

- (131) Misra, R.; Bhattacharyya, S. P. *Intramolecular Charge Transfer: Theory and Applications*, 1st ed.; Wiley, 2018. <https://doi.org/10.1002/9783527801916>.
- (132) Samanta, P. K.; Misra, R. Intramolecular Charge Transfer for Optical Applications. *J. Appl. Phys.* **2023**, *133* (2), 020901. <https://doi.org/10.1063/5.0131426>.
- (133) Wu, Y.; Bureš, F.; Jarowski, P. D.; Schweizer, W. B.; Boudon, C.; Gisselbrecht, J.; Diederich, F. Proaromaticity: Organic Charge-Transfer Chromophores with Small HOMO–LUMO Gaps. *Chem. – Eur. J.* **2010**, *16* (31), 9592–9605. <https://doi.org/10.1002/chem.201001051>.
- (134) Gorman, C. B.; Marder, S. R. An Investigation of the Interrelationships between Linear and Nonlinear Polarizabilities and Bond-Length Alternation in Conjugated Organic Molecules. *Proc. Natl. Acad. Sci.* **1993**, *90* (23), 11297–11301. <https://doi.org/10.1073/pnas.90.23.11297>.
- (135) Frederickson, C. K.; Haley, M. M. Synthesis and Optoelectronic Properties of Indeno[1,2-*b*]Fluorene-6,12-Dione Donor–Acceptor–Donor Triads. *J. Org. Chem.* **2014**, *79* (22), 11241–11245. <https://doi.org/10.1021/jo502009p>.
- (136) Grenz, D. C.; Schmidt, M.; Kratzert, D.; Esser, B. Dibenzo[*a, e*]Pentalenes with Low-Lying LUMO Energy Levels as Potential n-Type Materials. *J. Org. Chem.* **2018**, *83* (2), 656–663. <https://doi.org/10.1021/acs.joc.7b02250>.
- (137) Schipper, D. J.; Moh, L. C. H.; Müller, P.; Swager, T. M. Dithiolodithiole as a Building Block for Conjugated Materials. *Angew. Chem. Int. Ed.* **2014**, *53* (23), 5847–5851. <https://doi.org/10.1002/anie.201310290>.
- (138) Wilbuer, J.; Grenz, D. C.; Schnakenburg, G.; Esser, B. Donor- and Acceptor-Functionalized Dibenzo[*a, e*]Pentalenes: Modulation of the Electronic Band Gap. *Org. Chem. Front.* **2017**, *4* (5), 658–663. <https://doi.org/10.1039/C6QO00487C>.
- (139) Zeng, Y.; Duan, R.; Guo, Y.; Han, G.; Li, Q.; Yi, Y. Electronic, Optical, and Charge Transport Properties of A- π -A Electron Acceptors for Organic Solar Cells: Impact of Anti-Aromatic π Structures. *Chin. Chem. Lett.* **2019**, *30* (1), 211–216. <https://doi.org/10.1016/j.ccllet.2018.05.029>.
- (140) Gao, K.; Li, L.; Lai, T.; Xiao, L.; Huang, Y.; Huang, F.; Peng, J.; Cao, Y.; Liu, F.; Russell, T. P.; Janssen, R. A. J.; Peng, X. Deep Absorbing Porphyrin Small Molecule for High-Performance Organic Solar Cells with Very Low Energy Losses. *J. Am. Chem. Soc.* **2015**, *137* (23), 7282–7285. <https://doi.org/10.1021/jacs.5b03740>.
- (141) Wu, J.; Chen, Y.; Liu, J.; Pang, Z.; Li, G.; Lu, Z.; Huang, Y.; Facchetti, A.; Marks, T. J. Tuning the Antiaromatic Character and Charge Transport of Pentalene-Based Antiaromatic Compounds by Substitution. *J. Mater. Chem. C* **2022**, *10* (7), 2724–2731. <https://doi.org/10.1039/D1TC03156B>.
- (142) Gazdag, T.; Meiszter, E.; Mayer, P. J.; Holczbauer, T.; Ottosson, H.; Maurer, A. B.; Abrahamsson, M.; London, G. An Exploration of Substituent Effects on the Photophysical Properties of Monobenzopentalenes. *ChemPhysChem* **2024**, *25* (7), e202300737. <https://doi.org/10.1002/cphc.202300737>.
- (143) Sharma, H.; Ankita; Mittal, V.; Pandey, U. K.; Das, S. Syntheses and Properties of Hole-Transporting Biindenofluorenes. *Org. Lett.* **2024**, *26* (13), 2617–2622. <https://doi.org/10.1021/acs.orglett.4c00630>.

- (144) Payne, M. M.; Parkin, S. R.; Anthony, J. E. Functionalized Higher Acenes: Hexacene and Heptacene. *J. Am. Chem. Soc.* **2005**, *127* (22), 8028–8029. <https://doi.org/10.1021/ja051798v>.
- (145) Lehnher, D.; Waterloo, A. R.; Goetz, K. P.; Payne, M. M.; Hampel, F.; Anthony, J. E.; Jurchescu, O. D.; Tykwinski, R. R. Isomerically Pure *Syn*-Anthradithiophenes: Synthesis, Properties, and FET Performance. *Org. Lett.* **2012**, *14* (14), 3660–3663. <https://doi.org/10.1021/ol301503k>.
- (146) Marshall, J. L.; O’Neal, N. J.; Zakharov, L. N.; Haley, M. M. Synthesis and Characterization of Two Unsymmetrical Indenofluorene Analogues: Benzo[5,6]-*s*-Indaceno[1,2-*b*]Thiophene and Benzo[5,6]-*s*-Indaceno[2,1-*b*]Thiophene. *J. Org. Chem.* **2016**, *81* (9), 3674–3680. <https://doi.org/10.1021/acs.joc.6b00340>.
- (147) Shi, X.; Kueh, W.; Zheng, B.; Huang, K.; Chi, C. Dipolar Quinoidal Acene Analogues as Stable Isoelectronic Structures of Pentacene and Nonacene. *Angew. Chem. Int. Ed.* **2015**, *54* (48), 14412–14416. <https://doi.org/10.1002/anie.201507573>.
- (148) Kueh, W.; Shi, X.; Phua, T. W.; Kueh, H.; Liao, Y. C.; Chi, C. π -Extended S-Heterocyclic Naphthoquinodimethane with Dual Diradical and Dipolar Character. *Org. Lett.* **2022**, *24* (32), 5935–5940. <https://doi.org/10.1021/acs.orglett.2c02188>.
- (149) Mladenova, M.; Ventelon, L.; Blanchard-Desce, M. A Convenient Synthesis of Push-Pull Polyenes Designed for the Elaboration of Efficient Nonlinear Optical Materials. *Tetrahedron Lett.* **1999**, *40* (38), 6923–6926. [https://doi.org/10.1016/S0040-4039\(99\)01443-4](https://doi.org/10.1016/S0040-4039(99)01443-4).
- (150) Blanchard-Desce, M.; Alain, V.; Bedworth, P. V.; Marder, S. R.; Fort, A.; Runser, C.; Barzoukas, M.; Lebus, S.; Wortmann, R. Large Quadratic Hyperpolarizabilities with Donor–Acceptor Polyenes Exhibiting Optimum Bond Length Alternation: Correlation Between Structure and Hyperpolarizability. *Chem. – Eur. J.* **1997**, *3* (7), 1091–1104. <https://doi.org/10.1002/chem.19970030717>.
- (151) Gershoni-Poranne, R.; Rahalkar, A. P.; Stanger, A. The Predictive Power of Aromaticity: Quantitative Correlation between Aromaticity and Ionization Potentials and HOMO–LUMO Gaps in Oligomers of Benzene, Pyrrole, Furan, and Thiophene. *Phys. Chem. Chem. Phys.* **2018**, *20* (21), 14808–14817. <https://doi.org/10.1039/C8CP02162G>.
- (152) Bredas, J.-L. Mind the Gap! *Mater Horiz* **2014**, *1* (1), 17–19. <https://doi.org/10.1039/C3MH00098B>.
- (153) Leary, E.; Roldán-Piñero, C.; Rico-Sánchez-Mateos, R.; Zotti, L. A. Antiaromatic Non-Alternant Heterocyclic Compounds as Molecular Wires. *J. Mater. Chem. C* **2024**, *12* (12), 4306–4315. <https://doi.org/10.1039/D3TC04266A>.
- (154) Bredas, J.-L. Mind the Gap! *Mater Horiz* **2014**, *1* (1), 17–19. <https://doi.org/10.1039/C3MH00098B>.
- (155) Modular Synthesis of Hexaaryl-*s*-Indacene. *Synfacts* **2023**, *19* (06), 0559. <https://doi.org/10.1055/s-0042-1751912>.
- (156) Young, B. S.; Chase, D. T.; Marshall, J. L.; Vonnegut, C. L.; Zakharov, L. N.; Haley, M. M. Synthesis and Properties of Fully-Conjugated Indacenedithiophenes. *Chem Sci* **2014**, *5* (3), 1008–1014. <https://doi.org/10.1039/C3SC53181C>.
- (157) Garner, M. H.; Blaskovits, J. T.; Corminboeuf, C. Double-Bond Delocalization in Non-Alternant Hydrocarbons Induces Inverted Singlet–Triplet Gaps. *Chem. Sci.* **2023**, *14* (38), 10458–10466. <https://doi.org/10.1039/D3SC03409G>.

- (158) Nakajima, T.; Saijo, T.; Yamaguchi, H. Bond Length Alternation in S-Indacene. *Tetrahedron* **1964**, *20* (9), 2119–2124. [https://doi.org/10.1016/S0040-4020\(01\)98485-6](https://doi.org/10.1016/S0040-4020(01)98485-6).
- (159) Günther, K.; Grabicki, N.; Battistella, B.; Grubert, L.; Dumele, O. An All-Organic Photochemical Magnetic Switch with Bistable Spin States. *J. Am. Chem. Soc.* **2022**, *144* (19), 8707–8716. <https://doi.org/10.1021/jacs.2c02195>.
- (160) Van Noorden, R.; Castelvechi, D. World's Tiniest Machines Win Chemistry Nobel. *Nature* **2016**, *538* (7624), 152–153. <https://doi.org/10.1038/nature.2016.20734>.
- (161) Kudernac, T.; Ruangsapapichat, N.; Parschau, M.; Maciá, B.; Katsonis, N.; Harutyunyan, S. R.; Ernst, K.-H.; Feringa, B. L. Electrically Driven Directional Motion of a Four-Wheeled Molecule on a Metal Surface. *Nature* **2011**, *479* (7372), 208–211. <https://doi.org/10.1038/nature10587>.
- (162) Feringa, B. L. The Art of Building Small: From Molecular Switches to Molecular Motors. *J. Org. Chem.* **2007**, *72* (18), 6635–6652. <https://doi.org/10.1021/jo070394d>.
- (163) Day, R. W.; Bediako, D. K.; Rezaee, M.; Parent, L. R.; Skorupskii, G.; Arguilla, M. Q.; Hendon, C. H.; Stassen, I.; Gianneschi, N. C.; Kim, P.; Dincă, M. Single Crystals of Electrically Conductive Two-Dimensional Metal–Organic Frameworks: Structural and Electrical Transport Properties. *ACS Cent. Sci.* **2019**, *5* (12), 1959–1964. <https://doi.org/10.1021/acscentsci.9b01006>.